Mechanics of the Pad-Abrasive-Wafer Contact in Chemical Mechanical Polishing

A Dissertation Presented

by

Dinçer Bozkaya

to

The Department of Mechanical and Industrial Engineering

in partial fulfillment of the requirements
for the degree of

Doctor of Philosophy

in

Mechanical Engineering

Northeastern University
Boston, Massachusetts

May, 2009

NORTHEASTERN UNIVERSITY

Graduate School of Engineering

Dissertation Title: Mechanics of the Pad-Abrasive-Wafer Contact in Chemical Mechanical Polishing

Author: Dinçer Bozkaya

Department: Mechanical and Industrial Engineering

Approved for Dissertation Requirement for the Doctor of Philosophy Degree

Professor Sinan Müftü, Thesis Adviser	Date
Professor George G. Adams, Thesis Committee Member	Date
Professor Ahmed Busnaina, Thesis Committee Member	Date
Professor Kai-Tak Wan, Thesis Committee Member	Date
Professor Katherine Ziemer, Thesis Committee Member	Date
Department Chair: Professor Hameed Metghalchi	Date

Graduate School Notified of Acceptance:

Director of the Graduate School: Professor Yaman Yener	Date

Biography

The author was born on April 29th, 1979, in Mersin, Turkey. He completed his elementary school and high school education in Barbaros Elementary School and Içel Anatolian High School.

He received a BS degree from the Department of Mechanical Engineering of the Middle East Technical University, Ankara, Turkey. After graduating in 2001, he worked as a research assistant in the Mechanical and Industrial Engineering Department of Northerastern University, Boston, MA, while he studied toward an MS degree under the supervision of Professor Sinan Müftü. His MS thesis research was concerned with the biomechanics of dental implants, where he applied finite-element method to evaluate the stresses induced in bone by the implants and different implant-abutment connection mechanisms. He was awarded an MS degree in 2003. In the fall of 2003, he started his PhD studies in the Mechanical and Industrial Engineering Department of Northeastern University under the supervision of Professor Sinan Müftü. He worked as a teaching assistant until June 2004, when he started to work at H.C. Starck Inc. as a research engineer while continuing PhD studies as a part-time student. His PhD studies concentrated on the contact mechanics and finite element modeling of interactions between pad, abrasive and wafer in Chemical Mechanical Polishing (CMP).

Acknowledgements

I would like to express my deepest gratitude to my thesis advisor, Professor Sinan Müftü, for his excellent guidance and patience throughout this study. This dissertation would have never been completed without his friendship and support. I also would like to thank my thesis committee members for their comments that resulted in significant improvements in this work.

The financial support provided by H.C. Starck Inc. is gratefully acknowledged. I would like to thank my colleague and friend Peter Jepson for his encouragement and support. I extend my great appreciation for the support of my friends Seval and Barış Deniz, and Troy Efe Deniz who helped with the programming of this work at the age of 1.

This work would not be possible without the support and love of my family, specifically my mother and father.

I would like to dedicate this thesis to my love and beautiful wife Duygu Bozkaya for her continuous support, care and patience.

Abstract

In chemical mechanical polishing (CMP), a rigid wafer is forced on a rough, elastomeric polishing pad, while a slurry containing abrasive particles flows through the interface. The applied pressure on the wafer is carried partially by the 2-body pad-wafer contact (*direct contact*) and partially by the 3-body contact of pad, wafer and abrasive particles (*particle contact*). The fraction of the applied pressure carried by particle contacts is an important factor affecting the material removal rate (MRR) as the majority of the material is removed by the abrasive particles trapped between the pad asperities and the wafer. In this thesis, the contact of a rough, deformable pad and a smooth, rigid wafer in the presence of rigid abrasive particles at the contact interface is investigated by using contact mechanics and finite element (FE) modeling. The interactions between the pad, the wafer and the abrasive particles are modeled at different scales of contact, starting from particle level interactions, and gradually expanding the contact scale to the multi-asperity contact of pad and wafer. The effect of surface forces consisting of *van der Waals* and *electrical double layer* forces acting between the wafer and the abrasive particles are also investigated in this work. The wear rate due to each abrasive particle is calculated based on the wafer-abrasive particle contact force, and by considering *adhesive* and *abrasive wear* mechanisms. A passivated layer on the wafer surface with a hardness and thickness determined by the chemical effects is modeled, in order to characterize the effect of chemical reactions between slurry and wafer on the MRR.

The model provides accurate predictions for the MRR as a function of pad related parameters; pad elastic modulus, pad porosity and pad topography, particle related

parameters; particle size and concentration, and slurry related parameters; slurry pH, thickness and hardness of the passivated surface layer of wafer. A good qualitative agreement between the model and the experiments is found for the variation of the MRR with respect to these parameters. Furthermore, closed form equations are derived in order to optimize the CMP parameters for maximizing the *material removal efficiency*, which is a measure of the ability of pad to transmit the applied pressure on the abrasive particles. The optimization of the CMP parameters described in this thesis may be particularly important for the low-pressure CMP of ultra-low-k (ULK) dielectric materials, where it is difficult to achieve acceptable MRR without compromising the porous structure of ULK materials.

Table of Contents

BIOGRAPHY i
ACKNOWLEDGEMENTS ii
ABSTRACT iii
TABLE OF CONTENTS v
CHAPTER 1: INTRODUCTION 1
1.1 Background 1
1.2 Applications of CMP 3
1.3 Future Challenges for CMP 7
1.3.1 Shrinking device dimensions 7
1.3.2 Integration of ultra low-k dielectrics 8
1.4 Motivation 10
1.5 Problem Statement 11
1.6 Thesis Organization 13
References 13
CHAPTER 2: LITERATURE REVIEW 16
2.1 Slurry Flow 16
2.1.1 Lubrication regime 16
2.1.2 Sub-ambient fluid pressure 18
2.1.3 Effect of slurry flow on wafer passivation 19
2.1.4 Modeling of hydrodynamic lubrication 20
2.2 Chemical Effects 23
2.2.1 Effect of slurry chemicals 23
2.2.2 Effect of chemical interaction between wafer and abrasive particles 25
2.2.3 Effect of slurry pH 25
2.2.4 The measurements of wafer hardness 27
2.2.5 Modeling of passivated layer hardness 30
2.3 Effect of CMP Parameters on MRR 34
2.3.1 Effect of applied pressure and relative velocity 34
2.3.2 Effect of abrasive particle concentration 36
2.3.3 Effect of abrasive particle size 38
2.3.4 Effect of pad elastic modulus 39
2.3.5 Effect of pad porosity 40
2.3.6 Effect of pad roughness 41
2.4 Mechanical Modeling of CMP 42
2.4.1 Luo and Dornfeld's model 42
2.4.2 Ahmadi and Xia's model 44
2.4.3 Fu et al.'s model 46

2.4.4 Qin et al.'s model 46
2.4.5 Other mechanical models for boundary lubrication........ 47
2.4.5 Other mechanical models for mixed lubrication........ 49
2.5 Physical Parameters 50
References........ 53
CHAPTER 3: THEORY BACKGROUND........ 68
3.1 Contact Mechanics........ 68
3.1.1 Hertz contact 68
3.1.2 Greenwood and Williamson multi-asperity model 70
3.1.3 Contact of rough spheres (Greenwood and Tripp model) 79
3.2 Surface Forces........ 81
3.2.1 Van der Waals force........ 82
3.2.2 Electrical double layer force 85
3.3 Hyperelastic Material Behavior 93
3.3.1 Basic definitions........ 94
3.3.2 Hyperelastic models........ 95
3.3.3 Mooney-Rivlin hyperelastic model........ 96
3.4 Mechanical Behavior of Porous Materials........ 99
3.5 Wear Mechanisms........ 103
3.5.1 Adhesive wear........ 103
3.5.2 Abrasive wear 104
References........ 107
CHAPTER 4: MECHANICAL MODELING OF PAD-PARTICLE-WAFER CONTACT 110
4.1 Overview........ 110
4.2 Non-Dimensionalization of Parameters........ 114
4.3 Single Particle (SP) Contact Model 115
4.3.1 Finite element model........ 117
4.3.2 Single particle contact relations 119
4.4 Multi-Particle (MP) Contact Model........ 126
4.4.1 Number of active particles 128
4.4.2 Particle contact regime........ 129
4.4.3 Mixed contact regime 131
4.4.4 Influence factor 133
4.4.5 Multi-particle contact model relations 135
4.5 Single Asperity (SA) Contact Model........ 140
4.5.1 Solution approach 140
4.5.2 Solution algorithm 146
4.5.3 Effect of interfacial particles on single asperity contact........ 148
4.6 Multi-Asperity (MA) Contact Model........ 160

4.6.1 Implementation of the SA contact model 163
4.6.2 Effect of particles on multi-asperity contact 164
4.7 Summary 170
References 172
CHAPTER 5: MODELING OF MATERIAL REMOVAL RATE 174
5.1 Overview 174
5.2 Removal Force Function (RFF) in SP Contact Model 177
5.2.1 Surface forces 178
5.2.2 Definition of removal force function (RFF) 181
5.2.3 Bi-layer hardness model 183
5.3 Removal Force Function (RFF) in MP Contact Model 187
5.4 Removal Force Function (RFF) in SA Contact Model 190
5.4.1 Contact pressure by SA contact model 191
5.4.2 Hertzian contact pressure 192
5.4.3 Mean Hertzian contact pressure 193
5.4.4 Removal force function (RFF) due to single asperity contact 194
5.4.5 Error of different contact pressure distributions on RFF of single asperity .. 196
5.5 Removal Force Function (RFF) in MA Contact Model 204
5.6 Implementation of Chemical Effects 206
5.7 Summary and Conclusions 207
References 210
CHAPTER 6: OPTIMIZATION OF CMP PARAMETERS FOR MAXIMUM MATERIAL REMOVAL EFFICIENCY 212
6.1 Overview 212
6.2 Multi-Particle Contact Model 213
6.2.1 MP contact model for constant particle size 213
6.2.2 The results of the MP contact model relations for constant particle size 218
6.3 Removal Force Function (RFF) in MP Contact Model 220
6.4 Removal Force Function (RFF) in MA Contact Model 222
6.4.1 Exponential distribution of the pad asperity summit heights 222
6.4.2 Uniform contact pressure 223
6.5 Optimization for Maximum Material Removal Efficiency 225
6.5.1 Definition of material removal efficiency 225
6.5.2 Optimization equation 225
6.5.3 Calculation of RFF at optimum conditions 227
6.6 Results and Discussion 229
6.6.1 Optimum particle concentration 229
6.6.2 RFF at optimum conditions 231
6.6.3 Effect of surface forces 234
6.7 Summary 238

References 239
CHAPTER 7: RESULTS AND DISCUSSION 240
7.1 Overview 240
7.2 Effect of Particles on RFF in Pad-Wafer Rough Contact 242
7.2.1 Effect of particle concentration 243
7.2.2 Effect of pad elastic modulus 244
7.2.3 Effect of particle size 247
7.2.4 Effect of pad topography 247
7.3 Effect of Pad Elastic Modulus and Pad Porosity 249
7.3.1 Variation of RFF with applied pressure 249
7.3.2 Effect of pad elastic modulus on RFF 254
7.3.3 Effect of porous elastic modulus ratio on RFF 258
7.3.4 Comparison with experiments 260
7.4 Effect of Particle Concentration 273
7.4.1 Variation of RFF with applied pressure 274
7.4.2 Effect of particle concentration on RFF 280
7.4.3 Comparison with experiments 286
7.5 Effect of Pad Topography 293
7.5.1 Variation of RFF with applied pressure 294
7.5.2 Effect of pad roughness on RFF 298
7.5.3 Effect of asperity radius on RFF 301
7.5.4 Effect of asperity density on RFF 302
7.5.5 Effect of skewness on RFF 304
7.5.6 Comparison with experiments 307
7.6 Effect of Surface Forces 309
7.6.1 Effect of van der Waals force on RFF 310
7.6.2 Effect of double layer forces on RFF 313
7.6.3 Comparison with experiments 318
7.7 Effect of Particle Size 322
7.7.1 Surface forces 323
7.7.2 Passivated surface layer 325
7.7.3 Single asperity contact behavior 331
7.7.4 Comparison with experiments 332
7.8 Wear Mechanism 334
7.9 Optimization of CMP Parameters 336
References 338
CHAPTER 8: SUMMARY AND CONCLUSIONS 343

CHAPTER 1

INTRODUCTION

1.1 Background

Chemical mechanical planarization (CMP) is a polishing method commonly used in the manufacturing of wafer based integrated circuits (ICs). Since CMP was first introduced to the integrated circuit manufacturing in the mid-1980s, by IBM, CMP became a key technology in generating planar surfaces for several semiconductor manufacturing processes [1].

CMP operation involves forcing the rotating wafer attached to a wafer carrier against a rotating polishing pad as seen in Fig. 1.1. The polishing pad is covered with liquid slurry, which contains abrasive particles. The chemical reactions between the CMP-slurry and the wafer are the primary driver for preparing the surface for polishing. The chemical composition of the surface is modified by the chemically reactive slurry, to favor higher wear-rates. In addition to the chemical interactions, the pad-wafer interface experiences the effects of contact and lubrication. Three-body contact due to the abrasive particles

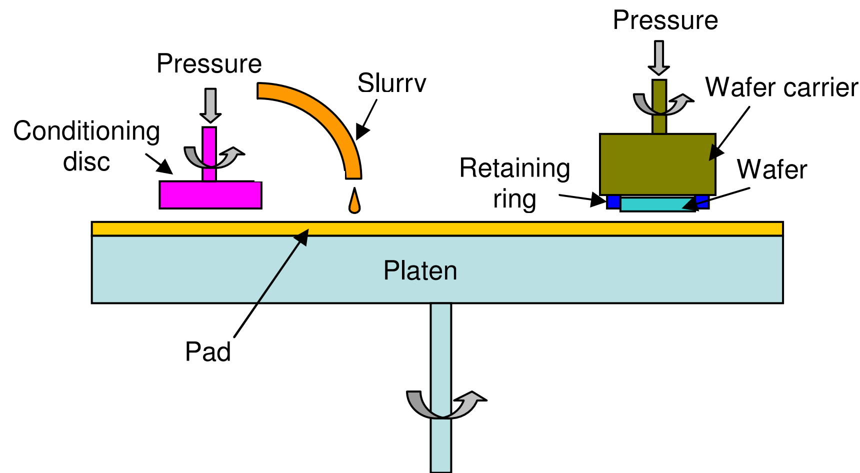

Fig. 1.1: Schematic of CMP Process

caught between the pad and the wafer (particle contact) provides the necessary physical force to remove the material from the wafer surface. While solid-body contact is taking place, the interface of the pad and the wafer experiences the lubricating effect of the slurry flow between the pad and the wafer.

The abrasive particles used in conventional polishing techniques are 2.5-3 times harder than the workpiece material. These techniques cause scratches and pitting on the surface, and cracks in the sub-surface of the workpiece. The passivation of the surface layer of the wafer (workpiece) is important to achieve smooth and planarized surfaces without any surface and sub-surface defects [2]. For this reason, an effective CMP process should provide a balance between the chemical and mechanical effects. In case there is not enough oxidizer near the surface of the wafer, the material removal rate (MRR) is limited by chemical effects, and material removal is achieved by abrasion of the unpassivated wafer material from the surface. This may result in wafer surface damage. In contrast,

high oxidizer concentration causes the mechanical abrasion to be the limiting factor limiting MRR.

Polishing pad plays a crucial role in determining the success of the CMP to obtain planar surfaces [3]. Polishing pads are made of polymeric foam and has a porous structure [4]. The pad properties are altered due to the pad wear and closing of the pores by the debris, which affects the polishing performance. Hence an essential part of the CMP process is pad conditioning that is used to stabilize the pad properties during polishing. Pad conditioning involves the pressing of the spinning abrasive wheel covered with diamond tips protruding a specified amount on the pad surface (Fig. 1.1). The abrasive wheel is connected to the conditioner arm, which sweeps across the polishing area [3].

Fig. 1.2 shows the relationship between the slurry, pad and process parameters that determine the performance of CMP. The performance of CMP is evaluated by the output parameters, such as the roughness and planarity of the polished surface, the material removal rate (MRR), within-die-non-uniformity (WIDNU), within-wafer-non-uniformity (WIWNU), planarization length, dishing and erosion, surface defects and degradation of the dielectric. The slurry parameters include the abrasive properties (abrasive size, concentration, material and shape) and the slurry chemistry. The properties of pad (the roughness, elasticity, thickness and macro-channels of the pad) also influence the output parameters of CMP. The effect of slurry and pad parameters is controlled via the process parameters (pressure, velocity and slurry flow rate).

1.2 Applications of CMP

Several key processes in ultra-large scale integration (ULSI) manufacturing including Al metallization, Cu damascene and shallow trench isolation (STI) processes require CMP

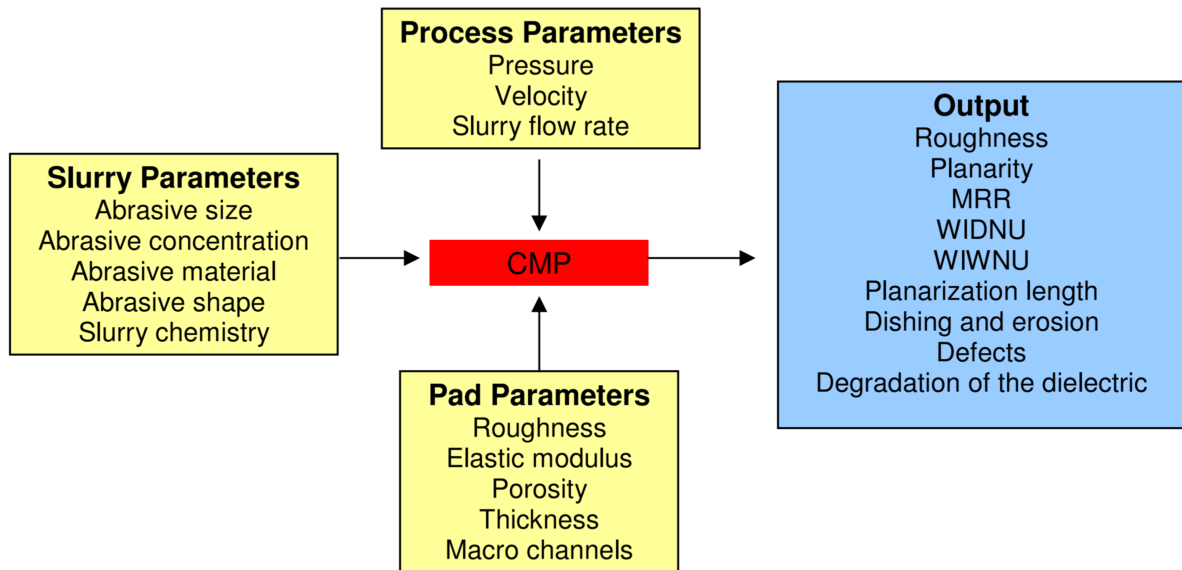

Fig. 1.2: Input and output parameters of CMP

for planarization and smoothening of the deposited layers. In Al metallization (Fig. 1.3a), the interlayer dielectric (ILD) (usually silicon dioxide) is deposited on patterned Al layer to provide isolation between the successive Al layers. CMP is then used on the ILD layer to establish a smooth surface for another layer of Al interconnects. The non-uniformity of material removal introduces several problems. The material removal rate depends on the pattern density as seen in Fig. 1.3b. The high pattern density areas tend to get polished at a smaller rate as compared to low pattern density areas, which causes a difference in the film thickness between high and low pattern density areas. This is a result of the larger pad deformation at the high density areas with larger contact area and contact force. *Planarization length* is a measure of this problem and defined as the distance over which the film thickness between areas of different density changes. Fig. 1.3c shows another characteristic of CMP, which requires over-polishing of the ILD layer. As the high areas above the Al interconnects are polished, the points between the high areas get polished at

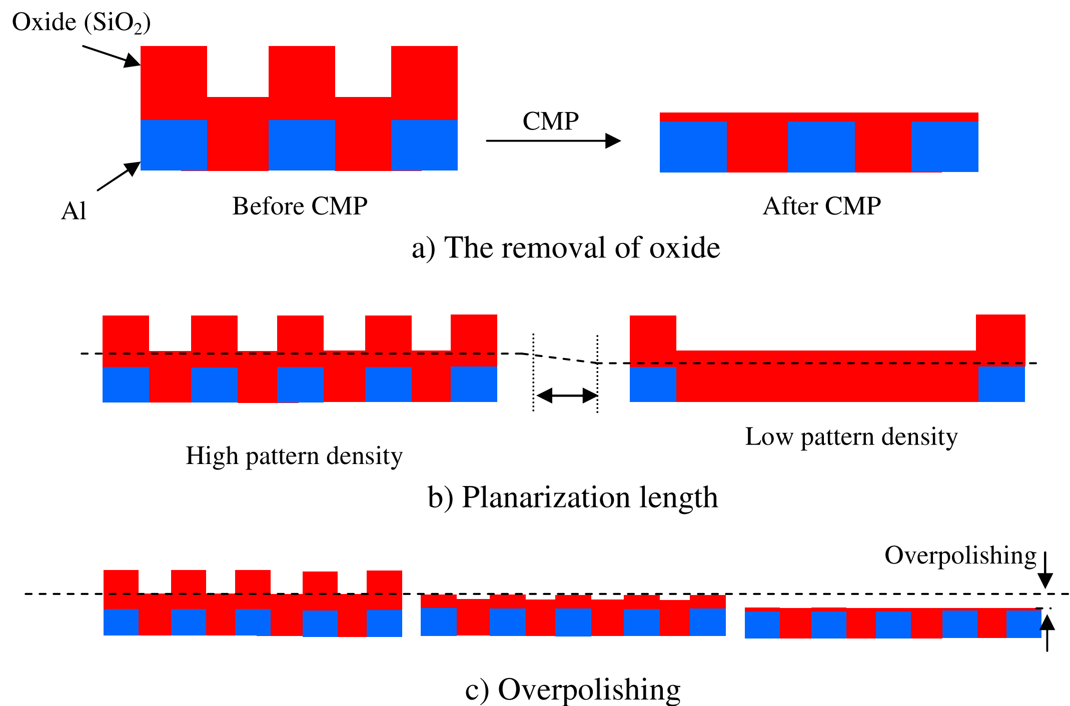

Fig. 1.3: Oxide CMP for Al metallization a) the removal of oxide with CMP, b) and c) the defects seen in oxide CMP.

the same time. Although the material removal rate at these points is small, the whole ILD layer needs additional polishing once the high areas are removed.

CMP step in Cu damascene process is shown in Fig. 1.4. Due to the problems associated with etching and patterning the Cu layer, this layer is deposited on the patterned oxide layer forming trenches filled with Cu interconnects after the deposition of the barrier layer. Excess Cu and barrier layer deposited on the oxide layer needs to be removed before another set of oxide and Cu interconnects is stacked up. Dishing (Fig. 1.4b) and erosion (Fig. 1.4d) are important problems affecting the reliability of the structure. Dishing occurs at a smaller scale than the erosion and it is due to the higher removal rate of the Cu in the trench before the excess Cu and barrier layer is polished away. *Erosion*, on the other hand, is the result of several trenches that are over-polished (Fig. 1.4c). This

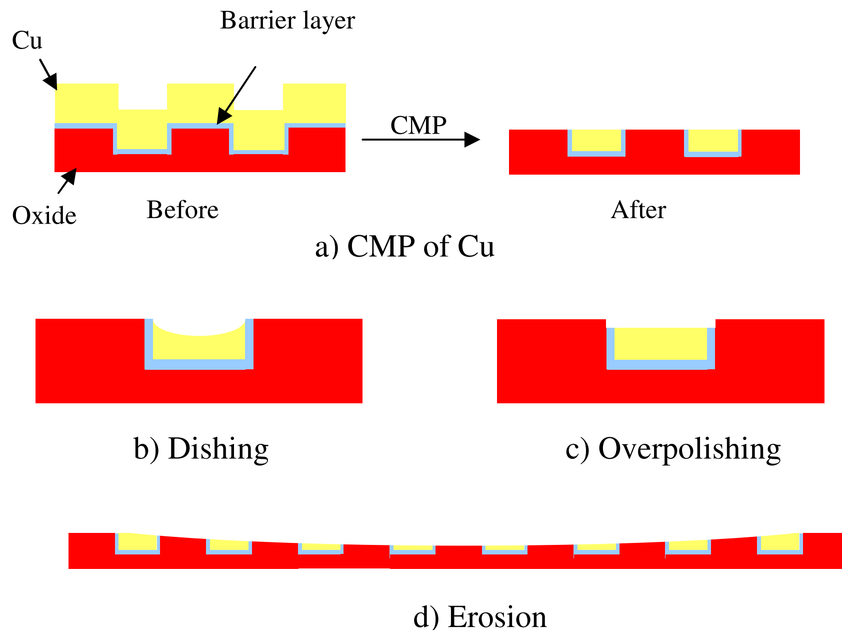

Fig. 1.4: CMP for Cu damascene a) the removal of Cu and barrier layer with CMP, b)-d)) the defects seen in CMP for Cu damascene.

can be described as follows. The removal rates of the oxide and Cu layers are different. The polishing behavior of areas with high metallization density are dominated by Cu polishing, whereas oxide polishing is the determining factor for the overall CMP process in low density areas. This difference in the polishing rates, and metallization density induced by the selectivity of the slurry and the pad deformation is the responsible mechanism for erosion.

Shallow Trench Isolation (STI) is an enabling technique allowing tighter packing of the transistors. CMP step is necessary to remove the excess oxide and planarize the surface by removing as little nitride as possible since the transistors are located in the place of the nitride layer once the nitride layer is removed. Similar challenges seen in ILD CMP exist in this application. The removal rate of silicon dioxide is usually greater than silicon

nitride, which enables the control of dishing and erosion. The selectivity of the slurry is sometimes increased to improve the polishing behavior of the structure.

Outside the integrated circuit (IC) industry, the enabling feature of CMP to smoothen surfaces and planarize patterns makes CMP an attractive solution for the micro electro mechanical systems (MEMS). As MEMS devices evolve, more sophisticated patterns need to be smoothened and planarized, which can be achieved by the CMP technology.

1.3 Future Challenges for CMP

Although CMP emerged as an enabling technology for planarizing and smoothening surfaces, the shrinking device dimensions and the integration of new materials (i.e. ultra-low-k dielectrics) present future challenges for CMP.

1.3.1 Shrinking device dimensions

The number of components on a metal-oxide-semiconductor (MOS) device doubles every two years following Moore's law [5]. This requires the shrinkage of the device dimensions to accommodate more components in a smaller area. One of the most important requirements for the planarity of the surface in ILD stem from the difficulties in lithography if the planarity of the surfaces is not satisfactory [6]. The lithography system allows only a certain amount of variation in the height of the surface to be able to resolve features on the surface. The maximum allowable variation in the surface height is defined as the depth of focus (σ). The depth of focus can be determined using the minimum feature size b and the wavelength of the projection light λ [6] as,

$$\sigma = 10.75\frac{b^2}{\lambda} \tag{1.1}$$

It is seen that the depth of focus σ is proportional to the square of the minimum feature size b. The requirement for the depth of focus σ, hence the planarity of the surface, increases rapidly as the minimum feature size b decreases. The depth of focus can also be improved if the wavelength of the projection light λ is decreased with innovations in the lithography systems, however the further improvements in the planarization of the surfaces is still essential to meet future challenges for the depth of focus with decreasing device dimensions [7].

1.3.2 Integration of ultra low-k dielectrics

One of the factors limiting the speed of the microelectronic circuits is the resistance-capacitance (RC) delay in the interconnects between the transistors. Copper has replaced aluminum because of its lower resistance to improve RC delay. The RC delay is further decreased by using low-k materials instead of silica as the insulator layer, which lowers the capacitance. The development of the low-k materials is a significant challenge and the industry has not been able to catch up with the International Technology Roadmap for Semiconductors (ITRS) roadmap requirements in the past years.

Fluorinated silica glass (FSG) and organic-doped silica glass (OSG) with dielectric constant of 3.7 and 2.8, respectively are used for achieving lower dielectric constant [8]. A further reduction in the dielectric constant is essential to meet the requirements of the 45 nm node. According to the latest ITRS roadmap, ultra-low-k (ULK) dielectrics with dielectric constant in the range $2.1 < k < 2.4$ are needed for 45 nm node [7]. The introduction of the nanopores in the dielectric material is considered to be the logical approach to decrease the dielectric constant. The nanopores facilitate lowering the dielectric constant due to the small dielectric constant of air (k~1) [9].

One of the draw-backs of this approach is that the nanopores cause degradation of the mechanical properties, which causes severe problems in the microfabrication processes [10]. Higher porosity promotes lower dielectric constant, however causes a decrease in the elastic modulus and the strength of the dielectric material [11]. The adhesion strength of the ULK dielectric layer to the barrier layer also presents a problem [12].

A typical Cu damascene process integrated with ULK dielectrics involves the planarization of layers by removing the excess copper and barrier material once copper and barrier layer is deposited on the ULK dielectric layer patterned with vias and trenches [13]. CMP remains to be the enabling technology to achieve the desired planarization, which is crucial for the manufacturing of multi-level interconnects. As a result, the ULK dielectric materials are exposed to CMP and are required to be resistant to high pressures and slurry chemistries used in CMP [14].

The delamination of ULK dielectric/barrier interface and the fracture of ULK dielectric are the two modes of mechanical failure of the damascene structure associated with ULK dielectric materials [9]. Various approaches are pursued to minimize the occurrence of the failures related to ULK materials. Low-pressure CMP is proposed to be an approach to decrease the probability of mechanical failure [15,16]. The application of the abrasive-free slurries is investigated to enable material removal with enhanced chemical reactions and minimal pressure [17]. The adhesion strength of the layers may be improved by applying pre-treatment to the surfaces [18]. The residual stress in the dielectric layer is also shown to be an important factor that determines the adhesion strength. The residual stress in the dielectric layers may be minimized by optimizing the deposition techniques and the alteration of the Cu layer [12].

1.4 Motivation

The continuous miniaturization of the devices and integration of new materials in the semiconductor industry depend on the development of an understanding of the CMP process, which may enable the improvement of process optimization and control. The demand for improved planarity due to the shrinking device dimensions and the integration of new materials call for stringent requirements from the CMP process [1]. These requirements can be met if the mechanisms underlying the CMP process are understood. Although there has been a considerable number of studies focusing on constructing a basis to understand the mechanisms acting in CMP, these mechanisms are not adequately understood and modeled yet due to the complex interactions among many variables [19].

The mechanical modeling of the MRR may contribute to the understanding of the CMP process. The effect of various parameters on the output of the CMP process may be analyzed by using reliable mechanical models. The planarity of the surfaces can be improved, if the variation of the MRR from point to point across the wafer is minimized. The conditions necessary for uniform MRR may be determined as a result of the modeling efforts.

The failure of the porous ULK dielectric layer may be prevented if the stresses generated by the contact pressure due to abrasive and direct contact, and the resulting friction force due to the relative movement of the surfaces are minimized. Excessive stresses may result in the fracture of the ULK dielectric layer. High shear stresses at the interface of the ULK dielectric and Cu layers may cause delamination. The material removal rate should be reasonably high as the probability of failure of ULK dielectric layers increases with large

polishing times. The mechanical modeling of the CMP process, which can be used to calculate the forces through the abrasives and pad-wafer direct contact may help minimize the stresses induced in the ULK dielectric layer is minimized and appreciable material removal rate is achieved.

1.5 Problem Statement

In chemical mechanical polishing (CMP), the majority of the material is removed by the abrasive particles trapped between the pad asperities and the passivated wafer surface. The applied pressure is carried partially by the 2-body contact of the pad to the wafer (direct contact) and the 3-body contact of the pad, wafer and the abrasive particles (particle contact). The fraction of the applied pressure distributed to the direct and particle contact is an important factor affecting the material removal rate (MRR). An essential prerequisite to predict the MRR in CMP by modeling is to accurately characterize the contact of the rough elastic pad, rigid abrasive particles and the rigid smooth wafer. The objective of this work is therefore to develop a model in order to predict the MRR by considering the interactions between the pad, the wafer and abrasive particles.

The proposed model uses the contact mechanics and finite element modeling to enable the accurate calculation of the 3-body contact force due to the contact of the pad, the wafer and the abrasive particles and 2-body contact force between the pad and the wafer as a function of the important parameters. The influence of the pad-related parameters (pad elastic modulus, pad porosity and pad topography), abrasive particle-related parameters (particle size and concentration), passivation rate-related parameters (hardness and thickness of passivated surface layer), surface force-related parameters

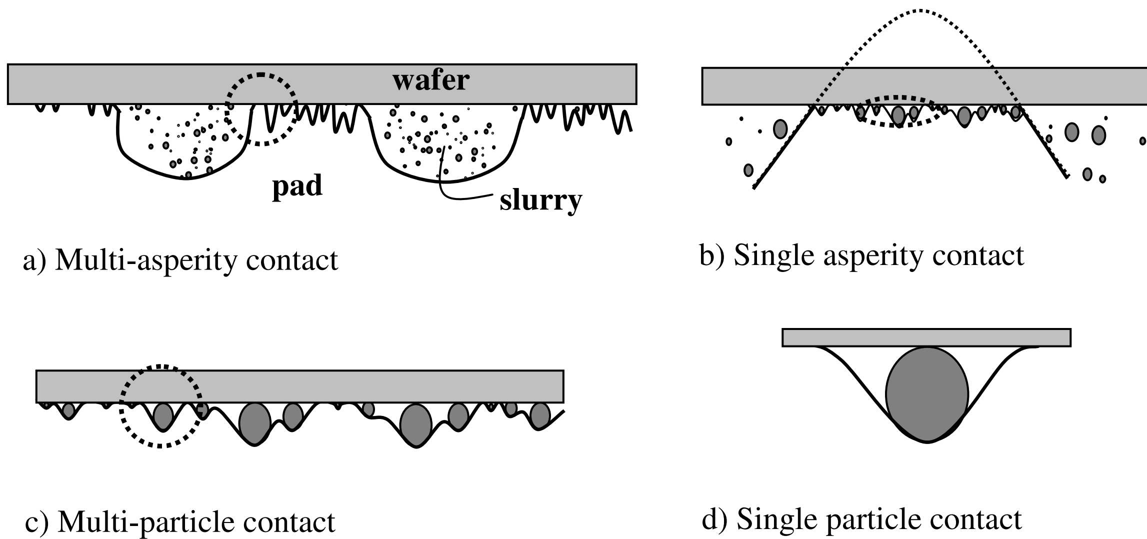

Fig. 1.5: Cross-sectional view of the wafer-pad interface at different scales of contact.

(Hamaker constant, zeta potential of wafer and particles and molar concentration of electrolyte) and process parameters (pressure and velocity) on the MRR and the interactions between various parameters are determined.

The interactions between the pad, wafer and the abrasive particles are modeled at different contact scales; starting from the single particle interactions shown in Fig. 1.5d to the interactions between all the particles active in contact with the rough pad and the wafer described in Fig. 1.5a. The results of each model for smaller contact scale is used as an input for the next model to increase the contact scale gradually until the final model including all the necessary interactions is achieved. Once the mechanical forces acting on the abrasive particles, consisting of pad-to-particle contact and wafer-to-particle surface forces, are calculated, wear equations are utilized in order to model the MRR. The effects of slurry chemicals, which influence the hardness and the thickness of the passivated surface layer of the wafer are then considered.

1.6 Thesis Organization

The literature for the previous experimental and theoretical work on CMP is reviewed in Chapter 2. The MRR model explained in this thesis is based on the basic theory of the contact mechanics, surface forces (van der Waals and electrical double layer forces), hyperelastic material behavior, mechanical behavior of porous materials and wear mechanisms, which are explained briefly in Chapter 3. The single particle (SP), multi-particle (MP), single asperity (SA) and multi-asperity (MA) contact models are introduced in Chapter 4. The wear equations are implemented in Chapter 5 in order to model the MRR considering the effect of surface forces and wafer hardness influenced by passivated surface layer of wafer. In Chapter 6, the model developed in Chapters 4 and 5 is simplified by considering additional assumptions, thus leading to closed-form equations for calculating the optimum conditions in order to maximize material removal efficiency in CMP. Chapter 7 focuses on the results of the model for evaluating the effect of each parameter, which is validated by comparing with experimental results found in literature. The conclusions drawn form the work presented in this thesis are given in Chapter 8.

References

1. Oliver M.R. (Editor), 2004. Chemical mechanical planarization of semiconductor materials. Springer Verlag, New York.

2. Fu G., Chandra A., Guha S., Subhash G., 2001. A plasticity-based model of material removal in chemical-mechanical polishing. IEEE Trans Semiconduct Manuf, 14, 406-417.

3. Hooper B.J., Byrne G., Galligan S., 2002. Pad conditioning in chemical mechanical polishing. J Mater Process Technol, 123, 107-113.

4. Gouda S.D., Bastawros A., Chandra A., 2003. Multi-scale characterization of pad role on material removal rate in CMP. Mater Res Soc Symp Proc, 767, 2.5.1-2.5.6.

5. Moore G. E., 1965. Cramming more components onto integrated circuits. Electronics, 38, 8.

6. Wolf S., Tauber R. N., 1986. Silicon processing for the VLSI Era: Vol. 1 – Process technology. Lattice Press, Sunset beach CA, Chapter 13.

7. International Technology Roadmap for Semiconductors. International SEMATECH, 2006.

8. Rouffignac P., Li Z., Gordon R. G., 2004. Sealing porous low-k dielectrics with silica. Electrochem Solid State Letters, 7 (12), 306-308.

9. Vella J.B., Adhihetty I. S., Junker K., Volinsky A. A., 2003. Mechanical properties and fracture toughness of organo-silicate glass (OSG) low-k dielectric thin films for microelectronic applications. International Journal of Fracture, 119/120, 487-499.

10. Guyer E. P., Dauskardt R. H., 2005. Effect of porosity on reducing cohesive strength and accelerating crack growth in ultra low-k thin-films. Proceedings of the IEEE 2005 International Volume, 223.225.

11. Yoon B. U., Kondo S., Tokitoh S., et al., 2004. Characterization of patterned low-k film delamination during CMP for the 32 nm-node Cu/ultra low-k (k=1.6-1.8) integration. IEEE International Volume 7-9, 239-241.

12. Balakumar S., Wong G., Tsang C. F., et al., 2004. Enhancement of adhesion strength of Cu layer on single and multi-layer dielectric film stack in Cu/low k multi-level interconnects. Microelectronic Engineering, 75, 183-193.

13. Chang T. C., Tsai T. M., Liu P. T., et al., 2004. CMP of ultra low-k material porous-polysilazane (PPSZ) for interconnect applications. Thin Solid Films, 447-448, 524-530.

14. Chandrasekaran N., Ramarajan S., Lee W., 2004. Effects of CMP process conditions on defect generation in low-k materials. J Electrochem Soc, 151, 882-889.

15. Kondo S., Yoon B. U., Tokitoh S., et al., 2003. Low pressure CMP for 300-mm ultra low-k (k=1.6-1.8)/Cu integration. IEEE International Volume 8-10, 6.4.1-6.4.4.

16. Tokitoh S., Kondo S., Yoon B. U., et al., 2004. Enhancement in electrical via-yield of porous low-k/Cu integration by reducing CMP pressure. IEEE International Volume 7-9, 130-132.

17. Matsuda T., Takahashi H., Tsurugaya M., et al., 2003. Characteristics of abrasive-free micelle slurry for copper CMP. J Electrochem Soc, 150, 532-536.

18. Schulze K., Schulz S. E., Fruhauf S., et al., 2004. Improvement of mechanical integrity of ultra low k dielectric stack and CMP compatibility. Microelectronic Engineering, 76, 38-45.

19. Jeng Y.R., Tsai H.J., 2003. Improved model of wafer/pad powder slurry for CMP. J Electrochem Soc, 150, 348-354.

CHAPTER 2

LITERATURE REVIEW

In this chapter, the experimental and theoretical studies as related to the modeling work presented in this thesis are reviewed.

2.1 Slurry Flow

2.1.1 Lubrication regime

The lubrication regime operating in the pad-wafer interface is an important factor affecting the material removal rate (MRR) [1]. The relative magnitude of hydrodynamic pressure generated due to slurry flow and applied pressure determines the lubrication regime. If the hydrodynamic pressure is sufficiently high such that a continuous slurry film separates pad and wafer, all the applied pressure is carried by hydrodynamic pressure. This regime is called the *hydrodynamic lubrication* regime or non-contact mode, as pad-wafer contact does not occur in this regime [2]. In the *boundary lubrication* regime (contact mode), the hydrodynamic pressure is relatively small, and the majority of

the applied pressure is carried by the pad-wafer contact. A transition regime exists between boundary and hydrodynamic lubrication regimes, in which the applied pressure is partially carried by hydrodynamic pressure and pad-wafer contact. This is called the *mixed lubrication* regime (partial contact mode).

Stribeck number [3], which is defined as the ratio of viscous forces responsible for hydrodynamic pressure to normal pressure, is commonly used to characterize the lubrication regime. Stribeck number, S_r can be calculated using the dynamic viscosity of the slurry η, relative velocity V_r and normal pressure P_o as,

$$S_r = \frac{\eta V_r}{P_o} \tag{2.1}$$

The coefficient of friction at pad-wafer interface has been measured during CMP in order to determine the lubrication regime [1, 2, 4-6] as the coefficient of friction is a strong function of the lubrication regime; in fact, the friction coefficient in the hydrodynamic lubrication regime is 1-2 orders of magnitude smaller than the boundary lubrication regime [1]. Friction coefficient was found to be ~0.001 for hydrodynamic lubrication, ~0.01-0.1 for mixed lubrication and ~0.1 for boundary lubrication [1]. A typical variation of friction coefficient with respect to Stribeck number is plotted in Fig. 2.1. In addition to the friction coefficient measurements, the lubrication regime was investigated by measuring the slurry film thickness [6, 7] and interfacial fluid pressure during CMP [8-12].

The friction coefficient measurements [1, 2, 4, 5] indicated that friction coefficient in CMP is around ~0.1, i.e. much larger than 0.001 typical for hydrodynamic lubrication

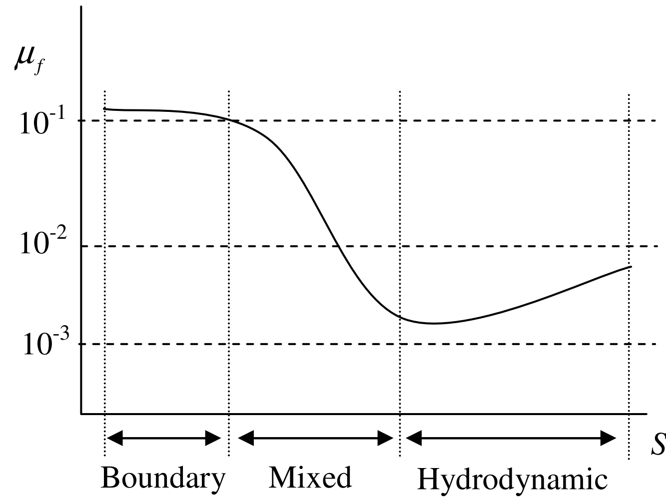

Fig 2.1: The variation of the friction coefficient μ_f with lubrication regime.

regime. The slurry film thickness was measured to be in the range 20-25 μm [6], which is on the same order of magnitude as the height of pad asperities. Furthermore, scratches formed due to pad-abrasive-wafer contact were found on the wafer surface [13]. These findings suggest that the lubrication regime in CMP is most likely to be either mixed or boundary lubrication and hydrodynamic lubrication is not seen for typical conditions in CMP.

2.1.2 Sub-ambient fluid pressure

The sub-ambient hydrodynamic pressure forming in the pad-wafer interface is the main factor driving lubrication regime to mixed or boundary lubrication. The experimental and theoretical work by Danyluk, Tichy and their co-workers explained the sub-ambient pressure by considering the soft elastohydrodynamic lubrication taking place in the pad-wafer interface [8-12, 14]. The contact pressure between the pad and the wafer is not uniform due to the effect of friction force, which causes the contact pressure to be greater at the leading edge of the pad-wafer contact. Higher contact pressure causes the elastic

pad to undergo more deformation, resulting in a net diverging slurry film. Such a net diverging slurry film results in sub-ambient fluid pressure [11].

The magnitude and the distribution of the hydrodynamic pressure depend on the parameters such as fluid viscosity, pad structure and elastic modulus, relative velocity, pad roughness and wafer curvature [12]. The magnitude of the sub-ambient pressure increases with pad roughness and relative velocity [11, 12, 14]. Higher pad elastic modulus causes sub-ambient pressure to become smaller, while the magnitude of sub-ambient pressure increases with higher viscosity [12]. A convex wafer results in positive pressure whereas a concave wafer increases the tendency for higher sub-ambient pressure [12]. The effect of applied pressure is relatively small as compared to other parameters [12]. The magnitude of sub-ambient pressure was found to be as large as 50-100% of applied pressure under some conditions [11, 12]. Therefore, the effect of sub-ambient pressure may be significant for MRR and within-wafer-non-uniformity (WIWNU).

2.1.3 Effect of slurry flow on wafer passivation

One of the important functions of slurry flow is to distribute the chemicals and the abrasive particles of the slurry uniformly over the wafer surface. The wear debris forming during removal of wafer material is transported away from the wafer surface by the slurry flow. Since fresh slurry is fed into the system and material removal occurs concurrently, the slurry becomes a mixture of slurry reacted slurry chemicals, wear debris and unreacted fresh slurry [15]. The mean residence time (MRT) of the slurry, defined as the mean time required for the fresh slurry to replace the old slurry, is a function of applied pressure, relative velocity, slurry flow rate, pad roughness and pad morphology [7, 15].

The passivation rate of the wafer with reacted and unreacted slurry is different, therefore a variation of the passivated layer on the wafer arises, and the WIWNU increases if the unreacted slurry is not transported uniformly across the wafer, i.e. MRT varies across the wafer. Shorter MRT in general causes the MRR to increase [15]. If the slurry flow is not able to transport the wear debris away from the wafer effectively, entraining of the wear particles under the pad asperities results in surface scratches and decreases finish quality of the wafer [15].

Temperature at the wafer surface is also an important consideration as the passivation rate of the wafer surface is a strong function of temperature [16-19]. The temperature at the wafer surface is a result of the thermal equilibrium of the heat generated due to friction force and the cooling effect of the fresh slurry introduced into the system. Therefore, the slurry flow becomes a critical factor for the MRR and WIWNU as the temperature at wafer surface is controlled by the slurry flow [18].

2.1.4 Modeling of hydrodynamic lubrication

The hydrodynamic lubrication in CMP was first modeled by Runnels and Eyman [20] by solving three-dimensional (3-D) Navier-Stokes equation. Since the slurry film thickness is small, the flow in the thickness direction can be neglected for typical CMP conditions without loss of accuracy [21]. This assumption leads to the Reynolds equation, which was used to determine the slurry flow in CMP in both 2-D [14, 22, 23] and 3-D [21, 24-27] models. The Reynolds equation was further simplified to reduce the equation to a more manageable form [28]. The effect of porosity and compressibility of pad were also included [21, 24]. In these models, the equilibrium position of wafer as determined by

slurry film thickness and tilt angle of wafer was found by iteratively finding the equilibrium of the applied pressure on the wafer and the hydrodynamic pressure generated by the slurry flow [20]. In addition to the equilibrium of forces, the balance of moments about the pivot (gimbal) point was used to calculate the equilibrium position of wafer [21].

The outputs of the models concerned with hydrodynamic lubrication are slurry film thickness, hydrodynamic pressure and slurry velocity distribution. It was shown that the slurry film thickness is over-predicted by 2-D models as compared to 3-D models due to the fact that slurry flow in one of the directions is neglected in 2-D models [21]. Thakurta et al. [21] calculated the minimum slurry film thickness of 20-50 μm. The slurry film thickness was found to increase with lower applied pressure, higher relative velocity, lower pad porosity and compressibility and larger slurry viscosity [21].

The experimentally observed sub-ambient hydrodynamic pressure was not detected in the early models as these models neglected the elasticity and roughness of the pad [21-26]. The sub-ambient hydrodynamic pressure was calculated by the models, where a deformable pad was incorporated [10, 11, 14, 27]. The results of these studies indicate that the deformation of pad alters the slurry flow significantly and the soft elastohydrodynamic lubrication (EHL) is the main reason for the sub-ambient hydrodynamic pressure measured in the experiments [27].

The models reviewed so far in this section neglected the effect of abrasive particles on the slurry flow. The granular lubrication theory was employed to simulate the slurry flow in CMP [29-32] by considering the influence of abrasive particles in the slurry. The

models were further improved by including the effect of pad roughness on slurry flow [30, 31]. The results of these studies showed that pad roughness influences the slurry flow more significantly for large abrasive particles, high applied pressure and low relative velocity [31]. The slurry film thickness increased with greater particle size and pad roughness [31].

The outputs of the models were used in order to calculate the MRR in CMP. The models considering a continuous slurry film between the pad and wafer assume that the shear stress induced on the wafer surface due to the slurry flow is sufficiently high to cause material removal [20]. The MRR was evaluated by calculating the shear stress from the solution of flow field. An energy approach was also used to simulate the material removal in hydrodynamic lubrication regime by considering the abrasive particles as energy transmitting mechanism from slurry to wafer [33]. The energy of abrasive particles was found to be proportional to the shear stress generated in the flow and as a result, the MRR increases with greater shear stress generated by the flow.

In the models taking pad-wafer contact into account, i.e. mixed lubrication regime, the MRR was determined by considering the contact of abrasive particles and wafer. The calculation of the MRR in these models is similar to that of the material removal models used for boundary lubrication. The details of the calculations utilized by the models for the MRR in boundary lubrication are given in Section 2.4.

The solution for the velocity distribution of the slurry flow enabled the use of the mass transport equations introduced by Subramanian et al. [34] in order to evaluate the role of slurry flow for preparing the wafer surface for material removal [23, 24]. The mass

transport of the chemicals in the slurry was calculated, and the concentration of slurry chemicals at the wafer surface was determined, which was then used in reaction kinetics models to predict the passivation rate of wafer surface [24]. These models indicated that the distribution of slurry chemicals is critical for achieving a uniform MRR across the wafer.

2.2 Chemical Effects

The role of chemical reactions in CMP is to passivate the wafer surface, thereby reduce the hardness of wafer material facilitating the mechanical removal of wafer material. Although the wafer passivation may involve multiple reactions occurring sequentially [35], a simplified two-step material removal mechanism is widely used to describe the material removal in CMP [16, 36, 37]. The first step is the formation of a passivated wafer surface layer, and the second step is the mechanical removal of the passivated material by abrasive particles. An optimized CMP process requires a balance of chemical reaction rate at the wafer surface and the rate of mechanical removal of the passivated wafer surface [16, 35, 37]. The chemical reaction rate becomes the limiting factor for the MRR if material is removed before the wafer surface becomes passivated by the chemicals, whereas mechanical removal determines the MRR if the chemical reactions are taking place more rapidly than mechanical removal [35, 37].

2.2.1 Effect of slurry chemicals

The slurry chemicals play an important role for the passivation of wafer surface. The oxidizers and inhibitors in the slurry determine the reaction kinetics controlling the

passivation of wafer surface [38]. The effect of different oxidizers, e.g. hydrogen peroxide (H_2O_2), and inhibitors, e.g. benzotriazole (BTA), on the MRR was investigated for CMP of oxide [39], copper [40-45], tantalum [45, 46] and tungsten [47, 48] films. It was shown that the reactions with slurry chemicals result in different compositions based on the oxidizer and inhibitor. The overall MRR is influenced by the existence of different compositions at the wafer surface due to the fact that some of these compositions readily dissolve in the slurry contributing to the MRR, while some compositions are more difficult to remove from surface [41, 44]. Furthermore surface hardness is also a strong function of composition affecting the wear rate of wafer material [40, 44, 45, 47].

Slurry chemicals have also been shown to influence the zeta potential [39, 45, 49-51]. Experimental studies showed that citric acid introduced in the slurry causes a significant change in zeta potential of alumina particles [52] whereas zeta potential of silica particles remains almost the same [51]. Luo et al. [50] demonstrated that the addition of BTA reduces the zeta potential of alumina particles. Different ionic salts were also shown to have an influence on zeta potential [39]. This behavior was explained by the adsorption of the chemicals on abrasive particles causing the zeta potential to decrease [51, 52]. The zeta potential is a controlling factor for the agglomerate size of abrasive particles [53] and double layer forces between wafer and abrasive particles [45]. For this reason, the variation of zeta potential with respect to different slurry chemicals has important consequences for the MRR, which is discussed further in Section 2.2.3.

2.2.2 Effect of chemical interaction between wafer and abrasive particles

Li et al. [54] investigated the influence of different abrasive materials on the MRR of tantalum and copper films. It was found that MRR of tantalum film is low, when diamond abrasive particles are used, whereas high MRR is achieved for tantalum in the case of silica abrasive particles. In contrast to the behavior seen for tantalum, diamond abrasive particles result in higher MRR for copper as compared to silica particles. Although copper is typically softer than tantalum, higher MRR of tantalum seen in the case of silica abrasive particles indicate that abrasive particles react with wafer material during material removal [54-56]. This was further studied by measuring the distribution of abraded material in the slurry, pad and abrasive particles [54]. Abraded copper and tantalum material were found on the surface of silica abrasive particles, which is an indication for the reaction between wafer and abrasive particles. Whereas the amount of abraded material on alumina abrasive particles was small indicating alumina particles do not react with wafer material. The silica particles are considered to have a "chemical tooth" as they react with wafer material [54-56]. The material removal of copper occurs due to abrasive wear since the MRR of copper increases as the abrasive particles become harder [56]. An adhesive wear mechanism seems to be more appropriate for tantalum [55].

2.2.3 Effect of slurry pH

Although studies have shown the effect of slurry chemicals on zeta potential as summarized in Section 2.2.2, the slurry pH is the primary factor affecting the zeta potential of abrasive particles and wafer [57, 58]. The electrical double layer forces

between particles prevent the abrasive particles from forming agglomerates as the particles tend to attract each other due to the influence of van der Waals forces. This phenomenon is well known and studied under colloidal science theory and the background for this theory can be found in many textbooks [59]. The double layer forces between particles of the same material are repulsive in the slurry and the magnitude of these forces increases with higher zeta potential. In CMP, it was shown that the effective abrasive particle size increases significantly due to particle agglomeration, as the slurry pH approaches the isoelectric point (IEP) where the zeta potential becomes zero [57, 58, 60-62]. Stable abrasive particle size was obtained as the slurry pH was varied if the zeta potential remained at high levels [13, 53, 61].

The slurry pH also influences the zeta potential of the wafer. The double layer forces between the wafer and the abrasive particles depend on the zeta potential of both the wafer and the particles. Magnitude of the double layer forces between wafer and abrasive particles has been shown to have an effect on the MRR [13, 45, 62, 64, 65]. It was demonstrated that the MRR is high when abrasive particles and wafer are oppositely charged and a decrease in the MRR is observed as abrasive particles and wafer accompany the same charge [62, 64]. This behavior can be explained by considering the contact force between wafer and abrasives becoming large when double layer forces are attractive causing the MRR for each abrasive to increase [65]. Furthermore, when double layer forces become attractive, the impacting frequency of abrasive particles on wafer surface during the slurry flow at pad-wafer interface becomes larger, thereby increasing the number of active abrasive particles participating in material removal [45].

The hardness and thickness of passivated layer were also found to be a function of slurry pH [66-68]. Different oxidation rate and oxide compounds were observed as pH was varied in the acidic and alkaline regimes [68]. Due to the fact that passivated layer thickness and hardness has a strong influence on the MRR [66, 67], it is desirable to optimize the slurry pH in order to obtain favorable conditions for the MRR.

2.2.4 The measurements of wafer hardness

The hardness of passivated surface layer is different than that of the bulk wafer material [37, 69]. The chemical reactions, which lead to the passivation of the wafer surface, are different for different wafer materials, and slurry chemicals, as explained in Section 2.2.1. Hardness of the passivated layer is an important input parameter for the models predicting MRR. However, the measurement of the passivated layer hardness in CMP is challenging as the hardness and thickness of passivated layer was shown to depend on the slurry chemicals [70], the contact time of the slurry with wafer [71] and the thickness of film [71, 72]. In this section, the measurements for characterizing the passivated layer and bulk wafer hardness are reviewed.

The hardness values reported in the literature for different materials are listed in Table 2.1. Jindal and Babu [56] measured the hardness of copper after exposure to slurry with 5% peroxide at pH 2, 7 and 12. The hardness measurements of copper with and without exposure to the slurry at pH of 7 and 12 yielded similar results. The hardness was maximum at 25 nm (~2.25 GPa) and gradually decreased to 1.25 GPa at 250 nm. A similar trend was also observed for the hardness of tantalum exposed to the same slurry. A maximum hardness of 4 GPa was measured at 25 nm and the hardness decreased to 1.5

GPa at 200 nm in the case of tantalum. Ihnfeldt and Talbot [40] observed a similar behavior for copper film, where the hardness was at its maximum near the surface and approached the hardness of bulk material as the indentation depth was increased. This behavior changed as copper film was exposed to slurry with different pH. The hardness of bulk material was measured to be 2.2-2.8 GPa. It was shown that hardness near the surface of copper film at an indentation depth of 22-60 nm may become greater than 10 GPa or smaller than 1 GPa based on the slurry. The hardness at an indentation depth of 7-24 nm varied in the range 0.3-4.6 GPa. The decay in hardness found in this experiment as the indentation depth became larger, is in contrast to the assumption of softer passivated layer forming at the wafer surface. However in some cases, certain oxides and hydroxides formed at surface may actually be harder than the bulk material as explained by Ihnfeldt

Reference	Material	Hardness (GPa)	Indentation Depth (nm)
Jindal and Babu [56]	Cu	0.1 - 2.25	25-250
Ihnfeldt and Talbot [40]	Cu	0.3 – 16	7 – 60
Lin et al. [71]	Cu	0.1 - 3	25 – 300
Jindal and Babu [56]	Ta	1.5 - 4	25-200
Chandrasekaran et al. [77]	low-k	0.68 – 4.6	-
Vella et al. [78]	low-k	1-1.4	10 – 200
Sikder et al. [75]	low-k	0.3 – 6.3	
Wang et al. [72]	low-k	0.16 – 0.52	-

Table 2.1: Hardness measurements

and Talbot [40] considering the hardness of different oxides of copper increasing in the order $Cu(OH)_2 < Cu < CuO < Cu_2O$ [73].

Jindal and Babu [56] found that copper exposed to the slurry at pH = 2 exhibited significantly smaller hardness (0.5-0.75 GPa) than that of pH of 7 and 12, indicating the formation of a softer passivated layer in acidic solutions while the hardness of tantalum remained almost constant when exposed to the same slurry. No significant variation in hardness of copper was seen as a function of indentation depth in the range 25-250 nm for pH = 2. The experiments were repeated for different slurry with 5% peroxide and 1% glycine. The hardness of copper exposed to this slurry became even smaller at pH = 2 (~0.1 GPa).

The hardness of copper exposed to slurry decreased with indentation depth in experiments conducted by Lin et al. [71]. Note that slurry used in this experiment was more aggressive than the slurry used in experiments by Jindal and Babu [56]. The hardness was measured to be ~0.1 GPa at 25 nm and increased to 3 GPa at 300 nm depth. The hardness of tungsten was shown to vary with different oxides [74]. The hardness of tungsten was found to be in the range 1-6.5 GPa where higher oxygen content decreased the hardness.

Sikder et al. [75] carried out nano-indentation tests to determine the hardness of low-k dielectric films. It was determined that the hardness of the films was a function of the deposition method. The hardness of different low-k materials varied in the range of 0.3-6.3 GPa. The hardness of ultra-low-k dielectric films was measured to be lower 0.16-0.52 GPa due to the fact that porosity was introduced in these films to ensure low dielectric constant [76]. In addition, hardness of 0.68-4.6 GPa was reported for different low-k

dielectric materials [77]. Vella et al. [78] measured the hardness of porous dielectric material to be 1 GPa at 10 nm indentation depth and hardness was shown to increase up to 1.4 GPa when indentation depth was increased to 200 nm.

Several measurements were made to find the thickness of passivated layer. Trogolo and Rajan [79] determined a low density layer of 2 nm thickness in oxide CMP. The density of the material starting increasing as a function of indentation depth beyond this layer and the density reached the bulk density of material at 15-20 nm depth. The X-ray photoelectron spectroscopy (XPS) analysis of niobium surface revealed an oxide layer of ~5 nm thickness [80]. Considering the depth of cut of abrasive particles 1-10 nm for particle with a diameter of 10-200 nm [81], the abrasive particles may indent into the bulk wafer based on the chemical reactions, i.e. thickness and hardness of passivated layer and indentation depth of particles.

2.2.5 Modeling of passivated layer hardness

The hardness of passivated surface layer has been taken into consideration in a few studies focusing on the calculation of the MRR. Bastaninejad and Ahmadi [69] assumed that the oxidizer the slurry diffuses into the wafer material altering the hardness of wafer. The oxidizer concentration near wafer surface was considered to be constant and the oxidizer concentration as a function of distance from wafer surface was calculated. The derivation for the equation giving the variation of wafer hardness as a function of distance from wafer surface is explained next.

The diffusion of the oxidizer can be quantified by Fick's second law in the following form, if diffusivity D_o is constant [82],

$$\frac{\partial C_o}{\partial t} = D_o \left(\frac{\partial^2 C_o}{\partial y^2} \right) \quad (2.2)$$

where C_o is the oxidizer concentration and y is the distance from wafer surface. The steady-state material removal rate (*MRR*) if defined as the rate of wafer thickness reduction, can be expressed as,

$$MRR = -\frac{dy}{dt} \quad (2.3)$$

The term, $\frac{\partial C_o}{\partial t}$ in Eqn (2.2) can be combined with Eqn (2.3) using the chain rule as,

$$\frac{\partial C_o}{\partial t} = \frac{\partial C_o}{\partial y}\frac{dy}{dt} = -\frac{\partial C_o}{\partial y} MRR \quad (2.4)$$

Eqn (2.2) reduces to the following form using Eqn (2.4)

$$-\frac{MRR}{D_o}\frac{\partial C_o}{\partial y} = \frac{\partial^2 C_o}{\partial y^2} \quad (2.5)$$

The 2nd order differential equation can be reduced to the 1st order by substituting $V = \frac{\partial C_o}{\partial y}$ in Eqn (2.5) as,

$$-\frac{MRR}{D_o} V = \frac{dV}{dy} \quad (2.6)$$

The solution of this equation is [83],

$$V = \frac{dC_o}{dy} = C_1 e^{-\frac{MRR}{D_o} y} \quad (2.7)$$

where C_1 is a constant. C_o can be found by integrating Eqn (2.7) as,

$$C_o = \int C_1 e^{-\frac{MRR}{D_o}y} dy = -\frac{D_o C_1}{MRR} e^{-\frac{MRR}{D_o}y} + C_2 \tag{2.8}$$

where the constants C_1 and C_2 can be determined by using the boundary conditions. The following conditions are used to calculate C_1 and C_2 as,

$$C_o \to 0 \quad \text{as} \quad y \to \infty \tag{2.9}$$

$$C_o = C_\infty \quad \text{at} \quad y = 0 \tag{2.10}$$

which gives $C_2 = 0$ and $C_1 = -\frac{MRR}{D_o}$. Substituting constants C_1 and C_2 in Eqn (2.8), the variation of the oxidized concentration, C_o through the thickness of the wafer can be found as,

$$C_o = C_\infty e^{-\frac{MRR}{D_o}y} \tag{2.11}$$

The passivation reaction was considered to occur much more rapidly than the removal of the material from the surface by two successive abrasives [69]. It was assumed that the passivation of the wafer surface is linearly proportional to the oxidizer concentration. Following the two assumptions stated above, one can determine the variation of the wafer hardness through the thickness, H_w by replacing the variable C_o by H_w in Eqn (2.8) and using the following boundary conditions in Eqns (2.9) and (2.10) to find constants C_1 and C_2 as,

$$H_w \to H_{bw} \quad \text{as} \quad y \to \infty \tag{2.12}$$

$$C_o = H_{bw} \quad \text{at} \quad y = 0 \tag{2.13}$$

which gives $C_2 = H_{bw}$ and $C_1 = \frac{MRR_t}{D_o}\left(H_{bw} - H_{pw}\right)$. H_{pw} is the hardness of the wafer surface oxidized with oxidizer concentration, C_∞ and H_{bw} is the hardness of the bulk wafer in the absence of the oxidizers.

As a result, the variation of the hardness, H_w can be described by the following equation [69],

$$H_w = H_{bw} + \left(H_{pw} - H_{bw}\right)e^{-\frac{MRR_t}{D_o}y} \tag{2.14}$$

Eqn (2.14) implies that diffusivity and MRR determine the hardness variation from wafer surface. If MRR is significantly smaller than diffusivity, hardness of wafer material is dominated by passivated layer hardness $H_w \approx H_{pw}$. In the case of large MRR, the passivation of wafer material does not occur effectively and wafer hardness becomes equivalent to the hardness of bulk material, $H_w \approx H_{bw}$.

Eqn (2.14) indicates a smooth transition from passivated layer hardness near the surface to bulk wafer hardness as the indentation depth is increased. Qin et al. [37] assumed a sudden change from wafer passivated layer to bulk wafer hardness. A bi-layer model was used in the following form,

$$H_w(y) = \begin{cases} H_{pw} & y < t_{pw} \\ H_{bw} & y > t_{pw} \end{cases} \tag{2.15}$$

where passivated layer hardness H_{pw} is the relevant hardness, $H_w = H_{pw}$ when the distance from wafer surface is smaller than the passivated layer thickness, $y < t_{pw}$ whereas

hardness of bulk material H_{bw} becomes the relevant hardness, $H_w = H_{bw}$ at a distance greater than the passivated layer thickness, $y > t_{pw}$.

2.3 Effect of CMP Parameters on MRR

The most commonly cited empirical equation used to predict the MRR as a function of applied pressure P_o and relative velocity V_r is the Preston equation [84], which was developed based on the observations for the variation of MRR in glass polishing experiments. The MRR is calculated using,

$$MRR = k_p P_o V_r \tag{2.16}$$

where k_p is the Preston constant. Preston constant k_p implicitly includes the effect of the parameters such as abrasive particle size and concentration, pad elasticity, morphology and roughness, and slurry chemistry. Eqn (2.16) indicates that the MRR increases linearly with pressure and velocity, and the other parameters determine the rate of increase.

The CMP experiments conducted in order to investigate the effect of various parameters on the MRR showed that the Preston equation is valid in some cases while non-Prestonian behavior is observed in other cases. Moreover, experiments shed more light on the effect of the parameters such as abrasive particle size and concentration, pad elastic modulus, topography and porosity on the MRR. This is discussed next.

2.3.1 Effect of applied pressure and relative velocity

The validity of Preston equation in CMP was investigated by experiments. Ouma [85] found that the MRR of tetraethyloxysilane (TEOS) films increases linearly with the

product of applied pressure P_o and relative velocity V_r, P_oV_r at different slopes for small and large values of P_oV_r. The rate of increase in the product P_oV_r becomes smaller at large P_oV_r. Stein et al. [86] carried out experiments for CMP of TEOS films with hard and soft pads. The results of this study showed MRR increases linearly with P_oV_r for a hard pad, whereas a sub-linear variation is observed for a soft pad.

Guo and Subramanian [87] conducted CMP experiments for polishing copper films using both soft and hard pads. MRR increased linearly with applied pressure when a hard pad was used. The rate of increase was determined to be different at low and high pressures. On the other hand, MRR increased sub-linearly with applied pressure for the whole range of applied pressure used in the experiments in the case of soft pad. Nguyen et al. [43] found that the MRR of copper increases linearly with applied pressure; however, the rate of increase is a strong function of slurry chemicals. Chandrasekaran et al. [77] detected a highly non-linear variation of MRR with respect to applied pressure for different low-k dielectric materials and the variation was significantly different for each low-k material.

Hocheng et al. [88] conducted oxide CMP experiment in order to evaluate the effect of relative velocity V_r on the MRR. A sub-linear variation, MRR $\propto V_r^{0.65}$, was observed for the three values of applied pressure studied. Tseng and Wang [89] showed that the MRR increases with relative velocity as MRR $\propto V_r^{0.50}$ for oxide CMP and this relation remained constant for different levels of applied pressure used in the study. Copper CMP experiments conducted by Guo and Subramanian [87] indicated that MRR increases linearly at low relative velocity and a saturation effect is seen as relative velocity is increased. The experiments illustrated that the effect of applied pressure and relative

velocity on MRR may be linear (Prestonian) under some conditions, while a non-linear variation for MRR with respect to applied pressure and relative velocity was also observed.

2.3.2 Effect of abrasive particle concentration

Bielmann et al. [90] studied the effect of particle concentration on the MRR of tungsten films polished with alumina slurry containing particles of different size. The MRR was found to increase linearly with particle concentration at low particle concentration. The MRR leveled off at high particle concentration exhibiting a saturation effect. This saturation effect occurred when particle concentration was 5-10%. Particle size seemed to have an effect on this behavior, as no saturation effect was determined when particle size was greater than 300 nm in the range of particle concentration, 2-15% studied. Guo and Subramanian [87] carried out copper CMP experiments with alumina slurry. A saturation effect at high particle concentration, 5% was also found in this study. The experimental work by Stein et al. [86] for tungsten CMP with alumina slurry indicated a lower saturation particle concentration as compared to other experiments [87, 90]. Saturation particle concentration seemed to become higher with the product of applied pressure and relative velocity P_oV_r, where saturation particle concentration was 0.5% at low P_oV_r, and increased to 1.5% at high P_oV_r [86].

Silica slurry with particle concentrations in the range, 0-6.5% was used by Forsberg [91] to polish silicon film. The saturation effect was observed at a particle concentration of ~6%. Choi et al. [13] investigated the influence of silica particle concentration on the MRR seen for oxide CMP. A wide range of particle concentrations, 0-30% were used in

this study. In addition to the particle concentration, particle size was also varied in the range of 0.2-1.5 µm. The MRR was found to increase linearly with higher particle concentration when particle concentration was 0-30% and no saturation effect was detected for small particle size ~0.2 µm. A different behavior was observed for large particle size ~0.5-1.5 µm, where the MRR became saturated at particle concentration ~1-5%. In fact, MRR started to decrease with higher particle concentration above saturation particle concentration for large particles. This behavior was attributed to the rolling/sliding motion of particles, where particles tend to roll on wafer surface for large particle size, which reduces the MRR as compared to that due to sliding motion.

Tamboli et al. [92] investigated the effect of silica abrasive particle concentration for CMP of copper, tantalum and TEOS films by varying the particle concentration in the range, 0-14 %. In this range, the MRR of copper and TEOS films were found to increase linearly with particle concentration, whereas a saturation effect was observed at particle concentration of ~4-5% for tantalum film.

Although the effect of particle concentration depends on the slurry and polished material, a general trend is that the MRR increases linearly with particle concentration up to a saturation concentration, above which a further increase in particle concentration does not result in larger MRR. This behavior has been commonly seen in alumina slurry; while no saturation effect was seen for silica slurry even at high particle concentration ~30% in some cases [93].

2.3.4 Effect of abrasive particle size

The effect of silica abrasive particle size (25-200 nm) on the MRR of tantalum and TEOS films in CMP was studied by Tamboli et al. [92]. This work shows that the MRR increases with larger particle size for both tantalum and TEOS films. A similar observation was made by Lai [1] for the CMP of copper film with alumina slurry containing particles with diameter 50-1000 nm.

In contrast to these results indicating that the MRR increases with larger particle size, Bielmann et al. [90] found that the MRR decreases when alumina abrasive particle size is increased from 250 to 1800 nm in tungsten CMP. In fact, studies conducted by Mahajan [94] and Choi et al. [13] showed that the variation of the MRR with respect to particle size depends on the particle concentration for oxide CMP with silica abrasive particles. The MRR was shown to reach its maximum at a different particle size as the particle concentration was varied [13, 94]. Choi et al. [13] determined that MRR increases with particle size (200 – 1500 nm) when particle concentration is high (10-30 %), and an opposite trend was seen for small particle concentration (<5%). At intermediate particle concentration (5-10%), the maximum MRR was detected at different particle size.

These contradictory results were also realized by other researchers [95, 96]. The greater tendency of the particles to roll on the wafer surface as particle size becomes larger was explained to be one of the reasons for this contradictory behavior [13, 95]. This explanation was supported by in-situ friction force measurements showing a decrease in friction coefficient above a critical particle concentration for large particles, which occurred in parallel with the decrease in MRR [13]. Moreover, it was suggested for some

particle-wafer systems that the chemical interactions between abrasive particles and wafer causes the MRR to increase with smaller particle size since the total surface area of particles becomes larger as particle size is decreased providing more area for the interactions to occur [95]. The opposite behavior was attributed to the indentation of abrasive particles increasing with larger particle size [95].

2.3.5 Effect of pad elastic modulus

In Section 2.3.1, it was mentioned that the variation of the MRR with respect to the parameter P_oV_r depends on the pad elastic modulus. The MRR increases sub-linearly with P_oV_r for a soft pad, whereas the variation is linear, much like Preston equation for a hard pad. In addition, the MRR is expected to vary with pad elastic modulus. However, it is very difficult to isolate the effect of pad elastic modulus due to the fact that there are other parameters, such as pad porosity and pad topography that are different between soft and hard pads. Due to this difficulty, it is not possible to evaluate the effect of pad elastic modulus directly from the experiments; nevertheless it is stated that the general trend is increase of MRR with increasing pad elastic modulus [87].

This difficulty was overcome in the experiments conducted by Castillo-Mejia et al. [97], where the same type of pad was used for the polishing of TEOS films with silica slurry, by using identical CMP parameters except that the immersion time of pad prior to polishing was varied. The variation in immersion time was shown to have an effect on the solid elastic modulus of pad material, where pad elastic modulus decreases with longer immersion time due to the penetration of the water molecules in pad material. The experiments showed that the MRR decreases as the immersion time is increased, which

implied that smaller pad elastic modulus has a negative effect on the MRR. In fact, one of the conclusions drawn from this experiment was that pad conditioning is critical for maintaining a stable MRR since the softened pad material is effectively removed by conditioning thus providing a constant pad elastic modulus during polishing.

The measurements carried out by Sikder et al. [98] indicated that pad material exhibited viscoelastic behavior. This behavior was shown to be important for the MRR achieved in CMP [99]. CMP experiments conducted by Stein et al. [100] illustrated that the pad topography changes significantly in the early stages of polishing, when pad conditioning is not applied. The pad topography was found to remain stable in the later stages. However the MRR was determined to continuously decay during the entire polishing process. Fu et al. [99] attributed this continuous decay to the viscoelastic behavior of pad material, which causes the pad material to become softer as the polishing progresses.

2.3.6 Effect of pad porosity

The majority of pads are made of porous materials [93]. This is an important factor affecting the MRR in CMP [101, 102]. The pad acts as a conveyor to transfer the fresh slurry introduced in the system to wafer surface [103]. This is facilitated by the pores of the pad acting as passageways for slurry flow. Pad conditioning unclogs the pores closed by the abrasive particles, and polished material. This was suggested to be one of the reasons for the decay in the MRR in the absence of pad conditioning [100, 104-106].

The porosity of pad also causes the mechanical behavior of the pad to be different in different contact scales. The study conducted by Gouda et al. [107] showed that the bulk

response of the pad was dominated by the porous structure (porous pad elastic modulus), while the local mechanical behavior was determined by the solid pad elastic modulus.

Moon et al. [101, 102] conducted CMP experiments with pad of different density and compressibility. The MRR was shown to increase as the density of pad decreases. Although the density of solid pad material is not known, lower density is an indication for higher porosity. Therefore, it can be concluded that the MRR increases with higher porosity. In the experiments conducted by Fury et al. [108], two different pads made of the same polyurethane material were used but one of the pads had a porous structure. The MRR was shown to be greater for the porous pad as compared to the non-porous pad.

2.3.7 Effect of pad roughness

The pad roughness was shown to have an important effect on the MRR [109]. The pads used in the experiments conducted by Park et al. [109] were conditioned using different mechanical pad conditioners. The surface topography was measured to be significantly different for the pads based on the conditioner geometry. Not only the standard deviation of asperity summit heights, but also the mean height of asperities and skewness of height distribution were found to be different. The CMP experiments conducted using these pads showed that the MRR obtained using the pad with smaller roughness is greater. The skewness of the asperity summit height distribution was considered to play an important role for the ability of the pad to distribute the slurry over the wafer surface. According to the work of Park et al. [109], a pad with a positive skewness enables the slurry flow more effectively as compared to a pad with negative skewness.

2.4 Mechanical Modeling of CMP

In this section, the mechanical models developed in order to predict the MRR in CMP are reviewed. These models were constructed considering the interactions between a wafer, abrasive particles and a pad. The majority of the models in this section neglect the effect of hydrodynamic lubrication. The studies concerned with the modeling of hydrodynamic lubrication and slurry flow has been reviewed in Section 2.1.4.

2.4.1 Luo and Dornfeld's model

In this model [110], the pad and the wafer were assumed to undergo fully-plastic deformation due to contact with abrasive particle. Following this assumption, the indentation depth of particle in wafer and pad was calculated using the hardness of wafer and pad, respectively. The mean real contact pressure due to the rough contact between pad and wafer was calculated by considering a periodic (wavy) rough pad surface, which leads to closed-form equations for real contact area and mean real contact pressure. The mean real contact pressure was assumed to be acting on the particle as a result of the assumption that abrasive particles were embedded in the pad. The pad-particle contact force on each particle was determined using the mean real contact pressure and the cross-section area of the particle. The abrasive wear achieved by each particle was then calculated by using the volume swept by each particle, which was determined from the indentation depth of each particle in the wafer due to the pad-particle contact force.

The particles larger than the gap between pad and wafer were considered to participate in material removal. The pad-wafer gap was determined by subtracting the indentation

depth of the largest particle in pad and wafer, from the diameter of the largest particle. Using the number of active particles and the abrasive wear achieved by each particle, the total MRR was calculated.

The results of this model showed that MRR increases sub-linearly with applied pressure. This result stems from the assumption of wavy pad roughness, which leads to the relation between applied pressure P_o and real contact area A_r as $A_r \propto P_o^{2/3}$. A soft pad was determined to result in a greater MRR than a hard pad [110]. This is due to the fact that particle penetrates deeper into the pad for a soft pad, decreasing the pad-wafer gap and resulting in more active particles. As standard deviation of particle size distribution increases, the model predicts a lower MRR, as the maximum particle size controlling the pad-wafer gap becomes larger [110, 111].

Incremental improvements were made after the introduction of this model [112-114]. A bi-layer hardness model considering the hardness of a passivated surface layer was implemented [112]. Some of experimental trends for the variation of the MRR with particle concentration were explained by this model. The saturation effect for MRR at high particle concentration was attributed to the passivated layer hardness, which increases at high particle concentration, as the rate of passivation is not sufficiently high to maintain low hardness near the surface.

Thagella et al. [113] improved the Luo-Dornfeld model by using a different approach to calculate the number of active abrasives. The number of active abrasives was obtained from the slurry volume trapped between pad and wafer, which was calculated using the real contact area between pad and wafer, and the mean height of pad asperities. The

comparison of model results with experiments showed that the error of the model increases with increasing relative velocity. When the relative velocity is increased above a critical value in the experiments, the MRR decreases due to the fact that the hydrodynamic effects become significant. The proposed model, however predicted increasing MRR in this range, as the model was based on boundary lubrication regime.

Jeng and Huang [114] extended the model by including the effect of the abrasive particles on the load balance at pad-wafer interface, whereas pad-wafer contact was considered to be the only contact mechanism supporting the applied load in Luo-Dornfeld model. This was achieved by subtracting the contact area at wafer-particle interface from the real contact area between pad and wafer. The results of this model suggested a decreasing MRR for larger particle size due to larger gap at pad-wafer interface.

Zhao and Chang [115] presented a similar model as Luo-Dornfeld model. Zhao and Chang found that pad-particle contact is essentially elastic for typical CMP parameters in contrast to the assumption of plastic deformation for pad-particle contact in Luo-Dornfeld model. This finding was based on their previous work investigating the elastic-plastic contact of two rough surfaces [116, 117]. Luo and Dornfeld treated the pad roughness to be periodic, whereas Zhao and Chang assumed random pad roughness. The MRR was found to be inversely proportional to the square of particle size in their study.

2.4.2 Ahmadi and Xia's model

Ahmadi and Xia [118] calculated the load on the abrasive particles with a different formulation for a soft and a hard pad that have different characteristics to distribute the

load on the particles based on the observation of Shi and Zhao [119]. In the case of a hard pad, most of the applied pressure is carried by particle contacts. As the applied pressure is increased, the load on each particle becomes larger. However, for a soft pad, the particles are embedded in the pad, therefore pad-wafer contact supports most of the load. An increase in the applied pressure does not cause an increase in the force on the particle but the number of active particles increases. Both elastic and plastic deformation of the pad and the wafer were taken into account for the contact with the particles. The van der Waals forces between wafer and particles were included. Abrasive and adhesive wear were considered to be the mechanisms that cause material removal. The model was studied for periodic and random pad roughness.

This study showed that inclusion of the van der Waals forces into the model causes an increase in the MRR. In addition, smaller particle size causes larger MRR, due to the influence of van der Waals forces. The variation of the MRR with applied pressure P_o was found to be linear (MRR α P_o) for random pad roughness and a sub-linear (MRR α $P_o^{2/3}$) dependence was observed for wavy pad roughness. This was attributed to the variation of real contact area with applied pressure for random and wavy surface roughness.

This model was improved by including the effect of the roughness of abrasive particles on the magnitude of van der Waals forces [120]. This was achieved by modeling the abrasive particles as spheres with hemispherical bumps on the surface. Bumpy (rough) abrasive particles were shown to have a lower MRR as compared to smooth particles due to the reduction in van der Waals forces for rough particles. In addition to the van der

Waals forces, the electrical double layer forces were considered in an extension of this model [121]. The experimentally observed variation of the MRR with slurry pH was attributed to the effect of slurry pH on zeta potential influencing the magnitude of double layer forces.

2.4.3 Fu et al.'s model

Fu et al. [81] developed a mechanical model by considering the occurrence of pad-wafer and pad-particle-wafer contact simultaneously. In order to achieve this, the pad was modeled as a thin elastic beam, supported by abrasive particles at the ends. The partition of applied pressure to pad-wafer direct contact and pad-particle-wafer contact was determined by solving for the deformation of the thin elastic beam. Furthermore, abrasive wear rate of each particle was calculated based on the shape of the particle (spherical or sharp). The authors concluded that the dependence of the MRR on various parameters is sensitive to the degree of pad-wafer direct contact. The assumption of soft pad with low abrasive concentration was determined to be valid for typical CMP conditions. In this regime, the MRR was found to increase with applied pressure P_o as MRR $\propto P_o^{9/8}$ and MRR $\propto P_o^{3/4}$ for spherical (blunt) and sharp abrasive particles, respectively. The model showed that the MRR increases with higher particle concentration up to a critical concentration above which MRR decreases.

2.4.4 Qin et al.'s model

Qin et al. [37] considered the abrasive particles to be embedded in the pad and calculated the force on each particle using the real contact pressure between pad and wafer, and the

radius of particle as similar to Luo-Dornfeld model. The number of active particles was the determined by considering the slurry volume when the pad-wafer separation distance is the equal to the particle diameter. A bi-layer hardness model was adopted, in order to capture the effect of passivated layer thickness and hardness on the MRR. The results of the model indicated that the MRR is linearly proportional to applied pressure MRR $\propto P_o$. The MRR was illustrated to decrease significantly as the indentation depth of particles becomes larger than the passivated layer thickness. In this case, the MRR is limited by the chemical effects. The MRR is determined by the mechanical effects if the indentation depth of particles is smaller than the passivated layer thickness. It was concluded that the optimal polishing performance can be obtained by the balance of the mechanical and chemical effects.

2.4.5 Other mechanical models for boundary lubrication

Fu and Chandra [122] derived the contact pressure distribution due to the contact of a rigid curved wafer and a pad modeled as an elastic half space. The contact pressure was found to be Hertzian at small applied pressure indicating that maximum MRR would be at the center of wafer (edge-slow). As the contact force was increased, a singularity formed at the edge of wafer, causing the maximum contact pressure and MRR to occur at the edge of the wafer (edge-fast). The contact pressure was determined to be relatively uniform at an intermediate applied pressure in transition between the edge-slow and edge-fast MRR behavior. A combination of wafer curvature and applied pressure were used to optimize the contact pressure distribution, by modeling arbitrary wafer shapes in a separate study [123]. This model was further improved to include the viscoelastic pad

properties [99]. The experimentally observed MRR decay in the absence of pad conditioning was explained by viscoelastic behavior of pad, as the contact pressure was determined to be altered in time due to the viscoelasticity.

Castillo-Mejia et al. [124] calculated the von Mises stresses induced in the wafer due to the contact with a pad, by using an axisymmetric finite element model for the pad-wafer contact. The calculated non-uniform von Mises stress distribution in the wafer was found to qualitatively agree with the experimentally observed non-uniformity in the MRR. Lin and Lo developed a similar model, by including the effect of different elastic layers for pad and wafer [125, 126]. The effect of surface roughness on the pad-wafer contact was implemented in the finite element model, as a separate elastic layer with a stiffness calculated by a multi-asperity contact model [127]. Inclusion of the rough surface layer improved the correlation between the calculated contact pressure distribution and experimentally observed MRR profiles.

The pad-particle-wafer contact was investigated by using a finite element model of a single particle with a pad and a wafer. The non-linear material behavior of the pad obtained from experiments was used in the model [128]. The distribution of the load to pad-wafer and pad-particle-wafer contact was studied. Different experimentally observed behavior for the dependence of MRR on applied pressure was attributed to the distribution of the load to pad-wafer and pad-abrasive-wafer contact. It was shown that low particle concentration, high applied pressure and small pad elastic modulus promote pad-wafer contact, whereas pad-particle-wafer contact becomes dominant when particle concentration is high, applied pressure is low and a hard pad is used.

The van der Waals forces between wafer and abrasive particles were considered in a model by Zhang et al. [129]. The wafer-particle contact force was a result of the combination of forces due to pad-particle contact and wafer-particle adhesion. This study concluded that van der Waals forces may have an effect on the MRR in CMP.

2.4.5 Other mechanical models for mixed lubrication

Tichy et al. [14] presented the first material removal model to simulate mixed lubrication in CMP. The bulk pad was modeled as a semi-infinite elastic half space, whereas Winkler model was used to model the deformation of the pad asperities. The slurry film thickness was assumed to be the same as the average height of pad asperity summits. The hydrodynamic pressure was calculated using 1-D Reynolds equation. The model was successful in determination of sub-ambient hydrodynamic pressure explained in Section 2.1.2. It was concluded that increasing pad roughness and relative velocity increase the magnitude of sub-ambient pressure.

Jeng and Tsai [29,30] applied a grain flow model, developed for thin film lubrication including the effect of abrasive particles, for modeling the mixed lubrication in CMP. The equilibrium slurry film thickness was iteratively found by using the equilibrium of the pad-wafer contact force, applied pressure and hydrodynamic pressure. It was concluded that the abrasive particles have an effect on slurry film thickness and hydrodynamic pressure, and larger particle size increases the slurry film thickness.

The study conducted by Lin et al. [71] formulated the effect of pad deformation on the MRR in a model for mixed lubrication. The slurry flow was obtained by solving the

Reynold's equation with Patir/Cheng's flow factors [130] in order to include the effect of pad roughness on hydrodynamic lubrication. The equilibrium position of the wafer was calculated by the equilibrium of hydrodynamic pressure, applied pressure and contact pressure at pad-wafer rough contact interface. Both adhesive and abrasive wear were considered in the model. It was concluded that high MRR with low non-uniformity can be achieved by decreasing the composite hardness of the wafer via increasing the thickness of the passivated layer. The MRR was shown to increase with applied pressure and relative velocity, but the within-wafer-non-uniformity (WIWNU) increases with larger relative velocity and decreases with higher applied pressure.

The model developed by Kim et al. [131] combined the effects hydrodynamic lubrication and pad-wafer rough contact. Mooney-Rivlin hyperelastic model was used to simulate pad material behavior. The abrasive particles were not directly included in the model but the MRR was correlated to the contact stress induced at the wafer surface due to pad-wafer contact. The effect of wafer curvature was investigated in this model. The MRR at the edge of wafer was found to be greater for concave wafers, whereas convex and flat wafers resulted in a smaller MRR at the wafer edge.

2.5 Physical Parameters

In this section, the range of values reported in the literature for the physical parameters utilized in the model developed in this work is investigated. The elastic modulus of the pad was measured by tensile [97] and compression [128] tests. The elastic modulus of different types of pad was found to be varying in the range 3 MPa $< E_s <$ 372 MPa as shown in Table 2.2. The soaking of the pad in water was found to have a significant

effect on the pad elastic modulus. Castillo-Mejia et al. [97] measured the pad elastic modulus to be E_s = 372 MPa for a dry pad and the pad elastic modulus decreased to E_s = 280 MPa when the pad was soaked in water.

Surface profilometer was commonly used to determine the surface parameters of the pad including asperity radius R_s, asperity density η_s and roughness σ_s [132, 133]. The findings of different studies for these parameters are listed in Table 2.2. It was indicated that the conditioning of the pad plays an important role for the values of these parameters. Park et al. [109] studied the effect of different conditioner geometry on pad roughness σ_s. The roughness of a pad conditioned with two different conditioner geometry was measured to

Reference	E_s (MPa)	σ_s (μm)	R_s (μm)	η_s (1/μm^2)
Yu et al. [132]	-	25	30	1.2x10^{-3}
Stein et al. [100]	-	20-29	-	-
Shan et al. [11]	12	5	100	4x10^{-4}
Castillo-Mejia et al. [97]	280 - 372	-	-	-
Shan [133]	-	5	50	2x10^{-4}
Levert et al. [9]	40	-	-	-
Baker [Baker 96]	29	-	-	-
Lin et al. [71]	-	15	50	4.3x10^{-5}
Kim et al. [131]	3	-	-	-
Steigerwald et al. [135]	100	-	-	-
Kim [136]	5	-	-	-
Bastawros et al. [128]	180	-	-	-
Park et al. [109]	-	2.96-4.94	-	-
Tso et al. [137]	16			

Table 2.2: Measurements for pad parameters in CMP

be σ_s = 2.96 and σ_s = 4.94 µm, while the roughness of the unconditioned pad was found as σ_s = 3.71 µm. It is seen that pad roughness varies in the range 3 µm < σ_s < 29 µm, asperity radius 30 µm < R_s < 100 µm and asperity density $4.2 \times 10^{-5}/\mu m^2 < \eta_s < 1.2 \times 10^{-3}/\mu m^2$.

The effective Hamaker constant A_{wsp} due to the interaction of alumina (Al_2O_3) with different materials in nitrogen (N_2) and water (H_2O) was reported by Cooper et al. [138]. The values for Hamaker constant listed in Table 2.3 show that the effective Hamaker constant A_{wsp} in water is significantly lower than that in nitrogen. The effective Hamaker constant in water varied in the range 1.3×10^{-20} J < A_{wsp} < 6.6×10^{-20} J while the range of Hamaker constant in nitrogen was 9.7×10^{-20} J < A_{wsp} < 22.6×10^{-20} J. Cooper et al. [138] showed that the roughness of particles influence the van der Waals forces between wafer and particles significantly. This is attributed to the effect of low Hamaker constant of water, $A = 4.38 \times 10^{-20}$ J [139]. Furthermore, Eichenlaub et al. [140] measured the Hamaker constant of copper (Cu) and silica (SiO_2) as listed in Table 2.4.

System	A_{wsp} ($\times 10^{-20}$ J)
Cu / N_2 / Al_2O_3	21.7
SiO_2 / N_2 / Al_2O_3	9.7
W / N_2 / Al_2O_3	22.6
Cu / H_2O / Al_2O_3	6.2
SiO_2 / H_2O / Al_2O_3	1.3
W / H_2O / Al_2O_3	6.6

Table 2.3: Hamaker constant of alumina (Al_2O_3) with different materials in water and nitrogen [138].

System	A_{wsp} (x10^{-20} J)
$Cu / N_2 / Cu$	27.1
$SiO_2 / N_2 / SiO_2$	7.2
$Cu / N_2 / SiO_2$	13.9

Table 2.4: Hamaker constants of copper and silica in nitrogen [140].

References

1. Lai J. Y., 2001. Mechanics, mechanisms and modeling of the chemical mechanical polishing process. Ph.D. Dissertation, Massachusetts Institute of Technology, Massachusetts.

2. Philipossian A., Olsen S., 2003. Fundamental tribological and removal rate studies of inter-layer dielectric chemical mechanical planarization. Jpn J Appl Phys, 42, 6371-6379.

3. Stachowiak G. W., Bachelor A. W., 2001. Engineering Tribology. Butterworth-Heinemann, Boston.

4. Liang H., Xu G.H., 2002. Lubricating behavior in chemical-mechanical polishing of copper. Scripta Materialia, 46, 343-347.

5. Denardis D., Sorooshian J., Habiro M., Rogers C., Philipossian A., 2003. Tribology and removal rate characteristics of abrasive-free slurries for copper CMP applications. Jpn Appl Phys, 42, 6809-6814.

6. Lu J., Rogers C., Manno V.P., Philipossian A., Anjur S., Moinpour M., 2004. Measurements of slurry film thickness and wafer drag during CMP. J Electrochem Soc, 151, 241-247.

7. Hocheng H., Cheng C., 2002. Visualized characterization of slurry film between wafer and pad during chemical mechanical planarization. IEEE Trans Semicond Manuf, 15, 45-50.

8. Levert J.A., 1997. Interface mechanics of chemical mechanical polishing for integrated circuit planarization. Ph.D. Dissertation, Georgia Institute of Technology, Atlanta, GA.

9. Levert J.A., Mess F.M., Salant R.F., Danyluk S., 1998. Mechanisms of chemical-mechanical polishing of SiO2 dielectric on integrated circuits. Tribol Trans, 41, 593-599.

10. Levert J. A., Danyluk S., Tichy T., 2000. Mechanism for subambient interfacial pressures while polishing with liquids. J Tribol Trans ASME, 122, 450-457.

11. Shan L., Levert J., Meade L., Tichy J., Danyluk., 2000. Interfacial fluid mechanics and pressure prediction in chemical mechanical polishing. J Tribol Trans ASME, 122, 539-543.

12. Shan L., Zhou C., Danyluk S., 2001. Mechanical interactions and their effects on chemical mechanical polishing. IEEE Trans Semiconduct Manuf, 14, 207-213.

13. Choi W., Abiade J., Lee S., Singh R.K., 2004. Effects of slurry particles on silicon dioxide CMP. J Electrochem Soc, 151, 512-522.

14. Tichy J., Levert J.A., Shan L., Danyluk S., 1999. Contact mechanics and lubrication hydrodynamics of chemical mechanical polishing. J Electrochem Soc, 146, 1523-1528.

15. Coppeta J., Rogers C., Racz L., Philipossian A., Kaufman F.B., 2000. Investigating slurry transport beneath a wafer during chemical mechanical polishing processes. J Electrochem Soc, 147, 1903-1909.

16. Liang H., Kaufman F., Sevilla R., Anjur S., 1997. Wear phenomena in chemical mechanical polishing. Wear, 211, 271-279.

17. Hocheng H., Huang Y. L., Chen L. J., 1999. Kinematic analysis and measurement of temperature rise on a pad in chemical mechanical planarization. J Electrochem Soc, 146, 4236-4239.

18. Li Z., Borucki L., Koshiyoma I., Philipossian A., 2004. Effect of slurry flow rate on tribological, thermal, and removal rate attributes of copper CMP. J Electrochem Soc, 151, 482-487.

19. Homma Y., Fukushima K., Kondo S., Sakuma N., 2003. Effects of mechanical parameters on CMP characteristics anayzed by two-dimensional friction force measurements. J Electrochem Soc, 150, 751-757.

20. Runnels S.R., Eyman L.M., 1994. Tribology analysis of chemical-mechanical polishing. J Electrochem Soc, 6, 1698-1701.

21. Thakurta D.G., Borst C.L., Schwendeman D.W., Gutmann R.J., Gill W.N., 2001. Three-dimensional chemical mechanical planarization slurry flow model based on lubrication theory. J Electrochem Soc, 148, 207-214.

22. Thakurta D. G., Borst C. L., Schwendeman, Gutmann R. J., Gill W. N., 2000. Pad porosity, compressibility and slurry delivery effects in chemical mechanical planaraization: modeling and experiments. Thin Solid Films, 366, 181-190.

23. Sundararajan S., Thakurta D.G., Schwendeman D.W., Murarka S.P, Gill W.N., 1999. Two-dimensional wafer-scale chemical mechanical planarization models based on lubrication theory and mass transport. J Electrochem Soc, 146, 761-766.

24. Thakurta D.G., Schwendeman D.W., Gutmann R.J., Shankar S., Jiang L., Gill W.N., 2002. Three-dimensional wafer-scale copper chemical-mechanical planarization model. Thin Solid Films, 414, 78-90.

25. Cho C.H., Park S.S., Ahn Y., 2001. Three-dimensional wafer scale hydrodynamic modeling for chemical mechanical polishing. Thin Solid Films, 389, 254-260.

26. Park S.S., Cho C.H., Ahn Y., 2000. Hydrodynamic analysis of chemical mechanical polishing process. Tribol Int, 33, 723-730.

27. Jin X., Keer L. M., Wang Q., 2005. A 3D EHL simulation of CMP. J Electrochem Soc, 152, 7-15.

28. Chen J.A., Fang Y.C., 2002. Hydrodynamic characteristics of the thin fluid film in chemical-mechanical polishing. IEEE Trans Semiconduct Manuf, 15, 39-44.

29. Tsai H.J., Jeng Y.R., 2002. An average lubrication equation for thin film grain flow with surface roughness effects. J Tribol Trans ASME, 124, 736-742.

30. Jeng Y.R., Tsai H.J., 2002. Tribological analysis on powder slurry in chemical mechanical polishing. J Phys D: Appl Phys, 35, 1585-1591.

31. Jeng Y.R., Tsai H.J., 2003. Improved model of wafer/pad powder slurry for CMP. J Electrochem Soc, 150, 348-354.

32. Sawyer W.G., Tichy J.A., 2001. Lubrication with granular flow: Continuum theory, particle simulations, comparison with experiment. J Tribol Trans ASME, 123, 777-784.

33. Su Y.T., 2000. Investigation of removal rate properties of a floating polishing process. J Electrochem Soc, 147, 2290-2296.

34. Subramanian R.S., Zhang L., Babu V., 1999. Transport phenomena in chemical mechanical polishing. J Electrochem Soc, 146, 4263-4272.

35. Paul E., 2002. A model of CMP, II. Polishing pressure and speed. J Electrochem Soc, 149, 305-308.

36. Paul E., Vacassy R., 2003. A model of CMP, III. Inhibitors. J Electrochem Soc, 150, 739-743.

37. Qin K., Moudgil B., Park C.W., 2004. A chemical mechanical polishing model incorporating both the chemical and mechanical effects. Thin Solid Films, 446, 277-286.

38. Chen K. W., Wang Y. L., 2007. Study of non-Preston phenomena induced from the passivated additives in copper CMP. J Electrochem Soc, 154, 41-47.

39. Choi W., Mahajan U., Lee S. M., Abiade J., Singh R. K., 2004. Effect of slurry ionic salts at dielectric silica CMP. J Electrochem Soc, 151, 185-189.

40. Ihnfeldt R., Talbot J. B., 2008. Effect of CMP slurry chemistry on copper nanohardness. J Electrochem Soc, 155, 412-420.

41. Deshpande S., Kuiry S. C., Klimov M., Obeng Y., Seal S., 2004. Chemical mechanical planarization of copper: role of oxidants and inhibitors. J Electrochem Soc, 151, 788-794.

42. Hernandez J., Wrschka P., Oehrlein G. S., 2001. Surface chemistry studies of copper chemical mechanical planarization. J Electrochem Soc, 148, 389-397.

43. Nguyen V. H., Daamen R., van Kranenburg H., et al., 2003. A physical model for dishing during metal CMP. J Electrochem Soc, 150, 689-693.

44. Xu G., Liang H., Zhao J., Li Y., 2004. Investigation of copper removal mechanisms during CMP. J Electrochem Soc, 151, 688-691.

45. Chiu S. Y., Wang Y. L., Liu C. P., Chang S. C., et al., 2006. High-selectivity damascene chemical mechanical polishing. Thin Solid Films, 498, 60-63.

46. Kuiry S. C., Seal S., Fei W., et al., 2003. Effect of pH and H_2O_2 on Ta chemical mechanical planarization. J Electrochem Soc, 150, 36-43.

47. Lim G., Lee J. H., Kim J., et al., 2004. Effects of oxidants on the removal of tungsten in CMP process. Wear, 257, 863-867.

48. Seo Y. J., Lee W. S., 2005. Effect of different oxidizers in the W-CMP performance. Mater Sci Eng B, 118, 281-284.

49. Lee B. C., Duquette D. J., Gutmann R. J., 2001. Synthesis of model alumina slurries for damascene patterning of copper. Mat Res Soc Symp Proc, 671, 2.7.1-2.7.12.

50. Luo Q., Campbell D. R., Babu S. V., 1996. Stabilization of alumina slurry for chemical-mechanical polishing of copper. Langmuir, 12, 3563-3566.

51. Hong Y. K., Han J. H., Kim T. G., Park J. G., Busnaina A. A., 2007. The effect of frictional and adhesion forces attributed to slurry particles on the surface quality of polished copper. J Electrochem Soc, 154, 36-40.

52. Kang Y. J., Hong Y. K., Song J. H., et al., 2005. The adsorption behaviors of citric acid on abrasive particles in Cu CMP slurry. Mater Res Soc Symp Proc, 867, 7.5.1-7.5.6.

53. Lee D. W., Kim N. H., Chang E. G., 2005. Effect of nonionic surfactants on the stability of alumina slurry for Cu CMP. Mater Sci Eng B, 118, 293-300.

54. Li Y., Zhao J., Wu P., et al., 2006. Interaction between abrasive particles and films during chemical-mechanical polishing of copper and tantalum. Thin Solid Films, 497, 321-328.

55. Harihaputhiran M., Li Y., Ramarajan S., Babu S. V., 2000. Chemical mechanical polishing of Ta. Electrochem Solid State Letters, 3, 95-98.

56. Jindal A., Babu S. V., 2004. Effect of pH of copper and tantalum. J Electrochem Soc, 151, 709-716.

57. Gopal T., Talbot J. B., 2006. Effects of CMP slurry chemistry on the zeta potential of alumina abrasives. J Electrochem Soc, 153, 622-625.

58. Ihnfeldt R., Talbot J. B., 2006. The effects of copper CMP slurry chemistry on the colloidal behavior of alumina abrasives. J Electrochem Soc, 153, 948-955.

59. Hiemenz P. C., 1986. Principles of colloid and surface chemistry. Marcel Dekker, New York.

60. Sorooshian A., Ashwani R., Choi H. K., et al., 2004. Effect of particle interaction on agglomeration of silica-based CMP slurries. Mat Res Soc Symp Proc, 816, 4.9.1-4.9.7.

61. Lee S. Y., Lee S. H., Park J. G., 2003. Interaction forces between silica particles and wafer surfaces during chemical mechanical planarization of copper. J Electrochem Soc, 150, 327-332.

62. Ramarajan S., Li Y., Hariharaputhiran M., et al., 2000. Effect of pH and ionic strength on chemical mechanical polishing of tantalum. Electrochem Solid State Letters, 5, 232-234.

63. Song M. G., Lee J. H., Lee Y. G., Koo J. H., 2006. Stabilization of gamma alumina slurry for chemical–mechanical polishing of copper. J Colloid Interface Sci, 300, 603-611.

64. Hegde S., Babu S. V., 2004. Study of surface charge effects on oxide and nitride planarization using alumina/ceria mixed abrasive slurries. Electrochem Solid State Letters, 7, 316-318.

65. Chen W. C., Lin S. C., Dai B. T., Tsai M. S., 1999. Chemical mechanical polishing of low-dielectric-constant polymers. J Electrochem Soc, 146, 3004-3008.

66. Akonko S. B., Li S. Y., Ziomek-Moroz M., et al., 2005. Effects of $K_3[Fe(CN)_6]$ slurry's pH value and applied potential on tungsten removal rate for chemical–mechanical planarization application. Wear, 259, 1299-1307.

67. Jindal A., Babu S. V., 2004. Effect of pH on CMP of copper and tantalum. J Electrochem Soc, 151, 709-716.

68. Kuiry S. C., Seal S., Fei W., et al., 2007. Effect of pH and H_2O_2 on Ta chemical mechanical planarization. J Electrochem Soc, 150, 36-43.

69. Bastaninejad M., Ahmadi G., 2005. Modeling the effects of abrasive size distribution, adhesion, and surface plastic deformation on chemical-mechanical polishing. J Electrochem Soc, 152, 720-730.

70. Jindal A., Hegde S., Babu S. V., 2003. Chemical mechanical polishing of dielectric films using mixed abrasive slurries. J Electrochem Soc, 150, 314-318.

71. Lin J. F., Chern J. D., Chang Y. H., Kuo P. L., Tsai M. S., 2004. Analysis of the tribological mechanisms arising in the chemical mechanical polishing of copper-film wafers. J Tribol Trans ASME, 126, 185-199.

72. Wang J., Shi F.G., Nieh T. G., Zhao B., et al., 2000. Thickness dependence of elastic modulus and hardness of on-wafer low-k ultrathin polytetrafluoroethylene films. Scripta Mater, 42, 684-694.

73. Szymanski A., Szymanski J. M., 1989. Hardness estimation of minerals rocks and ceramic materials. Elsevier Science Publishers, New York.

74. Kudo T., Okamoto H., 1986. Peroxopolytungstic acid synthesized by direct reaction of tungsten or tungsten carbide with hydrogen peroxide. Inorg Chim Acta, 111, L27–L28.

75. Sikder A. K., Irfan I. M., Kumar A., Anthony J. M., 2001. Nano-indentation studies of Xerogel and SiLK low-K dielectric materials. J Electron Mater, 30, 1527-1531.

76. Wang Y. H., Moitreyee M. R., Kumar R., Wu S. Y., et al., 2004. The mechanical properties of ultra-low-dielectric-constant films. Thin Solid Films, 462-463, 227-230.

77. Chandrasekaran N., Ramarajan S., Lee W., Sabde G. M., Meikle S., 2004. Effects of CMP process conditions on defect generation in low-k materials. J Electrochem Soc, 151, 882-889.

78. Vella J.B., Adhihetty I. S., Junker K., Volinsky A. A., 2003. Mechanical properties and fracture toughness of organo-silicate glass (OSG) low-k dielectric thin films for microelectronic applications. International Journal of Fracture, 119/120, 487-499.

79. Trogolo J. A., Rajan K., 1994. Near surface modification of silica structure induced by chemical/mechanical polishing. J Mater Sci, 29, 4554-4558.

80. Calota G., Maximova N., Ziemer K. S., Muftu S., 2008. Investigation of chemical mechanical polishing of niobium. STLE Tribology Transactions, submitted Nov 3 2008.

81. Fu G., Chandra A., Guha S., Subhash G., 2001. A plasticity-based model of material removal in chemical-mechanical polishing. IEEE Trans Semiconduct Manuf, 14, 406-417.

82. Smith W. F., 2003. Foundations of materials science and engineering. McGraw-Hill, New York.

83. Greenberg M. D., 1998. Advanced engineering mathematics. Prentice Hall, NJ.

84. Preston F.W., 1927. The theory and design of plate glass polishing machines. J Soc Glass Technol, 11, 214-256.

85. Ouma D. O., 1998. Modeling of chemical mechanical polishing for dielectric planarization. Ph.D. Dis., MIT, Cambridge, MA.

86. Stein D. J., Hetherington D. L., Cecchi J. L., 1999. Investigation of the kinetics of tungsten chemical mechanical polishing potassium-iodate slurries. J Electrochem Soc, 146, 376-381.

87. Guo L., Subramanian R.S., 2004. Mechanical removal in CMP of copper using alumina abrasives. J Electrochem Soc, 151, 104-108.

88. Hocheng H., Tsai H. Y., Su Y. T., 2001. Modeling and experimental analysis of the material removal rate in the chemical mechanical planarization of dielectric films and bare silicon wafers. J Electrochem Soc, 148, 581-586.

89. Tseng W. T., Wang Y.L., 1997. Re-examination of pressure and speed dependences of removal rate during chemical mechanical polishing processes. J Electrochem Soc, 144, 15-17.

90. Bielmann M., Mahajan U., Singh R. K., 1999. Effect of particle size during tungsten chemical mechanical polishing. Electrochem Solid State Letters, 2, 401-403.

91. Forsberg M., 2005. Effect of process parameters on material removal rate in chemical mechanical polishing of Si(1 0 0). Microelectron Eng, 77, 319-326.

92. Tamboli D., Banerjee G., Waddell M., 2004. Novel interpretations of CMP removal rate dependencies on slurry particle size and concentration. Electrochem Solid State Letters, 7, 62-65.

93. Oliver M.R. (Editor), 2004. Chemical mechanical planarization of semiconductor materials. Springer Verlag, New York.

94. Mahajan U., 2000. Fundamental studies on silicon dioxide chemical mechanical polishing. Ph.D. Thesis, University of Florida, FL.

95. Basim G.B., Adler J.J., Mahajan U., Singh R.K., Moudgil B.M., 2000. Effect of particle size of chemical mechanical polishing slurries for enhanced polishing with minimal defects. J Electrochem Soc, 147, 3523-3528.

96. Castillo-Mejia D., Beaudoin S., 2003. A locally relevant wafer-scale model for CMP of silicon dioxide. J Electrochem Soc, 150, 581-586.

97. Castillo-Mejia D., Gold S., Burrows V., Beaudoin S., 2003. The effect of interactions between water and polishing pads on chemical mechanical polishing removal rates. J Electrochem Soc, 150, 76-82.

98. Sikder A.K., Irfan I.M., Kumar A., Belyaev A. et al., 2001.Evaluation of mechanical and tribological behavior, and surface characteristics of CMP pads. Mater Res Soc Symp Proc, 671, 1.8.1-1.8.7.

99. Fu G., Chandra A., 2002. A model for wafer scale variation of removal rate in chemical mechanical polishing based on viscoelastic pad deformation. J Electron Mater, 31, 1066-1073.

100. Stein D., Hetherington D., Dugger M., Stout T., 1996. Optical interferometry for surface measurements of CMP pads. J Electron Mater, 25, 1623-1627.

101. Moon Y., Park I., and Dornfeld D. A., 1998. Mechanical properties and relationship to process performance of the polishing pad in chemical mechanical polishing (cmp) of silicon. ASPE 1998 Spring Topical Meeting on Silicon Machining, Monterey, CA, vol 17, 78–82., 1998.

102. Moon Y., Park I., and Dornfeld D. A., 1998. Investigation of the relationship between Preston’s coefficient and friction coefficient in chemical mechanical polishing (CMP) of silicon. ASPE 1998 Spring Topical Meeting on Silicon Machining, Monterey, CA, vol 17, 83–87, 1998.

103. Ng S. H., 2005. Measurement and modeling of fluid pressures in chemical mechanical polishing. PhD Dis., Georgia Inst. of Tech., Atlanta, GA.

104. Hooper B.J., Byrne G., Galligan S., 2002. Pad conditioning in chemical mechanical polishing. J Mater Process Technol, 123, 107-113.

105. Lawing A. S., 2002. Pad conditioning and pad surface characterization in oxide chemical mechanical polishing. Mater Res Soc Symp Proc, 732, 5.3.1-5.3.6.

106. Moy A.L., Cecchi J.L., Hetherington D.L., Stein D., 2001. Polyurethane pad degradation and wear due to tungsten and oxide CMP. Mater Res Soc Symp Proc, 617, 1.7.1-1.7.6.

107. Gouda S.D., Bastawros A., Chandra A., 2003. Multi-scale characterization of pad role on material removal rate in CMP. Mater Res Soc Symp Proc, 767, 2.5.1-2.5.6.

108. Fury M., James D., 1996. Relationships between physical properties and polishing performance of planarization pads. SPIE Microelectronic Manufacturing Symposium, Austin, TX.

109. Park K., Jeong H., 2008. Investigation of pad surface topography distribution for material removal uniformity in CMP process. J Electrochem Soc, 8, 595-602.

110. Luo J., Dornfeld D.A., 2001. Material removal mechanism in chemical mechanical polishing: Theory and modeling. IEEE Trans Semiconduct Manuf, 14, 112-133.

111. Luo J., Dornfeld D.A., 2003. Effects of abrasive size distribution in chemical mechanical planarization: Modeling and verification. IEEE Trans Semiconduct Manuf, 16, 469-476.

112. Luo J., Dornfeld D.A., 2003. Material removal regions in chemical mechanical planarization for submicron integrated circuit fabrication: Coupling effects of slurry chemicals, abrasive size distribution and wafer-pad contact area. IEEE Trans Semiconduct Manuf, 16, 45-56.

113. Thagella S., Sikder A.K., Kumar A., 2004. Tribological issues and modeling of removal rate of low-k films in CMP. J Electrochem Soc, 151, 205-215.

114. Jeng Y.R., Huang P.Y., 2004. Impact of abrasive particles on the material removal rate in CMP. Electrochem Solid State Letters, 7, 40-43.

115. Zhao Y., Chang L., 2002. A micro-contact and wear model for chemical-mechanical polishing of silicon wafers. Wear, 252, 220-226.

116. Zhao Y., Maietta D.M., Chang L., 2000. An asperity microcontact model incorporating the transition from elastic deformation to fully plastic flow. J Tribol Trans ASME, 122, 86-93.

117. Zhao Y., Chang L., 2001. A model of asperity interactions in elastic-plastic contact of rough surfaces. J Tribol Trans ASME, 123, 857-864.

118. Ahmadi G., Xia X., 2001. A model for mechanical wear and abrasive particle adhesion during the chemical mechanical polishing process. J Electrochem Soc, 148, 99-109.

119. Shi F.G., Zhao B., 1998. Modeling of chemical-mechanical polishing with soft pads. Appl Phys A, 67, 249-252.

120. Mazaheri A.R., Ahmadi G., 2002. Modeling the effect of bumpy abrasive particles on chemical mechanical polishing. J Electrochem Soc, 149, 370-375.

121. Mazaheri A.R., Ahmadi G., 2003. A model for effect of colloidal forces on chemical mechanical polishing. J Electrochem Soc, 150, 233-239.

122. Fu G., Chandra A., Guha S., Subhash G., 2001. A model for wafer scale variation of removal rate in chemical mechanical polishing based on elastic pad deformation. J Electron Mater, 30, 400-407.

123. Fu G., Chandra A., 2002. Normal indentation of elastic half-space with a rigid frictionless axisymmetric punch. J Tribol Trans ASME, 69, 142-147.

124. Castillo-Mejia D., Perlov A., Beaudoin S., 2000. Qualitative prediction of SiO2 removal rates during chemical mechanical polishing. J Electrochem Soc, 147, 4671-4675.

125. Lin Y.Y., Lo S.P., 2003. A study on the stress and nonuniformity of the wafer surface for the chemical-mechanical polishing process. Int J Adv Manuf Technol, 22, 401-409.

126. Lin Y.Y., Lo S.P., 2004. A study of a finite element model for the chemical mechanical polishing process. Int J Adv Manuf Technol, 23, 644-650.

127. Castillo-Mejia D., Kelchner J., Beaudoin S., 2004. Polishing pad surface morphology and chemical mechanical planarization. J Electrochem Soc, 151, 271-278.

128. Bastawros A., Chandra A., Guo Y., Yan B., 2002. Pad effects on material-removal rate in chemical-mechanical planarization. J Electron Mater, 31, 1022-1031.

129. Zhang F., Busnaina A.A., Ahmadi G., 1999. Particle adhesion and removal in chemical mechanical polishing and post-CMP cleaning. J Electrochem Soc, 146, 2665-2669.

130. Patir N., Cheng, H. S., 1979. Application of average flow model to lubrication between rough sliding surfaces. ASME J Lubr Technol, 101, 220-230.

131. Kim A.T., Seok J., Tichy J.A., Cale T.S., 2003. A multiscale elastohydrodynamic contact model for CMP. J Electrochem Soc, 150, 570-576.

132. Yu T., Yu C.C., Orlowski M., 1993. Statistical polishing pad model for chemical-mechanical polishing. Tech Dig Int Electron Devices Meet, 865-868.

133. Shan L., 2000. Mechanical interactions at the interface of chemical mechanical. polishing. Ph.D. Thesis, Georgia Institute of Technology, Atlanta, GA.

134. Baker A. R., 1996. The origin of the edge effect in CMP. Proc Electrochem Soc Meeting, 96, 228.

135. Steigerwald J., Murarka S., Gutmann R., 1997. Chemical Mechanical Planarization of Microelectronic Materials, John Wiley, New York.

136. Kim A. T., 2001. A soft elastohydrodynamic contact model for chemical mechanical planarization. Ph.D. Thesis, Rensselaer Polytechnic Institute, Troy, New York, 2001.

137. Tso P. L., Hsu R., 2007. Estimating chemical mechanical polishing pad wear with compressibility. Int J Adv Manuf Technol, 32, 682-689.

138. Cooper K., Gupta A., Beaudoin S., 2001. Simulation of particle adhesion: Implications in chemical mechanical polishing and post chemical mechanical polishing cleaning. J Electrochem Soc, 148, 662-667.

139. Israelachvili J. N., 1992. Intermolecular and surface forces. Academic Press.

140. Eichenlaub S., Chan C., Beaudoin S., 2002. Hamaker constants in integrated circuit metallization. J Colloid Interface Sci, 248, 389-397.

CHAPTER 3

THEORY BACKGROUND

3.1 Contact Mechanics

3.1.1 Hertz contact

The first satisfactory study of stresses due to the contact of two elastic spheres was developed by Hertz [1]. The Hertz theory is still widely used in contact mechanics for analysis of contact between two spheres. Hertz contact considers that the contact area is elliptical and the deformation of surfaces can be determined by considering the underlying solids as elastic half-spaces [2]. The contact radius is assumed to be small as compared to the radius of curvature of contacting solids. Material behavior is considered to remain elastic, i.e. the displacements are small. Only the normal pressure is assumed to be transmitted between surfaces, thus considering the contact interface to be frictionless.

It is shown that the displacement field within the contact zone of two contacting spheres is due to the contact pressure distribution, $p_c^s(r)$ in the form [2],

$$p_c^s(r) = p_o^s\left[1-\left(\frac{r}{a_s}\right)^2\right]^{1/2} \tag{3.1}$$

where p_o^s is the maximum contact pressure at the center of contact, r is the radial location and a_s is the radius of the circular contact area.

The contact of two elastic spheres with radii R_{s1} and R_{s2}, elastic moduli E_{s1} and E_{s2} and Poisson's ratios v_{s1} and v_{s2} can be reduced to the contact of one rigid flat surface and one elastic sphere (Fig. 3.1) with equivalent elastic modulus E_s and radius R_s as [3],

$$E_s = \left(\frac{1-\nu_{s1}^2}{E_{s1}} + \frac{1-\nu_{s2}^2}{E_{s2}}\right)^{-1} \tag{3.2}$$

$$R_s = \left(\frac{1}{R_{s1}} + \frac{1}{R_{s2}}\right)^{-1} \tag{3.3}$$

The contact radius a_s, penetration at the center of contact δ_o^s and maximum contact pressure p_o^s for the contact of a sphere with a rigid surface is given by Hertz contact as a function of contact force f_c^s as [3],

$$a_s = \left(\frac{3f_c^s R_s}{4E_s}\right)^{1/3} \tag{3.4}$$

$$\delta_o^s = \left(\frac{9{f_c^s}^2}{16R_s E_s^2}\right)^{1/3} \tag{3.5}$$

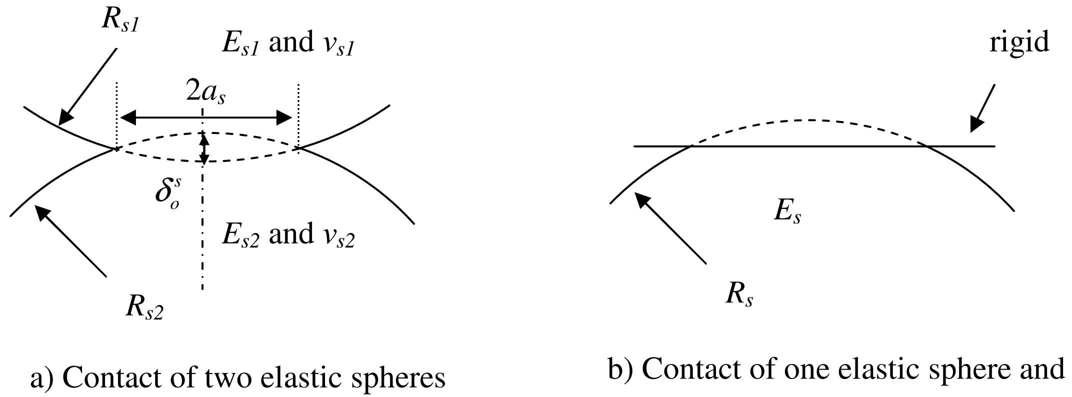

a) Contact of two elastic spheres

b) Contact of one elastic sphere and

Fig. 3.1: The contact of two elastic spheres can be reduced to the contact of one elastic sphere and one rigid flat surface.

$$p_o^s = \left(\frac{6 f_c^s E_s^2}{\pi^3 R_s^2} \right)^{1/3} \tag{3.6}$$

3.1.2 Greenwood and Williamson multi-asperity model

When two surfaces are brought into contact, the real contact area is only a fraction of the apparent contact area due to the roughness of surfaces. Initially, contact occurs at the tip of the tallest asperities. As the load is increased, not only the deformation of asperities increases but also number of asperities in contact becomes larger and as a result, contact spreads to a larger area.

One of the common solution methods to approach this problem is the utilization of the statistics of surface topography. Multi-asperity models such as Greenwood and Williamson [4] fall into this group. Numerical methods, such as the finite element model, can be used to model the contact of rough surfaces [5]. However due to the requirements for large number of elements, a few asperities can be modeled within a reasonable

computation time. Although numerical models are more accurate in the sense that the interactions between the asperities are also included in the models, the requirements for large memory and computation time limit their usage.

By far, the most widely used statistical model developed for the contact of two rough nominally flat surfaces is the classical model by Greenwood and Williamson (GW) [4]. In the GW multi asperity model, it is assumed that the height of asperity summits of both surfaces can be described statistically. Asperity summits are assumed to be spherical with a radius R_s. The height of asperities z_s, measured from a reference plane, varies according to a probability density function (PDF) $\Phi_s(z_s)$. The contact of two elastic rough surfaces can be reduced to the contact of an elastic rough and rigid smooth surface (Fig. 3.2) by using the equivalent standard deviation (SD) of surface roughness σ_s and elastic modulus E_s. The equivalent elastic modulus E_s is given in Eqn (3.2). The equivalent SD of surface roughness σ_s can be expressed as a function of the SD of surface roughness of contacting surfaces (σ_{s1} and σ_{s2}) as follows [4],

$$\sigma_s^2 = \sigma_{s1}^2 + \sigma_{s2}^2 \tag{3.7}$$

The number of asperity summits n_s per unit area in contact can be found by computing the probability of asperity summits with a height z_s greater than the separation d_{sep}, between the surfaces, $z_s > d_{sep}$ as follows,

$$n_s = \eta_s \int_{d_{sep}}^{\infty} \Phi_s(z_s)\, dz_s \tag{3.8}$$

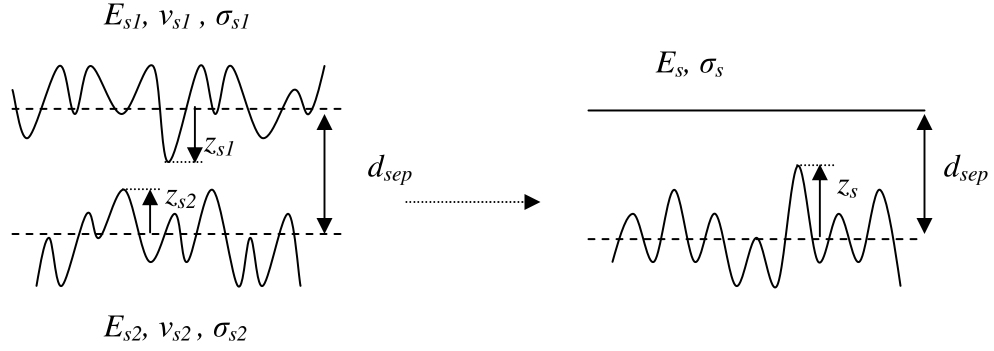

Fig. 3.2: The contact of two rough surfaces may be simplified by using equivalent surface and material properties that are obtained by combining the properties of individual surfaces.

where η_s is the total number of summits per unit area (asperity summit density). In the GW model, the Hertz contact is used for describing the behavior of each asperity contact. Thus, the contact area of each asperity, A_{r_i} , can be expressed for a given penetration depth at the center of contact $\delta_{s_i}^o = z_{s_i} - d_{sep}$ as,

$$A_{r_i} = \pi R_s \delta_{s_i}^o \tag{3.9}$$

The real contact area A_r is determined as a fraction of apparent contact area by integrating the real contact area of each asperity summit A_{r_i} for all asperity summits in contact using,

$$A_r = \pi \eta_s R_s \int_{d_{sep}}^{\infty} \left(z_s - d_{sep} \right) \Phi_s \left(z_s \right) dz_s \tag{3.10}$$

Hertz elastic contact gives the force on each asperity $f_{c_i}^s$ for a given penetration depth $\delta_{s_i}^o$ as,

$$f_{c_i}^{s} = \frac{4}{3} E_s R_s^{1/2} \delta_{s_i}^{o\,3/2} \tag{3.11}$$

The nominal pressure p_o can be found by summation of the contact force on each asperity $f_{c_i}^{s}$ for the contacting asperities as,

$$p_o = \frac{4}{3} \eta_s E_s R_s^{1/2} \int_{d_{sep}}^{\infty} \left(z_s - d_{sep} \right)^{3/2} \Phi_s \left(z_s \right) dz_s \tag{3.12}$$

Gaussian distribution

The asperity summit height z_s of a random rough surface can be described by a Gaussian probability density function (PDF) $\Phi_s(z_s)$ in the form,

$$\Phi_s(z_s) = \frac{1}{\sigma_s \sqrt{2\pi}} e^{-\frac{\left(z_s - z_s^m\right)^2}{2\sigma_s^2}} \tag{3.13}$$

where σ_s is standard deviation of surface roughness and z_s^m is the mean height of asperity summits. The contact behavior of a random rough surface can be obtained by using Eqn (3.13) for the PDF of asperity summit heights in Eqns (3.8), (3.10) and (3.12).

Exponential distribution

The exponential distribution can also be used to approximate the tail end of the Gaussian distribution of the summit heights [4],

$$\Phi_s \left(z_s \right) = \lambda_s \exp\left(-\lambda_s z_s \right) \tag{3.14}$$

where the parameter λ_s is given by $\lambda_s = 2 / \sigma_s$ which gives an agreement with Gaussian distribution at $z_s / \sigma_s = 1.12$. In Fig. 3.3, the PDFs based on Gaussian and exponential distributions are compared. It is seen that exponential distribution gives a reasonable approximation for Gaussian distribution for the range $z_s > \sigma_s$. Substituting Eqn (3.14) for PDF of asperity summit heights into Eqns (3.10) and (3.12), the real contact area A_r and the nominal pressure p_o can be found as,

$$A_r = \eta_s \pi R_s \lambda_s \exp\left(-\lambda_s d_{sep}\right) C_1 \tag{3.15}$$

$$p_o = \frac{4}{3} \eta_s E_s R_s^{1/2} \lambda_s \exp\left(-\lambda_s d_{sep}\right) C_{3/2} \tag{3.16}$$

where C_1 and $C_{3/2}$ are constants. Eqns (3.15) and (3.1) indicate that the real contact area is

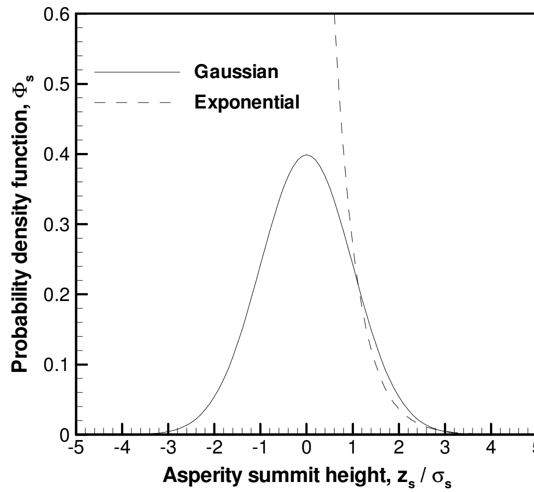

Fig. 3.3: The comparison of Gaussian and exponential PDF used for describing the asperity summit height distribution for a rough surface. The values of PDF for Gaussian and exponential distribution is identical when $z_s = 1.12\sigma_s$

linearly proportional to the nominal pressure, $A_r \propto p_o$. Following this relation, the mean contact pressure p_c^m $(= p_o / A_r)$ remains constant with respect to the nominal pressure p_o. The mean contact pressure p_c^m is a function of elastic modulus E_s, SD of surface roughness σ_s and asperity radius R_s as [3],

$$p_c^m \approx 0.39 E_s \sqrt{\frac{\sigma_s}{R_s}} \tag{3.17}$$

The mean contact pressure p_c^m predicted by the GW multi-asperity model using Gaussian and exponential distribution (Eqn (3.17)) is shown in Fig. 3.4 for a unit elastic modulus $E_s = 1$, asperity radius $R_s = 1$. It is seen that the mean contact pressure p_c^m predicted by

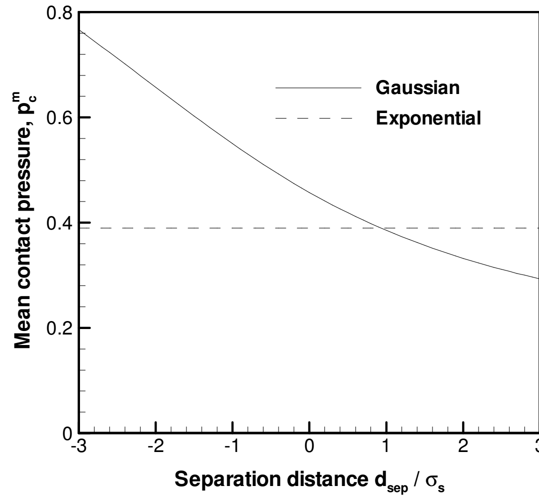

Fig. 3.4: The mean contact pressure p_c^m predicted by GW multi-asperity model using Gaussian and exponential PDF for asperity summit height z_s for a unit elastic modulus $E_s = 1$, asperity radius $R_s = 1$.

using Gaussian distribution is lower than exponential distribution when separation distance d_{sep} is large, $d_{sep} > 0.9\sigma_s$ while Gaussian distribution gives higher p_c^m for $d_{sep} < 0.9\sigma_s$. The mean contact pressure p_c^m calculated by using exponential distribution (Eqn (3.17)) is within 20% of p_c^m determined by Gaussian distribution when separation distance is in the range, $-0.3\sigma_s < d_{sep} < 2.2\sigma_s$.

<u>Weibull distribution</u>

The Gaussian distribution is a symmetrical PDF. Therefore the skewness of the summit heights' cannot be simulated by using the Gaussian distribution, but it can be taken into account by using the Weibull distribution [6,7]. The Weibull distribution, which can be used to duplicate the characteristics of a range of other PDF distributions is given as follows [7],

$$\Phi_s\left(\hat{z}_s\right) = \frac{\omega \hat{z}_s^{\omega-1}}{\eta^w} \exp\left(-\hat{z}_s / \eta\right)^{\omega} \tag{3.18}$$

where ω and η are the shape and scale parameters, respectively. The mean z_s^m and standard deviation σ_s of a variable with Weibull distribution are given as follows,

$$z_s^m = \eta B_1 \tag{3.19}$$

$$\sigma_s = \eta \left(B_2 - B_1^2\right)^{1/2} \tag{3.20}$$

where B_n can be found using gamma function Γ as $B_n = \Gamma\left(1+\frac{n}{\omega}\right)$.

The skewness S_s and kurtosis K_s of the Weibull distribution are found as,

$$S_s = \frac{B_3 - 3B_2B_1 + 2B_1^3}{\left(B_2 - B_1^2\right)^{3/2}} \tag{3.21}$$

$$K_s = \frac{B_4 - 4B_3B_1 + 6B_2B_1^2 - 3B_1^4}{\left(B_2 - B_1^2\right)^2} \tag{3.22}$$

The Weibull distribution variable is shifted as $z_s = \hat{z}_s - z_s^m$ so that $z_s = 0$ corresponds to the mean of asperity summit heights. The following form of Weibull distribution, where the distribution can be described by only one parameter ω is used [8],

$$\Phi_s\left(z_s\right) = \frac{\omega}{\sigma_s} C^{\omega} \left(\frac{z_s}{\sigma_s}\right)^{\omega-1} \exp\left(C\frac{z_s}{\sigma_s}\right)^{\omega} \tag{3.23}$$

where

$$C = \left(B_2 - B_1^2\right)^{1/2} \tag{3.24}$$

Note that skewness S_s and kurtosis K_s are related to each other and are also a function of shape parameter, ω. The shape parameter ω and kurtosis K_s are calculated for a given skewness S_s by using Eqns (3.20)-(3.22). The PDF for Gaussian and Weibull distributions are plotted in Fig. 3.5. It is seen that the skewness, S_s = -1 in Weibull distribution shifts the peak to a positive value, $z_s > 0$, while causing the tail to become longer on the negative side, $z_s < 0$ of the distribution (Fig. 3.5a). The skewness S_s = 1 has

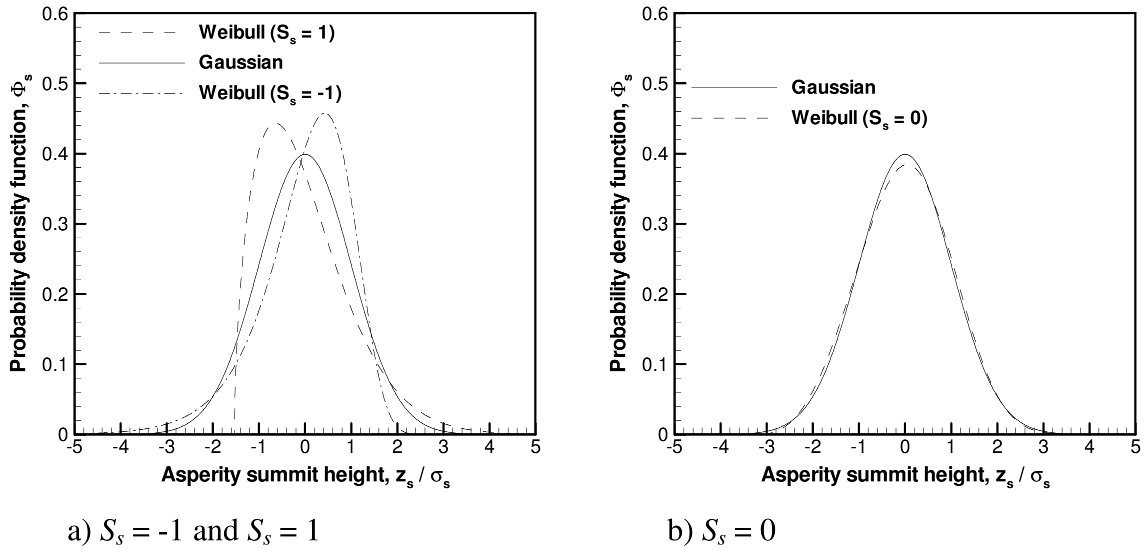

a) S_s = -1 and S_s = 1 b) S_s = 0

Fig. 3.5: The comparison of Gaussian and Weibull PDF with a) skewness S_s = 1 and S_s = -1 and b) S_s = 0 for describing the asperity summit height distribution for a rough surface.

an opposite effect to S_s = -1. Note that the practical values for skewness are in the range, -1 < S_s < 1 [9] and S_s = 0 can be used to approximate Gaussian distribution (Fig. 3.5b).

It is shown in Fig. 3.6 that the skewness S_s in Weibull distribution influences the relation between nominal pressure p_o and real contact area A_r, which is obtained by substituting the Weibull distribution given by Eqn (3.23) into Eqns (3.10) and (3.12). Since the intent of the calculations is to demonstrate the difference in the variation of real contact area A_r with respect to nominal pressure p_o for different distributions, a unit elastic modulus E_s = 1, asperity radius R_s = 1 and asperity density η_s = 1 are utilized. In the case of the Weibull distribution with skewness S_s = -1, the real contact area A_r becomes larger than that of Gaussian distribution for a given nominal pressure p_o. This stems from the fact that the tail of Weibull distribution with S_s = -1 on the positive side representing tall asperities is shorter. The number of tall asperities is smaller; as a result nominal pressure p_o is distributed more evenly on asperities causing real contact area A_r to increase. The

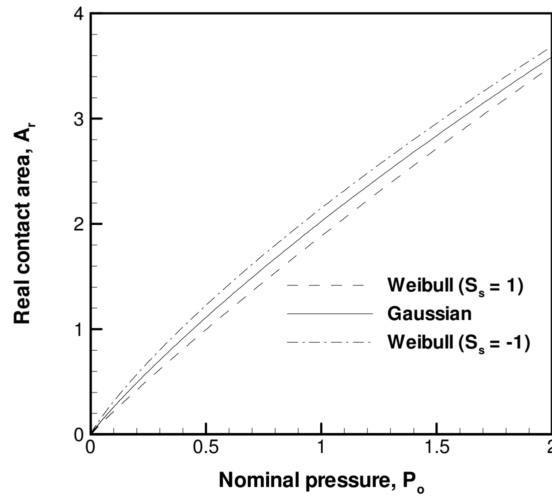

Fig. 3.6: The mean contact pressure p_c^m predicted by GW multi-asperity model using Gaussian and Weibull PDF for asperity summit height z_s for a unit elastic modulus E_s = 1, asperity radius R_s = 1 and asperity density η_s = 1.

existence of tall asperities for Weibull distribution with skewness $S_s = 1$ results in an opposite effect, thus decreasing the real contact area A_r for a given nominal pressure p_o as compared to Gaussian distribution.

3.1.3 Contact of rough spheres (Greenwood and Tripp model)

Greenwood and Tripp (GT) [10] studied the contact of a rough sphere with a flat surface by using GW multi-asperity model for determining rough contact behavior and elasticity theory for calculating the deformation of elastic surface. The bulk deformation of sphere $w_b\left(r\right)$ was calculated based on the contact pressure due to the local contact of asperities (Fig. 3.7). The contact region was divided into infinitesimally small contact segments, where the contact pressure at each segment due to the micro-contact of asperities, $p_c\left(r\right)$

was obtained from GW multi-asperity model [4]. Furthermore both asperities and bulk sphere were assumed to deform elastically.

The local separation distance at each contact point, $u(r)$ can be expressed as,

$$u(r) = u_o + \frac{r^2}{2R_s} + w_b(r) - w_b(0) \tag{3.25}$$

where R_s is the bulk radius of sphere and u_o is the separation distance at the center of contact, $r = 0$. The contact pressure for each contact segment $p_c(r)$ is found by replacing the separation distance d_{sep} in Eqn (3.12) by the local separation distance $u(r)$ given by Eqn (3.25).

The surface displacements for each contact segment are found by considering an elastic half space loaded with axisymmetric normal traction, where the normal traction is due to the rough contact. The solution to this problem can be derived from the Boussinesq solution for a concentrated load on an elastic half space [10] as,

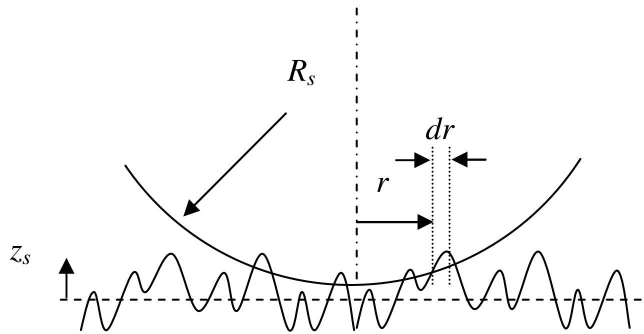

Fig. 3.7: The contact of a sphere and a rough flat surface

$$w_b(r) = \frac{4}{\pi E_s} \int_0^{a_s} \frac{t}{t+r} p(t) K(k) dt \tag{3.26}$$

where $K(k)$ is an elliptic integral with modulus, $k = \frac{2(rt)^{1/2}}{(r+t)}$ and a_s is the contact radius.

The displacement of each contact segment interacts with other contact segments via the bulk deformation. The contact pressure distribution $p_c(r)$ is iteratively solved using Eqns (3.25) and (3.26) until the equilibrium of local contact pressure and the resultant local deformation is established.

GT evaluated the effect of surface roughness on the contact behavior of a sphere by comparing the results of the model described above with Hertz contact, which is valid for smooth surfaces [10]. The effect of roughness on the contact pressure distribution was found to be small at large loads, while a significant difference was observed at small loads. The GT model found that the effect of roughness is to spread the contact to a larger area while lowering the maximum contact pressure.

3.2 Surface Forces

Surface forces play an important role for the contact of a spherical particle and a flat surface when the size of particle is small. Two different types of surface forces are considered, van der Waals and double layer forces. The calculation of van der Waals and double layer forces are explained in Section 3.2.1 and 3.2.2, respectively.

3.2.1 Van der Waals force

Lennard-Jones Potential

The Lennard-Jones potential gives the interaction force between two surfaces, separated by a distance d_o. The interaction force consists of the attractive van der Waals force (long range) and the Born repulsion force (short range) [11]. The attractive and repulsive forces are in equilibrium when the distance between surfaces is equal to the equilibrium distance d_o i.e. $d = d_o$. The potential energy between two surfaces, U varies as a function of the separation distance d [11] as,

$$U(d) = \frac{A}{12\pi d_o^2}\left[\left(\frac{d_o}{d}\right)^2 - \frac{1}{4}\left(\frac{d_o}{d}\right)^8\right] \tag{3.27}$$

where A is the Hamaker constant. The force per unit area, σ_c between two surfaces due to this interaction can be expressed as,

$$\sigma_c(d) = \frac{A}{6\pi d_o^3}\left[\left(\frac{d_o}{d}\right)^3 - \left(\frac{d_o}{d}\right)^9\right] \tag{3.28}$$

The potential energy (U) and the interaction force per unit area (σ_c) are plotted in Fig. 3.8. The van der Waals force for the contact of two rigid spheres with radius r_1 and r_2, can be found by using [11],

$$f_{vdw} = 2\pi r_{eq} W_a \tag{3.29}$$

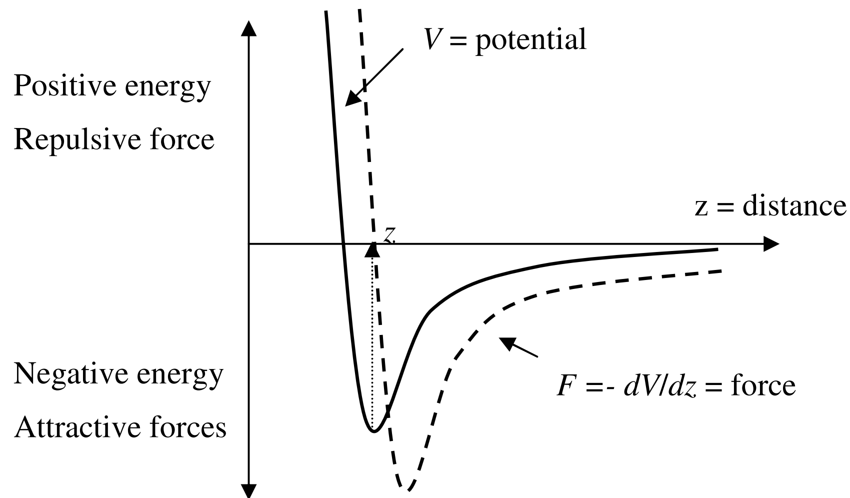

Fig. 3.8: Lennard-Jones potential and resultant force between two surfaces.

where r_{eq} is the equivalent radius and W_a is the work of adhesion. The equivalent radius, r_{eq} can be calculated from the radius of contacting spheres, r_1 and r_2 using Eqn (3.3).

The work of adhesion, W_a is defined as the energy required to separate a unit area of the interface between two materials. The work of adhesion can be determined as a function of the surface energies of contacting surfaces, γ_1 and γ_2, and the interface energy γ_{12} [11] as follows,

$$W_a = \gamma_1 + \gamma_2 - \gamma_{12} \tag{3.30}$$

The work of adhesion W_a can be found from the Hamaker constant, A and equilibrium distance d_o as follows,

$$W_a = \frac{A}{12\pi d_o^2} \tag{3.31}$$

The effective Hamaker constant A_{12} between two different materials (1 and 2) can be calculated from the individual values, A_{11} and A_{22} [12] as follows,

$$A_{12} \approx \left(A_{11}A_{22}\right)^{1/2} \tag{3.32}$$

The effective Hamaker constant A_{132} between two different materials (1 and 2) in a third medium (3) can be determined using the Hamaker constant of the third medium A_{33} [12] as follows,

$$A_{132} = (A_{11}^{1/2} - A_{33}^{1/2})(A_{22}^{1/2} - A_{33}^{1/2}) \tag{3.33}$$

<u>Maugis-Pollock Model</u>

Maugis-Pollock model describes the van der Waals interaction between a rigid sphere and a flat surface [13] which deforms in a fully-plastic manner. The contact pressure at the interface is taken to be equal to the hardness H_w. The contact force f_w is then found as follows,

$$f_w = \pi a_w^{\ 2} H_w \tag{3.34}$$

where a_w is the radius of the contact zone. The external load f_p and the van der Waals force f_{vdw} are balanced by the contact pressure H_w at the interface as,

$$f_p + f_{vdw} = \pi a_w^{\ 2} H_w \tag{3.35}$$

where van der Waals force f_{vdw} is given by Eqn (3.29). The contact radius a_w can be obtained as a function of the external load f_p in the presence of van der Waals force f_{vdw} using Eqn (3.35).

3.2.2 Electrical double layer force

Origin of double layer forces

Electrical double layer (dl) forces play an important role for the stability of colloidal systems. A complete analysis of dl forces and DLVO (Derjaguin, Landau, Verwey and Overbeek) theory, which forms the foundation of colloidal science, can be found in many textbooks [14-16]. Double layer force originates from the charging of particles immersed in a liquid. When an uncharged particle is placed in a liquid, the particle acquires surface charge (Fig. 3.9). The surface charge of the particle creates an electrostatic field and affects ions in bulk liquid. The electric field around the charged particle attracts the ions of opposite sign (counter-ions) and repels the ions of same sign (co-ions). As a result, a layer of counter-charge is created in the liquid due to the electrostatic field and the thermal motion of the ions. Some of the counter-ions are collected near the charged surface of the particle. This layer of strongly bound ions is called the Stern layer. The remaining counter-ions are located in the outer layer, which is called the diffuse layer. The ions in the diffuse layer are distributed according to Boltzmann distribution [14]. The combined Stern and diffuse layers constitute the electrical double layer.

Due to the distribution of ions in Stern and diffuse layers, the electrical potential ψ varies as a function of distance from the particle according to the Gouy-Chapman theory. A

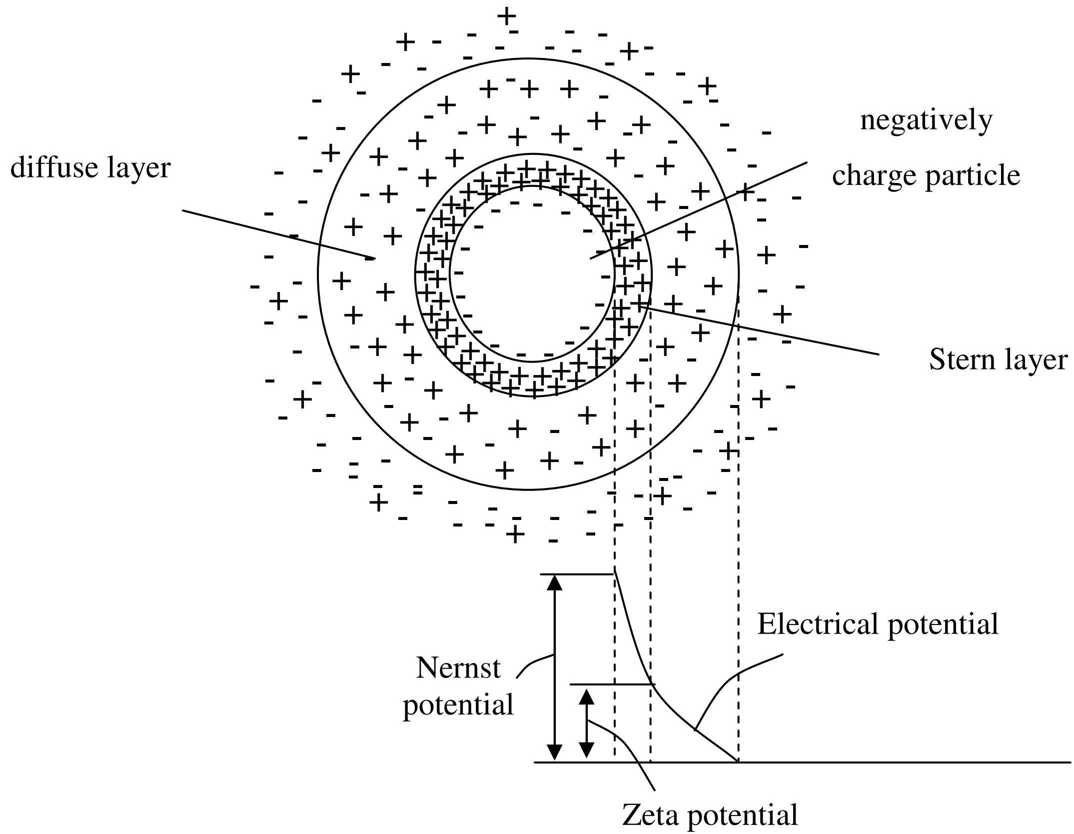

Fig. 3.9: Electrical double layer structure around a negatively charged particle.

typical variation of electrical potential is shown in Fig. 3.9. This potential can be calculated by the Poisson-Boltzmann equation using [14],

$$\Delta^2\psi = -\left(e / \varepsilon\varepsilon_o\right)\sum_i z_i n_{i\infty} e^{-z_i e\psi / kT} \tag{3.36}$$

where e is electrical charge, ε is dielectric constant of medium, ε_o is dielectric permittivity of vacuum, z_i is valence number, k is the Boltzmann constant, T is temperature and $n_{i\infty}$ is concentration of ions far away from the surface. Note that the electrical potential at the surface of particle is called as Nernst potential while zeta potential Ψ is the electrical potential just outside the Stern layer.

It is assumed that the surface potential ψ is small such that $z_i e\psi / kT < 1$, the Poisson-Boltzmann equation can be linearized by expanding the exponentials in Eqn (3.36) as a power series,

$$\nabla^2\psi = \kappa^2\psi \tag{3.37}$$

where κ is the Debye-Huckel reciprocal length parameter, κ, which can be expressed as,

$$\kappa^2 = \left(e^2 / \varepsilon\varepsilon_o kT\right)\sum_i z_i^{\,2} n_{i\infty} \tag{3.38}$$

The thickness of diffuse electric double layer is equal to the Debye length, which is the reciprocal of κ. The concentration of ions $n_{i\infty}$ can be calculated by using the molar concentration of the electrolyte M_i as follows,

$$n_{i\infty} = 1000 N_a M_i \tag{3.39}$$

where N_a is the Avogadro's number ($6.02\text{x}10^{23}$) and M_i (mol/liter) is the molar concentration of the electrolyte in the liquid.

Calculation of double layer forces

As two charged particles approach each other, the diffuse layers of the particles start to overlap [14]. The electrical potential between particles is determined as a combined effect of electrical potential around each particle, which is given by Eqn (3.37). The double layer force resulting from this interaction starts to become significant when the separation distance between surfaces is less than the Debye screening length $1/\kappa$.

Different assumptions are used to derive the double layer force between two charged particles. Two of the most widely used assumptions; constant potential and constant charge at the surface of particles are considered to be representative of two limiting conditions. The surface charge and surface potential of particles is assumed to remain constant as the particles approach in the constant charge and constant potential assumptions, respectively [14].

Hogg-Healy-Fuerstenau (HHF) equations for constant potential (HHF-CP) [17] and constant charge (HHF-CC) [18,19] assumptions are derived based on the linearized Poisson-Boltzmann equation. Therefore the accuracy of HHF equations depend on the zeta potential of surfaces since the linearization of the Poisson-Boltzmann equation leads to the over-estimation of double layer forces when the zeta potential is high (>50-60 mV) [16].

The interaction energy W between two flat surfaces can be found based on the constant potential assumption (HHF-CP) [17] as,

$$W\left(d_o\right) = -\varepsilon_o \varepsilon_r \left(\Psi_1^2 + \Psi_2^2\right) \frac{\kappa e^{-\kappa d_o}}{1 - e^{-2\kappa d_o}} \left(\frac{2\Psi_1 \Psi_2}{\Psi_1^2 + \Psi_2^2} - e^{-\kappa d_o} \right) \tag{3.40}$$

The interaction force f_{dl} between two spherical particles with radii r_1 and r_2 for HHF-CP can be found by assuming that the interaction energy W between two flat surfaces (Eqn (3.40)) is applicable. This assumption is known as the Derjaguin approximation and it leads to [16],

$$f_{dl}\left(d_o\right) = -2\pi\varepsilon_o\varepsilon_r \frac{r_1 r_2}{r_1 + r_2}\left(\Psi_1^2 + \Psi_2^2\right)\frac{\kappa e^{-\kappa d_o}}{1 - e^{-2\kappa d_o}}\left(\frac{2\Psi_1\Psi_2}{\Psi_1^2 + \Psi_2^2} - e^{-\kappa d_o}\right) \tag{3.41}$$

The interaction force f_{dl} between two spherical particles under the constant surface charge assumption (HHF-CC) [18,19] is given as,

$$f_{dl}\left(d_o\right) = -2\pi\varepsilon_o\varepsilon_r \frac{r_1 r_2}{r_1 + r_2}\left(\Psi_1^2 + \Psi_2^2\right)\frac{\kappa e^{-\kappa d_o}}{1 - e^{-2\kappa d_o}}\left(\frac{2\Psi_1\Psi_2}{\Psi_1^2 + \Psi_2^2} + e^{-\kappa d_o}\right) \tag{3.42}$$

As the separation distance d_o between two particles decreases, the surface charge of particles becomes smaller if the surface potential is considered to be constant or the surface potential becomes larger if the surface charge is constant. Under the constant charge assumption (HHF-CC), the surface potential of particles could become very high, violating small surface potential assumption of the linearized Poisson-Boltzmann equation [20]. This causes significant errors in the calculation of double layer forces at small separation distance when HFF equations are used. Gregory [20] used a different approach to find an expression for the double layer force which is considered to be valid at small separation. Based on the compression approximation (CA), the entire charge in the diffuse layer of particles is considered to be compressed in the area between particles as two surfaces approach. This leads to the following relationship based on CA, which can be used to calculate the double layer force between two spherical particles [20] as,

$$f_{dl}\left(d_o\right) = \frac{-4\pi n_\infty kT}{\kappa}\frac{r_1 r_2}{r_1 + r_2}\left[2\overline{y}\ln\left(\frac{B + \overline{y}\coth\left(\kappa d_o / 2\right)}{1 + \overline{y}}\right) - \ln\left(\overline{y}^{-2} + \cosh\kappa d_o + B\sinh\kappa d_o\right) + \kappa d_o\right] \tag{3.43}$$

where $\bar{y} = y_1 + y_2$, $y = ze\psi / kT$ and $B = \left[1 + \bar{y}^2 \operatorname{csc}h^2\left(\kappa d_o / 2\right)\right]^{1/2}$.

Eqn (3.43) is considered to be valid at high potentials (~ 50 mV) and small separation distance between the particles for constant charge assumption. Eqn (3.43) does not give good results when the charge of particles are opposite in sign but equal in magnitude. In this condition, Eqn (3.42) can be used for HHF-CC [21].

The linear superposition approximation (LSA) [22] assumes neither constant surface potential nor surface charge assumption, which are the two extreme approaches. According to the LSA, the potential between particles is determined by superposition of the potential of each particle, whereas the potential in the vicinity of each particle is due to the potential of that particle. The interaction force based on LSA is given [22] as,

$$f_{dl}\left(d_o\right) = \frac{-128\pi n_\infty kT\gamma_1\gamma_2}{\kappa} \frac{r_1 r_2}{r_1 + r_2} e^{-\kappa d_o} \tag{3.44}$$

where $\gamma = \tanh\left(ze\Psi / 4kT\right)$. Note that Eqn (3.44) is valid only for symmetric electrolytes* (z : z) and is applicable for high surface potentials.

Note that a minus "-" sign is introduced in Eqns (3.41) – (3.44) so that double layer force becomes negative $f_{dl} < 0$ when the interaction is repulsive while $f_{dl} > 0$ for attractive interaction. The deviation between different approaches used to calculate double layer force (HFF-CP, HHF-CC, CA, LSA) becomes more pronounced if the separation distance d_o between particles is small. HHF-CC and CA equation is experimentally found

---

* An electrolyte is symmetric if all the cations (z_+) and anions (z_-) have the same valency, $z_+ = -z_-$.

to be more accurate at small separation distance as compared to HHF-CP or LSA equations [15,21]. The limitation of HHF-CP and HHF-CC equations is that linearized Poisson-Boltzmann equation is utilized in the derivation of these equations, therefore the error becomes significant when surface potentials are high. In this case, the CA equation gives more reliable results as it is based on the non-linear Poisson-Boltzmann equation [20].

In Fig. 3.10, double layer force f_{dl} between a rigid flat surface ($r_1 \rightarrow \infty$) and a rigid spherical particle with radius $r_2 = r_p$, is plotted as a function of separation distance d_o using different equations based on the constant potential (HHF-CP), constant charge (HHF-CC), compression (CA) and linear superposition (LSA) assumptions. The separation distance is varied between 0.4 nm < d_o < 5 nm, where d_o = 0.4 nm is a typical separation distance between two atomically smooth surfaces. The separation distance effectively increases as the surfaces become rough. The zeta potential of surfaces is taken to be $\Psi_{1,2}$ = 50 mV, 50 mV for two surfaces with same charge, $\Psi_{1,2}$ = 50 mV, 0 mV for one charged and one neutral surface and $\Psi_{1,2}$ = 50 mV, -50 mV for two oppositely charged surfaces. The other parameters used in the calculations are listed in Table 3.1. It is seen that different assumptions give similar double layer force f_{dl} at large separation distance d_o while significant difference is seen for both the magnitude and the sign ($f_{dl} < 0$ for repulsive or $f_{dl} > 0$ attractive) of double layer force at small d_o. All the assumptions predict the double layer force f_{dl} to be repulsive when the charge of surfaces is the same (Fig. 3.10a). In this case, the double layer force f_{dl} predicted calculated by HHF-CP is the smallest whereas HHF-CC gives the largest f_{dl}. Fig. 3.10b indicates that the double layer force f_{dl} is determined to be repulsive, $f_{dl} < 0$ when HHF-CC assumption is used while the

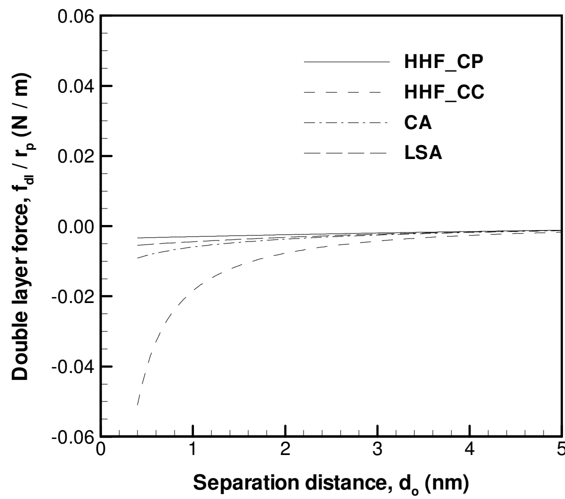

a) $\Psi_{1,2}$ = 50 mV, 50 mV

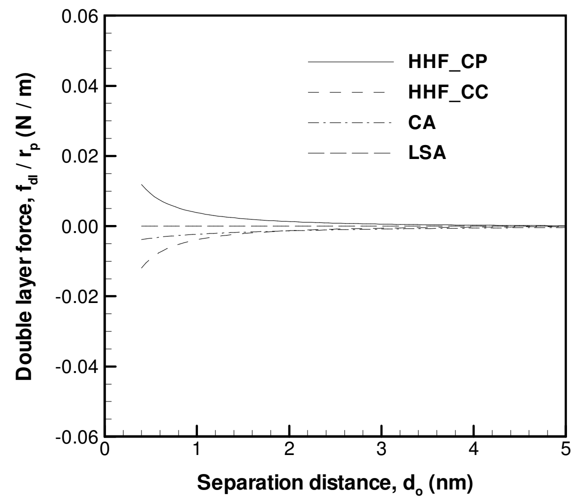

b) $\Psi_{1,2}$ = 50 mV, 0 mV

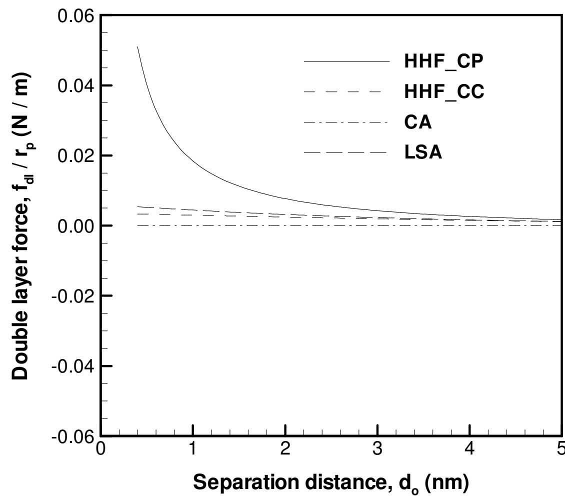

c) $\Psi_{1,2}$ = 50 mV, -50 mV

Fig. 3.10: The comparison of double layer force f_{dl} / r_p calculated based on constant potential (HHF-CP), constant charge (HHF-CC), compression (CA), and linear superposition (LSA) assumptions. Note that $f_{dl} < 0$ indicates repulsion.

double layer force is predicted to be attractive, $f_{dl} > 0$ for HHF-CP assumption. The magnitude of the double layer force f_{dl} is found to be much smaller for CA and LSA assumptions as compared to HHF-CP and HHF-CC assumptions. For the oppositely charged surfaces with the same zeta potential (Fig. 3.10c), CA predicts the double layer

Parameter	Value
Electron charge (e)	1.6×10^{-19} C
Avagadro's number (N_a)	6.02×10^{23}
Dielectric constant of water (ε_r)	78.4
Permittivity of vacuum (ε_o)	8.85×10^{-12} $C^2N^{-1}m^{-2}$
Temperature (T)	298 K
Boltzmann constant (k)	1.38×10^{-23}
Valence (z)	1
Molar concentration (M)	0.01 mol / liter

Table 3.1: Parameters used for the calculation of double layer forces.

force $f_{dl} = 0$. Equations for HHF-CP, HHF-CC and LSA assumptions give attractive double layer force $f_{dl} > 0$ in this case.

In this work, the double layer force due to the interactions between two contacting surfaces (wafer and abrasive particle) is considered. Due to the experiments [14,15,21] showing double layer force calculated by HHF-CC and CA to be in better agreement with the measured values when the separation distance is small, HHF-CC and CA assumptions are used in the following Chapter 5.

3.3 Hyperelastic Material Behavior

The majority of polishing pads used in CMP are made of polymeric materials [23], which exhibit hyperelastic material behavior. The hyperelastic material models for describing the mechanical behavior of polymeric materials are introduced in this section.

3.3.1 Basic definitions

The basic definitions of finite strain elasticity related to the hyperelastic material models are summarized in this section [24]. Deformation gradient, F is used to quantify the change in the element from reference (X) to deformed (x) configuration,

$$dx = \frac{\partial x}{\partial X} dX = F dX \tag{3.45}$$

In order to separate stretch and rotation components of a line element, the deformation gradient tensor, F can be decomposed into one positive symmetric tensor (U) and one orthogonal tensor (R) by right decomposition as,

$$F = RU \tag{3.46}$$

where R is the rotation tensor and U is the right stretch tensor. The right Cauchy-Green strain tensor C, which is a popular measure for strain in finite strain elasticity, can be obtained from the right stretch tensor U as,

$$C = F^T F = U^2 \tag{3.47}$$

The invariants I_i of the right Cauchy-Green strain tensor C can be expressed as a function of the stretch ratio, λ_i as,

$$I_1 = \lambda_1^2 + \lambda_2^2 + \lambda_3^2 \tag{3.48a}$$

$$I_2 = \lambda_1^2 \lambda_2^2 + \lambda_2^2 \lambda_3^2 + \lambda_1^2 \lambda_3^2 \tag{3.48b}$$

$$I_3 = J^2 = \lambda_1^2 \lambda_2^2 \lambda_3^2 \tag{3.48c}$$

where the stretch ratio, λ is defined using the initial (dL) and final length (dl) of the line element as,

$$\lambda_i = \frac{dl_i}{dL_i} \tag{3.49}$$

Note that the square root of the third invariant $J = \sqrt{I_3}$ is the ratio of the deformed volume over the reference volume. For an incompressible material, $I_3 = 1$.

3.3.2 Hyperelastic models

The mechanical behavior of a polymeric material can be characterized by using hyperelastic material models. The underlying principle of a hyperelastic material model is the conservation of the energy as the work done by inducing stresses in a material is considered to be converted to elastic strain energy. A material is considered to be hyperelastic if there is a strain-energy potential function W, which is a scalar function of one of the strain or deformation tensors [25].

If a material is isotropic, strain-energy potential function W is a function of the invariants (I_i) of right Cauchy-Green strain tensor C, $W = W\left(I_1, I_2, I_3\right)$. For an incompressible material $I_3 = 1$, and as a result, the strain energy potential is a function of the first two invariants, $W = W(I_1, I_2)$. The constitutive equation relating Cauchy (true) stress σ to the right Cauchy-Green strain tensor C for an incompressible and isotropic material reduces to [26],

$$\sigma_{ij} = -p\delta_{ij} + 2\frac{\partial W}{\partial I_1}C_{ij} - 2\frac{\partial W}{\partial I_2}C_{ij}^{-1} \tag{3.50}$$

where p is the hydrostatic pressure and δ_{ij} is the Kronecker delta.

Hyperelastic material models such as Neo-Hookean, Mooney-Rivlin, Ogen and Arruya-Boyce are constructed based on different forms of the strain energy potential function, W [25]. The appropriate form of the strain energy potential function, W is selected based on the material behavior observed in experiments.

3.3.3 Mooney-Rivlin hyperelastic model

The strain energy potential, W for an incompressible Mooney-Rivlin material is in the form [26],

$$W = \sum_{\alpha,\beta} A_{\alpha\beta} \left(I_1 - 3\right)^{\alpha} \left(I_2 - 3\right)^{\beta} \tag{3.51}$$

where $A_{\alpha\beta}$ are the Mooney-Rivlin constants. The strain energy potential, W reduces to the following form for a two-parameter Mooney-Rivlin model as,

$$W = a_{10}\left(I_1 - 3\right) + a_{01}\left(I_2 - 3\right) \tag{3.52}$$

where a_{10} and a_{01} are material constants. Eqn (3.52) for the strain energy potential W can be substituted in the constitutive equation to find Cauchy stress σ as a function of the right Cauchy-Green strain tensor C as follows,

$$\sigma_{ij} = -p\delta_{ij} + 2a_{10}C_{ij} - 2a_{01}C_{ij}^{-1} \tag{3.53}$$

In order to evaluate the non-linearity introduced by a two-parameter Mooney-Rivlin model, the stress-strain behavior of a material subjected to a uniaxial tension is considered. Selecting the coordinate system to coincide with the principal loading direction, the right Cauchy-Green strain tensor C can be expressed as a function of stretch λ as follows [26],

$$[C] = \begin{bmatrix} \lambda_1^2 & 0 & 0 \\ 0 & \lambda_2^2 & 0 \\ 0 & 0 & \lambda_3^2 \end{bmatrix} \tag{3.54}$$

where stretch λ is related to engineering strain ε as, $\lambda_i = 1 + \varepsilon_i$. If we assume λ_1 as the stretch in the loading direction, the stretch in other directions can be determined as, $\lambda_2 = \lambda_3 = \lambda_1^{-1/2}$ considering the incompressibility of the material, $\lambda_1 \lambda_2 \lambda_3 = 1$. Using Eqn (3.54) for the components of right Cauchy-Green strain tensor C and the stretch $\lambda_2 = \lambda_1^{-1/2}$, Eqn (3.53) can be used to calculate the Cauchy stress components σ_{11} and σ_{22} as,

$$\sigma_{11} = -p + 2a_{10}\lambda_1^2 - 2a_{01}\lambda_1^{-2} \tag{3.55a}$$

$$\sigma_{22} = -p + 2a_{10}\lambda_1^{-1} - 2a_{01}\lambda_1 = 0 \tag{3.55b}$$

Note that $\sigma_{22} = 0$ in Eqn (3.55b) since the material is loaded in 1-direction only. The hydrostatic pressure determined in Eqn (3.55b) can be substituted in Eqn (3.55a) to obtain;

$$\sigma_{11} = 2\left[a_{10}\left(\lambda_1^2 - \lambda_1^{-1}\right) + a_{01}\left(\lambda_1 - \lambda_1^{-2}\right)\right] \tag{3.56}$$

Note that the Mooney-Rivlin stress-strain variation is linear with a slope $E_s = 6(a_{10} + a_{01})$ at small strains [26]. Fig. 3.11 shows the effect of Mooney-Rivlin parameters (a_{10} and

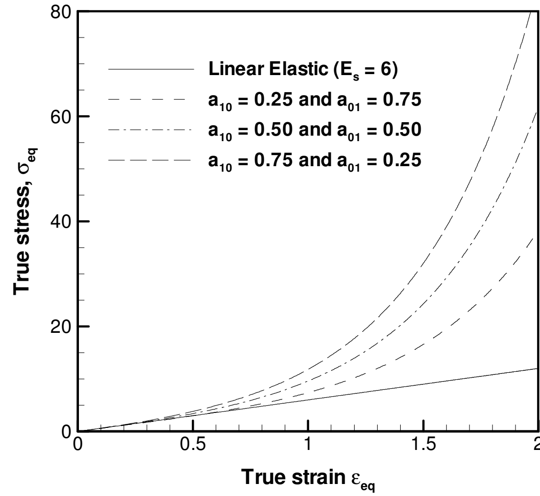

Fig. 3.11: The comparison of stress-strain behavior of two-parameter Mooney-Rivlin hyperelastic model and linear elastic material model. The elastic modulus for linear elastic material is taken to be $E_s = 6(a_{10} + a_{01})$.

a_{01}) on stress-strain behavior. It is seen that the linear elastic material behavior agrees well with the Mooney-Rivlin model at small strains. As strain becomes larger, $\varepsilon_{eq} > 0.5$, stress predicted by the Mooney-Rivlin model increases non-linearly deviating from the linear elastic behavior. The rate of increase of stress σ_{eq} with strain ε_{eq} seems to become greater when the second Mooney-Rivlin constant a_{01} gets larger. The deviation of the Mooney-Rivlin material model from linear elastic material behavior increases with larger second Mooney-Rivlin constant a_{01}. In this work, two-parameter Mooney-Rivlin model with constants $a_{10} = 0.5$ and $a_{10} = 0.5$ is used in the models presented in Chapter 4. This material model gives 10% higher stress σ_{eq} as compared to linear elastic material behavior for strain $\varepsilon_{eq} \approx 0.45$ and the difference increases to 60% when strain becomes as large as $\varepsilon_{eq} \approx 2$.

3.4 Mechanical Behavior of Porous Materials

The majority of CMP pads are porous materials [23]. Therefore it is important to understand the mechanical behavior of porous materials to characterize the mechanical response of a CMP pad. The mechanical behavior of a porous material (foam) depends on whether its cells are open or closed [27]. The cells are interconnected in an open-cell foam, whereas each cell is surrounded by a membrane-like structure and sealed off in a closed-cell foam. Both open and closed-cell foam structures are utilized for CMP pads [23].

The mechanical response of a foam to compression consists of three regimes based on the deformation of the cells [27]. Fig. 3.12 illustrates a typical stress-strain curve of a foam in compression. At small loads, foam behaves like an elastic material. This behavior is controlled by cell wall bending. The elastic modulus of an open-cell foam E_p can be estimated by using the relative density of foam ρ_{po} / ρ_{so} and the elastic modulus of solid material E_s [27] as,

$$\frac{E_p}{E_s} \approx \left(\frac{\rho_{po}}{\rho_{so}} \right)^2 \tag{3.57}$$

In a closed-cell foam, the bending of cell edges causes cell faces to stretch. The fraction of solid material contained in cell edges, ϕ determines the relative effect of cell wall bending and cell face stretching on elastic modulus. Furthermore, compression of the fluid in cells may play an important role for the closed-cell foams. Considering these three effects, the elastic modulus E_p of a closed-cell foam [27] can be expressed as,

$$\frac{E_p}{E_s} \approx \phi^2 \left(\frac{\rho_{po}}{\rho_{so}} \right)^2 + (1-\phi)\frac{\rho_{po}}{\rho_{so}} + \frac{p_o(1-2\nu_p)}{E_s(1-\rho_{po}/\rho_{so})} \quad (3.58)$$

where p_o is the fluid pressure and v_p is the Poisson's ratio. The fraction of the solid contained in cell edges, ϕ is found to be varying between 0.6 and 0.8 [27]. Poisson's ratio of 0.3, $v_p = 0.3$ is observed for both open and closed cell foams.

The cell walls of a foam start to buckle at high compressive stresses. The buckling of cell walls causes strain to increase rapidly with larger stress as indicated by the plateau in the stress-strain curve since the resistance to applied load is small in this region. The elastic stress σ_e that initiates the buckling of a cell wall can be estimated for open and closed cell foams [27] as,

$$\frac{\sigma_e}{E_s} \approx 0.05 \left(\frac{\rho_{po}}{\rho_{so}} \right)^2 \quad \text{for open-cell} \quad (3.59a)$$

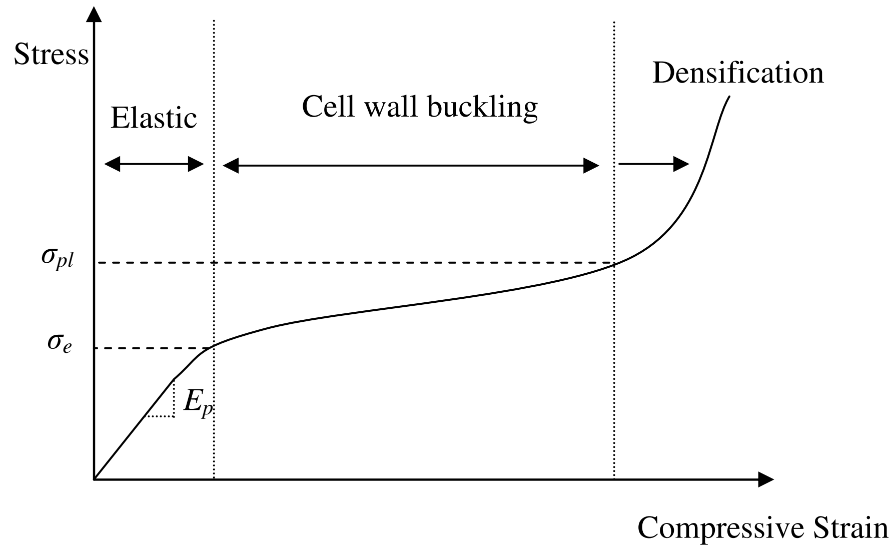

Fig. 3.12: Mechanical response of a typical porous material (foam) to compression consisting of three regions, elastic, cell wall buckling and densification.

$$\frac{\sigma_e}{E_s} \approx 0.05\left(\frac{\rho_{po}}{\rho_{so}}\right)^2 + \frac{(p_o - p_a)}{E_s} \quad \text{for closed-cell} \tag{3.59b}$$

where p_o is the fluid pressure in the cell and p_a is the atmospheric pressure.

The third (densification) regime shown in the stress-strain curve (Fig. 3.12) of a foam starts to operate once the cell walls of the foam collapses plastically and densification occurs. The plastic stress, σ_{pl} in this regime can be calculated by using the yield strength of solid material σ_{ys} as follows [27],

$$\frac{\sigma_{pl}}{\sigma_{ys}} \approx 0.3\left(\frac{\rho_{po}}{\rho_{so}}\right)^{3/2} \quad \text{for open-cell} \tag{3.60a}$$

$$\frac{\sigma_{pl}}{\sigma_{ys}} \approx 0.3\left(\phi\frac{\rho_{po}}{\rho_{so}}\right)^{3/2} + 0.4(1-\phi)\frac{\rho_{po}}{\rho_{so}} + \frac{(p_o - p_a)}{\sigma_{ys}} \quad \text{for closed-cell} \tag{3.60b}$$

The porous elastic modulus ratio E_s / E_p is calculated using Eqns (3.57) and (3.58) for open and closed-cell materials, respectively. The relative density is varied in the range, $0.4 < \rho_{po} / \rho_{so} < 1$. The calculations for closed-cell are carried out for a soft (E_s = 10 MPa) and a hard (E_s = 100 MPa) solid material and taking the fraction of solid contained in cell edges, ϕ = 0.8 and Poisson's ratio v_p = 0.3. Atmospheric pressure is used for the pressure inside the pores of a closed-cell material, p_o = 0.1 MPa. Fig. 3.13 shows that porous elastic modulus ratio is calculated to be $1 < E_s / E_p < 6$, where $E_s / E_p = 1$ for a non-porous pad $\rho_{po} / \rho_{so} = 1$ and $E_s / E_p = 6$ for a porous pad with relative density ρ_{po} / ρ_{so} = 0.4. Porous elastic modulus E_p of an open-cell foam is found to be smaller than that of a closed-cell foam at low relative density, $\rho_{po} / \rho_{so} < 0.6$, while the opposite is true at high relative density, $\rho_{po} / \rho_{so} > 0.6$.

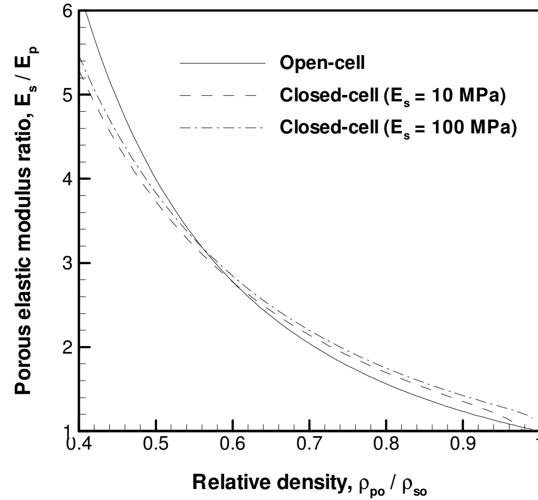

Fig. 3.13: The variation of porous elastic modulus ratio E_s / E_p with relative density ρ_{po} / ρ_{so} for open and closed-cell foams calculated using Eqns (3.57) and (3.58).

The pore structure of a typical (IC-1000) CMP pad is illustrated in Fig. 3.14. Fig. 3.14a shows the grooves with a width ~200 µm and depth ~250-300 µm. The spacing between grooves is ~1-1.2 mm. The diameter of pores as shown in Fig. 3.14b varies in the range 10-40 µm and the mean diameter is estimated to be ~ 20 µm. Note that IC-1000 has a closed-cell structure as demonstrated in Fig. 3.14b. The relative density of a IC-1000 pad is ρ_{po} / ρ_{so} $\approx$ 0.6 [23], which gives porous elastic modulus ratio of E_s / E_p $\approx$ 2.8 based on Fig. 3.13. Note that the ratio of equivalent elastic modulus is used in the contact models developed in the subsequent sections. The equivalent elastic modulus is obtained by using the elastic modulus and Poisson's ratio of materials in Eqn (3.2). The solid pad material is typically a polymeric material such as polyurethane exhibiting a nearly-incompressible material behavior with Poisson's ratio v_s $\approx$ 0.5 [28]. Considering the Poisson's ratio of a porous material v_p $\approx$ 0.3 [27], the ratio of equivalent porous elastic modulus ratio can be calculated using Eqn (3.2) as E_s / E_p $\approx$ 3.4 for ρ_{po} / ρ_{so} $\approx$ 0.6.

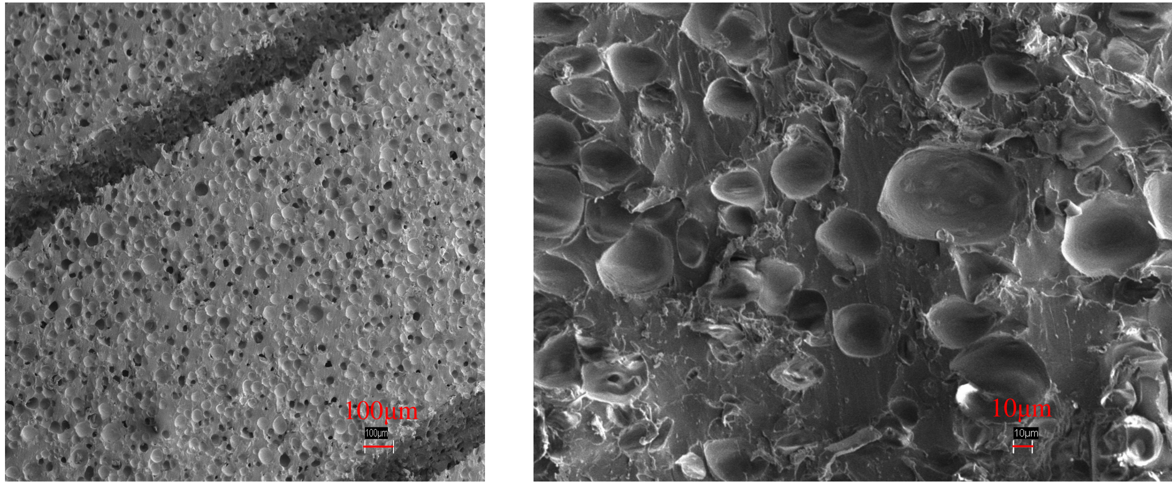

a) IC-1000 pad (low-magnification) b) IC-1000 pad (high-magnification)

Fig. 3.14: Porous structure of a typical (IC1000) CMP pad.

In this work, the effect of pad porosity is reflected on the results of the developed model due to its effect on porous elastic modulus ratio since the porous E_p and solid pad elastic modulus E_s plays a role in different scales of contact as explained in Chapter 4. The influence of pad porosity on the variation of material removal rate is investigated by varying porous elastic modulus ratio in the range $1 < E_s / E_p < 4$ in Chapters 6 and 7.

3.5 Wear Mechanisms

Adhesive and abrasive wear are the two wear mechanisms considered to take place in CMP. The wear equations are introduced for adhesive and abrasive wear next.

3.5.1 Adhesive wear

When two surfaces are brought together, there is a tendency of surfaces to adhere due to the attractive forces between the surface atoms of the contacting materials. As the surfaces are separated and brought together repetitively due to relative motion in normal

or tangential direction, this attractive force causes material to be removed from the original surface causing adhesive wear [29].

Experimental studies indicate that in adhesive wear, the wear rate is proportional to applied load f_w and sliding distance V_r and inversely proportional to hardness H_w of the worn material. Based on this observation, a wear rate equation for the volume of material worn RR_{ad}^{sp} by a single particle can be expressed following Archard's law [29] as,

$$RR_{ad}^{sp} = k_w^{ad} \frac{f_w V_r}{H_w} \tag{3.61}$$

where k_w^{ad} is the adhesive wear constant which depends on different parameters, e.g. contacting materials, surface conditions. Note that superscript "sp" representing the wear of a single abrasive particle is used as the equations given in this section will be utilized for calculating the wear of a single particle in Section 5.2. A wide range of values, $10^{-7} < k_w^{ad} < 10^{-1}$ has been found experimentally for the adhesive wear constant [29]. The wear constant of $1\text{x}10^{-5} < k_w^{ad} < 1\text{x}10^{-2}$ is found to be more typical for most of the materials.

3.5.2 Abrasive wear

When a hard surface slides over a soft surface, grooves form on the soft surface if the load is sufficiently high. Abrasive wear occurs as the material is displaced form the grooves in the form of loose wear particles [29]. The removal (wear) rate RR_{ab}^{sp} is proportional to the volume of material swept by the abrasive as $RR_{ab}^{sp} \propto A_{ab}^{sp}$, where the subscript "ab" indicates abrasion and the superscript "sp" indicates single particle. When one of the surfaces is a sphere and the other one is flat, the instantaneous abraded area

A_{ab}^{sp} (Fig. 3.15) can be found by assuming that the indentation depth is small as compared to particle radius $\delta_w << r_p$ [30],

$$A_{ab}^{sp} = a_w \delta_w \tag{3.62}$$

where a_w is the contact radius. This instantaneous abraded area A_{ab}^{sp} is multiplied by relative velocity V_r to find the total wear rate RR_{ab}^{sp}. Furthermore an abrasive wear constant k_w^{ab} has to be introduced as only a fraction of material displaced by the abrasive is actually worn away. Then the abrasive wear relationship becomes,

$$RR_{ab}^{sp} = k_w^{ab} V_r A_{ab}^{sp} \tag{3.63}$$

If we assume that the load on the abrasive is sufficiently high to cause fully-plastic deformation in the softer material, the elastic deformation of materials can be neglected. In this case, contact radius a_w can be expressed in terms of indentation depth δ_w as,

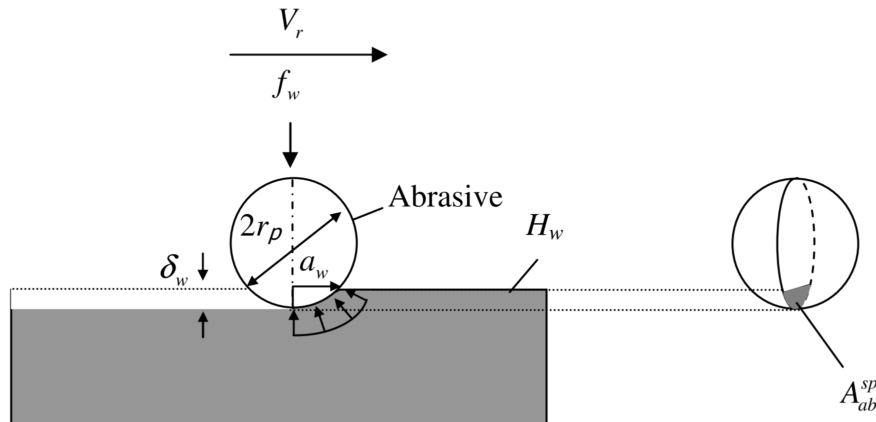

Fig. 3.15: Abrasive wear mechanism.

$$a_w = \sqrt{2\delta_w r_p} \quad (3.64)$$

Using Eqns (3.62)-(3.64), the abrasive wear rate RR_{ab}^{sp} can be found as a function of indentation depth δ_w as,

$$RR_{ab}^{sp} = k_w^{ab} V_r \sqrt{2r_p}\,\delta_w^{3/2} \quad (3.65)$$

The hardness of softer material is assumed to be the contact pressure acting at the interface considering the fully-plastic contact assumption. Since the particle is sliding over worn surface, the contact area is only half of the contact area if the particle is stationary. The force on particle f_w can be related to contact radius a_w and hardness H_w as,

$$f_w = H_w \frac{\pi a_w^2}{2} = H_w \pi \delta_w r_p \quad (3.66)$$

The abrasive wear rate RR_{ab}^{sp} can be calculated using force on abrasive f_w given by Eqn (3.66) as,

$$RR_{ab}^{sp} = k_w^{ab} V_r \sqrt{\frac{2}{\pi^3}} \frac{f_w^{3/2}}{r_p H_w^{3/2}} \quad (3.67)$$

Abrasive wear is an indentation based wear mechanism, therefore the wear rate for abrasive wear increases with contact force on abrasive as $RR_{ab}^{sp} \propto f_w^{3/2}$ while this relation for adhesive wear is $RR_{ad}^{sp} \propto f_w$. This difference, in the contact force dependence will be shown to be an important factor for the variation of material removal rate in Chapters 6 and 7.

The wear constant is determined in experimental studies. The wear constant for two-body and three-body abrasive wear is found to be respectively in the range of $6 \times 10^{-3} < k_w^{ab} < 6 \times 10^{-2}$ and $3 \times 10^{-4} < k_w^{ab} < 3 \times 10^{-3}$, respectively [29].

References

1. Hertz H., 1882. Über die Berührung fester elastischer Körper. J. reine angewandte Matematik, Vol 92, 156-171.
2. Johnson K. L., 1985. Contact mechanics. Cambridge University Press, Cambridge.
3. Williams J. A., 2000. Engineering tribology, Oxford University Press, UK.
4. Greenwood J. A., Williamson J. B. P., 1966. Contact of nominally flat surfaces. Proceedings of the Royal Society of London, Series A295, 300-319.
5. Bhushan B., 1998. Contact mechanics of rough surfaces in tribology: multiple asperity contact. Tribology Letters, 4, 1-35.
6. McCool J. I., 2000. Extending the capability of the Greenwood Williamson microcontact model. ASME J Tribol, 122, 496–502.
7. Johnson N., Kotz S., 1970. Continuous univariate distributions-I, Wiley, New York.
8. Adams G. G., Müftü S., 2005. Improvements to a scale-dependent model for contact and friction. J. Phys. D: Appl. Phys., Vol 38, 1402–1409.
9. Sahoo P., Mohamed Ali S., 2008. Elastic-plastic adhesive contact of non-Gaussian rough surfaces. Sadhana (Academy Proceedings in Engineering Sciences), Vol 33, 367-384.
10. Greenwood J. A., Tripp J. H., 1967. The elastic contact of rough spheres. ASME Journal of Applied Mechanics, Vol 34, 153-159.
11. Maugis D., 2000. Contact, adhesion and rupture of elastic solids. Springer-Verlag, Berlin.
12. Israelachvili J. N., 1992. Intermolecular and surface forces. Academic Press.

13. Maugis D., Pollock H. M., 1984. Surface forces, deformation and adherence at metal microcontacts. Acta Metall., Vol 9, 1323.

14. Gregory J., 2005. Particles in water: Properties and processes. Taylor and Francis, Routledge.

15. Hiemenz P. C., 1986. Principles of colloid and surface chemistry. Marcel Dekker, New York.

16. Hubbard A.T., 2006. Encyclopedia of surface and colloid science. Taylor & Francis, New York.

17. Hogg R., Healy T. W., Fuerstenau D. W., 1966. Trans Faraday Soc, Vol 62, 1638.

18. Wiese G. R., Healy T. W., 1970. Effect of particle size on colloid stability. Trans Faraday Soc, Vol 66, 490.

19. Usui S. J., 1973. J Colloid Interface Sci, Vol 44, 107.

20. Gregory J., 1975. Interaction of unequal double layers at constant charge. J. Colloid. Interface Sci., 51, 44.

21. Shan H., 2006. Effect of medium on particle adhesion and removal. Ph.D. Thesis, Northeastern Univ., Boston, MA.

22. Verwey E. J. W., Overbeek J. G., 1948. Theory of the stability of lyophobic colloids. Elsevier, Amsterdam.

23. Oliver M.R. (Editor), 2004. Chemical mechanical planarization of semiconductor materials. Springer Verlag, New York.

24. Malvern L. E., 1969. Introduction to the mechanics of a continuous medium. Prentice Hall, NJ.

25. Wu H. C., 2004. Continuum mechanics and plasticity. Chapman & Hall / CRC Press, Florida.

26. ANSYS Inc. ANSYS theory reference ver. 9.0. Southpointe, PA.

27. Gibson L. J., Ashby M F., 1997. Cellular solids: structure and properties. Cambridge University Press, New York.

28. Kim A.T., Seok J., Tichy J.A., Cale T.S., 2003. A multiscale elastohydrodynamic contact model for CMP. J Electrochem Soc, 150, 570-576.

29. Rabinowicz E., 1995. Friction and wear of materials. John Wiley & Sons, New York.

30. Ahmadi G., Xia X., 2001. A model for mechanical wear and abrasive particle adhesion during the chemical mechanical polishing process. J Electrochem Soc, 148, 99-109.

CHAPTER 4

MECHANICAL MODELING OF

PAD-PARTICLE-WAFER CONTACT

4.1 Overview

In this chapter, different scales of contact encountered in CMP, as illustrated in Figs 4.1a-d, are modeled starting from the smallest contact scale of a particle trapped between the pad and the wafer, and gradually expanding to the pad-wafer rough contact which is the broadest contact scale considered in this work.

Particle level interactions are modeled in two steps, *the single particle* (SP) contact model and *the multi-particle* (MP) contact model as shown in Figs 4.1d and 4.1c, respectively. In the SP contact model depicted in Fig. 4.2, the contact of a single particle with one deformable surface (pad) and one rigid surface (wafer) is characterized using the finite element (FE) method. The rigid particle and the flat surface are incrementally pushed toward the deformable surface. At small penetration values, only the particle makes

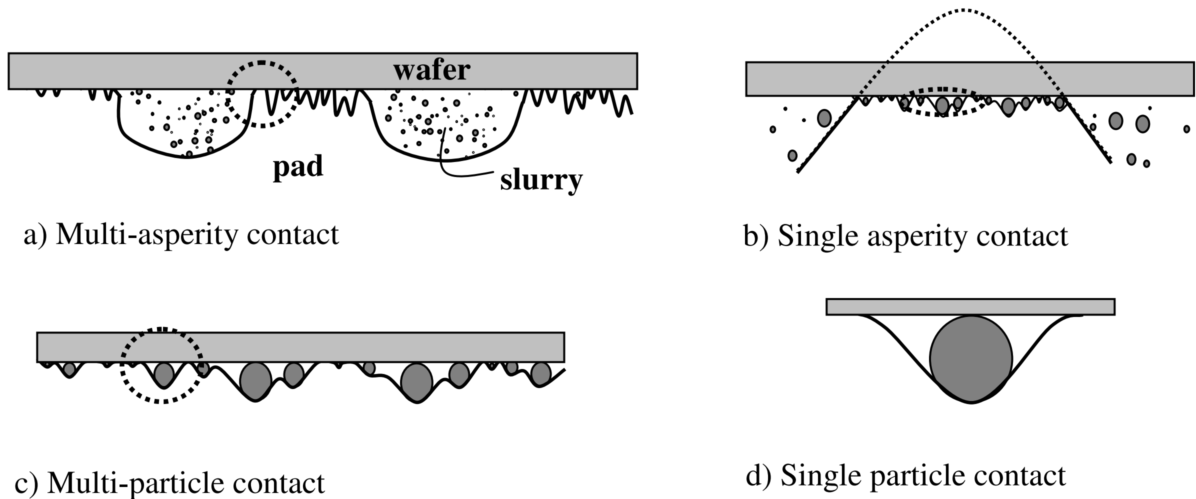

Fig. 4.1: Different scales of contact

contact with the deformable surface, and this is called *the particle contact regime*. In the particle contact regime, *the particle contact force* f_p^p is characterized as a function of *the penetration depth* δ_p. As the penetration depth δ_p becomes as large as the diameter of particle $2r_p$, *direct contact* of the rigid and the deformable flat surfaces occurs and *direct contact pressure* p_d^m develops at the contact interface. A combination of particle and direct contacts carry the total contact force in this contact regime, named *the mixed contact regime*. In the mixed contact regime, important parameters, which are used to characterize the contact behavior, are the particle contact force f_p^m, *the influence radius* r_i and the direct contact pressure p_d^m. The influence radius r_i is defined in Fig. 4.2 and changes with penetration δ_p. Particle contact force f_p^m gives the fraction of total force carried by a particle, while the influence radius r_i and the direct contact pressure p_d^m are used to calculate the force at direct contact interface. In order to generalize the model in the mixed contact regime, the results are defined as a function of an *average compressive*

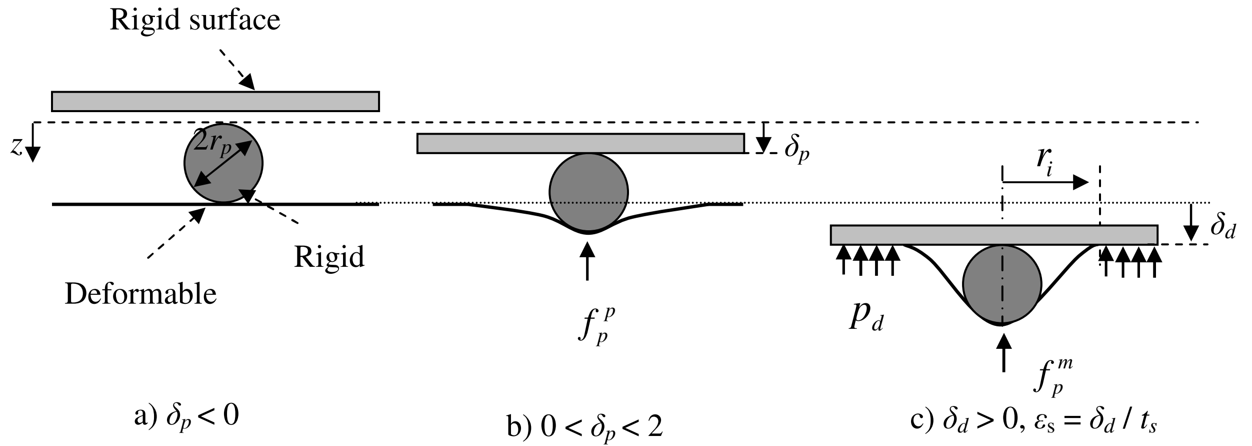

Fig. 4.2: The single particle (SP) contact model at different particle penetration.

strain ε_s due to direct contact of flat surfaces instead of penetration depth as used in the particle contact regime.

Once the contact behavior of a single particle is characterized in the SP contact model, the overall effect of multiple particles on the contact of two flat surfaces (one rigid and one deformable) is modeled in the MP contact model (Fig. 4.1c). A statistical contact approach is used to integrate the effect of each particle over all of *the active particles* in contact. In the MP contact model, a particle moving freely between surfaces due to slurry flow gets engaged in contact and becomes active when the separation distance becomes smaller than the diameter of particle. Both *the number of active particles* η_a^{mp} and *the particle contact pressure* p_p^{mp-p} increase in the particle contact regime of the MP contact model as two surfaces approach each other. The mixed contact regime in the MP contact model starts to operate as separation distance becomes zero, $d_{sep} = 0$. Direct contact of surfaces does not develop at zero separation distance as particles retard the occurrence of

direct contact. Similar to the SP contact model, an average compressive strain ε_p due to direct contact of surfaces is used to define the results of mixed contact regime. At a critical average compressive strain $\varepsilon_p = \varepsilon_p^m$, direct contact of surfaces occurs. Overall contribution of direct contacts to force equilibrium between surfaces is quantified by the direct contact pressure p_d^{mp} and *the direct contact area* A_d^{mp}, which are computed using relations found in the SP contact model. Important outcomes of the MP contact model are the fraction of total pressure carried by particle contacts p_p^{mp} / p_c^{mp}, the direct contact area A_d^{mp}, and the number of active particles η_a^{mp} for a given separation distance d_{sep} in the particle contact regime or an average compressive strain ε_p in the mixed contact regime.

The results of the MP contact model are used in *the single asperity* (SA) contact model to characterize the contact of a single asperity with a flat surface in presence of interfacial particles (Fig. 4.1b). The SA contact model utilizes an approach similar to the contact of rough spheres studied by *Greenwood and Tripp (GT)* (Section 3.1.3). Here, the deformation of a pad asperity is influenced by pad-particle-wafer interactions. The MP contact model provides the necessary relations for the local contact. The displacement of a contact point at interface consists of local penetration of surfaces and bulk deformation. The MP contact model gives local deformation for a given contact pressure. In order to determine bulk deformation, the contact pressure distribution is transferred to a FE model and the model is solved for displacements at each contact point. The global equilibrium for local and bulk deformation at each contact point is iteratively established and the contact pressure distribution at single asperity contact is obtained. The contact pressure distribution is then substituted into the MP contact model to find the fraction of contact

pressure due to particle contacts, the direct contact area and the number of active particles in single asperity contact.

In *the multi-asperity* (MA) contact model (Fig. 4.1a), the contact of a deformable rough (pad) surface and a rigid smooth surface (wafer) is considered with rigid spherical interfacial particles (abrasives). In this model, the behavior of the asperities is characterized by the SA contact model. In the MA contact model, a statistical multi-asperity model is used to integrate the effect of each asperity to obtain overall rough contact behavior of the two surfaces. This model allows the prediction of the contribution of particle and direct contacts in the MA contact conditions.

Modeling approach described in this chapter forms the foundation for calculating material removal rate due to pad-wafer rough contact. Material removal is assumed to be achieved by particle contacts only while direct contact does not result in material removal. The model results give the fraction of applied pressure transferred to particles in pad-particle-wafer contact, which is considered to be the main mechanical driver resulting in material removal.

4.2 Non-Dimensionalization of Parameters

In the single particle (SP) contact model, the parameters are non-dimensionalized with respect to particle radius r_p and pad elastic modulus E_s. Particle size is not constant in the multi-particle (MP) or the single asperity (SA) contact models, therefore standard deviation σ_p of particle size distribution is used instead of particle radius r_p for non-dimensionalization. Pad elastic modulus, E_s is utilized for the non-dimensionalization of

pressure terms as E_s dominates the contact at MP or SA contact scale. Porous pad elastic modulus E_p and standard deviation (SD) of pad roughness σ_s become the relevant scaling parameters when rough contact of surfaces is considered in the MA contact model. Non-dimensionalization of length (L), pressure (P) and force (F) terms, and the inter-relation of non-dimensional parameters are summarized in Table 4.1. Note that the superscript "*" indicates non-dimensional variables in the SP contact model, "~" is used for the MP contact and the SA contact models, and "-" is utilized in the multi-asperity (MA) contact model.

The values for the non-dimensional parameters studied in the models are selected to reflect the range of physical values commonly used in CMP. Table 4.2 and 4.3 lists the actual and non-dimensionalized values utilized in the models, respectively. The ranges of values listed in Table 4.3 are used to investigate the effect of each parameter while other parameters are kept constant at their base values.

4.3 Single Particle (SP) Contact Model

Contact mechanics of a rigid spherical particle, with radius r_p, trapped between two flat surfaces (one rigid and one deformable), as shown in Fig. 4.2, is investigated. The

SP Contact Model			MP & SA Contact Model			MA Contact Model		
L^*	F^*	P^*	$\tilde{L}$	$\tilde{F}$	$\tilde{P}$	$\bar{L}$	$\bar{F}$	$\bar{P}$
$\frac{L}{r_p}$	$\frac{F}{E_s r_p^2}$	$\frac{P}{E_s}$	$L^* \frac{r_p}{\sigma_p}$	$F^* \frac{r_p^2}{\sigma_p^2}$	P^*	$\tilde{L}\frac{\sigma_p}{\sigma_s}$	$\tilde{F}\frac{E_s}{E_p}\frac{\sigma_p^2}{\sigma_s^2}$	$\tilde{P}\frac{E_s}{E_p}$

Table 4.1: Non-dimensionalization of parameters in the contact models.

Parameter	Base	Range
SD of particle radius (σ_p) Mean particle diameter ($2\mu_p = 8\sigma_p$)	6.25 nm 50 nm	3.125 – 12.5 nm 25 – 100 nm
Particle concentration (η_w)	2.5%	1.25% - 5%
Particle to slurry density ratio (ρ_p/ρ_s)	3.7 (alumina)	NA
Asperity radius (R_s)	50 µm	25 – 100 µm
Asperity density (η_s)	$2\text{x}10^{-4}$ / µm^2	$1\text{x}10^{-4}$ – $4\text{x}10^{-4}$ / µm^2
Solid pad elastic modulus (E_s)	10, 100 MPa	10 - 100 MPa
Porous pad elastic modulus ratio (E_s/E_p)	1	1 - 4
Applied pressure (P_o)	0.007 MPa, 0.07 MPa 1 psi, 10 psi	0.007 – 0.07 MPa 1 - 10 psi

Table 4.2: Physical values for parameters used in non-dimensionalization.

Parameter	MP and SA contact models		MA contact model	
	Base	Range	Base	Range
SD of particle size (σ_p)	N/A	N/A	$1.25\text{x}10^{-3}$	$6.25\text{x}10^{-4}$ – $2.5\text{x}10^{-3}$
Particle concentration (η_w)	2.5%	1.25% - 5%	2.5%	1.25% - 5%
Asperity radius (R_s)	8000	4000 - 16000	10	5 - 20
Asperity density (η_s)	N/A	N/A	$5\text{x}10^{-3}$	$2.5\text{x}10^{-3}$ - $1\text{x}10^{-2}$
Particle density ratio (ρ_p/ρ_s)	3.7	N/A	3.7	N/A
Porous elastic modulus ratio (E_s/E_p)	N/A	N/A	1	1-4

Table 4.3: Non-dimensional parameters in the MP, SA and MA contact models.

separation distance between the surfaces is initially large and particle is not in contact with rigid surface (Fig. 4.2a). At small loads, the contact is supported only by *particle contact* (Fig. 4.2b). When the penetration of particle δ_p becomes sufficiently large $\delta_p \geq 2$

r_p, the flat surfaces come into *direct contact*. In this work, the condition where the contact is supported by a combination of particle and direct contacts is called *the mixed contact* (Fig. 4.2c). In this regime, an important parameter is *the influence radius* r_i of the particle, which is used to quantify the non-contact region around the particle. Also note that, due to the reasons that will become clear shortly, deformation in the particle contact regime is characterized with respect to the penetration of particle δ_p, but deformation in the mixed contact regime is characterized with respect to the average compressive strain $\varepsilon_s = \delta_d / t_s$, where δ_d $(= \delta_p - 2r_p)$ is the displacement of deformable medium due to direct contact.

4.3.1 Finite element model

This problem is investigated with an axisymmetric FE model, using Ansys 9.0 (Canonsburg, PA). The outer radius r_o of deformable domain is taken as 200r_p, which is sufficiently large to ensure that the results do not depend on this parameter. The thickness

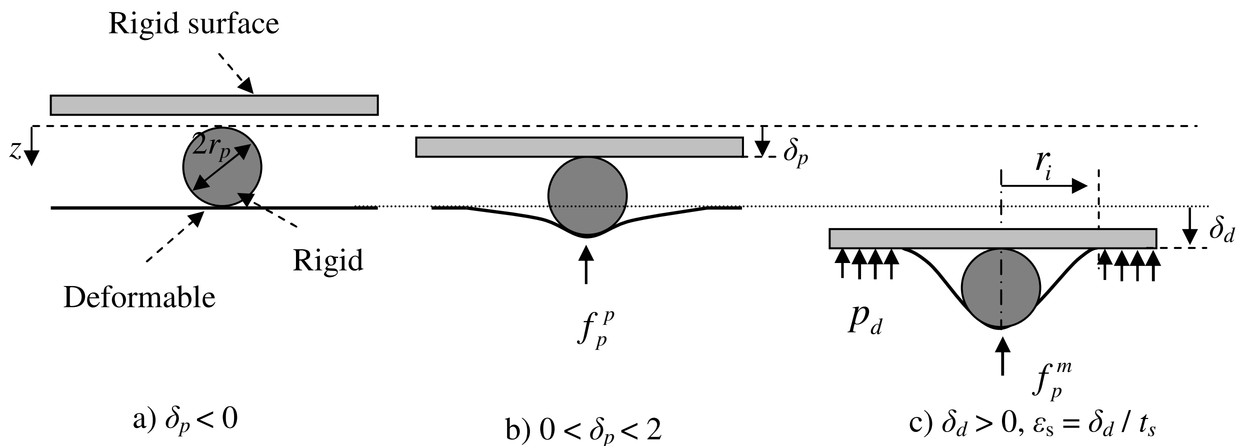

Fig. 4.2: The single particle (SP) contact model at different particle penetration.

of deformable medium t_s however affects particle and direct contacts as particle becomes completely embedded in deformable medium. The model is run using $t_s = 250r_p$, $500r_p$ and $1000r_p$ for a total average compressive strain of $\varepsilon_s = 0.45$. It is confirmed that the results presented in this section are independent of the thickness of the deformable medium, t_s if the results are defined as a function of the average compressive strain ε_s in the mixed contact regime. In the FE model, the nodes attached to particle and rigid surface are coupled and displaced incrementally toward deformable medium to a particle penetration depth of $\delta_p = 227r_p$, or average compressive strain of $\varepsilon_s = 0.45$ for a thickness of the deformable medium of $t_s = 500r_p$. The model consists of 71,000, 4-noded axisymmetric elements (PLANE182), by using the non-linear finite deformation definition (NLGEOM command). The mesh in the vicinity of particle is finer and is gradually coarsened away from particle as shown in Fig. 4.3. Two different frictionless contact pairs for the contact of particle and deformable medium, and rigid surface and deformable medium are defined with contact elements (CONTA172) for deformable medium (pad) and rigid target elements (TARGE169) for rigid particle (abrasive particle) and surface (wafer). The nodes attached to the bottom surface of the deformable medium are constrained in the direction of particle movement.

Two parameter Mooney-Rivlin hyperelastic material model is used to simulate the material behavior of the pad. In this model, strain energy density function is expressed in terms of two material constants, a_{10} and a_{01} as explained in Section 3.3. Here a_{10} and a_{01} are taken to be 0.5 MPa, which yields $E_s = 6$ MPa [1]. The Poisson's ratio of elastic

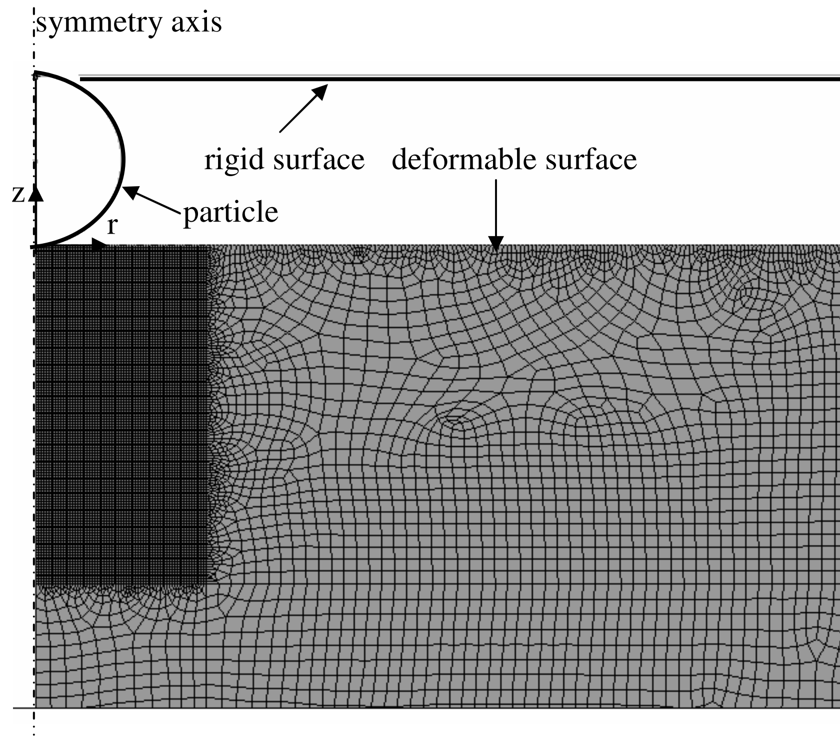

Fig. 4.3: Finite element mesh near the particle in the SP contact model. The mesh near the contact region is finer and adjusted to be coarser away from the contact zone.

surface, $\nu_s = 0.49$, which is typical for nearly incompressible, rubber-like materials, is used in the model.

4.3.2 Single particle contact relations

The FE model described above is solved for each displacement increment, δ_p^* and particle contact force, f_p^* is calculated by summing the forces at contact nodes attached to deformable medium in contact with particle. The force acting on particle is indicated by $f_p^{p^*}$ or $f_p^{m^*}$ depending on whether the contact represents the particle contact or the mixed contact situations, respectively.

Fig. 4.4 shows the variation of particle contact force in particle contact regime $f_p^{p^*}$ (0 < δ_p^* < 2) and mixed contact regime $f_p^{m^*}$ (0 < ε_s < 0.45). It is illustrated that Hertz contact is valid for small penetration depths δ_p^*, however the SP contact model results start to deviate from Hertz contact as δ_p^* is increased due to the fact that assumptions of Hertz contact becomes invalid at large δ_p^*. Hertz contact assumes linear elastic material behavior for deformable surface. Furthermore deformations are considered to be small and the radius of particle is assumed to be large as compared to contact radius. Both of these assumptions play a role for the discrepancy of results found by using the SP contact model and Hertz contact at large penetration depths δ_p^*. In order to explore the role of each assumption and understand the sensitivity of results to hyperelastic material parameters characterizing material non-linearity, the SP contact model is run for linear

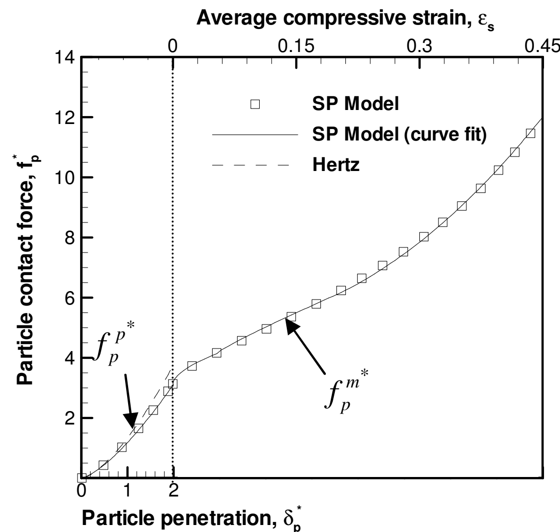

Fig. 4.4: The particle contact force, f_p^* as a function of particle penetration, δ_p^* in particle contact regime and average compressive strain, ε_s in mixed contact regime.

elastic material behavior as well as hyperelastic material behavior with different sets of Mooney-Rivlin constants (a_{10} = 0.25, a_{01} = 0.75 and a_{10} = 0.75, a_{01} = 0.25). Fig. 4.5 shows that Hertz contact can be used without loss of accuracy up to particle penetration of δ_p^* = 0.75. However as penetration depth becomes larger, δ_p^* > 0.75, large displacements start to influence the results as indicated by the deviation between Hertz contact and the SP contact model with linear elastic material behavior. Hertz contact over-estimates particle contact force, $f_p^{p^*}$ due to large displacements. A further increase in penetration depth, δ_p^* causes non-linear material behavior to affect contact force $f_p^{p^*}$. Hyperelastic material behavior results in a particle contact force, $f_p^{p^*}$ larger than that of linear elastic material behavior at the same penetration depth δ_p^* when δ_p^* > 1. It is observed that as first Mooney-Rivlin constant a_{10} becomes smaller, the deviation

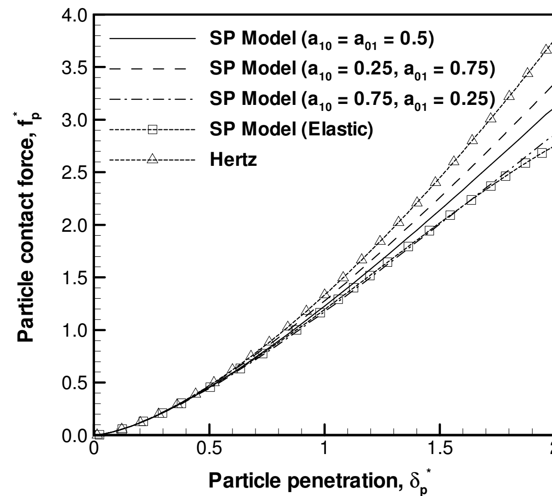

Fig. 4.5: The comparison of particle contact force in the particle contact regime, $f_p^{p^*}$ for hyperelastic and linear elastic material behavior.

becomes greater, which is in agreement with the stress-strain behavior shown in Fig. 3.11 for different a_{10} and a_{01} values, indicating a_{10} causes greater deviation in stress-strain behavior as compared to the stress-strain behavior of a linear elastic material. In fact, the SP contact model with linear elastic and hyperelastic material behavior with a_{10} = 0.75 and a_{01} = 0.25 agree well in the entire range of particle penetration, $0 < \delta_p^* < 2$, and the effect of non-linear material behavior becomes negligible. For hyperelastic material constants used in this study (a_{10} = 0.50 and a_{01} = 0.50), the error of particle contact force predicted by Hertz contact ($f_p^{h^*} = \frac{4}{3}\delta_p^{*3/2}$) increases up to ~20% as particle penetration δ_p^* approaches 2.

The effect of non-linear material behavior is also evaluated by considering the strain induced in deformable medium at different particle penetration depths δ_p^* (Fig. 4.6). The maximum von Mises strain is ε_{eq} = 0.56 at penetration depth, δ_p^* = 1 (Fig. 4.6a). Non-linear material behavior is not expected to have an effect at this penetration depth since the stress-strain behavior for a hyperelastic material can be represented well by linear elastic material behavior at this strain level (Fig. 3.11). The maximum von Mises strain increases up to ε_{eq} = 0.96 when penetration depth becomes larger, δ_p^* = 2. At this strain level, hyperelastic material model gives stresses higher than linear elastic material, and as a result, contact force, $f_p^{p^*}$ calculated by the SP contact model is greater as seen in Fig. 4.5.

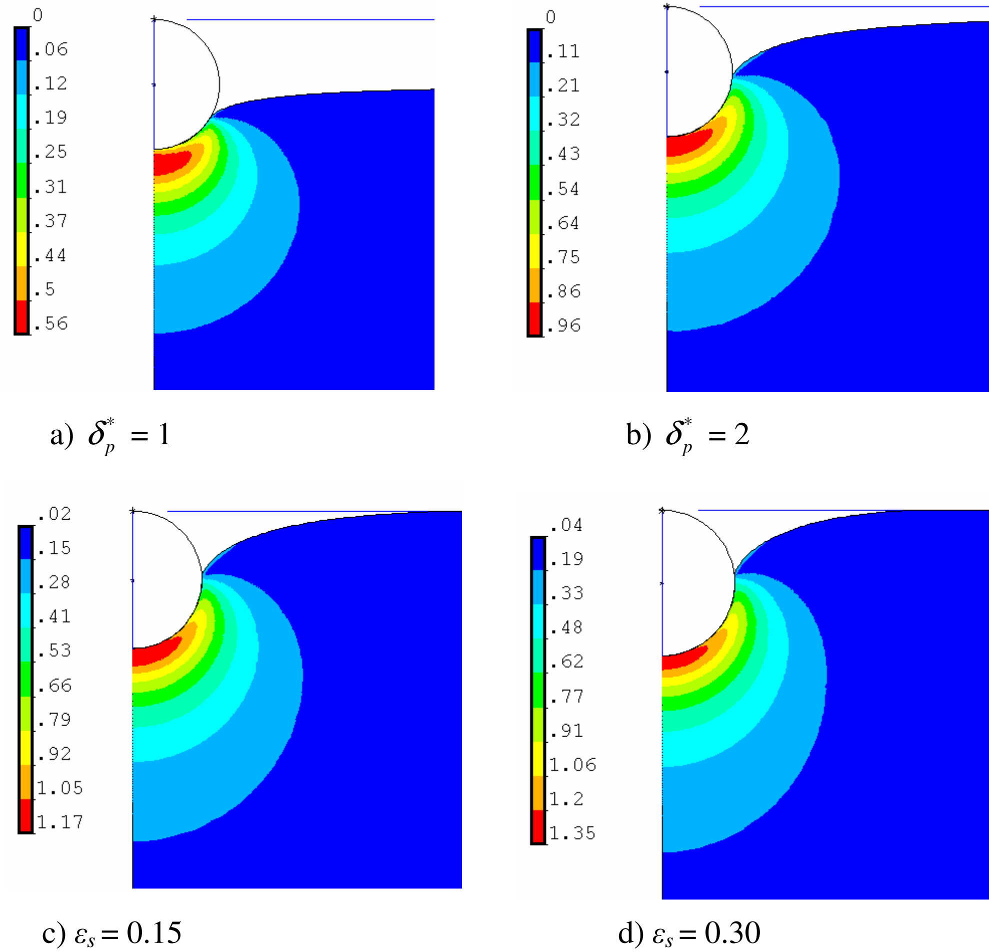

a) $\delta_p^* = 1$ b) $\delta_p^* = 2$

c) $\varepsilon_s = 0.15$ d) $\varepsilon_s = 0.30$

Fig. 4.6: The non-dimensional von Mises strain distribution ε_{eq} at different penetration depths using Mooney-Rivlin material behavior ($a_{10} = 0.5$ and $a_{01} = 0.5$).

The von Mises strain distribution ε_{eq} is also plotted for different average compressive strain, ε_s in mixed contact regime, $\delta_p^* > 2$. The maximum von Mises strain is $\varepsilon_{eq} = 1.17$ and $\varepsilon_{eq} = 1.35$ for average compressive strain, $\varepsilon_s = 0.15$ and $\varepsilon_s = 0.3$, respectively (Fig. 4.6c and 4.6d). The non-linear material behavior is considered to be influential at these penetration depths as strains are sufficiently high to result in significant deviation in the stress-strain relation from linear elastic material behavior.

A curve fit for particle contact force $f_p^{p^*}$ can be described by using a correction term for Hertz contact as follows,

$$f_p^{p^*}\left(\delta_p^*\right)=\frac{4}{3}\delta_p^{*3/2}-0.10\delta_p^{*2.89} \quad \text{for } 0<\delta_p^*<2 \tag{4.1}$$

In mixed contact regime (δ_p^* > 2), the penetration is measured with respect to displacement of deformable surface, $\delta_d\,(=\delta_p-2r_p)$, as depicted in Fig. 4.2c, which is non-dimensionalized as $\varepsilon_s=\delta_d/t_s$, with respect to thickness of deformable medium, t_s. This gives a measure of average compressive strain in deformable medium. In this contact regime, the rate of increase of contact force on particle, $f_p^{m^*}$ is smaller as shown in Fig. 4.4 due to the influence of direct contact. The contact force acting on particle in mixed contact regime, $f_p^{m^*}$ is expressed by using the following curve-fit relation,

$$f_p^{m^*}(\varepsilon_s)=\begin{cases} 5.4\left(\varepsilon_s\right)^{0.57}+3.12, & \text{for } \quad 0<\varepsilon_s<0.05 \\ 11.1\left(\varepsilon_s-0.05\right)^{0.90}+4.10, & \text{for } \quad 0.05<\varepsilon_s<0.2 \\ 40.94\left(\varepsilon_s-0.2\right)^2+13.14\left(\varepsilon_s-0.2\right)+6.11, & \text{for } \quad 0.2<\varepsilon_s<0.45 \end{cases} \tag{4.2}$$

The force carried by wafer-to-pad direct contact is determined by using influence radius, r_i^* and maximum direct contact pressure, $p_d^{m^*}$. Direct contact pressure, p_d^* varies along the contact interface as shown in Fig. 4.7a, for different average compression strain ε_s values. Direct contact pressure, p_d^* is zero at the outer edge of the particle contact region and increases gradually to its maximum, $p_d^{m^*}$. The influence radius, r_i^* is corrected to

take this transition region into account. The influence radius r_i^* is found by integrating p_d^* over direct contact interface to find the total direct contact force, which is then used to calculate the correction term to give the same contact force with pressure, $p_d^{m^*}$ as,

$$r_i^* = \frac{1}{p_d^{m^*}} \int_{r_i^*}^{r_o} p_d^* dr \tag{4.3}$$

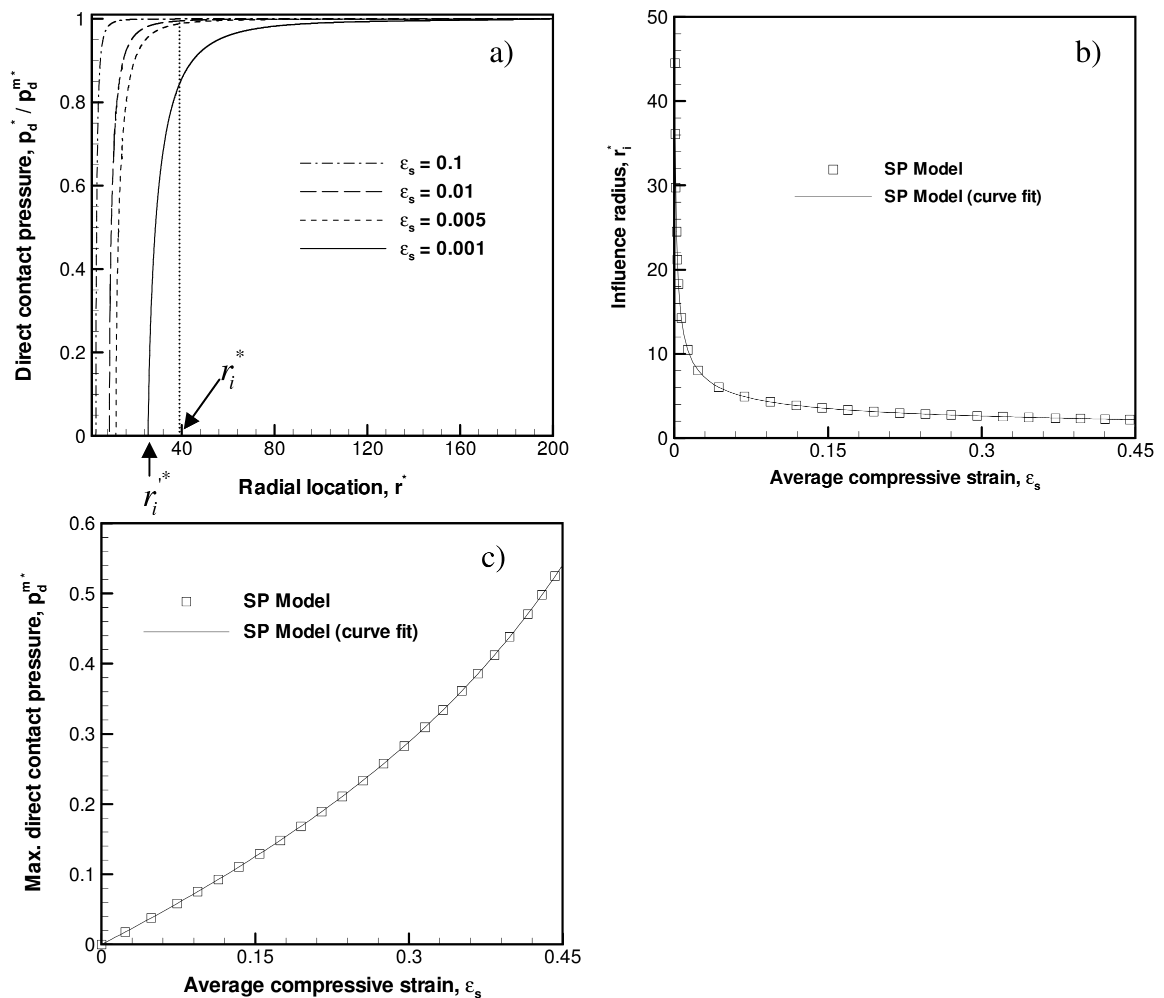

Fig. 4.7: a) The variation of the direct contact pressure, p_d^* along the contact interface for different penetration depths δ_p^*, obtained by FEA. b) influence radius r_i^* and c) maximum direct contact pressure, $p_d^{m^*}$ as a function of average compressive strain ε_s.

The influence radius, r_i^* thus found varies with average compressive strain ε_s as shown in Fig. 4.7b and it can be curve-fit to the following relation,

$$r_i^*(\varepsilon_s) = 1.52(\varepsilon_s)^{-0.45} \quad \text{for } 0 < \varepsilon_s < 0.45 \tag{4.4}$$

The maximum contact pressure, $p_d^{m^*}$ increases linearly with penetration into the deformable pad for small pad compression, ε_s values, and it becomes eventually non-linear at large ε_s as shown in Fig. 4.7c. The variation of maximum contact pressure, $p_d^{m^*}$ can be described by the following curve-fit equations,

$$p_d^{m^*}(\varepsilon_s) = \begin{cases} 0.76\varepsilon_s, & \text{for} \quad 0 < \varepsilon_s < 0.015 \\ 0.85(\varepsilon_s - 0.015) + 0.011, & \text{for} \quad 0.015 < \varepsilon_s < 0.2 \\ 1.8(\varepsilon_s - 0.2)^{1.16} + 0.17, & \text{for} \quad 0.2 < \varepsilon_s < 0.45 \end{cases} \tag{4.5}$$

4.4 Multi-Particle (MP) Contact Model

The contact of a rigid-flat surface with a deformable-flat surface is considered when there are rigid spherical particles with different sizes entrapped in the interface. Such a condition is depicted in Fig. 4.8. Mean particle radius μ_p, standard deviation of the particle radii σ_p, and probability density function (PDF) of particle radii $\tilde{\Phi}_p(\tilde{r}_p)$ are assumed to be known. In this interface, the light external forces are transmitted between two surfaces by particle contacts; and, direct contact of surfaces occurs as the external force is increased. Therefore, the mean contact pressure, $\tilde{p}_c^{mp}$, is defined as follows,

$$\tilde{p}_c^{mp} = \begin{cases} \tilde{p}_p^{mp-p} & \text{if } \tilde{d}_{sep} > 0 \\ \tilde{p}_p^{mp-m} + \tilde{p}_d^{mp} & \text{if } \tilde{d}_{sep} < 0 \end{cases} \tag{4.6}$$

where $\tilde{d}_{sep}$ is the separation of the two surfaces as defined in Fig. 4.8, $\tilde{p}_p^{mp-p}$ is the mean contact pressure for the particle contact regime (Fig. 4.8b), and $\tilde{p}_p^{mp-m}$ and $\tilde{p}_d^{mp}$ are the mean contact pressure acting on particles and the direct wafer-to-pad contact pressure in the mixed contact regime (Fig. 4.8c), respectively. As in the SP contact model, the contact interactions are characterized with respect to approach of two surfaces $\tilde{d}_{sep}$ in particle contact regime, and with respect to average compressive strain $\varepsilon_p = d_{sep} / t_s$ in direct contact regime, where t_s is the thickness of deformable medium. The particle contact regime is computed in the range $0 < \tilde{d}_{sep} < 12$. The mixed contact regime, which is encountered when $\tilde{d}_{sep} < 0$, is evaluated in the range $-0.45 < \varepsilon_p < 0$. Note that average compressive strain ε_p is negative in the MP contact model due to the definition of separation distance $\tilde{d}_{sep}$ as shown in Fig. 4.8.

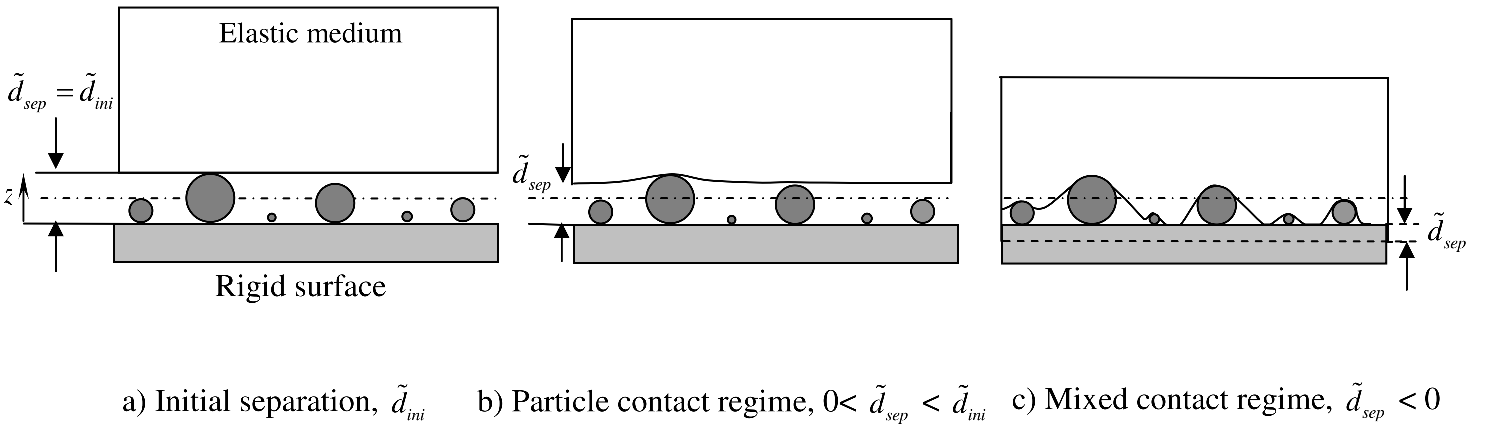

a) Initial separation, $\tilde{d}_{ini}$ b) Particle contact regime, $0 < \tilde{d}_{sep} < \tilde{d}_{ini}$ c) Mixed contact regime, $\tilde{d}_{sep} < 0$

Fig. 4.8: The multi-particle (MP) contact model.

4.4.1 Number of active particles

Only a fraction of particles in the slurry are trapped between the surfaces and become active in contact at a given separation distance, $\tilde{d}_{sep}$ (Fig. 4.8a). In the particle contact regime, as separation distance $\tilde{d}_{sep}$ decreases, more particles get trapped between the surfaces and become active (participate) in contact (Fig. 4.8a). Particles with diameter ($2\tilde{r}_p$) larger than separation distance, $\tilde{d}_{sep}$ are considered to be captured in the contact interface, whereas smaller particles can move freely between the surfaces [2]. The number of particles per unit area $\tilde{\eta}_a^{mp}$ which are active in contact can be found from volumetric particle concentration $\tilde{\eta}_v$ and the available volume $\tilde{V} = A_u \tilde{d}_{sep}$ between surfaces, using $\tilde{\eta}_a^{mp} = \tilde{\eta}_v \tilde{V}$ where $A_u = 1$ for unit area. However, one needs to consider that the separation distance $\tilde{d}_{sep}$ at which a particle becomes active depends on the size of the particle, $\tilde{d}_{sep} = 2\tilde{r}_p$. Therefore number of active particles, $\tilde{\eta}_a^{mp}$ at a separation distance, $\tilde{d}_{sep}$ can be obtained by the summation of $\tilde{\eta}_a^{mp}$ becoming active at larger $\tilde{d}_{sep}$. Using the PDF, $\tilde{\Phi}_p(\tilde{r}_p)$ of particle radii, this summation gives,

$$\tilde{\eta}_a^{mp}(\tilde{d}_{sep}) = \tilde{\eta}_v \int_{\frac{\tilde{d}_{sep}}{2}}^{\infty} 2\tilde{r}_p \tilde{\Phi}_p(\tilde{r}_p) d\tilde{r}_p \qquad (4.7)$$

In the mixed contact regime, where pad and wafer also engage in contact, the number of active particles $\tilde{\eta}_a^{mp-m}$, is considered to be constant and is calculated by setting $\tilde{d}_{sep} = 0$ in Eqn (4.7).

Particle concentration by weight-ratio η_w (also called as solids loading in CMP) is the common measure used for slurries for quantifying amount of particles in slurry and can be converted to volumetric particle concentration, $\tilde{\eta}_v$ for spherical particles by using the following relation,

$$\tilde{\eta}_v = \frac{\rho_s}{\rho_p} \frac{\eta_w}{\int_0^{\infty} \frac{4}{3} \pi \tilde{r}_p^3 \tilde{\Phi}_p \left(\tilde{r}_p \right) d\tilde{r}_p} \qquad (4.8)$$

where ρ_p and ρ_s are the mass densities of the particles and slurry, respectively. As a result of non-dimensionalization of variables in Eqn (4.7) and (4.8), areal η_a^{mp}, and volumetric η_v particle densities can be non-dimensionalized, respectively as $\tilde{\eta}_a^{mp} = \eta_a^{mp} {\sigma_p}^2$ and $\tilde{\eta}_v = \eta_v {\sigma_p}^3$.

4.4.2 Particle contact regime

In the case of contact of two rough surfaces, Greenwood and Williamson (GW) model (Section 3.1.2) shows that number of asperities that are in contact n_s and nominal pressure p_o between two rough surfaces separated by a distance d_{sep} can be found as follows [3],

$$n_s = \eta_s \int_{d_{sep}}^{\infty} \Phi_s(z_s) dz_s \quad \text{and} \quad p_o = \eta_s \int_{d_{sep}}^{\infty} f_c^s(\delta_o^s) \Phi_s(z_s) dz_s \,, \qquad (4.9)$$

where $\delta_o^s = z_s - d_{sep}$ is penetration of each asperity, $f_c^s(\delta_o^s)$ is a function describing load-displacement behavior of a single asperity, z is asperity height, $\Phi_s(z_s)$ is probability density function (PDF) of asperity summit heights, and η_s is number of asperities per unit area. In this work, the contact between particles and two surfaces is modeled by replacing asperities of rough surface with interfacial particles. This requires interchanging asperity height with particle radius, $z_s = 2r_p$, as shown in Fig. 4.9. Then, the non-dimensional penetration depth of each particle, as defined in the SP contact model, becomes $\delta_p^* = (2r_p - d_{sep}) / r_p$. By using number of the active particles, $\tilde{\eta}_a^{mp}(\tilde{d}_{sep})$ from Eqn (4.7), the load-displacement function of a single particle in particle contact regime $f_p^{p^*}$ from Eqn. (4.1), and the PDF of particle radii $\tilde{\Phi}_p$, the mean particle contact pressure, $\tilde{p}_p^{mp-p}$, due to the particles caught in the interface of two flat surfaces can be found as follows,

$$\tilde{p}_p^{mp-p} = \tilde{\eta}_v \int_{\frac{\tilde{d}_{sep}}{2}}^{\infty} 2\tilde{r}_p \tilde{f}_p^{p}(\tilde{\delta}_p)\tilde{\Phi}_p(\tilde{r}_p) d\tilde{r}_p \quad \text{for } \tilde{d}_{sep} > 0 \tag{4.10}$$

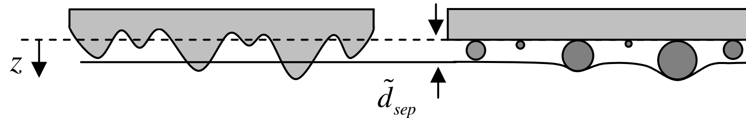

Fig. 4.9: Asperity-particle analogy in the MP contact model.

4.4.3 Mixed contact regime

The mean contact pressure $\tilde{p}_p^{mp-m}$ due to particle contacts in the mixed contact regime ($\tilde{d}_{sep} < 0$) is found in a way similar to Eqn. (4.10), by using Eqn. (4.2) for $\tilde{f}_p^m$, and by taking lower limit of the integral as 0, as number of active particles, $\tilde{\eta}_a^{mp-m}$ is constant in this regime. Note that force acting on particles $\tilde{f}_p^m$ in the SP contact model is expressed in terms of average compressive strain ε_s of deformable medium, which becomes $\varepsilon_p = d_{sep} / t_s$ in mixed contact regime of the MP contact model. The mean contact pressure $\tilde{p}_p^{mp-m}$ due to particle contacts in the mixed contact regime is then found as follows,

$$\tilde{p}_p^{mp-m} = \tilde{\eta}_v \int_0^\infty 2\tilde{r}_p \tilde{f}_p^m(-\varepsilon_p)\tilde{\Phi}_p(\tilde{r}_p)d\tilde{r}_p \quad \text{for } \tilde{d}_{sep} < 0 \qquad (4.11)$$

Note that a "–" sign is introduced in Eqn. (4.11) and following ones, for using ε_p, as compressive strain is defined negative in the MP contact model, but positive in the SP contact model.

The computation of direct contact pressure $\tilde{p}_d^{mp}$ requires knowledge on direct contact area A_d^{mp} = 1 - A_i, where A_i is *total influence area* shown in Fig. 4.2c for a single particle. The total influence area of particles as a fraction of total area, A_i can be found by the summation of the influence areas of individual particles $\pi\tilde{r}_i^2$ (Fig. 4.10) as follows,

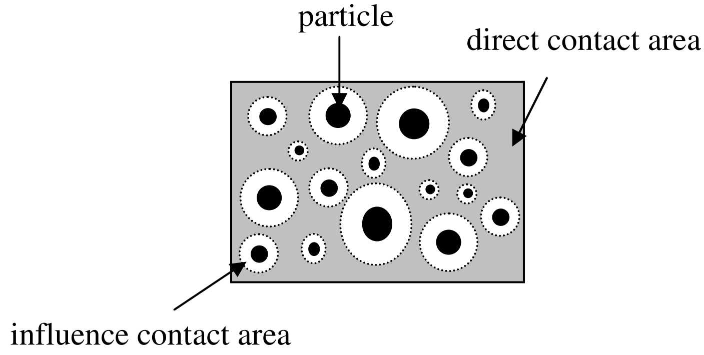

Fig. 4.10: Influence A_i^{mp} and direct A_d^{mp} contact areas

$$A_i^{mp} = \tilde{\eta}_v \int_0^{\infty} 2\tilde{r}_p \pi \tilde{r}_i^2 (-\varepsilon_p) \tilde{\Phi}_p(\tilde{r}_p) d\tilde{r}_p \tag{4.12}$$

where $\tilde{r}_i$ is given by Eqn. (4.4). The direct contact area ratio A_d^{mp} increases as two contacting surfaces are pushed further into each other in mixed contact regime $\tilde{d}_{sep} < 0$ (Fig. 4.8c). The direct contact area consists of small areas on the (originally) flat surface which engage in contact at different levels of compression ε_p. For a given amount of compression ε_p, each particle creates a different contact area, which should be added for all particles to give $A_d^{mp}(\varepsilon_p) = 1 - A_i^{mp}(\varepsilon_p)$, using Eqn. (4.12). Therefore, direct contact pressure, $\tilde{p}_d^{mp}$ is not uniform and depends on local compression of each direct contact area. As the compression of pad, ε_p is increased, the sections coming into initial contact start to experience low pressure, whereas the sections that have already been in direct contact accumulate more pressure. This cumulative effect is expressed by using the following relation for direct contact pressure $\tilde{p}_d^{mp}$,

$$\tilde{p}_d^{mp} = \int_{\varepsilon_p^m}^{\varepsilon_p} \tilde{p}_d^m \left(\varepsilon_p^r - \varepsilon_p\right) \frac{dA_d^{mp}}{d\varepsilon_p^r} d\varepsilon_p^r \tag{4.13}$$

Fig. 4.11 shows a typical (calculated) variation of A_d^{mp} with ε_p, where it can be seen that direct contact starts at a threshold strain ε_p^m, where $A_d^{mp}(\varepsilon_p^m) = 0$.

4.4.4 Influence factor

The number of active particles $\tilde{\eta}_a^{mp}$ is shown, in Eqn. (4.7), to depend on particle size $\tilde{r}_p$ and separation distance $\tilde{d}_{sep}$. In fact, another factor which influences this density is the distribution of particles in horizontal plane. The effect of horizontal inter-particle spacing $\tilde{d}_s$ on density of active particles $\tilde{\eta}_a^{mp}$ is analyzed next. Fig. 4.12a shows an idealized configuration of seven identical particles, assuming that particles are evenly spaced at the corners of a hexagon. There are a total of 3 particles in the hexagon, which has a non-dimensional area of $\tilde{A}_h = 3\sqrt{3}\tilde{d}_s^{\,2}/2$. In this case, particle density, $\tilde{\eta}_a^{mp}$ can be related to

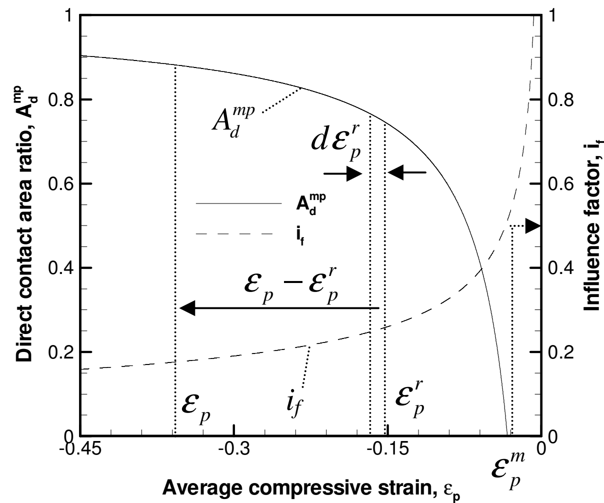

Fig. 4.11: The variation of direct contact area ratio A_d^{mp} and influence factor i_f with average compressive strain ε_p.

mean spacing between particles, $\tilde{d}_s$ as,

$$\tilde{\eta}_a^{mp} = \frac{3}{\tilde{A}_h} = \frac{2}{\sqrt{3}\tilde{d}_s^{\,2}} \quad \text{or} \quad \tilde{d}_s = \sqrt{\frac{2}{\sqrt{3}\tilde{\eta}_a^{mp}}} \tag{4.14}$$

For a more generic particle configuration, $\tilde{d}_s$ can be generalized as,

$$\tilde{d}_s = \sqrt{\frac{1}{C_p \tilde{\eta}_a^{mp}}} \tag{4.15}$$

where C_p is a constant, which will depend on the relative distances between a group of particles. Mean influence radius of the particles, $\tilde{r}_i^m$ is calculated by,

$$\tilde{r}_i^m = \frac{\tilde{\eta}_v}{\tilde{\eta}_a^{mp-m}} \int_0^\infty 2\tilde{r}_p \tilde{r}_i(-\tilde{\varepsilon}_p)\tilde{\Phi}_p(\tilde{r}_p) d\tilde{r}_p \tag{4.16}$$

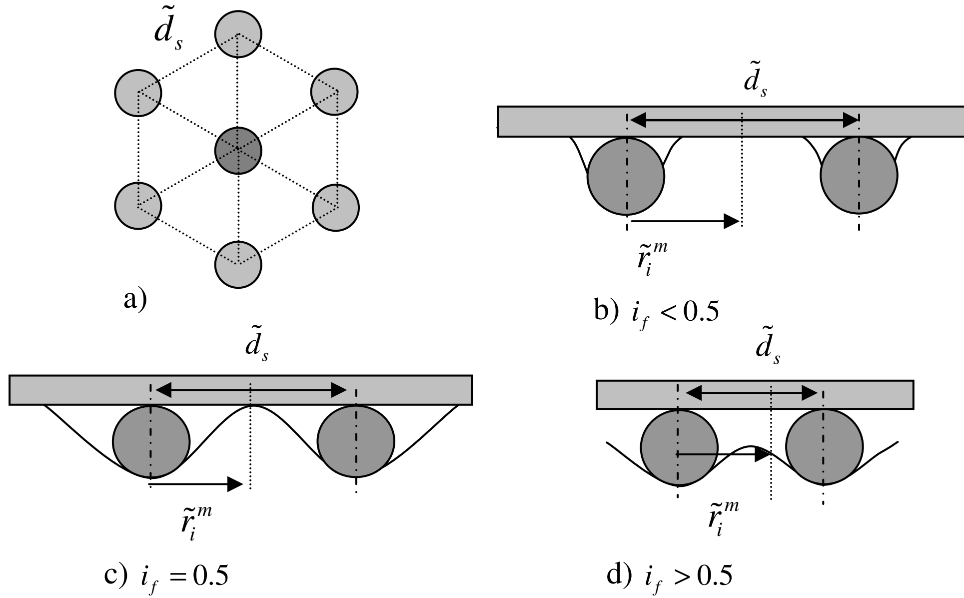

Fig. 4.12: a) Top view of a particle and its six neighbors. b)-d) different levels of influence factor, i_f.

Influence factor, i_f characterizes overlap of influence areas between particles and defined by the following equation,

$$i_f = \frac{\tilde{r}_i^m}{\tilde{d}_s} \tag{4.17}$$

Note that in order for the MP contact model described in this work to be accurate, mean *influence radius* $\tilde{r}_i^m$ should be greater than $\tilde{d}_s / 2$ ($i_f < 0.5$) as schematically demonstrated in Figs. 4.12b-d. Particles start to interact when $i_f = 0.5$, which corresponds to the separation distance at which direct contact area ratio A_d^{mp} starts to grow as shown in Fig. 4.11. As influence factor, i_f becomes larger, the interaction between particles becomes more significant and the error of the model increases.

4.4.5 Multi-particle contact model relations

<u>Effect of particle concentration</u>

The effect of particle concentration, η_w on the contact conditions in the multi-particle (MP) contact model is investigated next. The relation between concentrations based on weight η_w and volume $\tilde{\eta}_v$ of particles is given in Eqn (4.8). For a slurry with alumina particles, particle and slurry density are related by $\rho_p / \rho_s = 3.7$. The effects of different particle concentration η_w are investigated in the range 1.25% < η_w < 5%, and for mean particle radius of $\tilde{\mu}_p = 4$. PDF for particle size $\tilde{\Phi}_p$ is assumed to be Gaussian and is given as follows,

$$\tilde{\Phi}_p\left(\tilde{r}_p\right)=\frac{1}{\sqrt{2\pi}}e^{-\frac{\left(\tilde{r}_p-\tilde{\mu}_p\right)^2}{2}} \tag{4.18}$$

Fig. 4.13a shows the variation of mean contact pressure $\tilde{p}_c^{mp}$ for different separation distances $\tilde{d}_{sep}$. In the range, where $0 < \tilde{d}_{sep} < 12$, applied load is transferred through particles, and Eqns. (4.6) and (4.10) apply. In this range, the mean contact pressure $\tilde{p}_c^{mp}$ increases rapidly as separation distance $\tilde{d}_{sep}$ approaches 0. This figure also demonstrates that for a given separation distance $\tilde{d}_{sep}$, the mean contact pressure $\tilde{p}_c^{mp}$ increases with higher particle concentration η_w. For example, when $\tilde{d}_{sep} = 0$, $\tilde{p}_c^{mp}$ is found to be 0.005, 0.01 and 0.02 for η_w = 1.25, 2.5 and 5%, respectively.

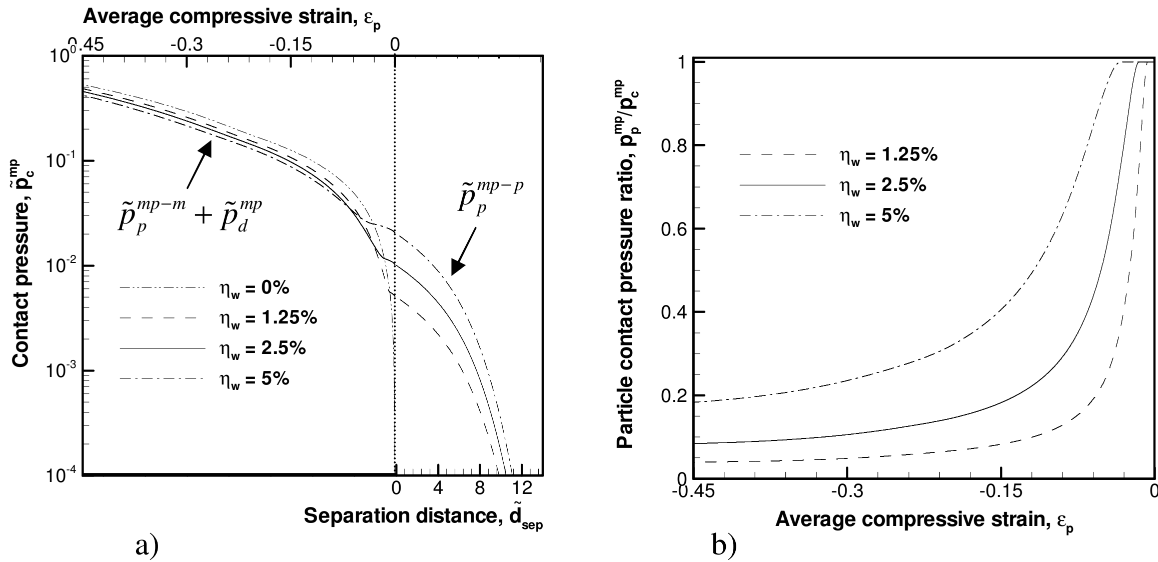

Fig. 4.13: a) The contact pressure, $\tilde{p}_c^{mp}$ in particle ($\tilde{p}_p^{mp-p}$) and mixed ($\tilde{p}_p^{mp-p} + \tilde{p}_d^{mp}$) contact regimes for different particle concentrations, η_w = 1.25%, 2.5% and 5%, and b) particle contact pressure ratio p_p^{mp-m} / p_c^{mp} .

Mixed contact regime is investigated in the range of average compressive strain, -0.45 < ε_p < 0, in Fig. 4.13a, where mean contact pressure $\tilde{p}_c^{mp}$ is computed by using Eqns (4.6), (4.11) and (4.13). In this regime, number of active particles $\tilde{\eta}_a^{mp-m}$ remains constant, however penetration of each particle increases, and direct contact starts to occur with increasing compression ε_p. Combination of these effects causes mean contact pressure, $\tilde{p}_c^{mp}$ to increase. At large compression ε_p, mean contact pressure $\tilde{p}_c^{mp}$ depends predominantly on direct wafer-to-pad contact. On the other hand, when separation distance is near zero, a transition region exists where only particle contacts support the surfaces even though $\tilde{d}_{sep} < 0$. The fraction of mean particle contact pressure to total contact pressure, p_p^{mp-m} / p_c^{mp} as a function of compression ε_p is shown in Fig. 4.13b. This figure shows that in the mixed contact regime, as compression ε_p increases, the fraction of force carried by particle contacts decreases. This figure also shows that direct contact does not occur until a critical value, ε_p^m is reached. *Transition region* is, therefore, defined as $\varepsilon_p^m < \varepsilon_p < 0$. In transition region, the mean contact pressure, $\tilde{p}_c^{mp}$ is nearly constant, as contact is entirely enabled by particles. Beyond transition region, the mean contact pressure $\tilde{p}_c^{mp}$ (Fig. 4.13a) increases almost linearly with the pad compression, ε_p, much like in Eqn. (4.5). The critical compression values ε_p^m are approximately -0.007, -0.015, and -0.033 for particle concentrations, η_w = 1.25, 2.5 and 5%, respectively. At high particle concentrations η_w, the fact that there are more particles in the interface, retards the formation of direct contacts and allows particle contacts to support the load for deeper penetrations.

Fig. 4.14 shows direct contact area ratio A_d^{mp} (= 1 − A_i) computed from Eqn. (4.12), and influence factor i_f computed by using Eqn. (4.17). It is seen that direct contact area ratio A_d^{mp} is zero in transition region. As pad is compressed further ($\varepsilon_p \rightarrow -0.45$) mixed contact is established; direct contact area ratio A_d^{mp} increases rapidly with compression ε_p, gradually leveling off. Note that it appears that direct contact area ratio A_d^{mp} will level off to a value less than one, as part of the contact area is composed of spherical particles with influence contact area, A_i^{mp}. This figure also shows that for particle concentrations chosen here, influence factor i_f < 0.5 in the mixed contact regime indicating that influence areas of the particles are well separated.

The variation of number of active particles, $\tilde{\eta}_a^{mp}$ is plotted as a function of separation distance, $\tilde{d}_{sep}$ in the particle contact regime (Fig. 4.15). More particles get captured in

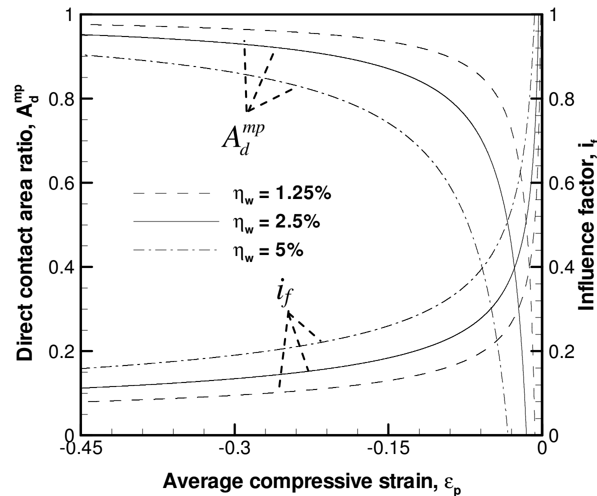

Fig. 4.14: The direct contact area ratio, A_d^{mp} and influence factor, i_f in mixed contact regime for different particle concentrations, η_w = 1.25%, 2.5% and 5%

contact as separation distance increases as expected. The mean contact pressure, $\tilde{p}_c^{mp}$ starts to increase as largest particle becomes active, which occurs at a separation distance equal to largest particle diameter, $\tilde{d}_{sep} \approx 2\left(\tilde{\mu}_p + 3\right)$. As separation distance, $\tilde{d}_{sep}$ approaches 0, number of active particles, $\tilde{\eta}_a^{mp}$ levels off. In fact, number of active particles, $\tilde{\eta}_a^{mp}$ remains constant in the mixed contact regime.

Effect of particle size

The results of the MP contact model do not depend on particle size σ_p*. The number of active particles is inversely proportional to particle size as, $\eta_a^{mp} \propto 1/\sigma_p^2$ while the single particle contact force varies as, $f_p \propto \sigma_p^2$. The number of active particles, η_a^{mp} decreases

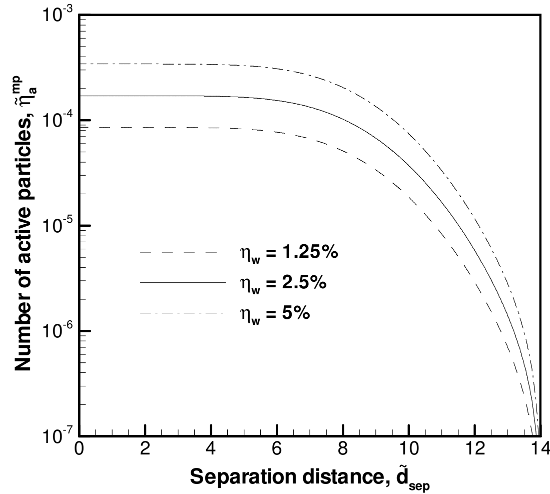

Fig. 4.15: The number of active particles in pure particle contact regime, $\tilde{\eta}_a^{mp}$. Note that number of active particles in mixed contact regime, $\tilde{\eta}_a^{mp-m} = \tilde{\eta}_a^{mp}\left(d_{sep} = 0\right)$.

---

* Note that the mean particle size μ_p is related to the standard deviation σ_p with the relationship, $\mu_p / \sigma_p = 4$.

as particles become larger (σ_p increases) but the contact force on each particle, f_p increases at the same rate. As a result, these two effects offset each other and the particle contact pressure, $\tilde{p}_p^{mp}$ remains constant. A similar argument can be made for the direct contact area ratio A_d^{mp} due to the fact that influence contact area of each particle, $\pi\tilde{r}_i^2$ increases as $\pi\tilde{r}_i^2 \propto \sigma_p^2$, which offsets the effect of decreasing number of active particles, η_a^{mp} as with larger particle size, σ_p. The only parameter that depends on particle size is the separation distance, d_{sep}. As particles becomes larger, particle starts to get engaged in contact and contact pressure, $\tilde{p}_c^{mp}$ develops at a greater separation distance, d_{sep}.

4.5 Single Asperity (SA) Contact Model

The single asperity (SA) contact model, where the contact of a spherical asperity with a flat deformable surface in the presence of rigid spherical particles entrapped in the asperity-flat-surface interface as shown in Fig. 4.1b, is analyzed. While the asperity considered in the SA contact model is made of a hyperelastic solid, it actually endures small deformations which are in the linear range of hyperelastic material behavior, as shown in Fig. 3.11. Therefore, no generality is lost when bulk deformation behavior of the system is represented by modeling asperity as a rigid sphere, and flat surface as a deformable medium [4].

4.5.1 Solution approach

A schematic description of the SA contact interface, shown in Fig. 4.16, assumes that a spherical asperity tip can be approximated as a parabola near the contact region.

Therefore, the local separation $\tilde{u}$ along radial direction $\tilde{\rho}$ can be approximated as $\tilde{u} = \tilde{u}_o + \tilde{\rho}^2 / 2\tilde{R}_s$, where $\tilde{u}_o$ is separation distance at the center of contact and $\tilde{R}_s$ is bulk radius of asperity. Considering the elastic deformation of deformable medium $\tilde{w}_b$, the relation for the local separation is expressed as [4],

$$\tilde{u} = \tilde{u}_o + \frac{\tilde{\rho}^2}{2\tilde{R}_s} + \tilde{w}_b \tag{4.19}$$

The diameter of a pad asperity is three orders of magnitude larger than the mean particle diameter, and the number of particles entrapped under deformed asperity is shown to be more than 100 as demonstrated later in Section 4.5.3. This situation is very similar to the elastic contact of rough spheres analyzed by Greenwood and Tripp [4] (Section 3.1.3). In this work, the effect of particles trapped in the interface is represented by introducing a "contact-layer" (Fig. 4.16) whose deformation behavior has been introduced in the multi-particle (MP) contact model, in Section 4.4. This layer is responsible for transferring the forces between the two surfaces considering the rough contact behavior at local contact.

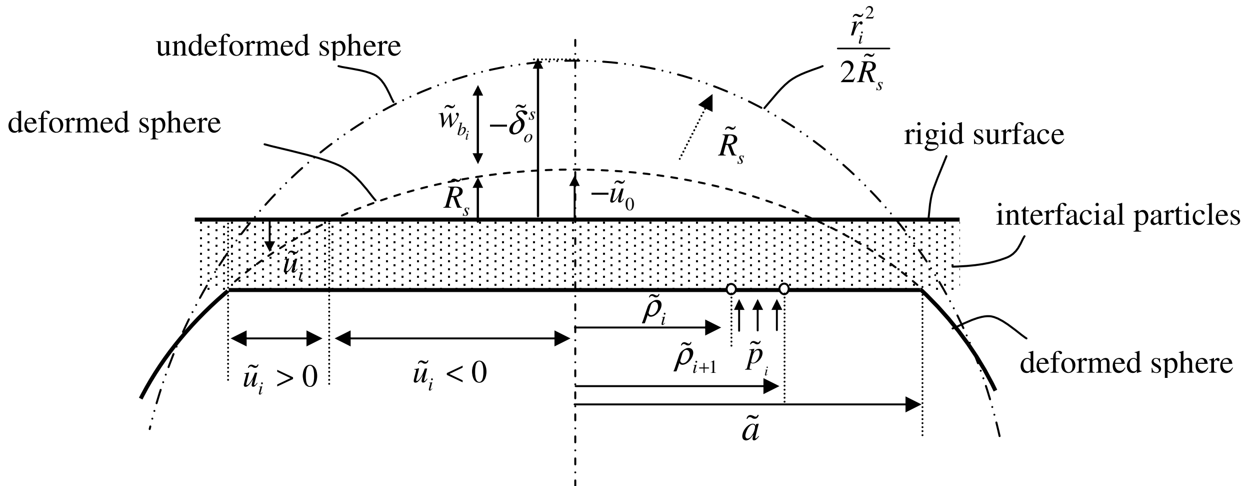

Fig. 4.16: Single asperity (SA) contact interface

The circular contact interface is divided into annular contact segments as shown in Fig. 4.16. Each contact segment is bound by the inner radius, $\tilde{\rho}_i$ and the outer radius $\tilde{\rho}_{i+1}$. The contact segments interact with each other through bulk deformation of deformable medium $\tilde{w}_{b_i}$. An axisymmetric FE model of deformable medium is constructed to obtain bulk deformation $\tilde{w}_{b_i}$ induced by local contact pressure, $\tilde{p}_i$ acting in each contact segment. Bulk deformation $\tilde{w}_{b_i}$ is determined by averaging the vertical displacement of nodes located at radial locations $\tilde{\rho}_i$ and $\tilde{\rho}_{i+1}$ in the FE model. Bulk deformation, $\tilde{w}_{b_i}$ is used to calculate local separation, $\tilde{u}_i$ which is then substituted into the MP contact model (Eqns. (4.10) – (4.13)) to obtain local contact pressure $\tilde{p}_i$. The equilibrium local contact pressure, $\tilde{p}_i$ is iteratively found by repeating these steps until contact force, $\tilde{f}_c^s$ converges.

Local contact pressure $\tilde{p}_i$ is found by using the MP contact model (Eqn. (4.6)) for a given local separation $\tilde{u}_i$. Note that particle contact pressure $\tilde{p}_p^s$ depends on local separation $\tilde{u}$ $(=\tilde{d}_{sep})$, whereas mixed contact pressure $\tilde{p}_p^s + \tilde{p}_d^s$ is a function of average compressive strain ε_p, and thus depends on layer thickness $\tilde{t}_s$. Therefore, a thickness value is required for the “contact-layer”, particularly where $\tilde{u}_i < 0$. The contact layer thickness is chosen by searching for the value of $\tilde{t}_s$ that minimizes the error between computed results and the exact solution for spherical contact (Hertz contact) by neglecting the effect of particles ($\eta_w = 0$) in mixed contact regime. Fig. 4.17 shows the deviation of computed maximum contact pressure $\tilde{p}_o^h$ with respect to Hertz contact

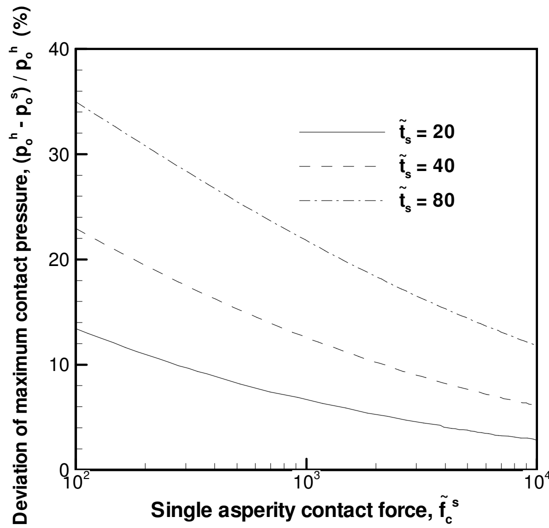

Fig. 4.17: The deviation of predicted maximum contact pressure by SA model, $\tilde{p}_o^s$ from Hertz contact, $\tilde{p}_o^H$ $\left(=\left(3\tilde{f}_c^s/(2\pi^3\tilde{R}_s^2)\right)^{1/3}\right), \left(\tilde{p}_o^H - \tilde{p}_o^s\right)/\tilde{p}_o^H$ utilizing different layer thickness $\tilde{t}_s$.

model $\tilde{p}_o^h = (3\tilde{f}_c^s/(2\pi^3\tilde{R}_s^2))^{1/3}$ for different values of layer thickness $\tilde{t}_s$. As expected, thinner layers give better predictions to Hertz contact, as in that case the compressive strain ε_p becomes large for a given separation $\tilde{u}$. However, computation times increase for thinner layers. It is in fact seen that, in mixed contact region, the "contact-layer" acts as a penalty parameter, used commonly in imposing contact conditions in FE analysis, but preserves particle contact behavior in particle contact region of the SA contact interface. Based on the accuracy of the solution and computation time, layer thickness $\tilde{t}_s$ = 20 is used in this study.

The deformable medium is discretized with 4,700, 4-noded axisymmetric elements (PLANE182). The mesh of deformable medium is finer near contact zone; in particular, element size is adjusted to be smaller near the outside edge of contact region as shown in Fig. 4.18, in order to compute contact radius $\tilde{a}$ accurately. Only bottom nodes of

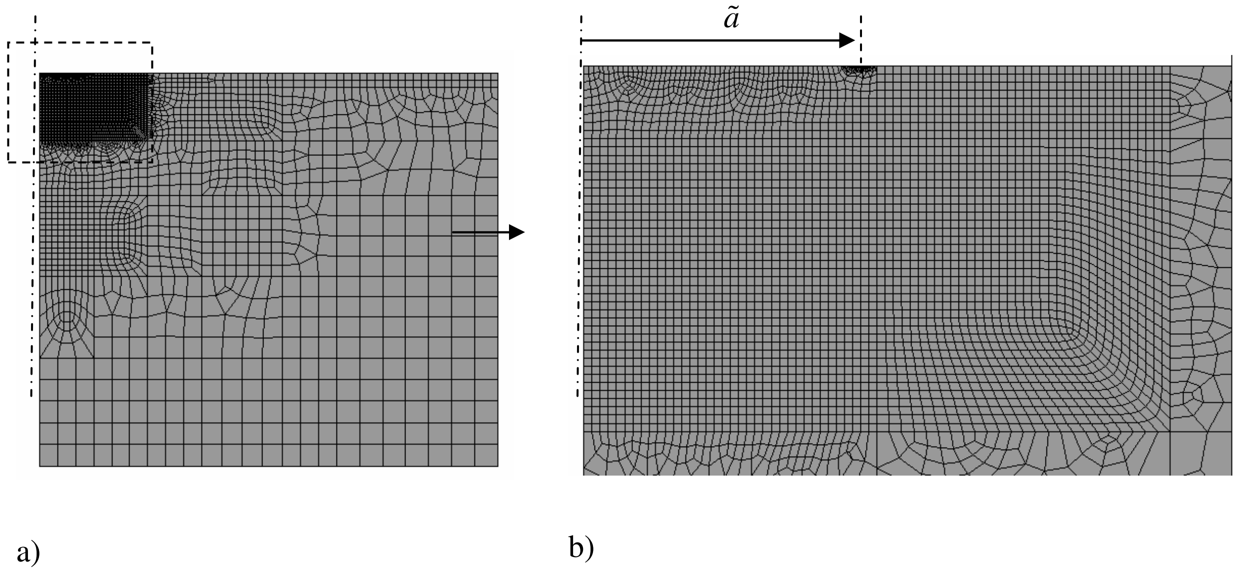

Fig. 4.18: Finite element mesh of the SA contact model near a) contact zone, b) contact radius, $\tilde{a}$.

deformable medium are constrained in the direction of bulk deformation, and all other boundaries are left free. Thickness and outer radius of deformable medium are taken as $7\tilde{a}$ and $8.5\tilde{a}$, respectively. These values are found by trial and error to be sufficiently large so that results are not influenced by remote boundary effects even for the largest applied loads.

The parameters of this model, which are non-dimensionalized as shown in Table 4.1, are mean particle size, μ_p, particle concentration, η_w and bulk radius of the asperity, $\tilde{R}_s$. Direct contact pressure, $\tilde{p}_d^s$, particle contact pressure, $\tilde{p}_p^s$, contact force, $\tilde{f}_c^s$, particle contact force, $\tilde{f}_p^s$, direct contact area, A_d^s and contact radius, $\tilde{a}$ are calculated for a given separation distance at the center of contact, $\tilde{u}_o$. The numerical algorithm (shown in Fig. 4.19) consisting of two main iteration steps employed to implement the outlined solution algorithm is explained as follows.

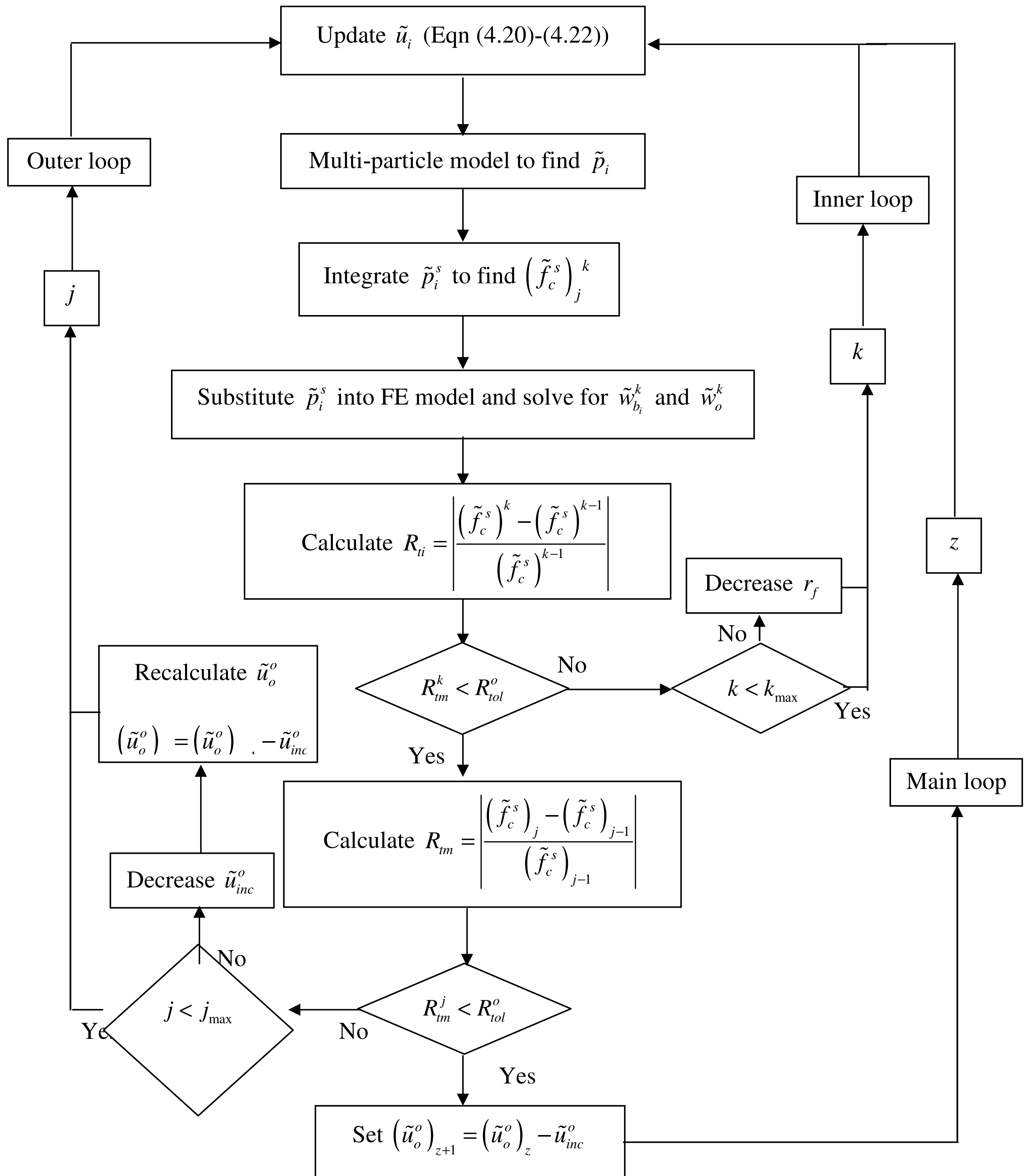

Fig. 4.19: Numerical algorithm used for the SA contact model

4.5.2 Solution algorithm

In the first iteration step controlled by the inner loop, the rigid part of separation distance, $\tilde{u}_i^{\,r}$ is fixed and the variable part, $\tilde{u}_i^{\,v}$ is updated using bulk deformation from the FE solution as,

$$\tilde{u}_i = \tilde{u}_i^{\,r} + \tilde{u}_i^{\,v} \tag{4.20}$$

where $\tilde{u}_i^{\,r}$ and $\tilde{u}_i^{\,v}$ for k^{th} iterative step of the inner loop are given as,

$$\left(\tilde{u}_i^{\,r}\right)^k = \tilde{u}_o + \frac{\tilde{\rho}_i^{\,2}}{2\tilde{R}_s} + \left(1 - r_f\right)\left(\tilde{w}_{b_i}^0 - \tilde{w}_{b_0}^0\right) \tag{4.21}$$

$$\left(\tilde{u}_i^{\,v}\right)^k = r_f\left(\tilde{w}_{b_i}^k - \tilde{w}_o^k\right) \tag{4.22}$$

The updated separation distance $\tilde{u}_i$ is substituted into the MP contact model to find local contact pressure $\left(\tilde{p}_c^s\right)_i$ acting in each contact segment (Eqns (4.10)-(4.13)). Local contact pressure $\left(\tilde{p}_c^s\right)_i$ is then applied on contact elements of FE model, which is solved to obtain bulk deformation $\tilde{w}_{b_i}$. Separation distance $\tilde{u}_i$ is calculated from updated bulk deformation $\tilde{w}_{b_i}$ using Eqn (4.20)-(4.22). Local contact pressure $\tilde{p}_i$ on contact elements is integrated to find contact force $\tilde{f}_c^s$. The inner loop ends as the variation of contact force $\tilde{f}_c^s$ between successive iterations, is smaller than the convergence tolerance for inner loop.

If solution does not converge as the number of iterations for inner loop, k exceeds the maximum number of iterations, k_{max} ($k > k_{max}$), separation distance, $\tilde{u}_i$ is re-calculated with a smaller relaxation factor, r_f in Eqns (4.21) and (4.22) so that the rigid part of separation distance $\tilde{u}_i^{\,r}$ becomes larger to enhance convergence behavior. Once convergence is obtained for inner loop $\tilde{u}_i^{\,r}$ is updated for the next iteration (j+1) of outer loop by using $\tilde{u}_i^{\,r}$ from the converged solution of (j-1)th and j^{th} step as,

$$\left(\tilde{u}_i^{\,r}\right)_{j+1} = \left(1-r_f\right)\left(\tilde{u}_i^{\,r}\right)_{j-1} + r_f\left(\tilde{u}_i^{\,r}\right)_j \tag{4.23}$$

Outer loop controls convergence behavior of contact force $\tilde{f}_c^{\,s}$ obtained from inner loop. If successive values of contact force $\tilde{f}_c^{\,s}$ from converged solution of inner loop varies within convergence tolerance, bulk deformation is assumed to be in equilibrium with contact pressure for a given separation distance at center of contact $\tilde{u}_o$. Once solution is obtained for direct contact pressure $\tilde{p}_d^{\,s}$, particle contact pressure $\tilde{p}_p^{\,s}$, contact radius $\tilde{a}$ using the converged bulk deformation $\tilde{w}_b$, the separation distance at center of contact $\tilde{u}_o$ is decreased with an increment $\tilde{u}_{inc}$.

The initial guess for the bulk deformation $\tilde{w}_{b_i}$ of the current step is taken from the converged solution of previous step. If convergence criteria cannot be satisfied in outer loop before the number of iterations for outer loop j becomes large ($j > j_{max}$), the increment $\tilde{u}_{inc}$ is decreased and outer loop is restarted with a new separation distance at the center of contact $\tilde{u}_o$ in the main loop. In the 1st step, contact force $\tilde{f}_c^{\,s}$ is small enough

to ensure convergence even when the initial guess for bulk deformation $\tilde{w}_{b_i}$ is taken to be 0.

Convergence rate is high for small contact force (small penetration depth) even when the initial guess for bulk deformation is taken to be $\tilde{w}_{b_i}$ = 0. However as penetration depth is increased, convergence behavior rapidly changes. Convergence for large penetration depths is achieved by improving the initial guess for the bulk deformation $\tilde{w}_{b_i}$. The initial guess for bulk deformation $\tilde{w}_{b_i}$ of each iteration is obtained from the previous iteration. This approach improves convergence behavior; however, convergence problems can still be encountered when penetration depth is further increased. In order to enhance convergence behavior, the rigid part of separation distance is not assumed to be spherical but a new shape is interpolated considering the bulk deformation $\tilde{w}_{b_i}$ from the previous iteration. A relaxation factor r_f, which is defined as the fraction of bulk deformation $\tilde{w}_{b_i}$ that is used for the variable part of separation distance is utilized. Relaxation factor r_f is reduced at large penetration depths to achieve convergence, with the cost of increased computation times.

4.5.3 Effect of interfacial particles on single asperity contact

The non-dimensional values of parameters studied here (Table 4.3) are chosen to reflect the physical ranges listed in Table 4.2. In the SA contact model, the separation distance at the center of contact $\tilde{u}_o$ is decreased with increments of $\tilde{u}_{inc}$ = 0.02. The initial value of relaxation factor r_f is 0.8 and gradually decreased to r_f = 0.025 as penetration is increased

(or separation distance is decreased) in order to achieve convergence, as controlled by numerical algorithm in Section 4.5.2.

Strain distribution in the SA contact model

One of the assumptions employed in the SA contact model is that bulk deformation $\tilde{w}_b$ of asperity is small such that resultant strains are in the range where material behavior is linear. This assumption is verified in Fig. 4.20 showing the von Mises strain ε_{eq} distribution in deformable medium at different contact force $\tilde{f}_c^s$. The maximum strain of $\varepsilon_{eq} \approx 0.08$ is found for high contact force, $\tilde{f}_c^s = 10^6$. This value for maximum strain is well-below the critical strain value ($\varepsilon_{eq} \approx 0.5$) at which material behavior becomes non-linear as shown in Fig. 3.11

Number of active particles in the SA interface

In the MP contact model, it was shown that the contribution of particle contacts to the overall force balance depends on number of active particles in contact with each asperity n_a^s. The SA contact model implicitly assumes that large number of particles is present at each asperity contact interface, so that the statistical definition of particle size distribution and the averaging of particle effects used in the model are justified. Therefore, it is important to evaluate number of active particles n_a^s in single asperity contact interface. This variable is computed by summing the number of particles trapped in each contact segment in the SA contact model by using the relation, $n_a^s = \sum_i^N \pi(\tilde{\rho}_{i+1}^2 - \tilde{\rho}_i^2)\tilde{\eta}_{ai}$, where non-dimensionalized concentration of active particles $\tilde{\eta}_{ai}$ for each contact segment is

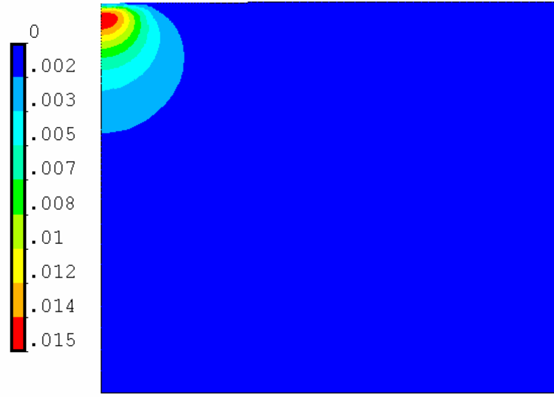

a) $\tilde{f}_c^s = 10^4$

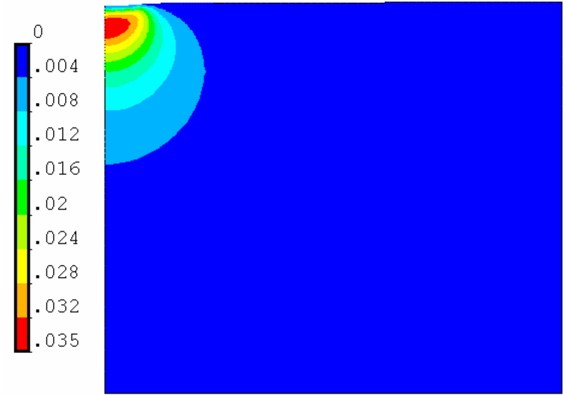

b) $\tilde{f}_c^s = 10^5$

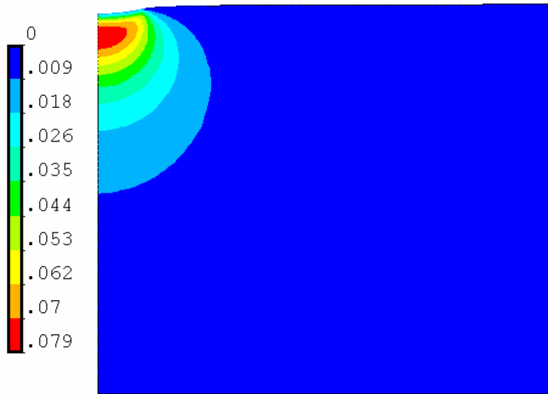

b) $\tilde{f}_c^s = 10^6$

Fig. 4.20: Von Mises strain ε_{eq} distribution in the SA contact model for different contact force $\tilde{f}_c^s$.

computed by using Eqn. (4.7) with lower limit of the integral as separation distance $\tilde{u}_i$ value used in Eqn. (4.19). Note that particle contact force $\tilde{p}_p^s$ and direct contact area $\tilde{A}_d^s$ are computed similarly, by using Eqns (4.6) and (4.12), respectively. Fig. 4.21 shows that number of active particles n_a^s in single asperity contact interface increases with particle concentration η_w and asperity radius, $\tilde{R}_s$ as expected. It should be noted that number of

active particles n_a^s remains greater than n_a^s > 30 for all particle concentration η_w and asperity radius $\tilde{R}_s$ studied when contact force, $\tilde{f}_c^s$ > 10^3 and n_a^s > 100 when $\tilde{f}_c^s$ > 10^4.

Effect of particles on contact interface

The computed contact pressure $\tilde{p}_c^s$ distribution in the asperity contact interface is plotted in Fig. 4.22, for three different values of contact force, $\tilde{f}_c^s$ = 10^3, 10^4 and 10^5. In Fig. 4.22a-b, it is seen that the presence of rigid particles in contact interface causes a significant deviation of contact pressure distribution from Hertz contact, when contact force is low $\tilde{f}_c^s = 10^3$ or $\tilde{f}_c^s = 10^4$. Particle concentration η_w has an important effect on this distribution. Fig. 4.22a-b also shows that contact area is predicted to be larger than that of Hertz contact when particles are involved in contact. In fact, this effect causes a reduction in the maximum contact pressure at center of contact $\tilde{p}_o^s$. The effect of particle

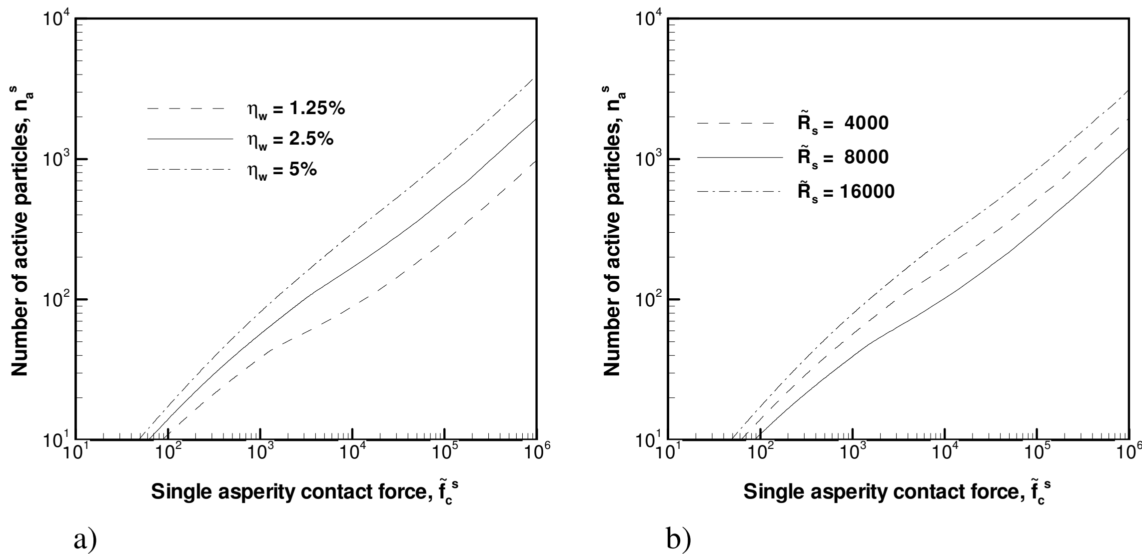

Fig. 4.21: The effect of a) particle concentration η_w and b) asperity radius $\tilde{R}_s$ on number of active particles n_a^s in single asperity contact.

concentration η_w on the deviation from Hertz contact is different for low and intermediate contact force $\tilde{f}_c^s = 10^3$ and $\tilde{f}_c^s = 10^4$ due to different regimes of contact operating at each $\tilde{f}_c^s$. Fig. 4.23a-b shows that the whole contact region is in the particle contact regime for low contact force, $\tilde{f}_c^s = 10^3$, while the outside edge of contact is in the

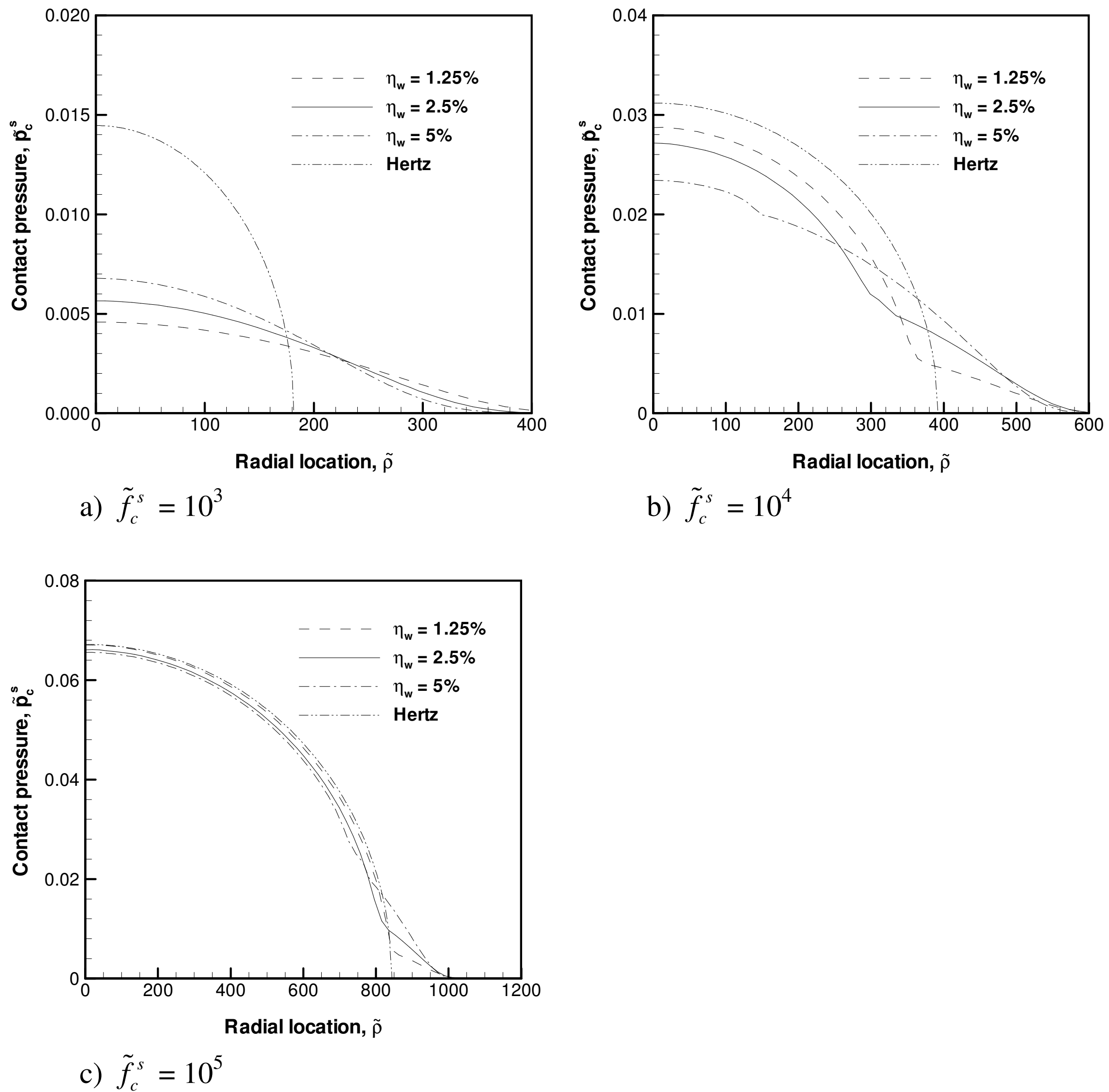

Fig. 4.22: The effect of particle concentration η_w on contact pressure distribution $\tilde{p}_c^s$ at different contact force, a) $\tilde{f}_c^s = 10^3$, b) $\tilde{f}_c^s = 10^4$ and c) $\tilde{f}_c^s = 10^5$.

particle contact regime and direct contact starts to occur near the center of contact for intermediate contact force, $\tilde{f}_c^s = 10^4$. At low contact force, $\tilde{f}_c^s = 10^3$, the deviation of maximum contact pressure predicted by the SA contact model from Hertz contact is smallest for lowest particle concentration, η_w = 1.25% as seen in Fig. 4.22a (also shown in Fig. 4.24b). This counter-intuitive behavior can be explained by the fact that as the number of active particles increases in the particle contact regime, the contact interface becomes stiffer, i.e the rate of decrease in separation distance with contact pressure is smaller. In the absence of interfacial particles, the separation distance between contacting surfaces remains to be zero, implying infinite stiffness at the contact interface. The increased stiffness at higher particle concentration η_w in the particle contact regime therefore causes a smaller deviation for contact pressure distribution of the SA contact model from Hertz contact at low contact force $\tilde{f}_c^s = 10^3$ as illustrated in Fig 4.22a.

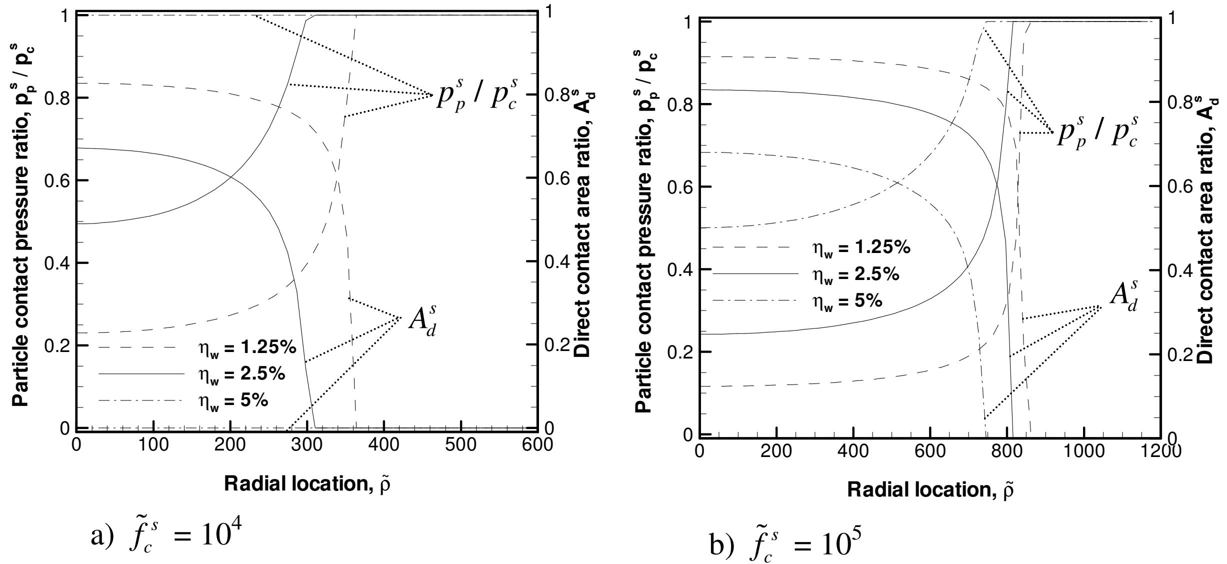

a) $\tilde{f}_c^s = 10^4$

b) $\tilde{f}_c^s = 10^5$

Fig. 4.23: The effect of particle concentration, η_w on the variation of particle contact pressure ratio p_p^s / p_c^s and direct contact area ratio A_d^s in contact zone at different contact force, a) $\tilde{f}_c^s = 10^4$ and b) $\tilde{f}_c^s = 10^5$.

In the mixed contact regime, the stiffness of contact interface is no longer determined by particle contacts only, but direct contact plays a role, which starts to appear in the contact zone at intermediate contact force, $\tilde{f}_c^s = 10^4$. Fig. 4.23a shows that direct contact area A_d^s decreases as particle concentration η_w becomes higher causing a greater deviation from Hertz contact. On the other hand, when contact force is high, $\tilde{f}_c^s = 10^5$, the contact pressure distribution $\tilde{p}_c^s$ for different particle concentrations η_w and Hertz contact become almost identical. This result stems from the fact that local penetration in contact zone is so large that direct contacts dominate the contact interface and the relative effects of particle contacts, which are limited to the outside edge of contact zone, becomes small. These figures show that higher elastic modulus (E_s) and larger particle size (σ_p) cause larger deviations from Hertz contact, considering the deviation from Hertz contact is more significant at lower contact force ($\tilde{f}_c^s = f_c^s(1-\nu_s^{\ 2}) / E_s\sigma_p^2$).

It is apparent from Fig. 4.22b-c that contact interface can be divided into three different regions, based on the effects of direct and particle contacts. In fact the presence of these regions can be explained better in Fig. 4.23, where fraction of particle contact pressure to contact pressure $\tilde{p}_p^s / \tilde{p}_c^s$ and direct contact area A_d^s in the interface are plotted. This figure shows that, at the outside edge of contact region, where $\tilde{p}_p^s / \tilde{p}_c^s = 1$, particle contact is the responsible mechanism for contact pressure. On the other hand, direct contact is the dominant mechanism near the center of contact, where $\tilde{p}_p^s / \tilde{p}_c^s < 1$, as particles become embedded in the elastic surface, causing an increase in direct contact area. There is a transition region between direct contact and particle contact dominant

regions in which the effects of particle and direct contact are comparable. Direct contact area is initially $A_d^s = 0$ at the outside edge of contact zone, and all the load is carried by particle contacts. Toward the center of contact, deformation of asperity increases, which in turn causes a larger area to come into direct contact. Of course the presence of particles delay the occurrence of direct contact, and as expected for higher particle concentration η_w, direct contact covers a smaller area.

Effect of contact force

The results explained above show that contact force $\tilde{f}_c^s$ acting on asperity could have a significant influence on the behavior of contact interface. It is therefore important to investigate the effect of contact force $\tilde{f}_c^s$. The contact radius $\tilde{a}$ and the maximum contact pressure $\tilde{p}_o^s$ are plotted as a function of contact force $\tilde{f}_c^s$ in Figs 4.24a and 4.24b, respectively. In agreement with contact pressure distribution $\tilde{p}_c^s$ for different contact force $\tilde{f}_c^s$ as shown in Fig. 4.22, the effect of particles is to increase contact area while reducing maximum contact pressure $\tilde{p}_o^s$. The maximum contact pressure, $\tilde{p}_o^s$ predicted by the SA contact model for different particle concentrations, η_w and Hertz contact become the same at high contact force, $\tilde{f}_c^s$ (Fig. 4.24b), whereas the deviation for contact radius, $\tilde{a}$ does not decrease to zero but remains at a certain level at high $\tilde{f}_c^s$ (Fig. 4.24a). This result can be explained by the definition of contact radius, $\tilde{a}$ in the SA contact model, which causes $\tilde{a}$ to be arbitrary based on the selection of maximum particle size $\tilde{r}_p^{\max}$. The contact radius $\tilde{a}$ in the SA contact model is defined as the distance from the

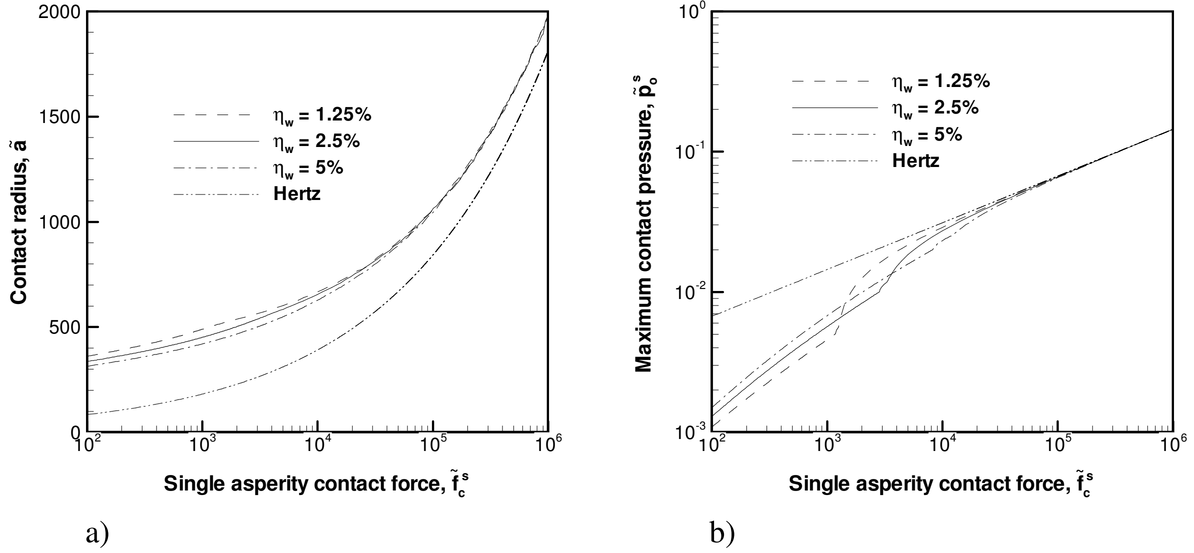

Fig. 4.24: The effect of particle concentration η_w on a) contact radius $\tilde{a}$ and b) maximum contact pressure $\tilde{p}_o^s$.

center of contact to the point where the largest particle is trapped between surfaces. According to Gaussian distribution for particle size, the probability of a particle with an infinite size is non-zero, which would result in infinite contact radius, $\tilde{a} \to \infty$. However particle size is bound in this study by considering mean, μ_p (= 4 σ_p) and standard deviation σ_p of particle radius, as $\tilde{r}_p^{\max}$ = $\mu_p + 3$ since only ~0.14% of particles are larger than $\tilde{r}_p^{\max}$ based on the Gaussian distribution. Fig. 4.25 shows the variation of fraction of contact force carried by particles f_p^s / f_c^s, and direct contact area A_d^s, as a function of contact force $\tilde{f}_c^s$ for three different particle concentrations η_w. This figure shows that for low contact force $\tilde{f}_c^s$, the entire load is carried by particles (f_p^s / f_c^s = 1). When direct contact starts to become significant at higher loads, this ratio gradually becomes f_p^s / f_c^s < 1. As expected, direct contact starts to become more significant for lower values of

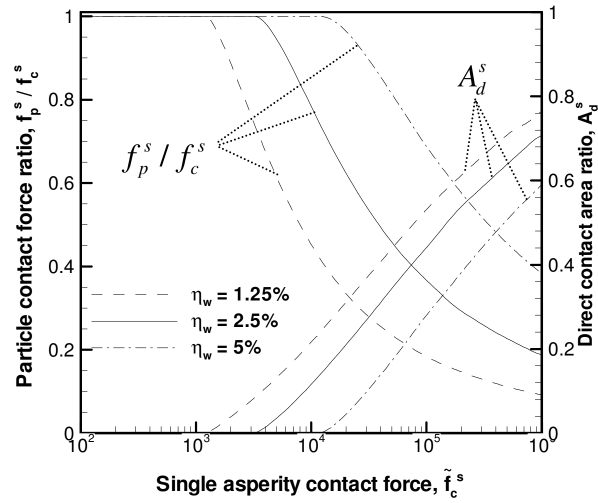

Fig. 4.25: The variation of particle contact force ratio, f_p^s / f_c^s and direct contact area, A_d^s with contact force, $\tilde{f}_c^s$ at different particle concentrations, η_w.

particle concentrations η_w. Following a similar trend, direct contact area A_d^s increases with higher contact force $\tilde{f}_c^s$.

Effect of penetration depth

According to Hertz contact model, single asperity contact force is expected to vary with penetration at the center of contact as $\tilde{f}_c^s \propto \tilde{\delta}_o^{s^{3/2}}$. The presence of particles in contact interface is expected to modify this relation. In this work, negative values of the penetration are assumed to cause contact of an idealized asperity as shown in Fig. 4.16. However, particles trapped in the interface cause contact even when penetration at center of contact, $\tilde{\delta}_o^s > 0$. The effect of penetration $\tilde{\delta}_o^s$ is plotted in Fig. 4.26. As expected, the model predicts that particles trapped between surfaces become engaged in contact, causing contact force, $\tilde{f}_c^s$ to become $\tilde{f}_c^s > 0$ when there is a clearance between surfaces, $\tilde{\delta}_o^s > 0$, while Hertz contact model, clearly, predicts $\tilde{f}_c^s = 0$. In this range, contact force

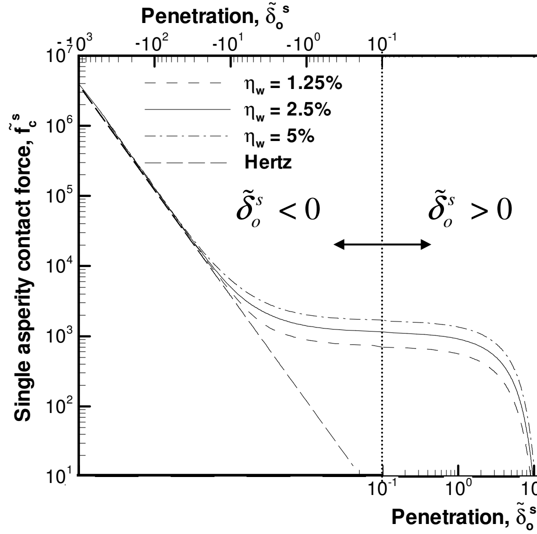

Fig. 4.26: The variation of single asperity contact force $\tilde{f}_c^s$ with penetration at the center of contact $\tilde{\delta}_o^s$ for different particle concentrations η_w.

$\tilde{f}_c^s$ increases with particle concentration η_w for the same amount of penetration, as more particles are present when η_w is high. Fig. 4.26 also shows what happens when penetration becomes $\tilde{\delta}_o^s < 0$. The contact force $\tilde{f}_c^s$ estimated by Hertz contact is smaller than the SA contact model for small penetration $\tilde{\delta}_o^s$. However as penetration is increased further, the variation of contact force $\tilde{f}_c^s$ with penetration $\tilde{\delta}_o^s$ becomes similar to that of Hertz contact. This result is in agreement with contact pressure distribution $\tilde{p}_c^s$ that is shown to be similar at high contact force $\tilde{f}_c^s$ in Fig. 4.22. It is also noted that effect of particle concentration η_w diminishes at large penetration depths $\tilde{\delta}_o^s$.

Effect of asperity radius

The effect of asperity radius $\tilde{R}_s$ is presented in Figs 4.27 - 4.30. The computed contact pressure $\tilde{p}_c$ variations in the contact interface of asperity is plotted in Figs. 4.28a-c for

contact force, $\tilde{f}_c^s$ = 10^3, $10^4$and 10^5, respectively. These figures show that, for a given contact force $\tilde{f}_c^s$, the predicted contact pressure distribution $\tilde{p}_c^s$ when particles are in the interface, deviates more with respect to Hertz contact, when asperity radius $\tilde{R}_s$ increases. The direct contact area A_d^s and particle contact force ratio f_p^s / f_c^s are plotted in Fig. 4.28

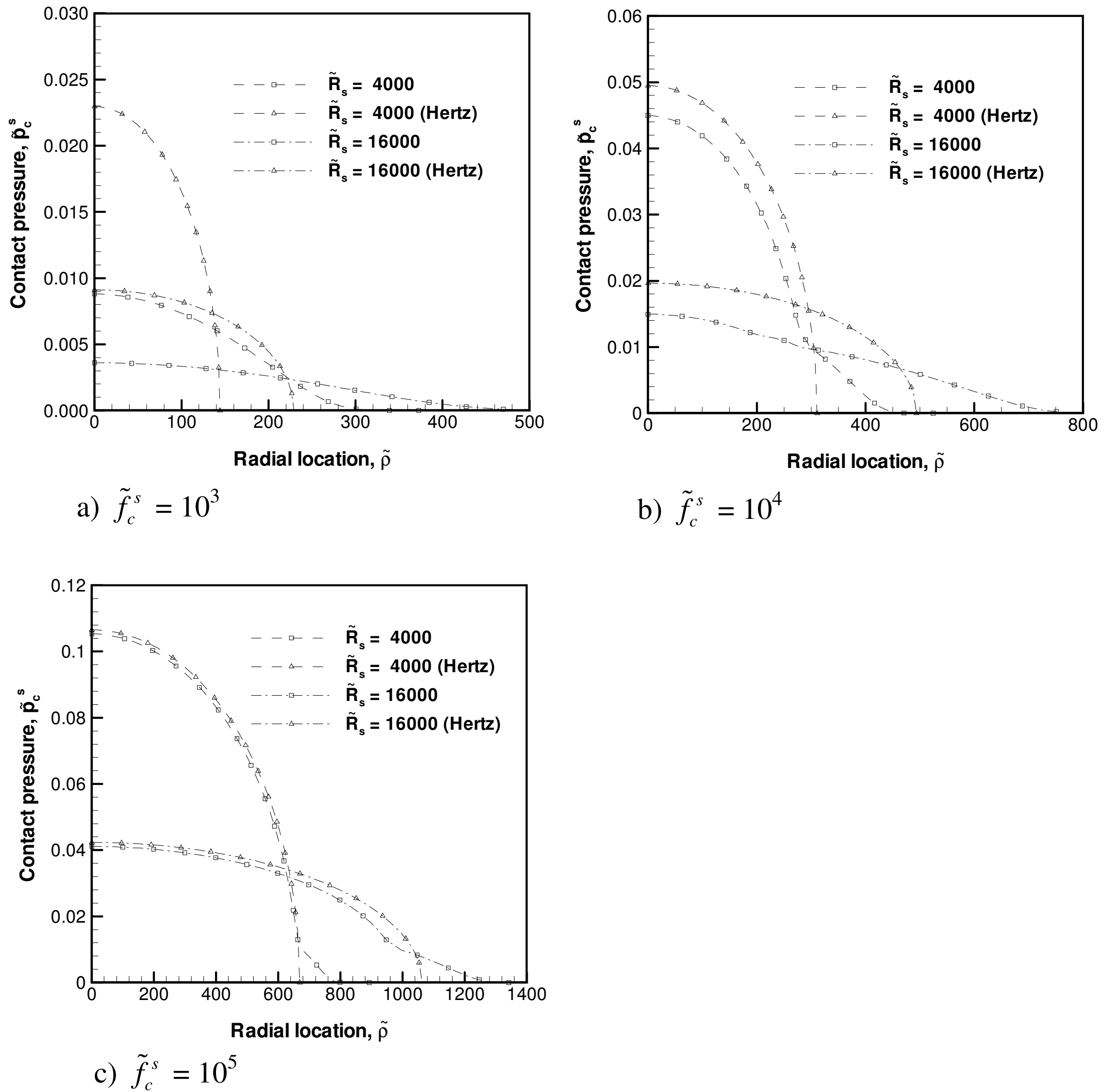

Fig. 4.27: The effect of asperity radius $\tilde{R}_s$ on contact pressure distribution, $\tilde{p}_c^s$ at different contact force, a) $\tilde{f}_c^s$ = 10^3, b) $\tilde{f}_c^s$ = 10^4 and c) $\tilde{f}_c^s$ = 10^5.

as a function of contact force $\tilde{f}_c^s$ for different asperity radii $\tilde{R}_s$. The contact force $\tilde{f}_c^s$ required to initiate direct contact becomes smaller, as asperity radius $\tilde{R}_s$ is decreased. Fig. 4.29 shows that a larger contact area (Fig. 4.29a), but lower contact pressure (Fig. 4.29b) is predicted when asperity radius $\tilde{R}_s$ increases for a given contact force $\tilde{f}_c^s$. In fact, this is also evidenced by Hertz contact relations for the contact radius $\tilde{a} = (3\tilde{f}_c^s \tilde{R}_s / 2)^{1/3}$ and the maximum contact pressure $\tilde{p}_o = (3\tilde{f}_c^s / (2\pi^3 \tilde{R}_s^{\,2}))^{1/3}$. As the contact pressure, $\tilde{p}_c^s$ is lower on a larger asperity radius $\tilde{R}_s$, particles will have a lower tendency to penetrate into deformable surface, and thus they will carry a larger proportion of applied load f_p^s / f_c^s, which is shown in Fig. 4.30. The direct contact area A_d^s for the smallest asperity radius, $\tilde{R}_s$ = 4000 remains to be larger in the whole range of contact force $\tilde{f}_c^s$ studied.

4.6 Multi-Asperity (MA) Contact Model

The behavior of a single asperity characterized by the SA contact model described in Section 4.5, is implemented in a multi-asperity model. Greenwood and Williamson (GW) multi-asperity model is used to integrate the effect of each asperity to obtain overall rough contact behavior of two surfaces. The SA contact model is used to replace the Hertzian behavior for each asperity in GW model. Interfacial particles captured at the interface alter rough contact of surfaces due to their influence on load-displacement function of a single asperity as plotted in Fig. 4.26. In addition to this effect, contact pressure distribution alters local contact characteristics such as direct contact area ratio, particle contact pressure ratio, number of active particles, etc; which become critical

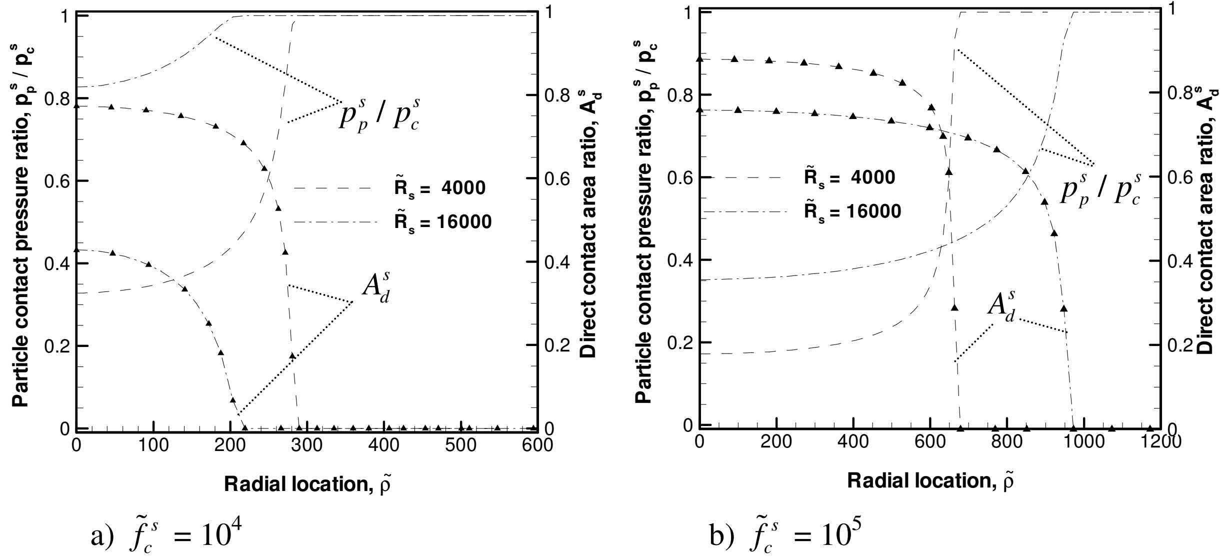

a) $\tilde{f}_c^s = 10^4$

b) $\tilde{f}_c^s = 10^5$

Fig. 4.28: The effect of asperity radius $\tilde{R}_s$ on the variation of particle contact pressure ratio p_p^s / p_c^s and direct contact area ratio A_d^s in contact zone at different contact force, a) $\tilde{f}_c^s = 10^4$ and b) $\tilde{f}_c^s = 10^5$.

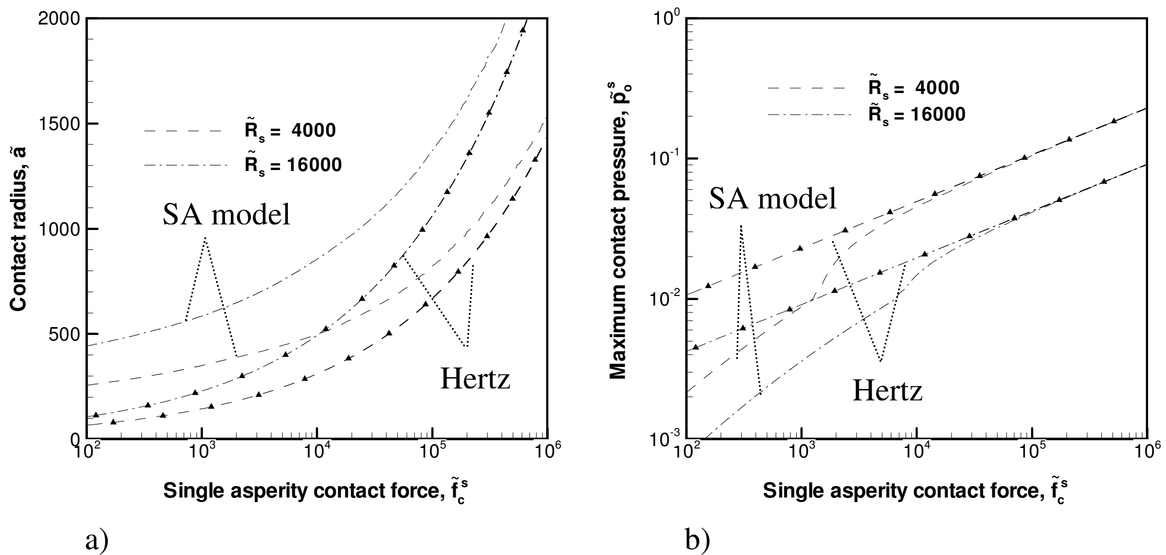

a)

b)

Fig. 4.29: The effect of asperity radius $\tilde{R}_s$ on a) contact radius $\tilde{a}$ and b) maximum contact pressure $\tilde{p}_o^s$.

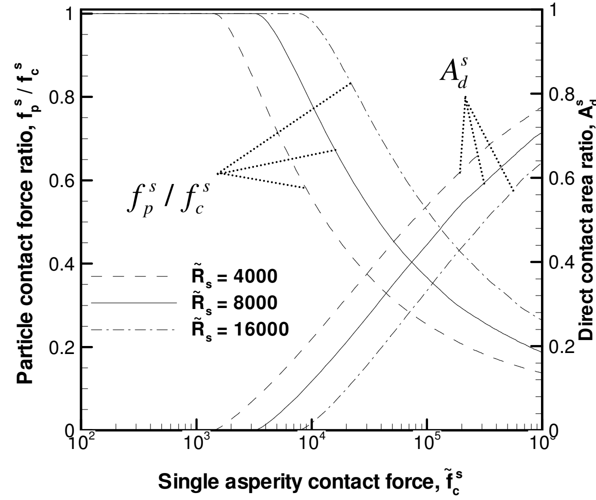

Fig. 4.30: The variation of particle contact force ratio f_p^s / f_c^s and direct contact area ratio A_d^s with contact force $\tilde{f}_c^s$ at different asperity radius $\tilde{R}_s$.

factors for material removal rate (MRR) calculations. The effect of single asperity contact behavior altered by interfacial particles on MRR in rough contact is studied in Chapter 5. In this section, the effect of different load-displacement function for each asperity influenced by interfacial particles is investigated in a multi-asperity contact model for the pad-wafer rough contact.

The non-dimensionalization used in the MA contact model is shown in Table 4.3. Note that the porous elastic modulus E_p in the MA contact model is used instead of solid pad elastic modulus in the SP, MP and SA contact models. The dimensionless solid pad elastic modulus $\bar{E}_s$ is also called as porous elastic modulus ratio E_s / E_p, which is used for the conversion of non-dimensional terms in the MP and SA contact models to the MA contact model (Table 4.1).

4.6.1 Implementation of the SA contact model

In the generalized form of GW multi-asperity model (Eqn (4.9)), the contact force of a single asperity f_c^s for a penetration at the center of contact δ_o^s, is given by Hertz contact as, $f_c^s = \frac{4}{3} E_s R_s^{1/2} \delta_o^{s\,3/2}$. This function for contact force $f_c^s\left(\delta_o^s\right)$ is replaced by the relations obtained in the SA contact model and plotted in Fig. 4.26 using a look-up table. Note that single asperity contact force $\tilde{f}_c^s \leq 10^6$ is studied in the SA contact model and it is shown in Section 4.5 that the SA contact model and Hertz contact gives almost identical results for load-displacement behavior at high contact force, $\tilde{f}_c^s \geq 10^6$ as demonstrated in Fig. 4.26. Therefore it is plausible to use Hertz contact when the single asperity contact force is high, $\tilde{f}_c^s \geq 10^6$. Furthermore, the lower limit of the integral in Eqn (4.9) is modified to take the interfacial particles engaging in contact into consideration when the separation distance d_{wp} between surfaces is smaller than the maximum diameter of particles $2\,r_p^{\max}$, $0 < d_{wp} < 2\,r_p^{\max}$. Eqn (4.9) reduces to the following equation in non-dimensional form as,

$$\bar{P}_o = \bar{\eta}_s \int_{\bar{d}_{wp}-2\bar{r}_p^{\max}}^{\infty} \bar{f}_c^s\left(\bar{\delta}_o^s\right)\Phi_s(\bar{z}_s)\,d\bar{z}_s \qquad (4.24)$$

where d_{wp} is equilibrium separation distance, $\bar{z}_s$ is asperity summit height and $\bar{\eta}_s$ is asperity density. Note that the penetration at the center of each asperity contact $\bar{\delta}_o^s$ is defined as $\bar{\delta}_o^s = \bar{z}_s - \bar{d}_{wp}$ if Hertz contact is used in Eqn (4.24). The penetration at the

center of contact is modified to be $\bar{\delta}_o^s = \bar{d}_{wp} - \bar{z}_s$ when the SA contact model is utilized so that two conditions between an asperity and contacting surface can be considered. When there is clearance between an asperity and contacting surface, penetration at the center of contact is $\bar{\delta}_o^s > 0$ while $\bar{\delta}_o^s < 0$ if an asperity is penetrating into contacting surface. As a result of this modification, asperities with a clearance smaller than maximum diameter of particles are considered to be engaged in contact as, $\bar{\delta}_o^s = \bar{d}_{wp} - \bar{z}_s$, where $\bar{z}_s \geq \bar{d}_{wp} - 2\bar{r}_p^{\max}$ and $\bar{\delta}_o^s \leq 2\bar{r}_p^{\max}$.

4.6.2 Effect of particles on multi-asperity contact

The variation of the single asperity contact force $\bar{f}_c^s$ with the penetration $\bar{\delta}_o^s$ at the center of contact determined in the SA contact model (Fig. 4.26) is substituted into Eqn (4.24) as $\bar{f}_c^s\left(\bar{\delta}_o^s\right)$ by means of look-up tables. The mean contact force $\bar{f}_s^m$ on the asperities engaged in rough contact is calculated using applied pressure $\bar{P}_o$ and number of asperities in contact $\bar{\eta}_s^a$ as $\bar{f}_s^m = \bar{P}_o / \bar{\eta}_s^a$. The effect of interfacial particles on the mean asperity contact force $\bar{f}_s^m$ is investigated for different non-dimensionalized values of porous elastic modulus ratio E_s / E_p, standard deviation (SD) of particle size $\bar{\sigma}_p$, particle concentration η_w, asperity radius $\bar{R}_s$, asperity density $\bar{\eta}_s$ in the ranges given in Table 4.3 determined based on the physical values given in Table 4.1. It is determined that the SA contact model and Hertz contact give very similar results for the mean asperity contact force $\bar{f}_s^m$ in the ranges of parameters studied when applied pressure $\bar{P}_o$ is varied as $10^{-7} < \bar{P}_o < 10^{-2}$. The most significant effect of particles on the mean asperity contact force $\bar{f}_s^m$

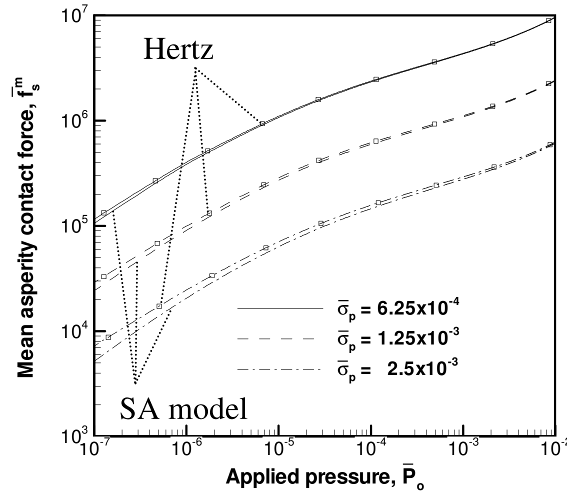

Fig. 4.31: The effect of particle size $\bar{\sigma}_p$ on mean asperity contact force $\bar{f}_s^m$.

is observed for large particles, e.g. the SD of particle size, $\bar{\sigma}_p$ = 2.5x10^{-3}. Fig. 4.31 illustrates the effect of particles captured by the SA contact model on the mean asperity contact force $\bar{f}_s^m$. Hertz contact predicts mean asperity contact force $\bar{f}_s^m$ to be slightly greater than the SA contact model since more asperities get engaged in contact when particles are present at the interface. For the range of typical values for applied pressure 0.007 MPa < P_o < 0.07 MPa and pad elastic modulus 10 MPa < E_s < 100 MPa used in CMP, dimensionless applied pressure $\bar{P}_o$ can be calculated to be 7x10^{-5} < $\bar{P}_o$ < 7x10^{-3}. Particles do not seem to play an important role even in the case of a large particle when applied pressure $\bar{P}_o$ used in CMP is considered.

This result can be explained by considering the effect of interfacial particles on single asperity contact behavior. Fig. 4.26 shows that influence of particles on single asperity contact behavior becomes negligible when penetration of an asperity is large, $\tilde{\delta}_o^s$ < -10 (or $\bar{\delta}_o^s$ < -10$\bar{\sigma}_p$). Considering the asperity summits of a rough surface varying in height making contact with a flat surface as illustrated in Fig. 4.32, it can be seen that some

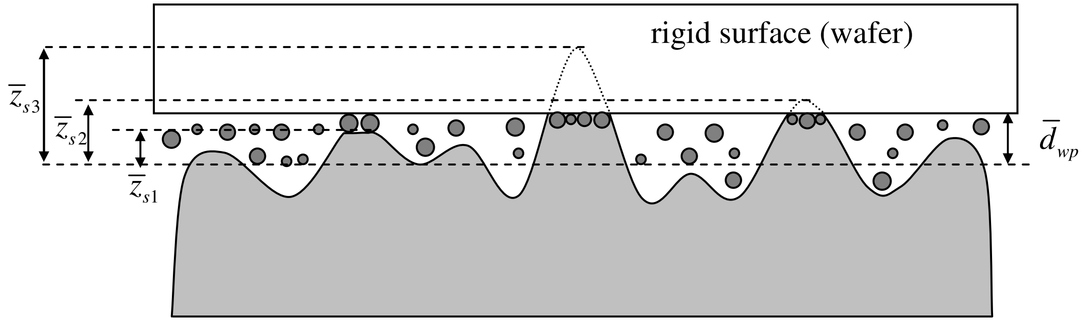

Fig. 4.32: Asperities with different amounts of penetration, $\bar{\delta}_o^s$.

asperities will undergo large deformation while the deformation of some asperities will be small. In Fig. 4.32, three different asperities with heights $\bar{z}_{s1}$, $\bar{z}_{s2}$ and $\bar{z}_{s3}$ are shown. An asperity with height, $\bar{z}_{s1}$ makes contact with rigid surface due to the large particles trapped between the asperity and rigid surface. The penetration for such an asperity is $0 < \bar{\delta}_o^s \leq 2\bar{r}_p^{\max}$. The penetration of an asperity with height $\bar{z}_{s2}$ is negative, but the penetration is small, $-10\bar{\sigma}_p \leq \bar{\delta}_o^s \leq 0$. The effect of interfacial particles on load-displacement function for these two asperities is considered to be important and the SA contact model can be used to capture this behavior. The penetration of an asperity with height, $\bar{z}_{s3}$ is large, $\bar{\delta}_o^s < -10\bar{\sigma}_p$ such that effect of interfacial particles is negligible. Hertz contact gives accurate results for this asperity. The influence of interfacial particles on rough contact behavior therefore depends on the contribution of the asperities with heights $\bar{z}_{s1}$ and $\bar{z}_{s2}$ in Fig. 4.32, subjected to small penetrations. This contribution is quantified by the fraction r_s^{sa} of applied pressure carried by asperities with $\bar{\delta}_o^s \geq -10\bar{\sigma}_p$. The applied pressure ratio r_s^{sa} can be found as,

$$r_s^{sa} = \frac{\int_{\bar{d}_{wp}-2\bar{r}_p^{\max}}^{\bar{d}_{wp}+10\bar{\sigma}_p} \bar{f}_c^s\left(\bar{\delta}_o^s\right)\bar{\Phi}_s(\bar{z}_s)d\bar{z}_s}{\int_{\bar{d}_{wp}-2\bar{r}_p^{\max}}^{\infty} \bar{f}_c^s\left(\bar{\delta}_o^s\right)\bar{\Phi}_s(\bar{z}_s)d\bar{z}_s} \quad (4.25)$$

In Figs 4.33 and 4.35, the applied pressure ratio r_s^{sa} carried by asperities with small penetration, $\bar{\delta}_o^s \geq -10\,\bar{\sigma}_p$ (Eqn (4.25)) is plotted as a function of applied pressure, $\bar{P}_o$ obtained by Eqn (4.24). The porous elastic modulus ratio E_s / E_p has an effect on the applied pressure ratio r_s^{sa} as shown in Fig. 4.33 as higher E_s / E_p causes r_s^{sa} to become larger. The applied pressure ratio r_s^{sa} also depends on applied pressure $\bar{P}_o$, particle-related parameters such as particle size $\bar{\sigma}_p$ and particle concentration η_w (Fig. 4.34) and pad topography related parameters such as asperity radius $\bar{R}_s$ and density $\bar{\eta}_s$ (Fig. 4.35). It is seen that the asperities influenced by interfacial particles carry a small fraction r_s^{sa} of applied pressure; in fact less than 0.1% of applied pressure, $r_s^{sa} < 0.001$ is on the asperities with small penetration, $\bar{\delta}_o^s \geq -10\,\bar{\rho}_p$.

The most influential parameter on applied pressure ratio, r_s^{sa} is particle size $\bar{\sigma}_p$ as shown in Fig. 4.34a, where larger particles increase the effect of particles on asperity contact which was also illustrated in Fig. 4.31. This can be explained by the relative value of the equilibrium separation distance, $\bar{d}_{wp}$ with respect to the maximum particle diameter ($14\bar{\sigma}_p$) and the penetration at which the effect of particles become negligible ($-10\bar{\sigma}_p$). The equilibrium separation distance $\bar{d}_{wp}$ is calculated using base parameters (Table 4.3)

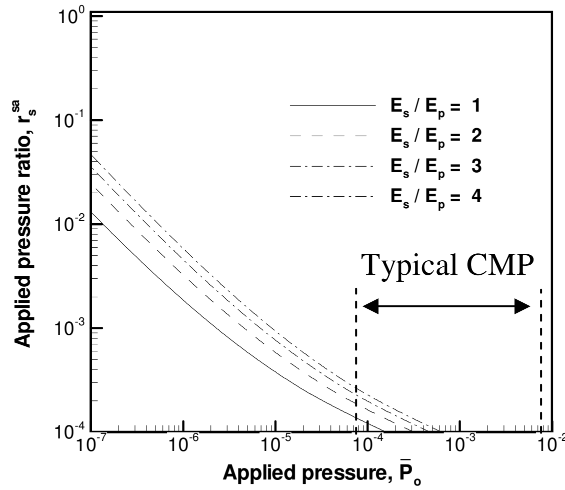

Fig. 4.33: The effect of porous elastic modulus ratio E_s/ E_p on applied pressure ratio, r_s^{sa} of asperities influenced by the SA contact model.

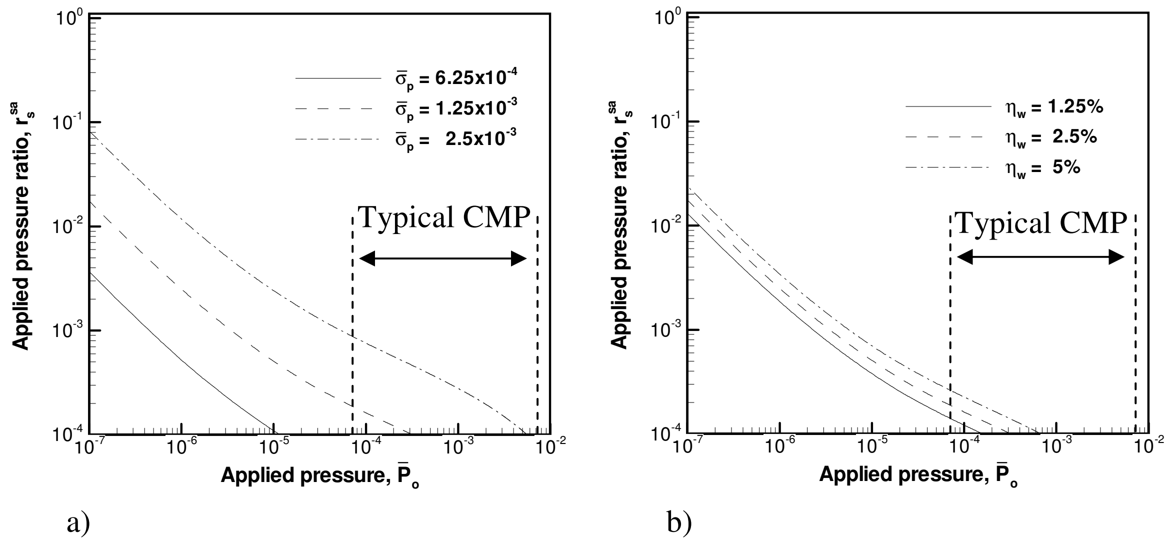

Fig. 4.34: The effect of a) particle size, $\bar{\sigma}_p$ and b) particle concentration, η_w on applied pressure ratio, r_s^{sa} of asperities influenced by the SA contact model.

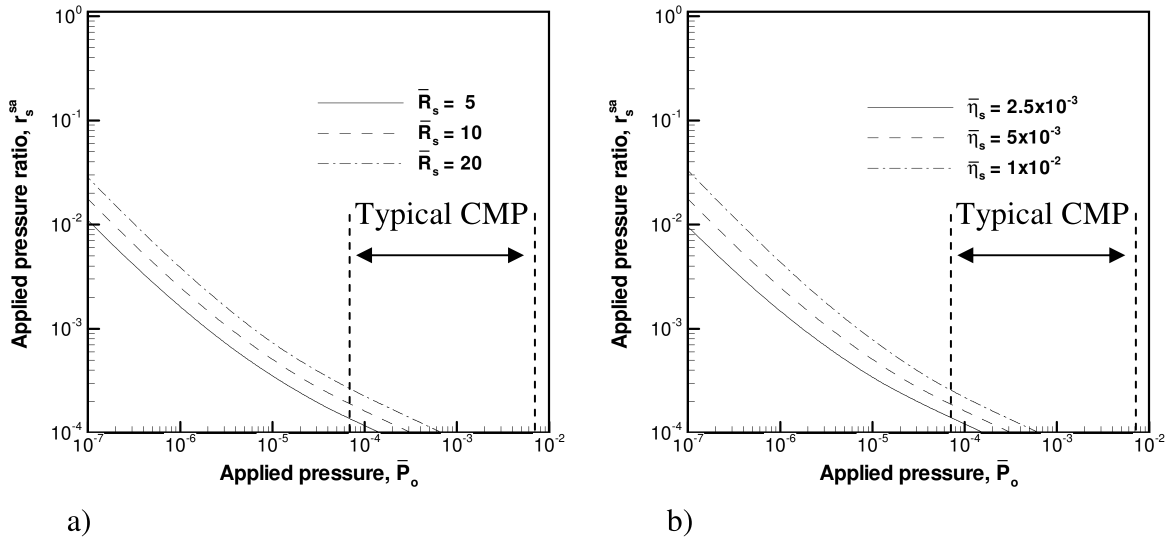

Fig. 4.35: The effect of a) asperity radius $\bar{R}_s$ and b) asperity density $\bar{\eta}_s$ on applied pressure ratio r_s^{sa} of asperities influenced by the SA contact model.

in Eqn. (4.24) and plotted in Fig. 4.36, which indicates that the equilibrium separation distance is in the range $0.2 < \bar{d}_{wp} < 2.1$ for typical dimensionless applied pressure in CMP, $7\text{x}10^{-5} < \bar{P}_o < 7\text{x}10^{-3}$. It is important to note that no significant difference is observed when Eqn (4.9) with Hertz contact assumption for single asperity behavior is used instead of Eqn (4.24) with the SA contact model implying that the effect of particles on multi-asperity contact is not significant. If we assume that the tallest asperity is located at $\bar{z}_s = 3$, penetration of asperities varies as, $0 < \bar{\delta}_o^s < 3$ for low applied pressure and hard pad, $\bar{P}_o = 7\text{x}10^{-5}$ and $0 < \bar{\delta}_o^s < 0.5$ for high applied pressure and soft pad, $\bar{P}_o = 7\text{x}10^{-3}$. For a typical particle size σ_p and SD of pad roughness σ_s, dimensionless particle size is found as $\bar{\sigma}_p = 1.25\text{x}10^{-3}$, which means that both maximum particle diameter ($14\bar{\sigma}_p$) and penetration at which the effect of particles become negligible ($-10\bar{\sigma}_p$) are several orders of magnitude smaller than maximum penetration of asperities seen for typical applied pressure in CMP. Although larger particle size $\bar{\sigma}_p$ increases the influence

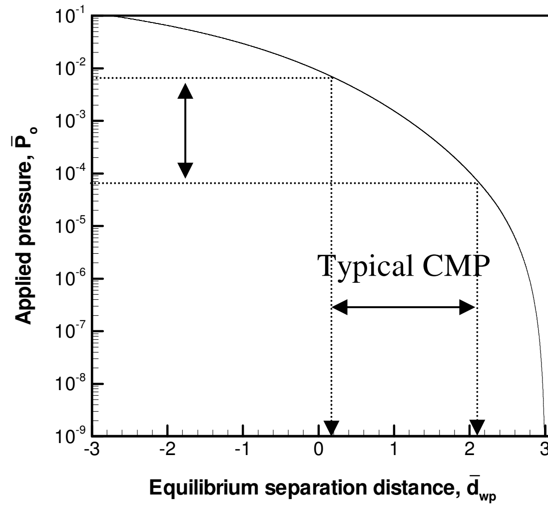

Fig. 4.36: The equilibrium separation distance, $\bar{d}_{wp}$ at typical range of applied pressure, $\bar{P}_o$ in CMP.

of interfacial particles, effect of interfacial particles remains small when typical CMP parameters are used for particle size $\bar{\sigma}_p$ and concentration η_w, asperity radius, $\bar{R}_s$ and density $\bar{\eta}_s$, and porous elastic modulus ratio E_s / E_p. Higher particle concentration η_w also increases the influence of interfacial particles on rough contact as depicted in Fig. 4.34b. As porous elastic modulus ratio E_s / E_p increases, the effect of particles becomes more significant. Larger asperity radius $\bar{R}_s$ and asperity density $\bar{\eta}_s$ cause the equilibrium separation distance $\bar{d}_{wp}$ to become smaller for a given applied pressure $\bar{P}_o$ which results in slightly greater applied pressure ratio r_s^{sa} carried by asperities with $\bar{\delta}_o^s \geq -10\,\bar{\sigma}_p$ (Fig. 4.34).

4.7 Summary

In this chapter, the contact of a rough pad and a wafer is investigated by modeling particle level interactions in the SP and MP contact models. These interactions are then

implemented first for a single asperity in the SA contact model and finally for multiple asperities engaged in contact due to pad-wafer rough contact in the MA contact model.

The MP contact model gives important characteristics of local contact. The results of the MP contact model show that direct contacts starts to dominate local contact as particles become embedded in the pad. The condition for occurrence of direct contact is a strong function of particle concentration and pad elastic modulus. The participation of particle and direct contacts for a given local contact pressure as determined by the MP contact model can either be used in the SA contact model, which considers the influence of interfacial particles on contact pressure distribution at pad asperity-wafer contact interface or Hertz contact if the effect of interfacial particles can be neglected.

The SA contact model shows that the external load on a single asperity is transferred to rigid surface by particles and by direct contact of the deformable pad to the rigid wafer. The degree to which particles become embedded into the deformable material affects the interfacial contact conditions. One of the effects of the particles, on the overall contact behavior is to distribute the contact over a larger area. Consequently, the maximum contact pressure at the center of contact decreases with respect to the prediction of Hertz theory. Interfacial particles play an important role in the single asperity contact, when force on the asperity is small, pad is hard and/or particle concentration is high. It is also shown that the particles will have a lower tendency to penetrate into the elastic solid, when they are caught in the interface of a relatively large asperity. For a given total contact force, this means that an increased proportion of total contact force will be carried by the particles if asperity radius is increased. As direct contact area develops between

surfaces due to increased external force on a single asperity, contact pressure distribution approaches Hertzian contact pressure distribution and effect of interfacial particles can be neglected.

The equilibrium separation distance between pad and wafer is calculated by *the MA contact model*. When typical CMP parameters are used, it is found that the effect of particles on load-displacement behavior of a single asperity captured by the SA contact model can be neglected. This is due to the fact that only a small fraction of applied pressure is carried by asperities with sufficiently small contact force for interfacial particles to be influential.

The results of the MP and SA contact models are used in Chapter 5 to compute material removal rate. If the effect of interfacial particles is neglected, the contact pressure distribution at single asperity contact can be assumed to be Hertzian. In this case, local contact pressure determined by Hertz contact is substituted in the MP contact model to determine particle and direct contact pressure, and number of active particles, which are required for calculating material removal rate achieved by active particles captured in contact between pad and wafer.

References

1. Kim A.T., Seok J., Tichy J.A., Cale T.S., 2003. A multiscale elastohydrodynamic contact model for CMP. J Electrochem Soc, 150, 570-576.

2. Qin K., Moudgil B., Park C.W., 2004. A chemical mechanical polishing model incorporating both the chemical and mechanical effects. Thin Solid Films, 446, 277-286.

3. Greenwood J.A., and Williamson J.B.P., 1966. Contact of nominally flat surfaces. Proceedings of the Royal Society of London, A295, 300-319.

4. Greenwood J.A., and Tripp J.H., 1967, “The Elastic Contact of Rough Spheres,” ASME J Appl. Mech., 34, pp. 153-160.

CHAPTER 5

MODELING OF MATERIAL REMOVAL RATE

5.1 Overview

This chapter focuses on the calculation of material removal rate (MRR) in CMP. The contact models developed in Chapter 4 are implemented by using adhesive and abrasive wear formulations. A general form of the wear equation for MRR (wear rate) due to applied pressure, P_o can be written as [1],

$$RR = k_w \frac{P_o V_r}{H_w} \tag{5.1}$$

where V_r is relative sliding velocity of surfaces and H_w is hardness of softer material, RR is the removal rate with units of L/T, and k_w is the unitless wear constant. Both adhesive and abrasive wear equations are in the same form except that wear constant k_w is different for each wear type. Wear constant k_w in Eqn (5.1) is usually determined empirically, and depends on the following parameters;

- Parameters related to particles (particle size σ_p and concentration η_w),
- Surface topography (pad roughness σ_s, skew S_s, asperity radius R_s and density η_s),
- Elasticity of pad (elastic modulus E_s and porosity of pad E_s / E_p)
- Material properties of wafer and particle that influence surface forces (effective Hamaker constant A_{wsp} and zeta potential of wafer and particle $\Psi_{1,2}$).

In addition, the wear rate RR does not vary linearly with applied pressure P_o as suggested by Eqn (5.1) but the RR-P_o relationship depends on the parameters listed above. Moreover, the relation between the wear rate, RR and hardness H_w is not linear, as the wafer hardness varies in the thickness direction of the wafer due to the chemical reactions taking place between the wafer and the slurry. A passivated surface layer with a thickness t_{pw} and hardness, H_{pw} different than the hardness of bulk material H_{bw} exists. Finally, experimental and modeling studies show that in CMP, the effect of relative velocity V_r on wear rate RR cannot be simply described as shown in Eqn (5.1) when hydrodynamic lubrication effects due to slurry flow between pad and wafer are considered. However hydrodynamic lubrication effects are not within the scope of this work, therefore wear rate RR is assumed to have linear dependence on relative velocity V_r as suggested by the general form of wear equation (Eqn (5.1)). In this work, Eqn (5.1) is investigated in the following form,

$$RR = k_w\left(\sigma_p, \eta_w, \sigma_s, S_s, R_s, \eta_s, E_s, E_s / E_p, A_{wsp}, \Psi_{1,2}\right)\frac{f(P_o)V_r}{g(H_{pw}, H_{bw}, t_{pw})} \quad (5.2)$$

where *f* and *g* are two functions that relate the effect of applied pressure and wafer hardness to wear rate. The effects of all the variables in Eqn (5.1) are investigated for different contact conditions introduced in Chapter 4.

In this work, only particle contacts are assumed to result in material removal due to both adhesive and abrasive wear, whereas pad-wafer direct contact does not cause material removal since pad is significantly soft as compared to wafer. Equilibrium contact force at wafer-particle interface provides the necessary mechanical action for material removal, while chemicals in slurry influence material removal by altering wafer hardness. In this chapter, equations are developed for calculating forces (or removal force function (RFF)), which are the mechanical driver for material removal. In Section 5.2, contact force applied by pad on a single particle is found by utilizing single particle (SP) contact model developed in Section 4.2. Surface forces including van der Waals and electrical double layer forces between wafer and a single particle are calculated and wafer-particle contact force is obtained by the equilibrium of pad-particle contact and surface forces.

Once the contact force between wafer and a single particle is computed, the RFF due to adhesive and abrasive wear achieved by a single particle is determined. The wafer-particle contact is assumed to be perfectly-plastic, which enables the calculation of indentation depth of each particle in wafer from wafer-particle contact force and wafer hardness. The RFF due to adhesive wear is proportional to contact area between wafer and particle while abrasive wear varies as a function of area abraded by a particle due to sliding on wafer (Section 3.5). This fundamental difference between the two wear mechanisms cause wear constant function k_w in Eqn (5.2) to be different.

The RFF for each particle is then integrated in the multi-particle (MP) model to find the RFF achieved by all active particles trapped between two flat surfaces (Section 5.3). The RFF due to the contact of two flat surfaces is substituted into the single asperity (SA) model for calculating the RFF of a single asperity (Section 5.4). The contact pressure distribution in single asperity contact given by the SA contact model considering the influence of interfacial particles as well as Hertz contact neglecting the effect of interfacial particles is used for the calculation of the RFF achieved by a single pad asperity. The RFF for each asperity contact is finally used in the multi-asperity (MA) model in order to compute the RFF of all asperities in pad-wafer rough contact (Section 5.5).

In Section 5.5, the calculation of the effective hardness by using the bi-layer hardness model is explained. Once the effective hardness is determined, the MRR is computed from the RFF and the effective hardness.

5.2 Removal Force Function (RFF) in SP Contact Model

A model for the RFF of a single particle trapped between one deformable pad and one rigid wafer as shown in Fig 5.1 is explained next. The effects of the surface forces acting between the wafer and the particle are considered in this model. The contact force at wafer-particle interface f_w is responsible for material removal due to wear of wafer. Fig. 5.1 shows the free-body force diagram of particle in contact with wafer. The wafer-particle contact force f_w consists of the force transmitted through pad-particle contact,

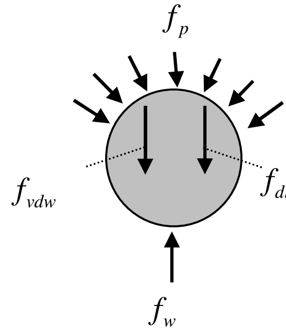

Fig. 5.1: Free-body diagram for forces on a particle in contact with pad and wafer in the presence of surface forces (van der Waals, f_{vdw} and double layer, f_{dl} forces).

f_p, and surface forces f_s, between wafer and particle including the van der Waals f_{vdw} and the electrical double layer forces f_{dl} as,

$$f_w = f_p + f_s = f_p + f_{vdw} + f_{dl} \tag{5.3}$$

The contact force on the particle applied by the pad, f_p is defined in the SP contact model as a function of penetration depth of particle into the pad δ_p, $f_p\left(\delta_p\right)$ in Section 4.3. The surface forces between the wafer and the particle on the other hand are constant for a given particle size, r_p. Considering the dependence of pad-particle contact force on the pad elastic modulus and particle size as $f_p \propto E_s r_p^2$ and the surface forces as $f_s \propto r_p$, the relative effect of surface forces, $f_s / f_p = 1 / E_s r_p$, is found to increase with softer pad and smaller particles.

5.2.1 Surface forces

The equilibrium separation distance d_o between a wafer and a particle is a significant factor in the magnitude of the van der Waals f_{vdw} and electrical double layer f_{dl} forces (Eqns (3.29) and (3.40)-(3.43)). For two contacting surfaces which are atomically

smooth, separation distance is $d_o = 4$ Å. The separation distance d_o increases effectively if contacting surfaces become rougher [2]. As illustrated in Fig. 5.2, van der Waals f_{vdw} and double layer, f_{dl} forces decrease with larger separation distance d_o. It is seen that van der Waals forces f_{vdw} are always positive (attractive) but the magnitude of f_{vdw} becomes smaller as effective Hamaker constant A_{wsp} decreases. Fig. 5.2b and 5.2c shows the variation of double layer forces f_{dl} predicted by the compression approximation (CA) and HHF constant charge assumption (HHF-CC) explained in Section 3.2.2, respectively using molar concentration $M = 0.01$ mole/liter. Note that the parameters listed in Table 3.1 are used to calculate the double layer forces f_{dl}. A significant difference between these two approaches to calculate double layer force f_{dl} is observed as the magnitude of f_{dl} is found to be much greater if HHF-CC assumption is used. The comparison of different assumptions for the calculation of double layer forces f_{dl} is further discussed in Section 3.2.2. The magnitude of double layer forces f_{dl} is a strong function of zeta potential of interacting surfaces $\Psi_{1,2}$ (wafer and particle) as shown in Fig. 5.2b and 5.2c. Both approaches indicate that double layer forces remain negative $f_{dl} < 0$ (repulsive) even when the surface charges of wafer and particle are opposite. A small attractive force is determined by HHF-CC assumption when the surfaces are oppositely charged with large zeta potential $\Psi_{1,2} = 50$mV, -50mV. In this case, CA assumption gives double layer force to be $f_{dl} = 0$.

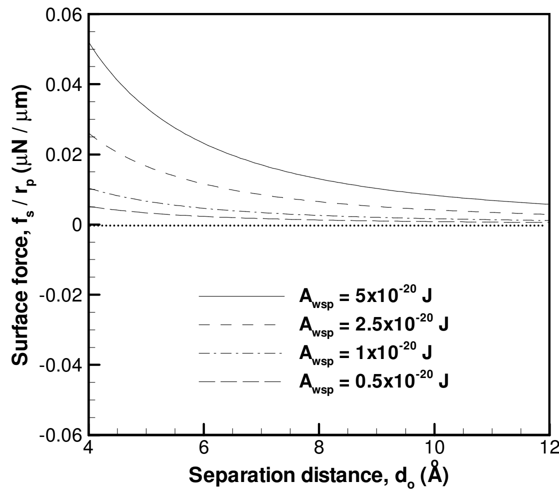

a) Van der Waals force f_{vdw}

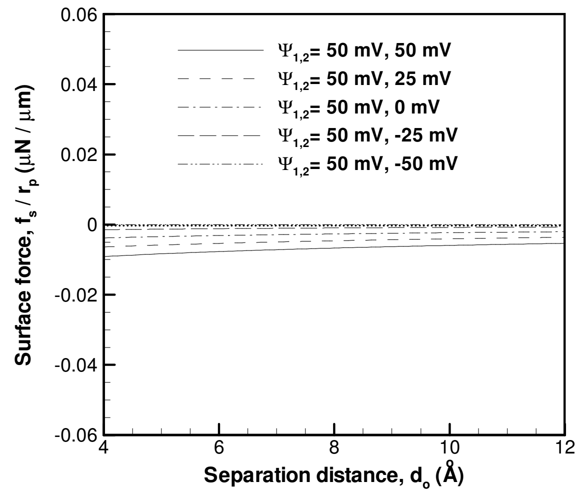

b) Double layer force f_{dl} (CA)

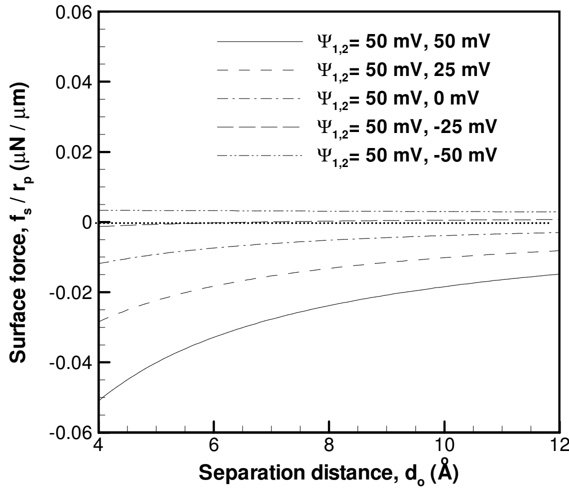

c) Double layer force f_{dl} (HHF-CC)

Fig. 5.2: The effect of separation distance d_o on a) van der Waals force f_{vdw} and b) c) double layer force f_{dl}, with HHF-CC and CA assumptions, respectively.

The effect of molar concentration M of the electrolyte on the magnitude of double layer forces f_{dl} is investigated in Fig. 5.3, where double layer forces f_{dl} are calculated using CA and HHF-CC assumptions while M is varied as 0.001 mole/liter $< M <$ 0.1 mole/liter. It is seen that CA assumption predicts the magnitude of double layer forces f_{dl} to

increase with larger molar concentration *M*, whereas f_{dl} decreases with *M* when HHF-CC assumption is used.

The van der Waals forces, f_{vdw} are always attractive and act in the same direction as pad-particle force f_p . Double layer forces f_{dl} on the other hand may be attractive or repulsive based on surface charges. However at small separation distance d_o, which is the case for two contacting surfaces, double layer forces f_{dl} are repulsive even for opposite charged surfaces as demonstrated in Figs 5.2b and 5.2c due to osmotic pressure component of the double layer force [3]. Therefore the effect of double layer forces f_{dl} is to decrease overall wafer-particle contact force f_w . This is expected to have a negative effect on the MRR.

5.2.2 Definition of removal force function (RFF)

Two different wear mechanisms, adhesive and abrasive wear, explained in Section 3.5, are considered in this study in order to predict MRR due to a single particle in the wafer-

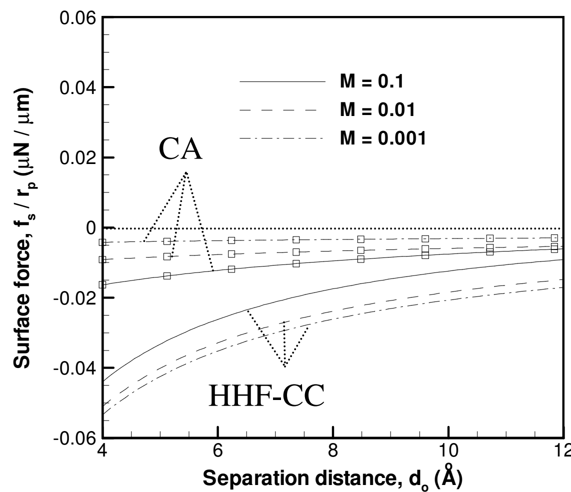

Fig. 5.3: The effect of molar concentration *M* of electrolyte on double layer force f_{dl} for $\Psi_{1,2}$ = 50 mV, 50 mV.

pad interface. Eqns (3.60) and (3.66) given for *material removal rate* due to *adhesive*, RR_{ad}^{sp} and *abrasive* wear, RR_{ab}^{sp}, respectively, are re-arranged as follows,

$$RR_{ad}^{sp} = f_w \left(\frac{k_w^{ad}}{H_w} V_r \right) = R_{ad}^{sp} \left(\frac{k_w^{ad}}{H_w} V_r \right) \tag{5.4}$$

$$RR_{ab}^{sp} = \left(\sqrt{\frac{2}{\pi^3}} \frac{f_w^{\ 3/2}}{r_p} \right) \left(\frac{k_w^{ab}}{H_w^{\ 3/2}} V_r \right) = R_{ab}^{sp} \left(\frac{k_w^{ab}}{H_w^{\ 3/2}} V_r \right) \tag{5.5}$$

Recall that V_r is relative velocity, f_w is wafer-particle contact force, r_p is particle radius, H_w is wafer hardness, k_w^{ad} and k_w^{ab} are wear coefficients for adhesive and abrasive wear, respectively. The MRR is investigated in our models by calculating the RFF for adhesive R_{ad}^{sp} and abrasive R_{ab}^{sp} wear, which are defined as,

$$R_{ad}^{sp} = f_w \tag{5.6}$$

$$R_{ab}^{sp} = \sqrt{\frac{2}{\pi^3}} \frac{f_w^{\ 3/2}}{r_p} \tag{5.7}$$

Note that a fundamental difference between the RFF due to adhesive and abrasive wear is the dependence on wafer-particle contact force, f_w. The RFF due to adhesive wear increases linearly with contact force $R_{ad}^{sp} \propto f_w$, whereas the RFF due to adhesive wear varies as $R_{ab}^{sp} \propto f_w^{\ 3/2}$. This difference is later shown to have a critical effect on the outcomes of adhesive and abrasive wear of the wafer.

5.2.3 Bi-layer hardness model

In CMP, material removal is achieved by a combination of mechanical and chemical effects. Chemicals in the slurry react with wafer surface forming a passivated layer and thus altering hardness H_w of the wafer. As shown in Eqns (5.4) and (5.5), change in hardness has direct consequences on MRR. However, note that MRR due to abrasive wear, RR_{ab}^{sp} has a stronger dependence on wafer hardness, RR_{ab}^{sp} α $1/H_w^{3/2}$ than MRR due to adhesive wear, RR_{ad}^{sp} α $1/H_w$. The "effective" hardness of wafer, H_w is used in Eqn (5.4) and (5.5) instead of passivated, H_{pw} or bulk wafer, H_{bw} hardness as hardness varies as a function of distance from wafer surface. The chemical reaction rate of wafer and chemicals in slurry, and the duration of the reaction determine hardness as a function of depth from surface. A diffusion driven mechanism has been proposed for reaction of wafer with slurry chemicals, where the chemicals responsible for passivation of wafer by forming oxides, also called oxidizers, are transported to wafer surface by slurry flow and diffuse into wafer thus creating a hardness gradient near the wafer surface [4]. Calota et al. [5] have shown experimentally for niobium wafers that various Nb_xO_y species are established within the top 7 nm of the surface. A bi-layer hardness model is adopted in this work in order to simply the hardness variation. The bi-layer hardness model [6] is described by three parameters, passivated wafer hardness H_{pw}, thickness t_{pw} of passivated layer, and bulk wafer hardness H_{bw} as follows, This model assumes that the wafer hardness, H_w is constant within the passivated layer, and wafer material at a depth, z larger than passivated layer thickness t_{pw}, $z > t_{pw}$ behaves as bulk wafer material as follows,

$$H_w(z) = \begin{cases} H_{pw} & z < t_{pw} \\ H_{bw} & z > t_{pw} \end{cases} \tag{5.8}$$

Note that a sudden transition from H_{pw} to H_{bw} is assumed at $z = t_{pw}$. In reality, the hardness of wafer is expected to vary more smoothly from surface into wafer [4,5]. The thickness of the passivated layer, t_{pw} relative to the indentation depth of particle, δ_w into the wafer is an important factor and it will affect the MRR. If the particle indentation δ_w is smaller than the thickness of passivated layer t_{pw}, ($\delta_w < t_{pw}$) (Fig. 5.4a), we assume that the contact pressure at wafer-particle interface is equal to hardness of passivated layer, H_{pw}. Then the wafer-particle contact force, f_w can be expressed by using the contact radius a_w as,

$$f_w = \frac{\pi a_w^2}{2} H_{pw} \qquad \text{for} \qquad \delta_w < t_{pw} \tag{5.9}$$

Note that the particle is considered to be sliding over the wafer, therefore only half of the contact area is engaged in contact. Fig. 5.4b shows the case where the contact force at

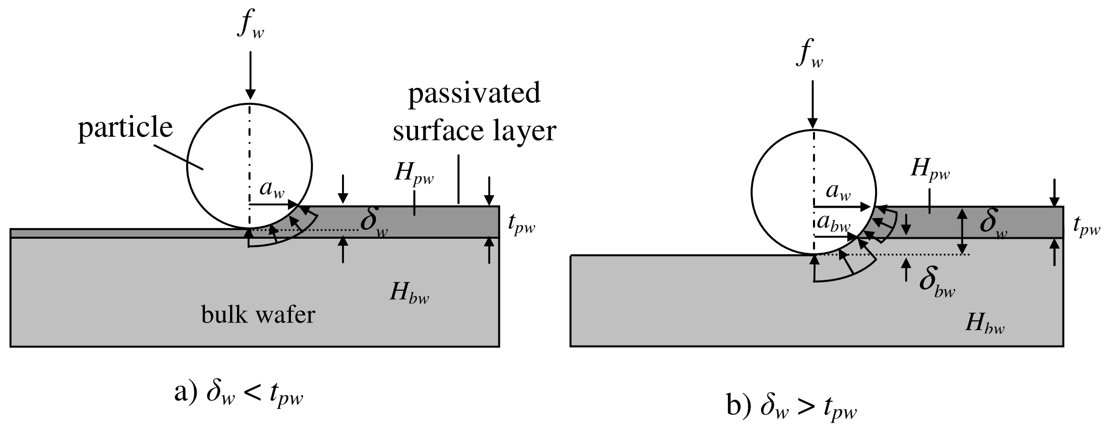

Fig. 5.4: Wafer-particle contact for two different conditions where a) indentation depth of particle is smaller than the thickness of passivated layer $\delta_w < t_{pw}$ and b) indentation depth of particle is larger than the thickness of passivated layer $\delta_w > t_{pw}$.

wafer-particle interface, f_w is sufficiently large for a particle to indent through passivated layer and make contact with bulk wafer, i.e indentation depth of the particle δ_w is larger than the thickness of passivated layer t_{pw}, ($\delta_w > t_{pw}$). The contact pressure acting at the wafer-particle interface is not uniform due to different hardness of passivated layer H_{pw} and bulk wafer H_{bw}. In this case, we assume that wafer-particle contact is sustained by the contributions from the contact pressure acting at particle-passivated layer and particle-bulk wafer interfaces as follows,

$$f_w = \frac{\pi\left(a_w^2 - a_{bw}^2\right)}{2} H_{pw} + \frac{\pi a_{bw}^2}{2} H_{bw} \qquad \text{for} \qquad \delta_w > t_{pw} \tag{5.10}$$

where a_w and a_{bw} are the contact radii at particle-passivated layer and particle-bulk wafer interfaces, respectively. By assuming that the indentation depths (δ_w and δ_{bw}) are small compared to particle radius r_p , the contact radii (a_{pw} and a_{bw}) can be shown to be related to the indentation depth as follows,

$$\delta_w = \frac{a_w^2}{2r_p} \qquad \text{and} \qquad \delta_{bw} = \frac{a_{bw}^2}{2r_p} \tag{5.11}$$

Using Eqns (5.9)-(5.11), the wafer-particle contact force, f_w can be expressed in terms of the indentation depth, δ_w as,

$$f_w = \pi r_p \delta_w H_{pw} \qquad \text{for} \qquad \delta_w < t_{pw} \tag{5.12}$$

$$f_w = \pi r_p \left(\delta_w - \delta_{bw}\right) H_{pw} + \pi r_p \delta_{bw} H_{bw} \qquad \text{for} \qquad \delta_w > t_{pw} \tag{5.13}$$

Indentation depth, δ_w is the summation of thickness of passivated layer, t_{pw} and indentation depth in bulk wafer, $\delta_w = t_{pw} + \delta_{bw}$. Therefore Eqn (5.13) reduces to;

$$f_w = \pi r_p \left[t_{pw} H_{pw} + \left(\delta_w - t_{pw} \right) H_{bw} \right] \qquad \text{for} \qquad \delta_w > t_{pw} \qquad (5.14)$$

Bulk wafer hardness, H_{bw} dominates wafer-particle contact if indentation depth δ_w is much larger than thickness of the passivated layer, $\delta_w >> t_{pw}$. In this condition, the effect of the passivated layer can be neglected and Eqn (5.14) can be simplified, by setting $t_{pw} = 0$, as follows,

$$f_w = \pi r_p \delta_w H_{bw} \qquad \text{for} \qquad \delta_w >> t_{pw} \qquad (5.15)$$

Eqns (5.12) and (5.14) can be summarized as follows:

$$f_w = \pi r_p \delta_w H_w(\delta_w) \qquad (5.16a)$$

where the effective wafer hardness H_w is defined as,

$$H_w(\delta_w) = \begin{cases} H_{pw} & \text{for} \quad \delta_w \le t_{pw} \\ \dfrac{t_{pw}}{\delta_w} H_{pw} + \left(1 - \dfrac{t_{pw}}{\delta_w} \right) H_{bw} & \text{for} \quad \delta_w > t_{pw} \end{cases} \qquad (5.16b)$$

Note that effective hardness is dominated by bulk wafer hardness, $H_w \rightarrow H_{bw}$ as indentation depth becomes very large $\delta_w \rightarrow \infty$. Eqn (5.16) is used in the model to characterize the effect of the slurry chemicals on the MRR. The implementation of Eqn (5.16) in the model will be explained later in this chapter (Section 5.6).

5.3 Removal Force Function (RFF) in MP Contact Model

The RFF in the multi-particle (MP) contact model, R^{mp}, is calculated by integrating the RFF due to each particle, R^{sp} over all particles active in contact in a form similar to Eqns (4.10) and (4.11), used to determine particle contact pressure p_p^{mp} in the MP contact model using the contact force on each particle f_p. The RFF in the MP contact model, R^{mp} for particle contact $d_{sep} > 0$ and mixed contact $d_{sep} < 0$ regimes can be calculated using,

$$R^{mp} = \begin{cases} \eta_v \int_{\frac{d_{sep}}{2}}^{\infty} 2r_p R^{sp} \Phi_p(r_p) dr_p & \text{if} \quad d_{sep} > 0 \\ \eta_v \int_0^{\infty} 2r_p R^{sp} \Phi_p(r_p) dr_p & \text{if} \quad d_{sep} < 0 \end{cases} \tag{5.17}$$

Note that R^{mp} given in Eqn (5.17) is a function of the separation distance d_{sep}. However, from a practical point of view, it makes more sense to report the RFF as a function of the contact pressure p_c^{mp} acting between the two surfaces. In order to obtain the RFF as a function of contact pressure p_c^{mp}, the separation distance d_{sep} is used as an intermediate parameter and the RFF is matched against contact pressure p_c^{mp} by means of look-up tables created for relating both p_c^{mp} and the RFF to d_{sep} using Eqns (4.10), (4.11) and (5.17). In fact, a similar approach is used to estimate other parameters such as particle contact pressure ratio p_p^{mp} / p_c^{mp} and direct contact area ratio A_d^{mp} as a function of contact pressure p_c^{mp}.

If we neglect the effect of surface forces in Eqn (5.3) $f_s = 0$, the wafer-particle contact force becomes equal to pad-particle contact force, $f_w = f_p$. Furthermore, using the non-dimensional parameters of the MP contact model (Table 4.1) in Eqns (5.6), (5.7) and (5.17), one can find that the RFF due to adhesive and abrasive wear in single particle (R_{ad}^{sp} and R_{ab}^{sp}) and multi-particle contact models (R_{ad}^{mp} and R_{ab}^{mp}) can be expressed in non-dimensional form as,

$$\tilde{R}_{ad}^{sp} = \frac{R_{ad}^{sp}}{E_s \sigma_p^2} \quad \text{and} \quad \tilde{R}_{ab}^{sp} = \frac{R_{ab}^{sp}}{E_s^{3/2} \sigma_p^2} \tag{5.18}$$

$$\tilde{R}_{ad}^{mp} = \frac{R_{ad}^{sp}}{E_s} \quad \text{and} \quad \tilde{R}_{ab}^{mp} = \frac{R_{ab}^{mp}}{E_s^{3/2}} \tag{5.19}$$

where E_s is pad elastic modulus and σ_p is the standard deviation of particle size distribution. The RFF due to adhesive $\tilde{R}_{ad}^{mp}$ and abrasive wear $\tilde{R}_{ab}^{mp}$ in the MP contact model is plotted in non-dimensional form in Fig. 5.5. It is seen that the RFF due to adhesive wear $\tilde{R}_{ad}^{mp}$ for different particle concentrations η_w are the same at low contact pressure, $\tilde{p}_c^{mp}$ where particle contact regime operates with direct contact area ratio, A_d^{mp} = 0 (Fig. 5.6a) and particle contact pressure ratio, $p_p^{mp} / p_c^{mp} = 1$ (Fig. 5.6b). Fig. 5.5a also shows that the RFF in the MP contact model $\tilde{R}_{ad}^{mp}$ is linearly proportional to particle contact pressure $\tilde{p}_p^{mp}$, ($\tilde{R}_{ad}^{mp} \propto \tilde{p}_p^{mp}$). This can be explained by recalling that the RFF of a single particle for adhesive wear is related to single particle contact force as $\tilde{R}_{ad}^{sp} \propto \tilde{f}_w$.

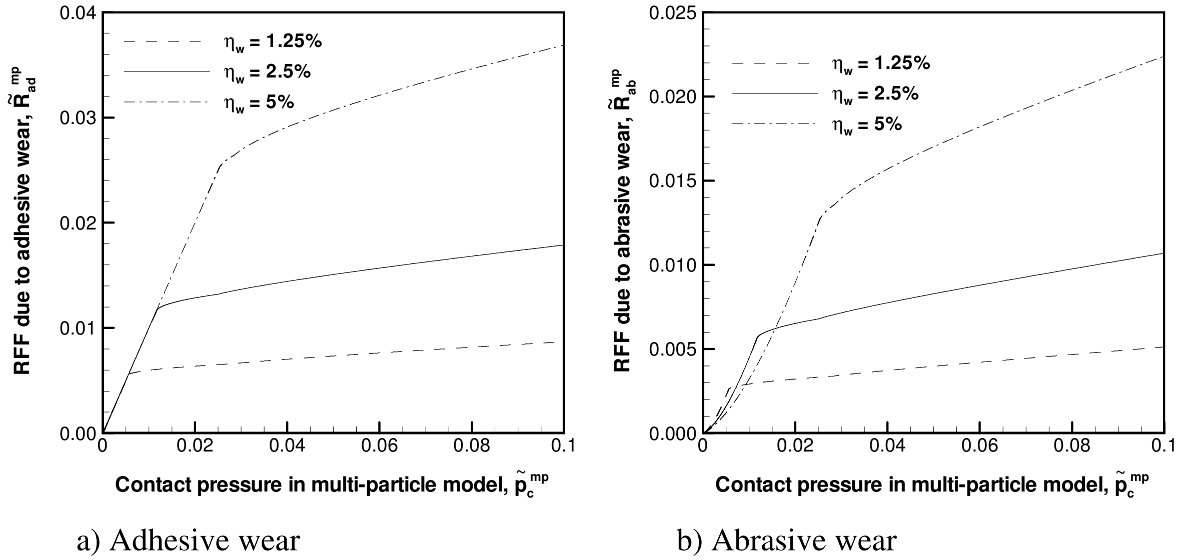

a) Adhesive wear b) Abrasive wear

Fig. 5.5: RFF due to adhesive, $\widetilde{R}_{ad}^{mp}$ and abrasive wear, $\widetilde{R}_{ab}^{mp}$ in multi-particle model for different particle concentrations η_w.

A different behavior is observed for the RFF due to abrasive wear $\widetilde{R}_{ab}^{mp}$, in Fig. 5.5b. In particle contact regime, the RFF due to abrasive wear $\widetilde{R}_{ab}^{mp}$ decreases with higher particle concentration η_w. This can be explained by considering the relation between the RFF of a single particle for abrasive wear $\tilde{R}_{ab}^{sp}$ and single particle contact force $\tilde{f}_w$ as $\tilde{R}_{ab}^{sp} \propto \tilde{f}_w^{3/2}$. As particle concentration η_w becomes higher, thus increasing the number of active particles $\tilde{\eta}_a^{mp}$, the mean contact force on each particle found by $\tilde{f}_w^m = \tilde{p}_p^{mp} / \tilde{\eta}_a^{mp}$ decreases since particle contact pressure $\tilde{p}_p^{mp}$ is constant in particle contact regime. This reduction in mean particle contact force $\tilde{f}_w^m$ causes the RFF due to abrasive wear $\tilde{R}_{ab}^{mp}$ to become smaller with higher particle concentration η_w. Fig. 5.5b also shows that the relationship between the RFF due to abrasive wear $\tilde{R}_{ab}^{sp}$ and the contact pressure p_c^{mp} is no longer linear in particle contact regime as opposed to the case of adhesive wear.

Fig. 5.6 shows that at a critical contact pressure p_c^{mp}, the transition from particle to mixed contact regime occurs. With higher particle concentration η_w, the occurrence of direct contact is retarded and the critical contact pressure for direct contact becomes higher. Once contact pressure, p_c^{mp} is above its critical value, i.e. mixed contact regime starts to operate, the rate of increase of the RFF due to adhesive and abrasive wear, R^{mp} becomes smaller due to the fact that a fraction of contact pressure is utilized by direct contact, $p_p^{mp} / p_c^{mp} < 1$ and available contact pressure p_p^{mp} for the RFF is lower.

5.4 Removal Force Function (RFF) in SA Contact Model

In this section, the RFF due to the particles trapped between a pad asperity and a flat wafer R^s is modeled. The contact pressure distribution p_c^s in the pad asperity-wafer interface is substituted into the MP contact model for obtaining the RFF for adhesive R_{ad}^s

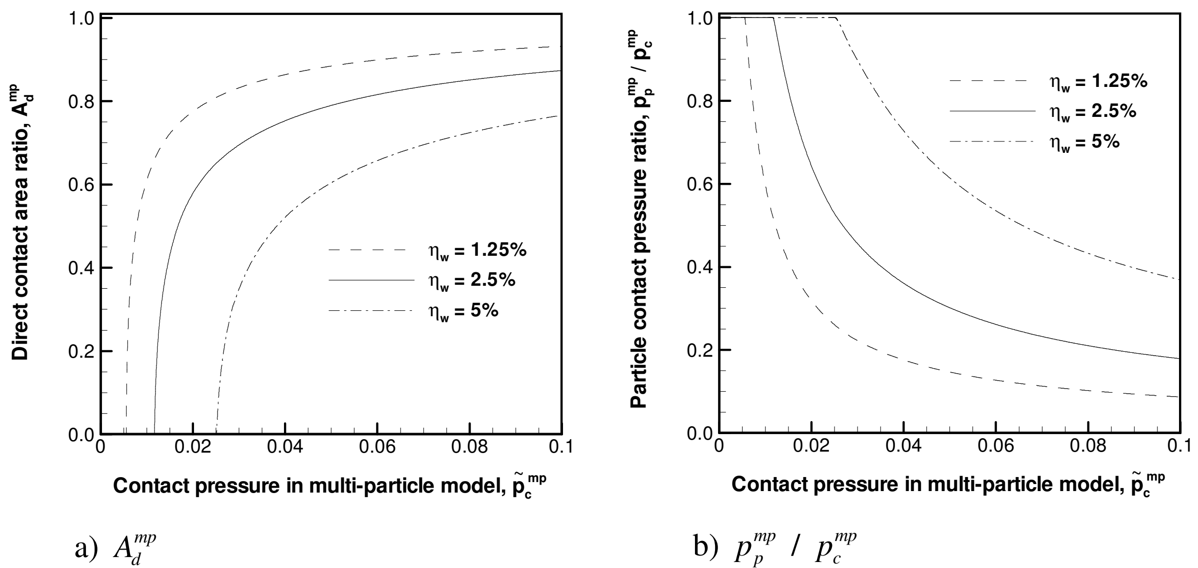

a) A_d^{mp} b) p_p^{mp} / p_c^{mp}

Fig. 5.6: The direct contact area ratio A_d^{mp} and particle contact pressure ratio, p_p^{mp} / p_c^{mp} in multi-particle model for different particle concentrations η_w.

and abrasive wear R^{s}_{ad} due to the contact of a single asperity. Different assumptions for contact pressure distribution p^{s}_{c} between the asperity and the wafer are employed. First, the interfacial particles are assumed to influence single asperity contact pressure p^{s}_{c} captured by the SA contact model, $p^{s}_{c} = p^{sa}_{c}$. In this case, the RFF is calculated by using the contact pressure distribution given by the SA contact model p^{sa}_{c} in Section 5.4.1. Next, the effect of the interfacial particles on single asperity contact behavior is neglected. And in this case, Hertz contact relations are utilized for calculating the RFF of a single asperity, using Hertz contact pressure distribution in Section 5.4.2 ($p^{s}_{c} = p^{H}_{c}$), and mean Hertz contact pressure in Section 5.4.3 ($p^{s}_{c} = p^{Hm}_{c}$).

5.4.1 Contact pressure by SA contact model

The contact pressure distribution p^{sa}_{c} obtained by the SA contact model is used to determine the RFF by a single asperity R^{s-sa}. This is considered to be most realistic situation for simulating actual contact condition at each pad asperity contact where the existence of interfacial particles may alter the contact pressure distribution p^{sa}_{c}.

The contact zone at pad asperity-wafer interface is assumed to consist of small annular contact segments with inner radius a_i, where the contact pressure in each contact segment is determined by the contact pressure distribution given by the SA contact model p^{sa}_{c}. The RFF in each contact segment is found by finding the RFF in the MP contact model R^{mp} corresponding to the contact pressure $p^{mp}_{c} = p^{sa}_{c}$. The RFF for a single asperity,

R^{s-sa} is then determined by integrating the RFF for each contact segment forming the entire contact interface as,

$$R^{s-sa} = \int_0^{a^{sa}} 2\pi a R^{mp}\left(p_c^{sa}(a)\right) da \tag{5.20}$$

where a^{sa} is the single asperity contact radius obtained from look-up tables produced by the SA contact model (Figs 4.25a and 4.30a).

5.4.2 Hertzian contact pressure

Each pad asperity contact can also be assumed to behave as Hertzian contact if the influence of particles on contact pressure distribution is neglected. This assumption leads to the simplification of the model to calculate the RFF of a single asperity, R^{s-H} as contact pressure distribution, p_c^H and contact radius, a^H in Eqn (5.20) can be described by closed-form equations;

$$R^{s-H} = \int_0^{a^H} 2\pi a R^{mp}\left(p_c^H(a)\right) da \tag{5.21}$$

where Hertz contact gives p_c^H and a^H as,

$$p_c^H(r^a) = \frac{3f_c^s}{2\pi {a^H}^2}\left[1-\left(\frac{r^a}{a^H}\right)^2\right]^{1/2} \text{ and } a^H = \left(\frac{3f_c^s R_s}{4E_s}\right)^{1/3} \tag{5.22}$$

5.4.3 Mean Hertzian contact pressure

This is a further simplification of the Hertz contact assumption, where mean contact pressure p_c^{Hm} predicted by Hertz contact is used to calculate the RFF for a single asperity R^{s-Hm}. In this case, the contact zone is not divided into contact segments, but the mean contact pressure p_c^{Hm} given by Hertz contact is assumed to be acting throughout the entire contact zone. The mean contact pressure p_c^{Hm} can be directly substituted into the MP contact model to find the RFF for a unit area of contact $R^{mp}\left(p_c^{Hm}\right)$, which can then be multiplied by the contact area $\pi {a^H}^2$ to obtain the RFF of a single asperity R^{s-Hm} as,

$$R^{s-Hm} = \pi {a^H}^2 R^{mp}\left(p_c^{Hm}\right) \tag{5.23}$$

where mean contact pressure p_c^{Hm} is given by Hertz contact as a function of contact force f_c^s as,

$$p_c^{Hm} = \frac{f_c^s}{\pi {a^H}^2} \tag{5.24}$$

In addition to the RFF, the approach explained in Sections 5.4.1 – 5.4.3, are used to compute the other important variables of a single asperity contact. These include the direct contact area, A_d^s (A_d^{sa}, A_d^H, A_d^{Hm}), the particle contact force, f_p^s (f_p^{sa}, f_p^H, f_p^{Hm}) and the number of active particles, n_a^s (n_a^{sa}, n_a^H, n_a^{Hm}). Similar equations to Eqns (5.20), (5.21) and (5.23) are used, where the RFF function R^{mp} for the MP contact model is

replaced by the functions for direct contact area A_d^{mp}, particle contact pressure p_p^{mp} and number of active particles n_a^{mp}.

5.4.4 Removal force function (RFF) due to single asperity contact

The non-dimensional RFF due to adhesive $\tilde{R}_{ad}^{s-sa}$ $(= R_{ad}^s / E_s \sigma_p^2)$ and abrasive wear $\tilde{R}_{ab}^{s-sa}$ $(= \dfrac{R_{ab}^s}{E_s^{3/2} \sigma_p^2})$ in single asperity contact are calculated as a function of dimensionless asperity contact force, $\tilde{f}_c^s$ $(= f_c^s / (E_s \sigma_p^2))$ in the range $10^3 < \tilde{f}_c^s < 10^6$ using the SA contact model as explained in Section 5.4.1. Fig. 5.7a shows that the RFF for adhesive wear $\tilde{R}_{ad}^{s-sa}$ does not depend on particle concentration η_w in particle contact regime, which prevails at low contact force, $\tilde{f}_c^s$. As the contact force $\tilde{f}_c^s$ is increased, the direct contact starts to occur for low particle concentration η_w causing the rate of increase in the RFF for adhesive wear $\tilde{R}_{ad}^{s-sa}$ with $\tilde{f}_c^s$ to become smaller. This trend is explained by considering the fraction of the applied load carried by particle contacts f_p^s / f_c^s, which decreases with higher asperity contact force $\tilde{f}_c^s$ (Fig. 4.25), thus having a detrimental effect on the RFF for adhesive wear $\tilde{R}_{ad}^{s-sa}$. A further increase in the contact force $\tilde{f}_c^s$ results in a similar effect for higher particle concentrations η_w. At high asperity contact force $\tilde{f}_c^s$, the RFF due to adhesive wear $\tilde{R}_{ad}^{s-sa}$ increases with higher particle concentration η_w.

A different trend is observed for the RFF due to abrasive wear $\tilde{R}_{ab}^{s-sa}$ in single asperity contact (Fig. 5.7b). The RFF for abrasive wear $\tilde{R}_{ab}^{s-sa}$ decreases with higher particle

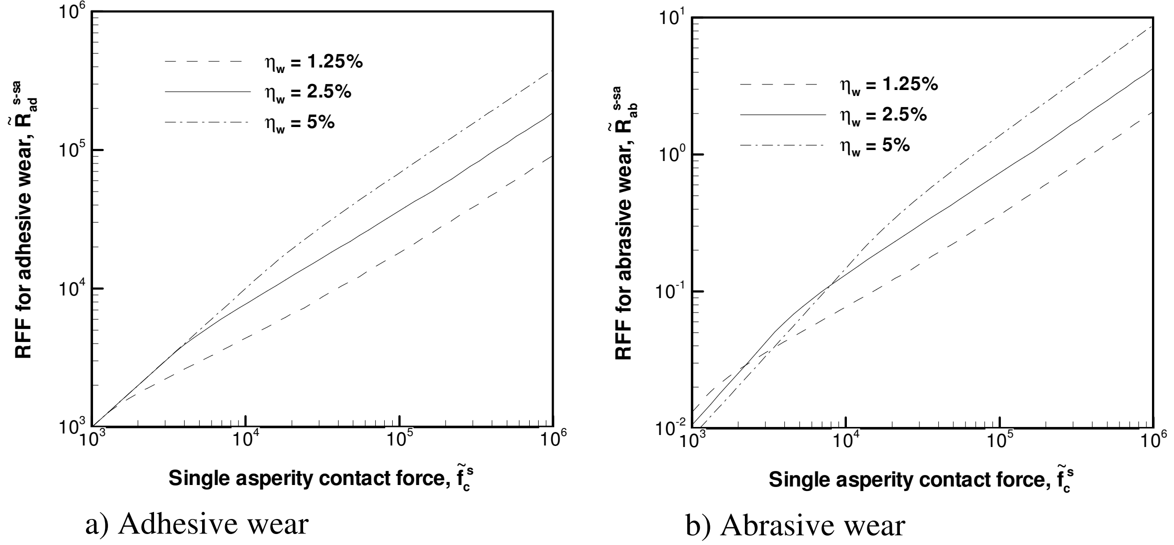

a) Adhesive wear   b) Abrasive wear

Fig. 5.7: The RFF due to the contact of a single asperity for a) adhesive wear $\tilde{R}_{ad}^{s-sa}$ and b) abrasive wear $\tilde{R}_{ab}^{s-sa}$ for different particle concentration η_w.

concentration η_w in particle contact regime at low contact force $\tilde{f}_c^s$. This trend was also determined the RFF due to abrasive wear R_{ab}^{mp} in the MP contact model (Fig. 5.5b). As the contact regime shifts to mixed contact at high asperity contact force $\tilde{f}_c^s$, the RFF due to abrasive wear $\tilde{R}_{ab}^{s-sa}$ increases with higher particle concentration η_w.

In Fig. 5.8, the RFF due to a single asperity contact $\tilde{R}^{s-sa}$ is plotted for different asperity radius $\tilde{R}_s$. It is seen that the RFF due to adhesive wear $\tilde{R}_{ad}^{s-sa}$ does not vary with asperity radius $\tilde{R}_s$ at low contact force $\tilde{f}_c^s$ as particle contact regime operates at low $\tilde{f}_c^s$ (Fig. 5.8a). In this regime, the RFF due to abrasive wear $\tilde{R}_{ab}^{s-sa}$ decreases with larger asperity radius $\tilde{R}_s$ (Fig. 5.8b). At high contact force $\tilde{f}_c^s$, the RFF due to both adhesive and abrasive wear ($\tilde{R}_{ad}^{s-sa}$ and $\tilde{R}_{ab}^{s-sa}$) increase as asperity radius $\tilde{R}_s$ becomes larger. This result

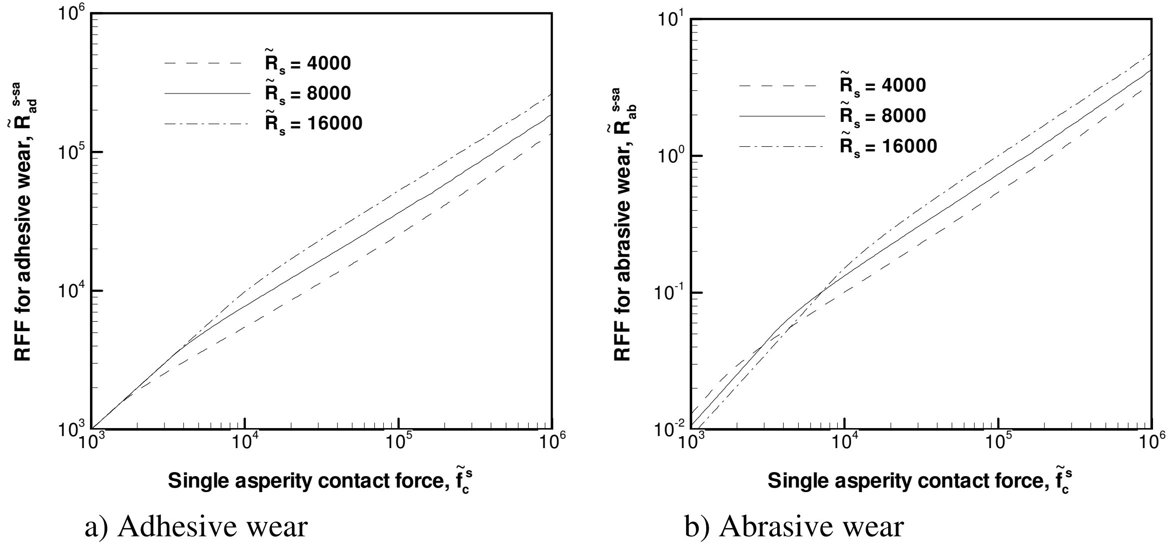

a) Adhesive wear b) Abrasive wear

Fig. 5.8: The RFF due to the contact of a single asperity for a) adhesive wear $\tilde{R}_{ad}^{s-sa}$ and b) abrasive wear $\tilde{R}_{ab}^{s-sa}$ for different asperity radius R_s.

can be explained by considering the particle contact force ratio f_p^s / f_c^s illustrated in Fig. 4.30 for different asperity radius $\tilde{R}_s$. The contact is spread over a larger area in the case of large asperity radius $\tilde{R}_s$, which decreases the tendency of particle to be embedded in the pad. As a result, particle contact force ratio f_p^s / f_c^s increases with larger asperity radius $\tilde{R}_s$, thus increasing the RFF for a single asperity $\tilde{R}^{s-sa}$.

5.4.5 Error of different contact pressure distributions on RFF of single asperity

In this section, different assumptions for single asperity contact pressure, p_c^s as explained in Sections 5.4.1 – 5.4.3 is used to model the RFF due to single asperity contact. The error introduced in the calculation of the RFF of a single asperity by using the Hertzian contact pressure R^s (R^{s-H} or R^{s-Hm}) instead of contact pressure given by the SA contact

model R^{s-sa} is quantified by the ratio $e^s = \left(R^{s-sa} - R^s\right) / R^{s-sa}$. The error is determined for the Hertzian contact pressure distribution e^{s-H} by setting $R^s = R^{s-H}$ and the mean Hertzian contact pressure e^{s-Hm} by setting $R^s = R^{s-Hm}$.

<u>Effect of particle concentration (RFF due to adhesive wear)</u>

Fig. 5.9 shows the error (e^H and e^{Hm}) of the RFF based on Hertzian contact pressure (R^{s-H} and R^{s-Hm}) for different particle concentration, $1.25\% < \eta_w < 5\%$ using asperity radius $\tilde{R}_s$ $(= R_s / \sigma_p) = 8000$. Fig. 5.9a shows that Hertzian contact assumption under-predicts the RFF due to adhesive wear, R_{ad}^s. The error increases with contact force, $\tilde{f}_c^s$ at small $\tilde{f}_c^s$, reaches a maximum and finally decreases as $\tilde{f}_c^s$ is further increased. This behavior is attributed to two separate events occurring at small and large contact force, $\tilde{f}_c^s$. At small $\tilde{f}_c^s$, all of the load on the asperity is carried by the particles, and as a result,

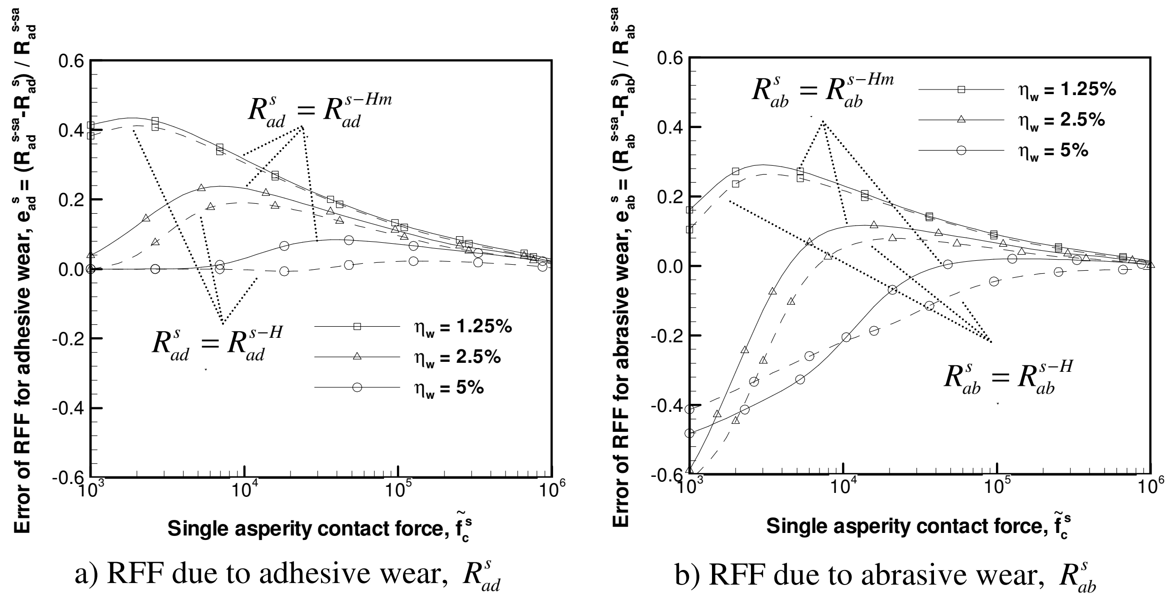

Fig. 5.9: The error of RFF of a single asperity for a) adhesive wear e_{ad}^s and b) abrasive wear e_{ab}^s introduced by contact pressure distribution based on Hertz contact ($p_c^s = p_c^H$ or $p_c^s = p_c^{Hm}$).

to adhesive wear, R_{ad}^{s} as a result. This is demonstrated in Fig. 5.10 indicating direct contact area $\tilde{A}_{d}^{s}$ (= A_{d}^{s} / $\sigma_p{}^2$) as $\tilde{A}_{d}^{s}$ = 0 and particle contact force ratio f_{p}^{s} / f_{c}^{s} as f_{p}^{s} / f_{c}^{s} = 1 at small contact force, $\tilde{f}_{c}^{s}$ especially for high particle concentration, i.e. η_w = 5%. As contact force, $\tilde{f}_{c}^{s}$ increases, the error of Hertz contact model increases because the

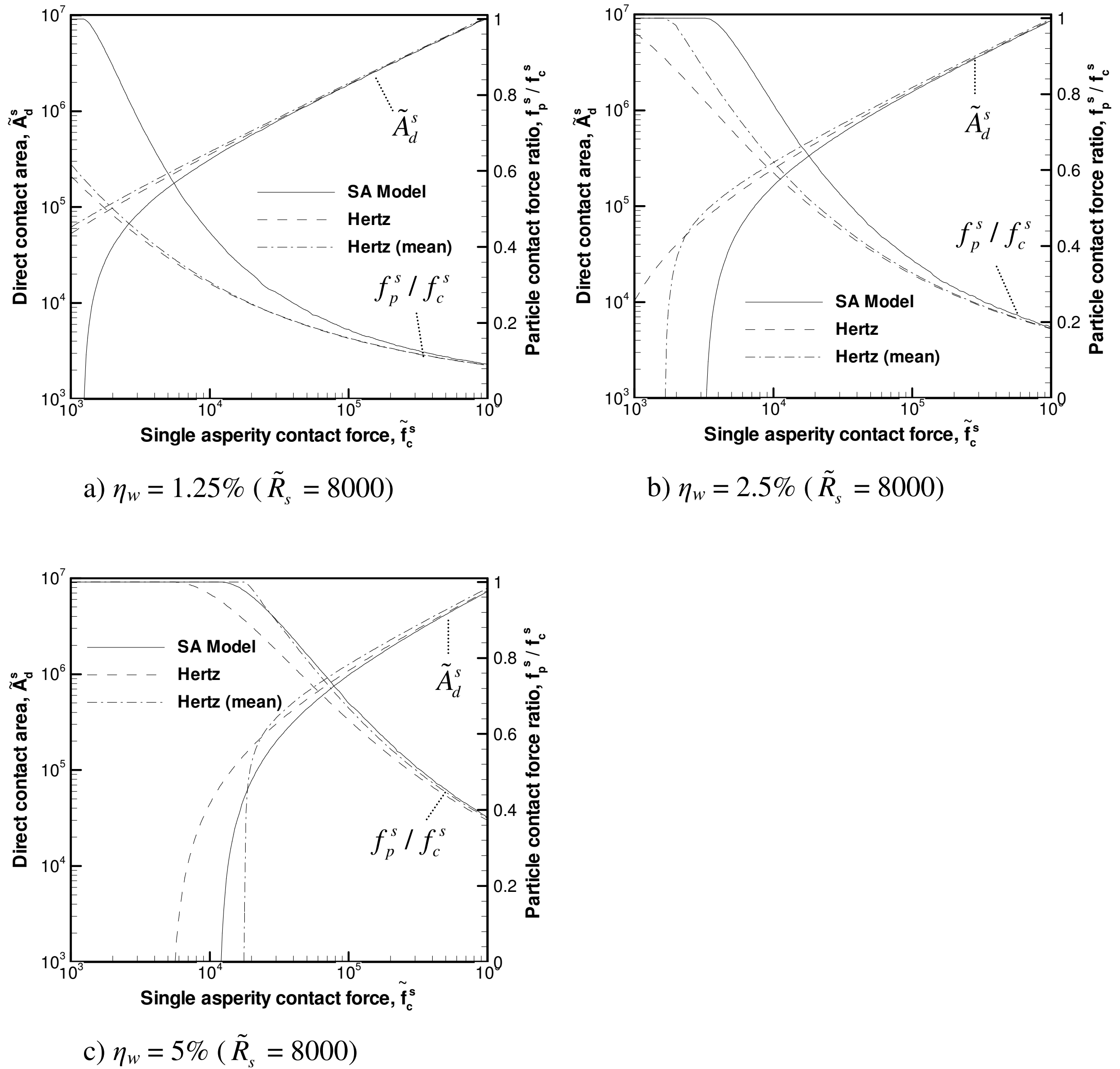

a) η_w = 1.25% ($\tilde{R}_s$ = 8000)

b) η_w = 2.5% ($\tilde{R}_s$ = 8000)

c) η_w = 5% ($\tilde{R}_s$ = 8000)

Fig. 5.10: The direct contact area $\tilde{A}_{d}^{s}$ and particle contact force ratio f_{p}^{s} / f_{c}^{s} for different particle concentration η_w.

direct contact between pad and wafer are predicted to start at different $\tilde{f}_c^s$ values by the SA contact model and Hertz contact. The interfacial particles in the SA contact model retard the direct contact by distributing the contact pressure over a larger area. Since direct contact prevails at small contact force $\tilde{f}_c^s$ for both of the Hertz contact assumptions, particle contacts is responsible for sustaining a smaller fraction of $\tilde{f}_c^s$, thereby decreasing the RFF due to adhesive wear, R_{ad}^s for Hertz contact assumptions relative to the SA contact model.

At high contact force $\tilde{f}_c^s$, the error of Hertz contact for calculating the RFF decreases since the effect of particles on contact pressure distribution captured by the SA contact model becomes small as all the particles become embedded in deformable surface of an asperity. Therefore the error of Hertz contact for calculating the RFF due to adhesive wear, R_{ad}^s becomes less than 10%, $e^s < 0.1$ for all particle concentrations, $1.25\% < \eta_w < 5\%$ studied when the contact force is greater than $\tilde{f}_c^s > 1\text{x}10^5$.

Another interesting result demonstrated in Fig. 5.9a is that the error of Hertz contact for calculating the RFF due to adhesive wear. R_{ad}^s is greatest for lowest particle concentration, $\eta_w = 1.25\%$ studied. This is in contrast with the findings of the SA contact model, where higher particle concentration, η_w induces a greater deviation for contact pressure from Hertz contact. This result can be explained by the occurrence of direct contact at different critical contact force, $\tilde{f}_c^s$ predicted by the SA contact model and Hertz contact causing a significant error for the RFF due to adhesive wear R_{ad}^s. In the

range of contact force where contact pressure distribution is significantly different for the SA contact model and Hertz contact, $\tilde{f}_c^s < 10^4$, particle contact regime is active for high particle concentration η_w, while direct contact already takes place for low η_w at different $\tilde{f}_c^s$ for the SA contact model and Hertz contact. Despite the fact that difference in contact pressure distribution between the SA contact model and Hertz contact is greater for higher particle concentration η_w, effect of direct contact is responsible for the increased error at low η_w.

Effect of particle concentration (RFF due to abrasive wear)

Fig. 5.9b shows a different trend for the RFF due to abrasive wear R_{ab}^s. It is seen that Hertz contact assumption for contact pressure may over- or under-predict the RFF due to abrasive wear depending on contact force $\tilde{f}_c^s$. The fundamental difference between material removal due to adhesive and abrasive wear is their dependence on number of active particles n_a^s in particle contact regime. The RFF due to adhesive wear R_{ad}^s does not vary with number of active particles n_a^s, whereas the RFF due to abrasive wear R_{ab}^s decreases with larger n_a^s. At small contact force $\tilde{f}_c^s$, the SA contact model predicts a smaller RFF for abrasive wear R_{ab}^s for high particle concentrations, η_w, as particle contact regime is active and number of active particles, n_a^s is greater for the SA contact model (Fig. 5.11). A smaller RFF due to abrasive wear R_{ab}^s is predicted by the Hertz contact model at low η_w, because the mixed contact regime is active. At large $\tilde{f}_c^s$, the RFF

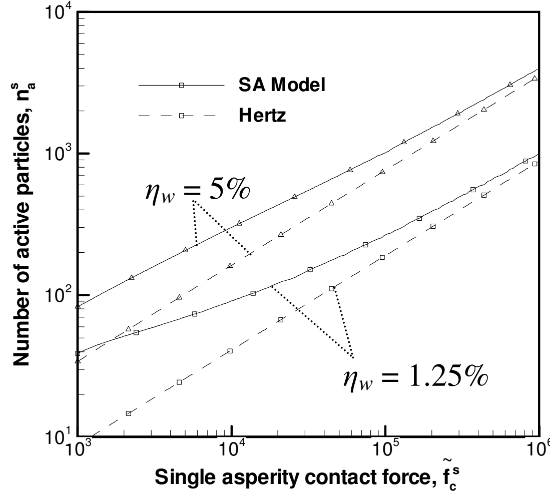

Fig. 5.11: The number of active particles n_a^s for different particle concentrations η_w.

predictions become similar for different models, i.e. the error is less than 10%, $e^s < 0.1$ for $\tilde{f}_c^s > 10^5$.

Effect of asperity radius

The effect of asperity radius, $\tilde{R}_s$ ($= R_s / \sigma_p^2$) on the error of Hertz contact (e_{ad}^s and e_{ab}^s) for calculating the RFF due to adhesive and abrasive wear is presented in Figs. 5.12 and 5.13, respectively. The effect of asperity radius $\tilde{R}_s$ on the error of Hertz contact e^s can be explained in a similar manner as the effect of particle concentration η_w. Although larger asperity radius $\tilde{R}_s$ increases the influence of particles on contact pressure distribution p_c^s, the maximum error e_{ad}^s found in the RFF due to adhesive wear R_{ad}^s for large asperity radius $\tilde{R}_s$ = 16000 is greater than small asperity radius $\tilde{R}_s$ = 4000. For an asperity with small radius e.g. $\tilde{R}_s$ = 4000, direct contact occurs at a smaller critical contact force $\tilde{f}_c^s$, which is different for the SA contact model and Hertz contact. As the

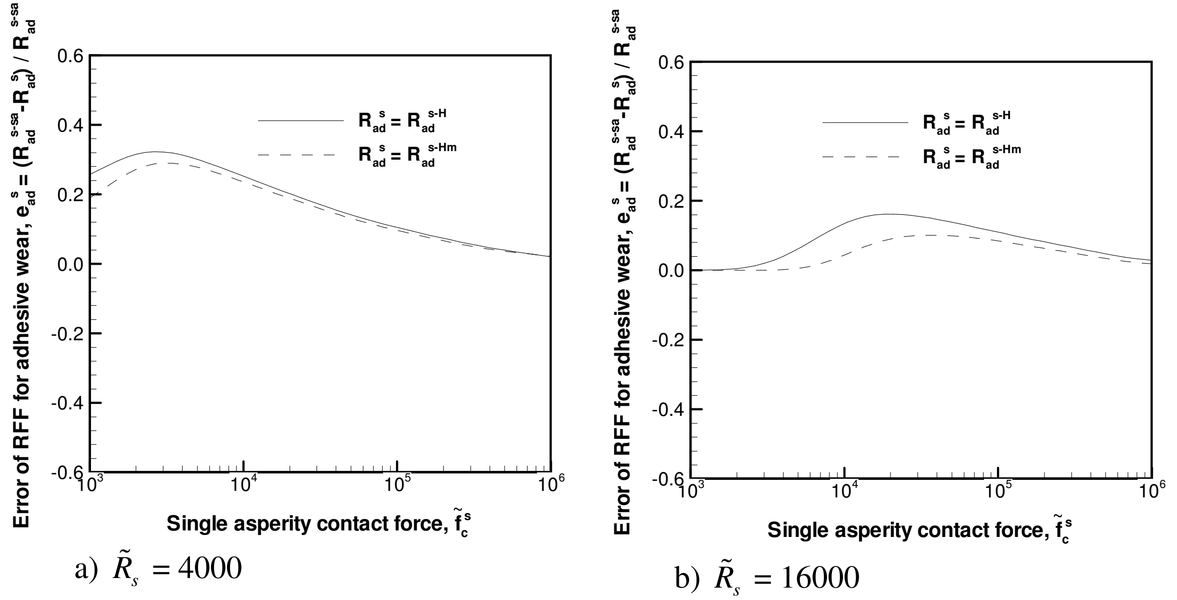

a) $\tilde{R}_s = 4000$ b) $\tilde{R}_s = 16000$

Fig. 5.12: The error of RFF due to adhesive wear e_{ad}^{s} of a single asperity introduced by contact pressure distribution based on Hertz contact ($p_c^s = p_c^H$ or $p_c^s = p_c^{Hm}$) for asperity radius a) $\tilde{R}_s = 4000$ and b) $\tilde{R}_s = 16000$.

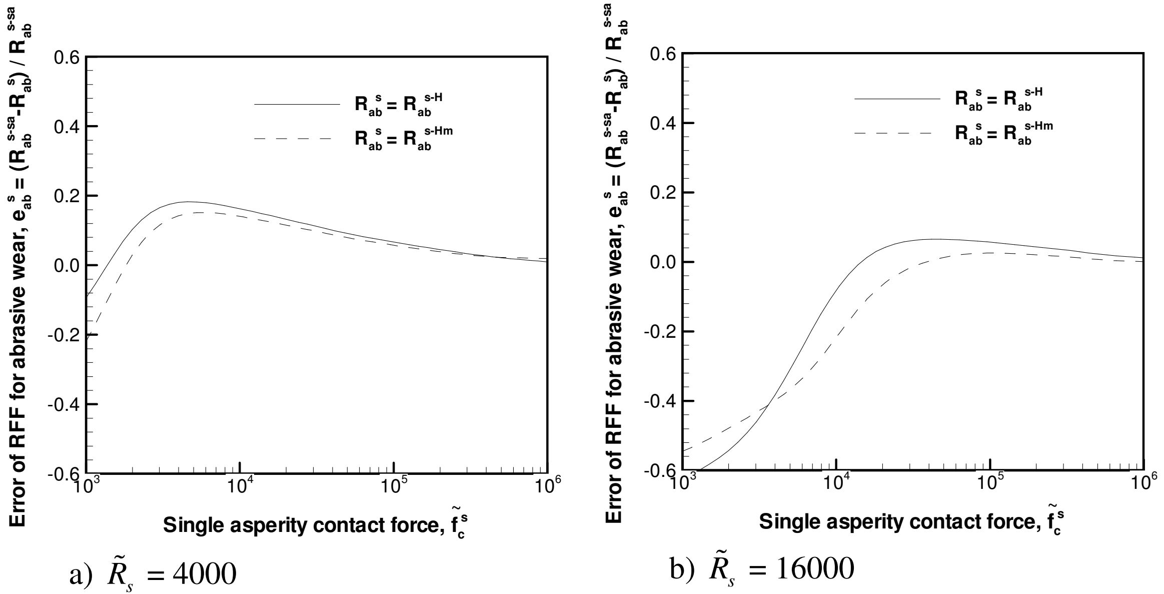

a) $\tilde{R}_s = 4000$ b) $\tilde{R}_s = 16000$

Fig. 5.13: The error of RFF due to abrasive wear e_{ab}^{s} of a single asperity introduced by contact pressure distribution based on Hertz contact ($p_c^s = p_c^H$ or $p_c^s = p_c^{Hm}$) for asperity radius a) $\tilde{R}_s = 4000$ and b) $\tilde{R}_s = 16000$.

contact force $\tilde{f}_c^s$ is increased, the error of Hertz contact e_{ad}^s becomes more significant since the direct contact starts to develop at different rates for the SA contact model and Hertz contact (Fig. 5.14). A further increase in contact force $\tilde{f}_c^s$ causes the effect of particles to diminish decreasing the error of Hertz contact e_{ad}^s at high $\tilde{f}_c^s$.

The maximum error of Hertz contact for the RFF due to abrasive wear e_{ab}^s increases with asperity radius $\tilde{R}_s$ as shown in Fig. 5.13b. This is attributed to the influence of asperity radius on contact pressure distribution p_c^s, where a greater deviation from Hertz contact is seen for a large asperity e.g. $\tilde{R}_s$ = 16000 when the effect of interfacial particles is considered. As a result of the difference in contact pressure distribution p_c^s, number of

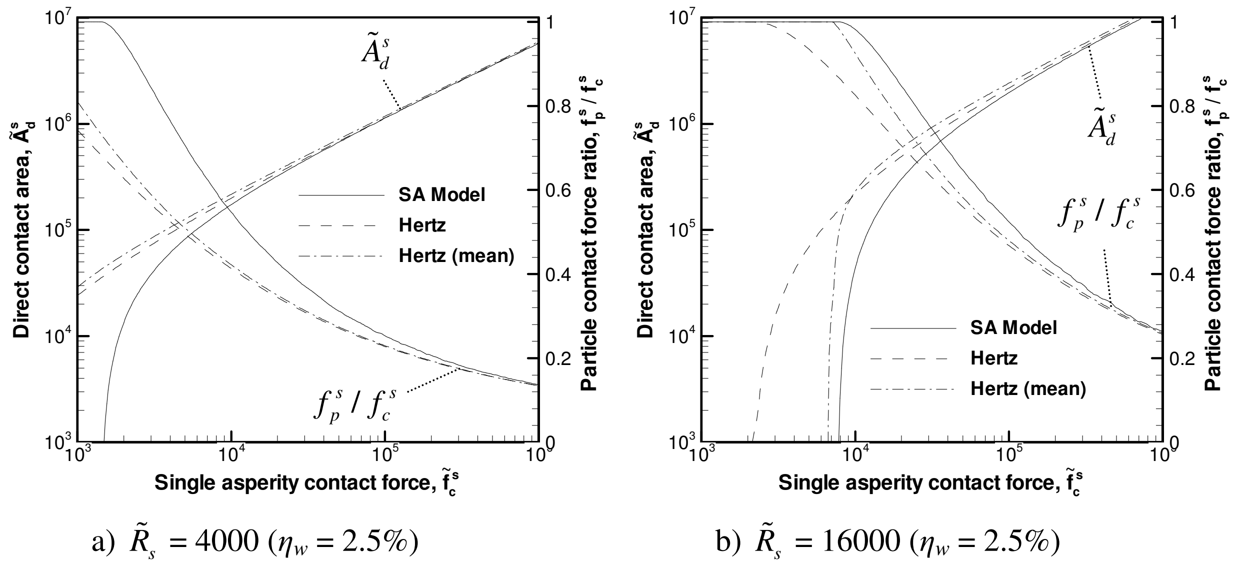

Fig. 5.14: The direct contact area $\tilde{A}_d^s$ and particle contact force ratio f_p^s / f_c^s for different asperity radius $\tilde{R}_s$.

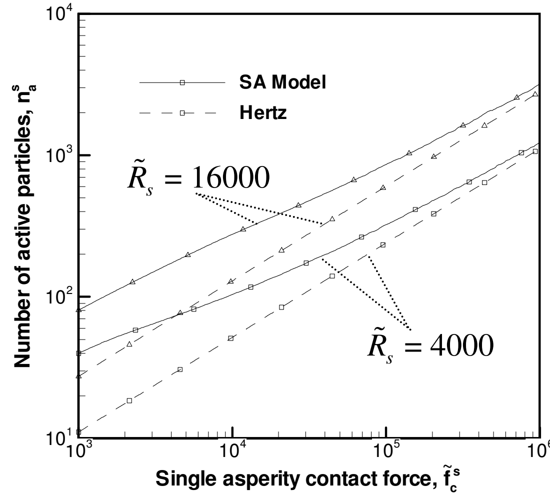

Fig. 5.15: The number of active particles n_a^s for different asperity radius $\tilde{R}_s$.

active particles n_a^s calculated using the SA contact model is higher than that of Hertz contact as shown in Fig. 5.15. Due to this effect, a larger RFF due to abrasive wear R_{ab}^s is predicted by Hertz contact and the error of Hertz contact increases with larger asperity radius $\tilde{R}_s$.

5.5 Removal Force Function (RFF) in MA Contact Model

The RFF calculated for a single asperity, R^s in Section 5.4 is used in a multi-asperity (MA) contact model to calculate the RFF of pad-wafer rough contact. For a given asperity density η_s, asperity radius R_s, asperity summit height distribution Φ_s and separation distance d_{wp}, the total RFF achieved by all asperities in contact can be determined as follows,

$$R = \eta_s \int_{d_{wp}}^{\infty} R^s \Phi_s\left(z_s\right) dz_s \qquad (5.29)$$

The RFF achieved by a single asperity R^s is obtained by using contact pressure distribution given by the SA contact model, $R^s = R^{s-sa}$ and mean Hertzian contact pressure acting at each asperity contact $R^s = R^{s-Hm}$ as explained in Section 5.4. Using R^{s-sa} (Eqn (5.20)) and R^{s-Hm} (Eqn (5.23)) to substitute for R^s in Eqn (5.29), one can find;

$$R^{sa} = \eta_s \int_{d_{wp}}^{\infty} \int_{0}^{a^{sa}} 2\pi a R^{mp} \left(p_c^{sa}(a) \right) da \Phi_s \left(z_s \right) dz_s \tag{5.30a}$$

$$R = \eta_s \int_{d_{wp}}^{\infty} \pi {a^H}^2 R^{mp} \left(p_c^{Hm} \right) \Phi_s \left(z_s \right) dz_s \tag{5.30b}$$

Hertz contact gives contact radius a^H and mean contact pressure p_c^{Hm} as,

$$a^H = \left(z_s - d_{wp} \right)^{1/2} {R_s}^{1/2} \tag{5.31}$$

$$p_c^{Hm} = \frac{4}{3\pi} E_p R_s^{-1/2} \left(z_s - d_{wp} \right)^{1/2} \tag{5.32}$$

where E_p is the porous pad elastic modulus in Eqn (5.32). Substituting Eqn (5.31) and (5.32) into Eqn (5.30b), the RFF in pad-wafer contact R can be expressed as,

$$R = \eta_s \int_{d_{wp}}^{\infty} \pi R_s \left(z_s - d_{wp} \right) R^{mp} \left(\frac{4}{3\pi} E_p R_s^{-1/2} \left(z_s - d_{wp} \right)^{1/2} \right) \Phi_s \left(z_s \right) dz_s \tag{5.33}$$

Note that the results presented in Chapter 7 are based on the calculations indicated by Eqn (5.33), except in Section 7.2, where the effect of contact pressure altered by interfacial particles is studied by calculating the RFF using Eqn (5.30a).

The applied pressure P_o, is the controlled parameter in CMP instead of equilibrium separation distance d_{wp}, which can be obtained from d_{wp} as,

$$P_o = \frac{4}{3}\eta_s E_p R_s^{1/2} \int_{d_{wp}}^{\infty} \Phi_s(z_s)(z_s - d_{wp})^{3/2}\, dz_s \qquad (5.34)$$

The direct contact area A_d, particle contact pressure P_p and number of active particles n_a can be calculated using an equation similar to Eqn (5.33) except that R^{mp} is replaced by respective functions for A_d^{mp} and η_a^{mp}. The effect of various parameters on the RFF in pad-wafer rough contact calculated as explained in this section is investigated in Chapter 7.

5.6 Implementation of Chemical Effects

In the model, the hardness of wafer, H_w is influenced by the chemical reactions at the wafer surface. A passivated surface layer on the wafer is considered by using a bi-layer hardness model introduced in Section 5.2.3. The thickness t_{pw} and hardness H_{pw} of passivated layer is used to characterize the influence of chemical reactions. Due to the presence of passivated layer, the effective wafer hardness H_w becomes a function of the indentation depth of particle δ_w if indentation depth is greater than the passivated layer thickness, $\delta_w > t_{pw}$ as given in Eqn (5.16b).

The indentation depth δ_w can be found as a function of mean contact force f_w by using Eqn (5.16a) as,

$$\delta_w = \frac{f_w}{\pi r_p H_w(\delta_w)} \tag{5.35}$$

where effective hardness H_w is given by Eqn (5.16b). In this work, the mean particle contact force f_w^m and mean particle radius μ_p are used in order to calculate the effective wafer hardness. The mean particle contact force f_w^m can be found by using the particle contact pressure and number of active particles as, $f_w^m = P_p / n_a$. Eqns (5.16b) and (5.35) are then solved iteratively to find the indentation depth δ_w and the effective hardness H_w as a result.

5.7 Summary and Conclusions

In this chapter, the wear equations introduced in Section 3.5 for adhesive and abrasive wear are used in order to predict MRR by considering the contact force applied by the pad on particle calculated using the models developed in Chapter 4. In the most general form of wear equation, only relative velocity, applied pressure and hardness appear explicitly while the effects of other parameters on wear rate are implicitly included in the wear coefficient term. Although the wear coefficient may be determined experimentally, it is difficult to understand the effect of each parameter on MRR since the effects of different parameters are lumped into one coefficient. MRR models developed in this chapter enable different CMP parameters to appear explicitly in equations, which could enhance the understanding of the effect of different CMP parameters.

The removal force function (RFF) introduced in this chapter is used as a measure for the effect of mechanical forces on adhesive and abrasive wear. The wear equations are

implemented at different contact scales including single particle (SP) (Section 5.2), multi-particle (MP) (Section 5.3), single asperity (SA) (Section 5.4) and multi-asperity (MA) contact models (Section 5.5).

In the SP contact model, both adhesive and abrasive wear are considered to be the active wear mechanisms. It is shown that the RFF due to adhesive wear achieved by a single particle is linearly proportional to the contact force on particle whereas the RFF due to abrasive wear increases with the contact force at a higher order. This fundamental difference of these wear mechanisms in terms of dependence on contact force will be re-visited in Chapter 7 when discussing the results for the RFF in pad-wafer rough contact.

The surface forces influence the force equilibrium at wafer-particle contact (Section 5.2). The attractive van der Waals forces cause particle contact force to increase, whereas double layer forces are repulsive and lower the particle contact force. Even when the particle and wafer are oppositely charged, double layer forces remain repulsive due to the small separation distance between particle and wafer since particle and wafer are in contact. Therefore van der Waals forces have a positive effect on the RFF while double layer forces decrease the RFF. When wafer and particles are atomically smooth, the separation distance is small and the magnitude of surface forces is large. Even in the case of two contacting surfaces, the separation distance may be effectively increased due to the roughness of wafer and particles. It is shown that the magnitude of surface forces decays rapidly with larger separation distance and as a result, their influence on the RFF decreases.

The RFF of particles trapped between two flat surfaces is studied in the MP contact model (Section 5.3). It is shown that the RFF increases with contact pressure at different rates based on the occurrence of direct contact. In particle contact regime, the RFF due to adhesive wear increases linearly with contact pressure and particle concentration does not have an influence on the RFF. The RFF due to abrasive wear on the other hand decreases with higher particle concentration in particle contact regime, since applied pressure is distributed among more particles reducing the mean contact force on each particle. Once direct contact is initiated in mixed contact regime, the RFF increases at a smaller rate with applied pressure as some fraction of applied pressure due to direct contacts does not participate in wear. In this regime, the RFF for both wear mechanisms becomes larger with higher particle concentration since non-contact regions around particles prevent direct contact more effectively if number of active particles is greater.

In Section 5.4, the behavior of the RFF in the MP contact model is used in the SA contact model developed in Section 4.5. The contact pressure distribution obtained in the SA contact model is introduced in the MP contact model for computing total RFF achieved by the particles trapped between a single pad asperity and wafer. In addition to the contact pressure predicted by the SA contact model, the contact pressure distribution given by Hertz contact is utilized for calculating the RFF. At low contact force, the error of Hertz contact is high for calculating the RFF for adhesive and abrasive wear and the error is a strong function of particle concentration, particle size and asperity radius. However the RFF of a single asperity can be calculated based on the contact pressure distribution in the SA contact model and Hertz contact agrees well at high asperity contact force and the effect of the particles on contact pressure distribution can be

neglected. In fact, mean Hertzian contact pressure can be assumed to be acting in the entire contact interface instead of contact pressure radially distributed based on Hertz contact without loss of accuracy at high contact force. This results in easier computation of the RFF of each pad asperity participating in multi-asperity contact.

The RFF calculated for each asperity is then integrated in a multi-asperity model to compute the total RFF achieved due to pad-wafer rough contact (Section 5.5). The RFF of each asperity calculated based on contact pressure distribution given by the SA contact model and Hertz contact is utilized.

The effective wafer hardness is iteratively calculated by utilizing the mean particle contact force and mean particle radius (Section 5.6). The MRR is then determined by using the RFF due to the particles tapped between pad and wafer and the effective hardness. This model is run for the ranges of different parameters relevant in CMP in order to investigate the effect of each parameter on the RFF. The results are studied in detail in Chapter 7.

References

1. Rabinowicz E., 1995. Friction and wear of materials. John Wiley & Sons, New York.
2. Shan H., 2006. Effect of medium on particle adhesion and removal. PhD Dis., Northeastern Univ., Boston, MA.
3. Israelachvili J. N., 1992. Intermolecular and surface forces. Academic Press.
4. Bastaninejad M., Ahmadi G., 2005. Modeling the effects of abrasive size distribution, adhesion, and surface plastic deformation on chemical-mechanical polishing. J Electrochem Soc, 152, 720-730.

5. Calota G., Maximova N., Ziemer K. S., Muftu S., 2008. Investigation of chemical mechanical polishing of niobium. STLE Tribology Transactions, submitted Nov 3 2008.

6. Qin K., Moudgil B., Park C.W., 2004. A chemical mechanical polishing model incorporating both the chemical and mechanical effects. Thin Solid Films, 446, 277-286.

CHAPTER 6

OPTIMIZATION OF CMP PARAMETERS FOR MAXIMUM MATERIAL REMOVAL EFFICIENCY

6.1 Overview

The calculation of the removal force function (RFF) formulated in this work requires the numerical computation of various integrals and the usage of look-up tables for interpolating values in order to exchange the relations developed across different models. In this chapter, alternatives for the RFF calculations are sought by making several simplifying assumptions.

The particle size is assumed to be constant while particle size varies according to a probability density function in Chapter 5. The height of pad asperity summits is assumed to follow exponential distribution, which is a valid approximation for the upper part of the Gaussian distribution used in Chapter 5 to describe the random pad roughness, as presented in Section 3.1.2. Moreover the contact pressure is considered to be uniform

across all asperities in contact and is taken to be equal to mean real contact pressure. As a result of this assumption, the effects of different asperities engaged in contact at different separation distances between the pad and the wafer are neglected.

Following these assumptions, an equation for optimizing CMP parameters to maximize the material removal efficiency is introduced. A closed-form solution is obtained for the RFF, due to adhesive and abrasive wear, at this optimal condition. The effects of surface forces, including the van der Waals and the double layer forces on the RFF are evaluated by considering the magnitude of surface forces relative to pad-particle contact force.

6.2 Multi-Particle Contact Model

In this section, equations developed for multi-particle (MP) contact model (Section 4.4) are simplified by assuming the particle size to be constant.

6.2.1 MP contact model for constant particle size

First, the single particle relations obtained in single particle (SP) contact model (Section 4.3) are re-visited. Non-dimensionalization of parameters is performed with respect to particle radius r_p and pad elastic modulus E_s as given in Table 4.1. The particle contact force in the particle $f_p^{p^*}$ and the mixed $f_p^{m^*}$ contact regimes is defined as a function of penetration depth δ_p^* and average compressive strain ε_s, respectively;

$$f_p^{p^*}\left(\delta_p^*\right) = \frac{4}{3}\delta_p^{*3/2} - 0.10\delta_p^{*2.89} \quad \text{for } 0 < \delta_p^* < 2. \tag{6.1}$$

$$f_p^{m^*}(\varepsilon_s)=\begin{cases}5.4(\varepsilon_s)^{0.57}+3.12, & \text{for} \quad 0<\varepsilon_s<0.05\\ 11.1(\varepsilon_s-0.05)^{0.90}+4.10, & \text{for} \quad 0.05<\varepsilon_s<0.2\\ 40.94(\varepsilon_s-0.2)^2+13.14(\varepsilon_s-0.2)+6.11, & \text{for} \quad 0.2<\varepsilon_s<0.45\end{cases} \tag{6.2}$$

The influence radius r_i^* and the maximum direct contact pressure $p_d^{m^*}$ are also defined as a function of average compressive strain ε_s as,

$$r_i^*(\varepsilon_s)=1.52(\varepsilon_s)^{-0.45} \quad \text{for } 0<\varepsilon_s<0.45 \tag{6.3}$$

$$p_d^{m^*}(\varepsilon_s)=\begin{cases}0.76\varepsilon_s, & \text{for} \quad 0<\varepsilon_s<0.015\\ 0.85(\varepsilon_s-0.015)+0.011, & \text{for} \quad 0.015<\varepsilon_s<0.2\\ 1.8(\varepsilon_s-0.2)^{1.16}+0.17, & \text{for} \quad 0.2<\varepsilon_s<0.45\end{cases} \tag{6.4}$$

In Section 4.3, particle size is assumed to vary according to a probability density function (PDF) Φ_p in the MP contact model. The equations developed in the MP contact model (Section 4.3) can be simplified if particle size is assumed to be constant. The particle concentration by weight-ratio η_w can be converted to the volumetric particle concentration η_v (number of particles per unit slurry volume) using density of slurry ρ_s and particle material ρ_p as,

$$\eta_v^*=\frac{3}{4\pi}\frac{\rho_s}{\rho_p}\eta_w \tag{6.5}$$

where dimensionless volumetric particle concentration is found as $\eta_v^*=\eta_v r_p^3$.

As the surfaces approach each other, all particles in the slurry become active at the same separation distance, when d_{sep}^* is equal to particle diameter, $d_{sep}^*=2$, (i.e. $d_{sep}=2r_p$).

The number of active particles, $\eta_a^{mp^*}$ $(=\eta_a^{mp}\ r_p^2)$ can be found by using this separation distance $d_{sep}^* = 2$ as,

$$\eta_a^{mp^*} = \begin{cases} 0 & d_{sep}^* > 2 \\ 2\eta_v^* & d_{sep}^* \le 2 \end{cases} \tag{6.6}$$

The particle contact pressure in particle contact $p_p^{mp-p^*}$ and mixed contact $p_p^{mp-m^*}$ regimes can be found by using the number of active particles $\eta_a^{mp^*}$ and contact force on each particle f_p^* as,

$$p_p^{mp-p^*} = 2\eta_v^* f_p^{p^*}(\delta_p^*) \tag{6.7}$$

$$p_p^{mp-m^*} = 2\eta_v^* f_p^{m^*}(-\varepsilon_p) \tag{6.8}$$

The influence contact area A_i^{mp} can be found by the summation of influence contact area of each particle, πr_i^{*2} over all active particles as $\eta_a^{mp^*}\pi r_i^{*2}$. Using Eqn (6.6) for the number of active particles $\eta_a^{mp^*}$, one can find the influence contact area A_i^{mp} as,

$$A_i^{mp} = 2\eta_v^*\pi\left(r_i^*(-\varepsilon_p)\right)^2 \tag{6.9}$$

The direct contact area, A_d^{mp} $(=1-A_i^{mp})$ is calculated using the influence contact area A_i^{mp} as,

$$A_d^{mp} = 1-2\eta_v^*\pi\left(r_i^*(-\varepsilon_p)\right)^2 \tag{6.10}$$

Substituting the volumetric particle concentration η_v^* (Eqn (6.5)) and influence radius r_i^* (Eqn (6.3)) into Eqn (6.10), the direct contact area A_d^{mp} can be expressed as a function of average compressive strain ε_p,

$$A_d^{mp} = 1 - 3.47 \frac{\rho_s}{\rho_p} \frac{\eta_w}{(-\varepsilon_p)^{9/10}} \tag{6.11}$$

Direct contact of surfaces occurs when the direct contact area becomes $A_d^{mp} \geq 0$. The critical average compressive strain ε_p^m at which direct contact starts to occur can be found by setting the direct contact area, $A_d^{mp} = 0$ (Eqn (6.11)) as,

$$\varepsilon_p^m = -3.98 \left(\frac{\rho_s \eta_w}{\rho_p} \right)^{10/9} \tag{6.12}$$

The particle contact pressure at this critical condition, $p_p^{mp-c^*} = p_p^{mp-m^*}\left(-\varepsilon_p^m\right)$ can be calculated using $\varepsilon_p = -\varepsilon_p^m$ in Eqn (6.8),

$$p_p^{mp-c^*} = 2\eta_v^* f_p^{m^*} (3.98 \left(\frac{\rho_s \eta_w}{\rho_p} \right)^{10/9}) \tag{6.13}$$

Direct contact pressure $p_d^{mp^*}$ can be calculated by considering the variation in direct contact area A_d^{mp},

$$p_d^{mp^*} = \int_{\varepsilon_p^m}^{\varepsilon_p} p_d^{m^*} (\varepsilon_p^r - \varepsilon_p) \frac{dA_d^{mp}}{d\varepsilon_p^r} d\varepsilon_p^r \tag{6.14}$$

Substituting direct contact area A_d^{mp} given in Eqn (6.11) into Eqn (6.14) and taking the derivative $\frac{dA_d^{mp}}{d\varepsilon_p^r}$ in Eqn (6.14), one can obtain direct contact pressure $p_d^{mp^*}$ as,

$$p_d^{mp^*} = 3.12\eta_w \frac{\rho_s}{\rho_p} \int_{\varepsilon_p^m}^{\varepsilon_p} \frac{p_d^{m^*}(-(\varepsilon_p - \varepsilon_p^r))}{(-\varepsilon_p^r)^{1.90}} d\varepsilon_p^r \tag{6.15}$$

The total contact pressure $p_c^{mp^*}$ in particle contact and mixed contact regimes can be determined using the particle contact pressure $p_p^{mp^*}$ (Eqns (6.7) and (6.8)) and direct contact pressure $p_d^{mp^*}$ (Eqn (6.15) as,

$$p_c^{mp^*} = \begin{cases} p_p^{mp-p^*} & \text{if } d_{sep}^* > 0 \\ p_p^{mp-m^*} + p_d^{mp^*} & \text{if } d_{sep}^* < 0 \end{cases} \tag{6.16}$$

The mean spacing between particles d_s^* can be calculated by assuming that the particles are evenly spaced on the corners of a hexagon as,

$$d_s^* = \sqrt{\frac{2}{\sqrt{3}\eta_a^{mp^*}}} \tag{6.17}$$

The number of active particles $\eta_a^{mp^*}$ given by Eqn (6.6) can be introduced in Eqn (6.17) to find mean spacing d_s^* as,

$$d_s^* = 1.55\sqrt{\frac{\rho_p}{\rho_s \eta_w}} \tag{6.18}$$

The influence factor, i_f can be calculated using Eqn (6.3) for influence radius r_i^* and Eqn (6.18) for mean spacing d_s^* in the following equation,.

$$i_f = \frac{r_i^*}{d_s^*} \tag{6.19}$$

6.2.2 The results of the MP contact model relations for constant particle size

Fig. 6.1 shows the variation of the contact pressure as a function of separation distance d_{sep}, in particle contact regime and average compressive strain ε_p in the mixed contact regime, for different particle concentrations η_w. Comparing the contact pressure in the mixed contact regime $\tilde{p}_c^{mp}$ for constant (Fig. 6.1a) and variable particle size (Fig. 4.13a), it seen that constant and variable particle size assumptions give the same $\tilde{p}_c^{mp}$ in mixed

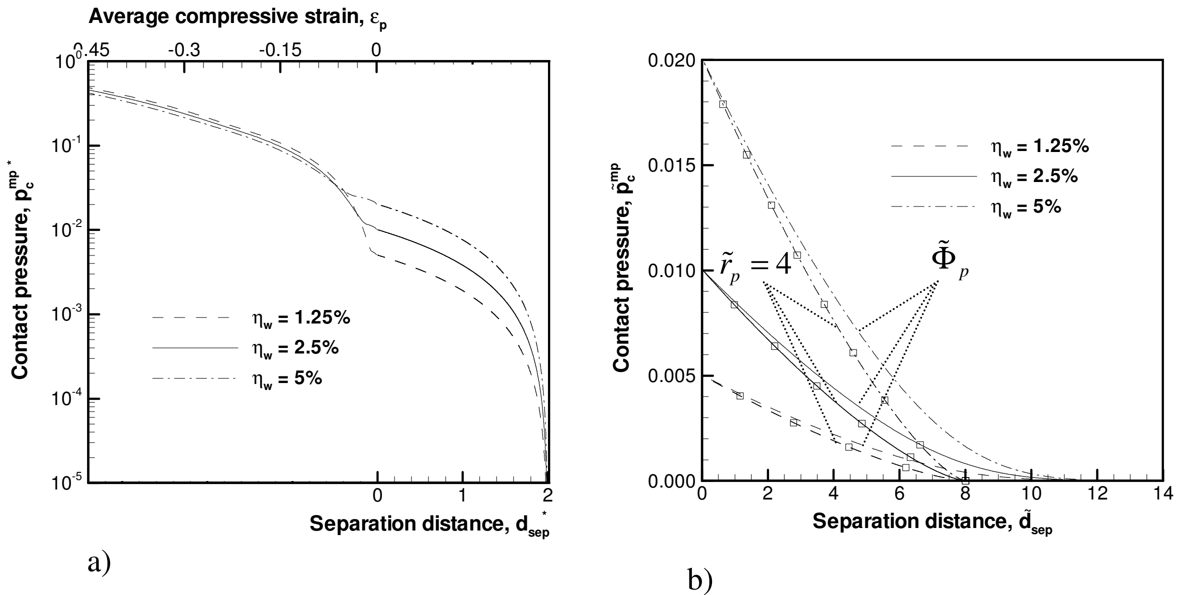

Fig. 6.1: The variation of contact pressure $p_c^{mp^*}$ in a) particle and mixed contact regimes for constant particle size and b) particle contact regime for both variable $\tilde{\Phi}_p$ and constant $\tilde{r}_p = 4$ particle size.

contact regime as a function of average compressive strain ε_p. This is explained by considering the fact that the contact pressure $\tilde{p}_c^{mp}$ in mixed contact regime is not influenced by particle size as discussed in Section 4.4.

On the other hand, in the particle contact regime, a difference is observed between the constant and variable particles size assumptions as shown in Fig. 6.1b. Note that in this figure, the separation distance $\tilde{d}_{sep}$ is d_{sep} / σ_p and the mean particle size is taken to be $\mu_p = 4\sigma_p$, where σ_p is the standard deviation of particle size distribution. In order to compare the contact pressure for constant and variable particle size assumptions, particle radius $\tilde{r}_p$ in the case of constant particle size is taken to be equal to the mean particle radius $\tilde{\mu}_p$ in the variable particle size assumption $\tilde{r}_p = \tilde{\mu}_p = 4$. The number of active particle $\tilde{\eta}_a^{mp}$ increases gradually with smaller separation distance $\tilde{d}_{sep}$ for the case of variable particle size, whereas all the particles get engaged in contact at the same separation distance $\tilde{d}_{sep} = 2\tilde{r}_p$ for the case of constant particle size. The contact pressure becomes non-zero $\tilde{p}_c^{mp} > 0$ due to the presence of large particles for variable particle size as compared to constant particle size where the contact pressure starts to increase when $\tilde{d}_{sep} = 2\tilde{r}_p$. The contact pressure for both assumptions reaches the same value as separation distance becomes $\tilde{d}_{sep} = 0$ and remains the same in the mixed contact regime $\tilde{d}_{sep} < 0$.

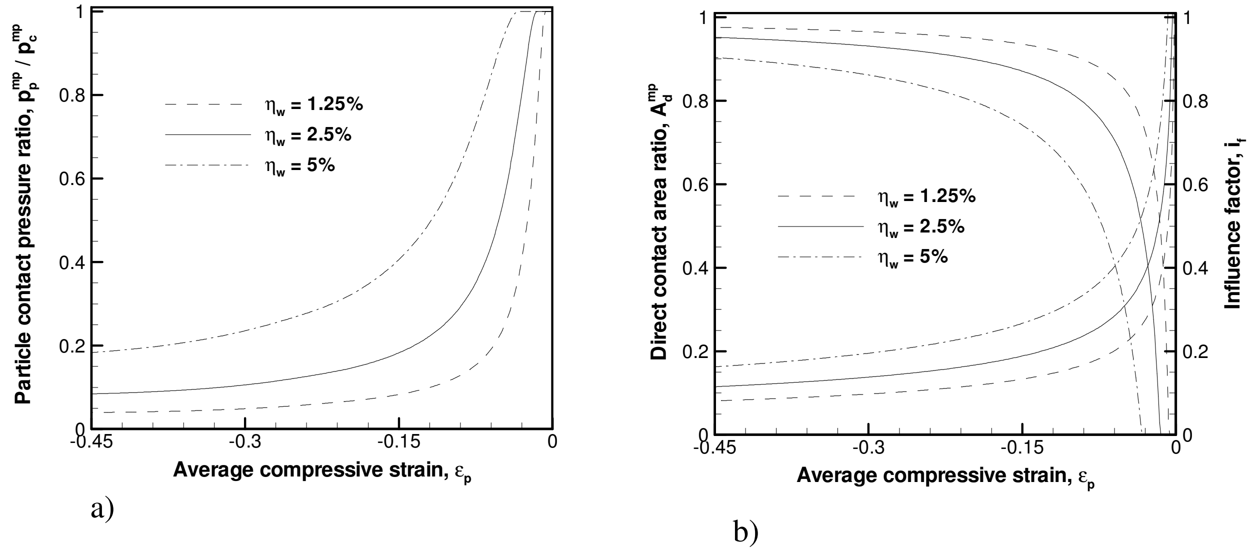

Fig. 6.2: The variation of a) particle contact pressure ratio p_p^{mp} / p_c^{mp} and b) direct contact area ratio A_d^{mp} and influence factor i_f with average compressive strain ε_p in mixed contact regime for constant particle size.

In addition to the contact pressure in mixed contact regime $\tilde{p}_c^{mp}$ (Fig. 6.1a), particle contact pressure ratio and direct contact area for constant particle size (as shown in Fig. 6.2) remain the same as in the case of variable particle size.

6.3 Removal Force Function (RFF) in MP Contact Model

The equations for the removal force function (RFF) of a single particle for adhesive R_{ad}^{sp} and abrasive R_{ab}^{sp} wear are re-visited in this section. These are:

$$R_{ad}^{sp} = f_w \tag{6.20}$$

$$R_{ab}^{sp} = \sqrt{\frac{2}{\pi^3}} \frac{f_w^{3/2}}{r_p} \tag{6.21}$$

where f_w is the wafer-particle contact force. The wafer-contact force consists of the particle contact force applied by pad f_p and surface forces f_s (van der Waals f_{vdw} and double layer f_{dl} force) as,

$$f_w = f_p + f_s = f_p + f_{vdw} + f_{dl} \tag{6.22}$$

Recall that MRR due to adhesive RR_{ad}^{sp} and abrasive RR_{ab}^{sp} wear can be found from the RFF (R_{ad}^{sp} and R_{ab}^{sp}) by using:

$$RR_{ad}^{sp} = R_{ad}^{sp}\left(\frac{k_w^{ad}}{H_w}V_r\right) \tag{6.23a}$$

$$RR_{ab}^{sp} = R_{ab}^{sp}\left(\frac{k_w^{ab}}{H_w^{\;3/2}}V_r\right) \tag{6.23b}$$

where H_w is effective wafer hardness, V_r is relative velocity, k_w^{ad} and k_w^{ab} are wear coefficients for adhesive and abrasive wear, respectively.

The RFF in multi-particle (MP) model, R^{mp} for particles with constant radius r_p can be found by using number of active particles η_a^{mp} and RFF achieved by each particle, R^{sp} as,

$$R^{mp} = \eta_a^{mp} R^{sp} \tag{6.24}$$

where the number of active particles $\eta_a^{mp}\ (= \eta_a^{mp^*} / r_p^2)$ for constant particle radius r_p is given by Eqn (6.6) and the RFF for each particle, R^{sp} can be calculated using Eqn (6.23).

6.4 Removal Force Function (RFF) in MA Contact Model

The RFF of the particles in pad-wafer rough contact (MA contact) is calculated by substituting the mean contact pressure p_c^m due to pad-wafer rough contact in the MP contact model to obtain the RFF for a unit real contact area. The real contact area ratio A_r is then used to determine the RFF due to pad-wafer rough contact for a unit apparent contact area.

6.4.1 Exponential distribution of the pad asperity summit heights

Greenwood and Williamson multi-asperity model [1] leads to a closed-form solution for the mean contact pressure p_c^m acting in the rough contact of two surfaces, if the distribution of the asperity summit heights can be approximated by an exponential probability density function (PDF) [1]. The exponential PDF is shown to be a good approximation for randomly rough surfaces described by the Gaussian distribution when equilibrium separation distance between surfaces is large, such that only the asperities included in the upper part of Gaussian PDF get engaged in contact as demonstrated in Section 3.1.2.

The exponential distribution in the following form is commonly used in contact mechanics in order to approximate the Gaussian distribution as [1],

$$\Phi_s\left(z_s\right) = \lambda_s \exp\left(-\lambda_s z_s\right) \tag{6.25}$$

where the parameter, λ_s is expressed in terms of the standard deviation, σ_s in Gaussian distribution, as, $\lambda_s = 2 / \sigma_s$. A closed-form expression for the mean contact pressure p_c^m

in rough contact of two surfaces is obtained using exponential distribution, Φ_s in Greenwood and Williamson multi-asperity model [2] as,

$$p_c^m \approx 0.39 E_p \sqrt{\frac{\sigma_s}{R_s}} \tag{6.26}$$

where R_s is the asperity radius and E_p is the porous pad elastic modulus.

6.4.2 Uniform contact pressure

The mean contact pressure due to pad-wafer rough contact is different for each pad asperity since each asperity summit is at a different height and gets engaged in contact at different equilibrium separation distance. Here, we assume that the mean contact pressure is the same for all pad asperities and can be found by using mean contact pressure p_c^m given by Eqn (6.26). The RFF for a unit contact area between the pad and the wafer can be found by substituting mean contact pressure p_c^m into the RFF function for the MP contact model, $R^{mp}\left(p_c^m\right)$ (Eqn 6.24). The RFF due to pad-wafer rough contact R can be found by using the real contact area A_r as,

$$R = A_r R^{mp}(p_c^m) \tag{6.27}$$

where A_r can be expressed as a function of applied pressure, P_o as,

$$A_r = \frac{P_o}{p_c^m} \tag{6.28}$$

Substituting Eqn (6.24) for R^{mp} in Eqn (6.27), the RFF in rough contact can be expressed as,

$$R = A_r \eta_a^{mp} R^{sp} \tag{6.29}$$

Note that the RFF in the MP contact model R^{mp} used to calculate the overall RFF in Eqn (6.27) is expressed as a function of separation distance d_{sep} in particle contact and average compressive strain ε_p in mixed contact regime. Whereas the function for the RFF in the MP contact model R^{mp} in Eqn (6.27) requires contact pressure p_c^{mp} to be the independent variable. Consequently, look-up tables obtained from Eqn (6.16) for relating contact pressure p_c^{mp} to separation distance d_{sep} and average compressive strain ε_p is utilized. In addition, the RFF in the MP contact model R^{mp} is related to the separation distance d_{sep}, and average compressive strain ε_p as given by Eqn (6.24). The RFF in the MP contact model R^{mp} is determined for a given contact pressure p_c^m by using the separation distance d_{sep} and average compressive strain ε_p as intermediate variables.

The RFF due to pad-wafer contact R can be obtained by substituting real contact area A_r (Eqn (6.28)) and mean contact pressure, p_c^m (Eqn (6.26)) into Eqn (6.27) as,

$$R = \frac{P_o}{0.39 E_p \sqrt{\frac{\sigma_s}{R_s}}} R^{mp} (0.39 E_p \sqrt{\frac{\sigma_s}{R_s}}) \tag{6.30}$$

Note that Eqn (6.30) indicates a linear relationship between the RFF in pad-wafer rough contact R and applied pressure P_o. This behavior is in agreement with Preston equation.

6.5 Optimization for Maximum Material Removal Efficiency

6.5.1 Definition of material removal efficiency

In this work, material removal is assumed to take place due to the contact of the wafer with abrasive particles. It is assumed that the pad-wafer direct contact does not result in material removal, as the pad is typically softer compared to the wafer. If the contact pressure at the tip of asperities is sufficiently high to cause the particles to be embedded in the pad, allowing direct contact to occur, the relative pressure on the particles becomes smaller, resulting in a negative effect on the material removal rate (MRR). Material removal efficiency is defined as the fraction of applied pressure carried by particle contacts causing material removal. Material removal efficiency in the MP contact model is maximum for the particle contact regime, as particle contact pressure ratio is, p_p^{mp} / p_c^{mp} = 1. An optimum condition can be found by maximizing the RFF (or MRR) and keeping the particle contact pressure ratio at p_p^{mp} / p_c^{mp} = 1. This condition occurs when the mean contact pressure acting at the tip of asperities is equal to the critical contact pressure causing the transition from particle to mixed contact regime in the MP contact model.

6.5.2 Optimization equation

The surface forces do not play a role in optimization of CMP parameters for maximum material removal efficiency although the RFF for the optimized CMP conditions is influenced by the surface forces. In order to find the optimized CMP parameters, effect of

surface forces are neglected for now, which leads to $f_w = f_p$. Note that the effect of surface forces will be considered when calculating the RFF later in this chapter.

Optimum condition for maximum material removal efficiency requires mean contact pressure, p_c^m in the pad-wafer contact (Eqn (6.26)) to be equal to the critical contact pressure p_p^{mp-c} in multi-particle contact for transition from particle contact to mixed contact regime given by Eqn (6.13), $p_c^m = p_p^{mp-c}\left(= E_s p_p^{mp-c^*}\right)$. Using Eqns (6.26) and (6.13), one can find the following relationship for the optimum condition as,

$$0.39E_p\sqrt{\frac{\sigma_s}{R_s}} = 2\eta_v E_s f_p^{m^*}(-3.98\left(\frac{\rho_s\eta_w}{\rho_p}\right)^{10/9}) \tag{6.31}$$

Replacing volumetric particle concentration η_v with weight-ratio η_w (Eqn (6.5)) and rearranging the terms in Eqn (6.31), the following relationship is obtained,

$$0.82\sqrt{\frac{\sigma_s}{R_s}}\frac{\rho_p}{\rho_s} = \eta_w \frac{E_s}{E_p} f_p^{m^*}(-3.98\left(\frac{\rho_p}{\rho_s}\frac{1}{\eta_w}\right)^{-10/9}) \tag{6.32}$$

The CMP parameters related to pad porosity E_s / E_p, pad surface topography σ_s / R_s, particle density ρ_p / ρ_s and particle concentration η_w $(=\eta_w^{opt})$ can now be optimized by using Eqn (6.32). Note that the optimum parameters do not depend on the applied pressure P_o, as the mean contact pressure p_c^m (Eqn (6.26)) remains constant with respect to P_o in rough contact of surfaces when exponential distribution is used for the distribution of the asperity summit heights [1].

6.5.3 Calculation of RFF at optimum conditions

All of the applied pressure P_o is carried by the particles when CMP parameters are optimized based on Eqn (6.32). Moreover, the load on each particle is the same following the assumptions of uniform contact pressure and constant particle size. As a result of these assumptions, the mean contact pressure p_c^{mp} can be calculated by the number of active particles η_a^{mp} per unit area and the critical force on each particle f_p^c as,

$$p_c^{mp} = \eta_a^{mp} f_p^c \tag{6.33}$$

where the critical force on each particle f_p^{sp-c} can be found by using,

$$f_p^c = f_p^m \left(-\varepsilon_p^m\right) \tag{6.34}$$

Using Eqn (6.33) for the mean contact pressure p_c^{mp} in Eqn (6.28), the applied pressure P_o can be expressed as,

$$P_o = A_r \eta_a^{mp} f_p^c \tag{6.35}$$

Substituting the RFF of a single particle R^{sp} given by Eqns (6.20) and (6.21) in Eqn (6.29), the RFF in the pad-wafer rough contact for adhesive R_{ad} and abrasive R_{ab} wear can be found as,

$$R_{ad} = A_r \eta_a^{mp} f_w^c \tag{6.38}$$

$$R_{ab} = A_r \eta_a^{mp} \sqrt{\frac{2}{\pi^3}} \frac{f_w^{c^{3/2}}}{r_p} \tag{6.39}$$

where wafer-particle contact force f_w^c at the optimum condition can be found using pad-particle f_p^c and surface forces f_s as,

$$f_w^c = f_p^c + f_s \tag{6.40}$$

The surface forces f_s consist of van der Waals forces f_{vdw} given by Eqn (3.29) and double layer forces f_{dl} calculated using Eqns (3.41) for HHF constant charge (HHF-CC) and (3.42) and compression approximation (CA) assumptions.

In the absence of surface forces $f_w^c = f_p^c$, the RFF due to adhesive R_{ad}^{sp} (Eqn (6.38)) and abrasive R_{ab}^{sp} (Eqn (6.39)) wear reduces to,

$$R_{ad} = A_r \eta_a^{mp} f_p^c \tag{6.41}$$

$$R_{ab} = A_r \eta_a^{mp} \sqrt{\frac{2}{\pi^3}} \frac{f_p^{c^{3/2}}}{r_p} \tag{6.42}$$

If applied pressure P_o in the form expressed in Eqn (6.35) is used in Eqns (6.41) and (6.42) and the contact force f_p^c on each particle is converted to its non-dimensional form ($f_p^c = E_s r_p^2 f_p^{c^*}$), the RFF due to adhesive R_{ad} and abrasive R_{ab} wear at the optimum condition can be found as,

$$R_{ad} = P_o \tag{6.40}$$

$$R_{ab} = P_o \sqrt{E_s \, f_p^{c^*} \frac{2}{\pi^3}} \tag{6.41}$$

6.6 Results and Discussion

6.6.1 Optimum particle concentration

The optimum particle concentration η_w^{opt} is plotted as a function of standard deviation (SD) of pad roughness to asperity radius ratio σ_s / R_s for different pad porosity E_s / E_p values in Fig. 6.3. For a typical SD of pad roughness (σ_s = 5 µm) and asperity radius (R_s = 50 µm) [3], the ratio is $\sigma_s / R_s = 0.1$. Note that the density ratio $\rho_p / \rho_s = 3.7$ for alumina particles and $\rho_p / \rho_s = 2.5$ for silica particles reported in parts -a and -b of this figure. The effect of pad topography is investigated by varying the SD of pad roughness to asperity radius ratio in the range $0.01 < \sigma_s / R_s < 1$ for different porous elastic modulus ratio $1 < E_s/E_p < 4$.

The optimum particle concentration η_w^{opt} is higher for alumina particles as compared to silica particles since density of alumina ($\rho_p / \rho_s = 3.7$) is greater than silica particles ($\rho_p/\rho_s = 2.5$) giving a higher particle concentration by weight-ratio η_w for the same volumetric particle concentration η_v as seen in Fig. 6.3. Fig. 6.3 shows that the optimum particle concentration η_w^{opt} increases with the parameter σ_s / R_s. The effect of this parameter can be explained by the variation of mean contact pressure p_c^m at the tip of asperities with this ratio σ_s / R_s as indicated by Eqn (6.26). The mean contact pressure p_c^m increases

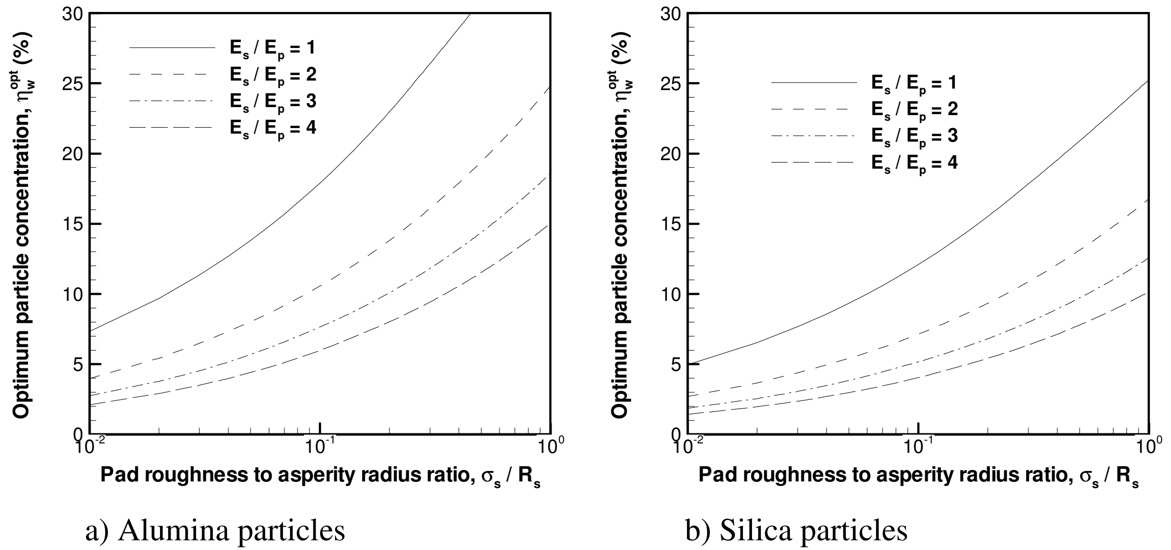

a) Alumina particles b) Silica particles

Fig. 6.3: The optimum particle concentration η_w^{opt} of a) alumina and b) silica particles as a function of pad topography σ_s / R_s for different porous elastic modulus ratio E_s / E_p.

with larger values of σ_s / R_s, which causes the particles to penetrate into the deformable pad surface and a larger number of particles (higher particle concentration η_w) is required to prevent direct contact.

The impact of porous elastic modulus ratio E_s / E_p is determined by the balance between mean contact pressure p_c^m due to pad-wafer rough contact controlled by porous pad elastic modulus E_p (Eqn 6.26) and the critical contact pressure $p_p^{mp-c^*}$ for the occurrence of direct contact in the MP contact model (Eqn 6.13), which is determined by pad elastic modulus E_s. Higher pad elastic modulus E_s decreases the ability of particle to penetrate into deformable pad surface and the critical contact pressure to induce direct contact between pad and wafer becomes larger. An increase in porous pad elastic modulus E_p causes higher mean contact pressure p_c^m at the tip of the asperities in pad-wafer rough contact, thus offsetting the effect of larger pad elastic modulus E_s. As a result, the

optimum particle concentration η_w^{opt} is not a function of pad elastic modulus E_s or porous pad elastic modulus E_p but porous elastic modulus ratio E_s / E_p influences η_w^{opt}.The optimum particle concentration η_w^{opt} with larger porous elastic modulus ratio E_s / E_p due to the fact that the critical contact pressure for inducing direct contact becomes high relative to the mean contact pressure p_c^m acting at the local contact interface.

6.6.2 RFF at optimum conditions

Eqn (6.40) and Eqn (6.41) indicate that the RFF due to both adhesive R_{ad} and abrasive R_{ab} wear is linearly proportional to applied pressure, P_o, much like Preston's equation when CMP parameters are optimized to prevent direct contact using Eqn (6.32). In fact, applied pressure, P_o is the only parameter affecting the RFF due to adhesive wear R_{ad} at optimum conditions. This is due to the fact that the RFF of a single particle is simply proportional to contact force (Eqn (6.20)) for adhesive wear, $R_{ad}^{sp} \propto f_w$.

In addition to the effect of applied pressure P_o, the RFF due to abrasive wear increases with pad elastic modulus $R_{ab} \propto E_s^{1/2}$ and contact force on each particle $R_{ab} \propto f_p^{c^{*1/2}}$ since abrasive wear is a function of indentation depth of particles. As the pad elastic modulus E_s increases, the force on each particle f_w becomes larger and the RFF due to abrasive wear for a single particle increases with $R_{ab}^{sp} \propto f_w^{3/2}$. The contact force $f_p^{c^*}$ at optimum condition given by Eqn (6.34) is a function of particle density ratio ρ_p / ρ_s and particle concentration η_w^{opt}. Fig. 6.4 shows the variation of the RFF due to abrasive wear R_{ab}^{opt} normalized by pad elastic modulus E_s and applied pressure P_o, $R_{ab}^{opt} / \left(P_o E_s^{1/2}\right)$ as a

function of optimum particle concentration η_w^{opt} for alumina (ρ_p/ρ_s = 3.7) and silica (ρ_p/ρ_s = 2.5) particles. Note that particle concentration η_w^{opt} is not the independent variable in this section but determined by the optimization of parameters in Eqn (6.32). It appears that the RFF due to abrasive wear R_{ab}^{opt} increases with higher particle concentration η_w^{opt} or smaller particle density ratio ρ_p/ρ_s. Smaller particle density ratio ρ_p/ρ_s causes the number of active particles η_a to increase for a given particle concentration η_w^{opt} (weight ratio). As the number of active particles η_a increases with higher particle concentration η_w^{opt} or smaller particle density ratio ρ_p / ρ_s, the direct contact of surfaces can only occur if the particles are subjected to large average compressive strain ε_p^m (Eqn (4.24)), thus causing the critical particle contact force $f_p^{c^*}$ at the onset of direct contact to become larger.

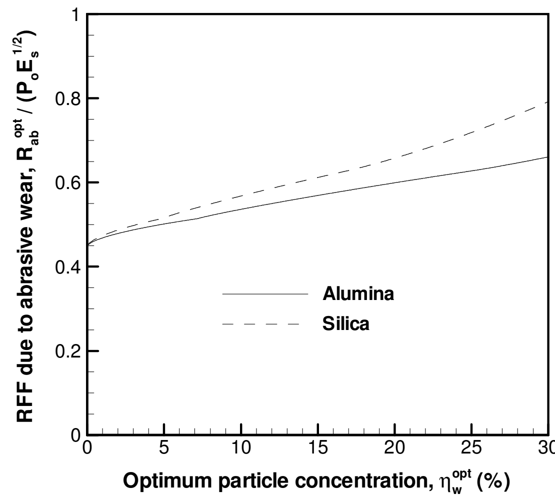

Fig. 6.4: The variation of normalized RFF due to abrasive wear $R_{ab}^{opt} / \left(P_o E_s^{1/2}\right)$ as a function of the optimum particle concentration η_w^{opt} for alumina and silica particles.

Eqns (6.40) and (6.41) give the RFF when the particle concentration is at its optimum value, $\eta_w = \eta_w^{opt}$, which is the minimum η_w required to shift the contact regime from mixed to particle contact regime. If the particle concentration is increased above its optimum value $\eta_w > \eta_w^{opt}$, the contact regime remains to be the particle contact regime, where particle contact pressure ratio is $P_p / P_o = 1$. In this case, the mean particle contact force decreases with higher particle concentration $f_p < f_p^c$ for $\eta_w > \eta_w^{opt}$ as $f_p \propto 1/\eta_w$. This causes the RFF due to abrasive wear R_{ab} to decrease with higher particle concentration $R_{ab} \propto 1/\eta_w^{1/2}$ due to the fact that R_{ab} is related to the mean particle contact force as $R_{ab} \propto f_p^{1/2}$ (Eqn (6.41)). The RFF due to adhesive wear R_{ad}, on the other hand, does not vary with particle concentration η_w as R_{ad} is only a function of applied pressure P_o as indicated by Eqn (6.40).

This saturation effect for MRR at high particle concentration was also observed in experiments conducted by Guo and Subramanian [4] for CMP of copper films and Bielmann et al. [5] for CMP of W films with alumina slurry. MRR normalized with respect to the maximum MRR found in experiments is plotted in Fig. 6.5 as a function of particle concentration η_w. The optimum (saturation) particle concentration was determined to be $\eta_w^{opt} \approx 5\%$ in experiments by Guo and Subramanian [4], and relative velocity did not have a significant influence on η_w^{opt} (Fig. 6.5a). Bielmann et al. [5] showed that saturation particle concentration varied in the range $5\% < \eta_w^{opt} < 10\%$ for mean particle radius 145 nm < μ_p < 300 nm (Fig. 6.5b). In these experiments, porous

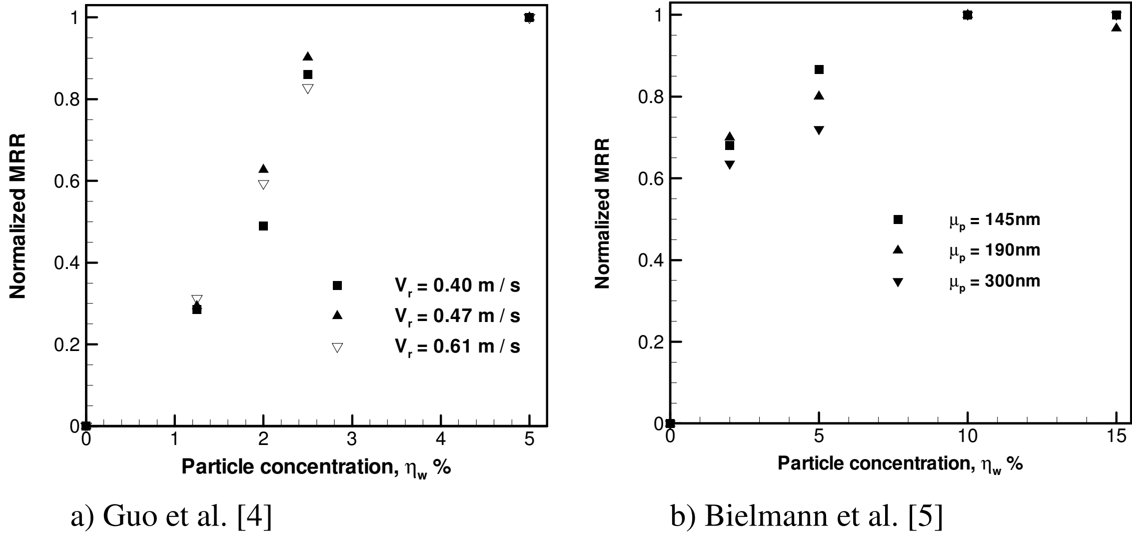

a) Guo et al. [4]   b) Bielmann et al. [5]

Fig. 6.5: Experimental observations for saturation of MRR at high particle concentration η_w. The RFF due to adhesive wear is predicted to remain constant when particle concentration η_w becomes larger than the optimum value.

pads were used. If we assume a porous elastic modulus ratio of E_s / E_p = 4 and using the base parameters for SD of pad roughness, σ_s = 5 μm and asperity radius, R_s = 50 μm, σ_s / R_s = 0.1, the optimum particle concentration is determined to be $\eta_w^{opt} = 6\%$ in Fig. 6.3a. This result for optimum particle concentration is in good agreement with the results of experiments conducted by Guo and Subramanian [4] and Bielmann et al. [5] showing the saturation of MRR at a critical (optimum) particle concentration.

6.6.3 Effect of surface forces

The surface forces f_s influence the wafer-particle contact force f_w^c as given by Eqn (6.40). The effect of surface forces f_s at optimized CMP conditions is evaluated by comparing the magnitude of f_s with respect to pad-particle contact force f_p^c, which is quantified by the ratio of surface f_s to pad-particle force f_p for a unit particle radius r_p

and pad elastic modulus E_s. This ratio $f_s\ /f_p\left(E_s r_p\right)$ is demonstrated for van der Waals force $f_s\ =\ f_{vdw}$ in Fig. 6.6a, and double layer forces $f_s\ =\ f_{dl}$ using compression approximation (CA) in Fig. 6.6b and constant charge (HHF-CC) assumptions in Fig. 6.6c. Van der Waals force f_{vdw} shown in Fig. 6.6a is positive $f_{vdw} > 0$ indicating that van der Waals interaction between wafer and particle is attractive causing the wafer-particle contact force f_w to increase. Note that van der Waals force f_{vdw} remains constant with respect to molar concentration M as f_{vdw} is not a function of M. The double layer force f_{dl} predicted by CA assumption is negative $f_{dl} < 0$ (repulsive) for all zeta potentials $\Psi_{1,2}$ studied. The magnitude of double layer force f_{dl} is at maximum when surface charge of surfaces are the same and zeta potential $\Psi_{1,2}$ is high. As zeta potential $\Psi_{1,2}$ becomes smaller or the charges of surface are opposite, the magnitude of double layer force f_{dl} decreases. In fact, CA assumption indicates the double layer force to be $f_{dl}\ = 0$ when zeta potential of surfaces is the same and opposite in sign, $\Psi_1 = -\Psi_2$. The double layer force f_{dl} calculated using HHF-CC assumption gives much higher magnitude for f_{dl}. According to HHF-CC assumption, the double layer force f_{dl} may become positive $f_{dl} > 0$ (attractive) when the zeta potential of surfaces $\Psi_{1,2}$ is high and surface charges are opposite, although the magnitude of attractive double layer force f_{dl} is small.

A different behavior is observed for the variation of double layer forces f_{dl} with respect to molar concentration M based on CA and HHF-CC assumptions. The magnitude of double layer forces f_{dl} is shown to increase with molar concentration M when CA

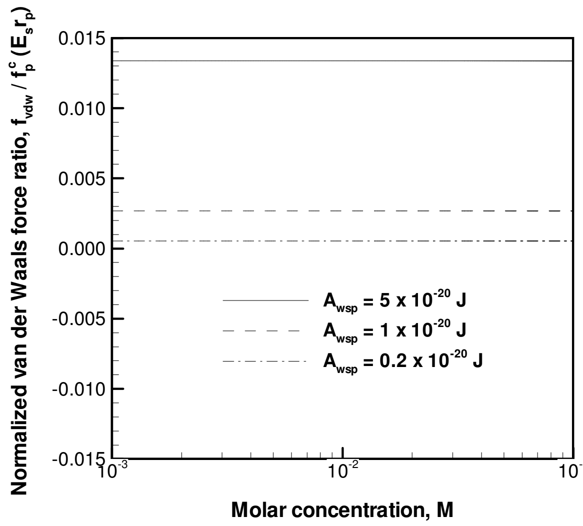

a) f_{vdw} / f_p^c

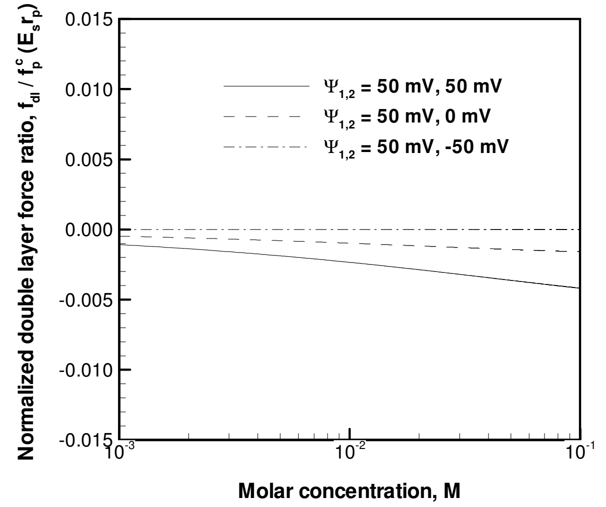

b) f_{dl} / f_p^c (CA assumption)

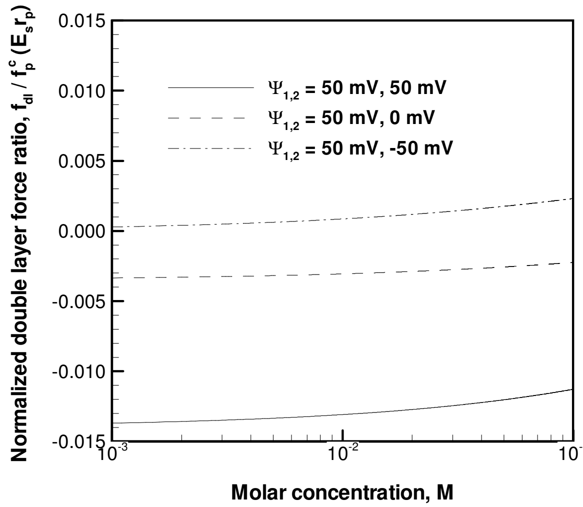

c) f_{dl} / f_p^c (HHF-CC assumption)

Fig. 6.6: The comparison of surface forces f_s and pad-particle force f_p as a function of molar concentration M for alumina particle with particle concentration $\eta_w = 5\%$.

assumption is used while a decrease in magnitude of f_{dl} is observed in the case of the HHF-CC assumption.

Note that surface forces f_s given by Eqn (3.29) (van der Waals force) and Eqns (3.41)-(3.42) (double layer forces) do not depend on the CMP parameters investigated here such

as particle concentration η_w, pad elastic modulus E_s, porous elastic modulus ratio E_s / E_p, particle density ratio ρ_p / ρ_s etc. The only parameter having an effect on both pad-particle contact force f_p and surface forces f_s is particle radius r_p, where pad-particle contact force increases with particle radius as $f_p \propto r_p^2$ while surface forces vary as $f_s \propto r_p$. Therefore the relative magnitude of surface forces becomes larger with smaller particle radius as indicated by the relation $f_s / f_p \propto 1/r_p$. In addition to the effect of particle radius r_p, the pad-particle contact force f_p increases linearly with the pad elastic modulus E_s while surface forces f_s are not influenced by E_s. Therefore the ratio of surface and pad-particle contact force f_s / f_p increases with smaller particle radius r_p and pad elastic modulus E_s. Based on the results shown in Fig. 6.6, it is concluded that surface forces f_s may play an important role for the RFF of a single particle R for a soft pad and small particle radius. For a soft pad ($E_s \approx$ 10 MPa) and small particle radius ($r_p \approx$ 0.005 μm), the product of E_s and r_p becomes $E_s r_p \approx$ 0.05. Note that in this case, the ratio of van der Waals and pad-particle contact force is $f_s / f_p = 0.26$ for $A_{wsp} = 5\text{x}10^{-20}$ J and $f_s / f_p = 0.01$ for $A_{wsp} = 0.2\text{x}10^{-20}$ J. This ratio varies in the range $-0.08 < f_s / f_p < 0$ for CA assumption and $-0.27 < f_s / f_p < 0.05$ for HHF-CC assumption when molar concentration is varied as $0.001 < M < 0.1$ and zeta potentials of $\Psi_{1,2}$ = 50mV, -50mV and $\Psi_{1,2}$ = 50mV, 50mV are used. In the case of hard pad ($E_s \approx$ 100 MPa) or large particle size ($r_p \approx$ 0.050 μm), the product $E_s r_p \approx$ 5, which means that the magnitude of surface forces is small compared to pad-particle force, $f_p >> f_s$ and therefore the effect of surface forces can be neglected.

6.7 Summary

In this section, the equations developed for the RFF in pad-wafer rough contact are simplified by considering the following assumptions; a) particle size is taken to be constant, b) randomly rough pad surface is approximated by using exponential distribution for the asperity summit heights and c) contact pressure acting at pad asperity-wafer contact interface is equal to mean contact pressure for every pad asperity. Although these assumptions lead to simplification for the computation of the RFF, the calculations still call for using look-up tables and carrying out numerical integrations.

A special case is studied, where material removal efficiency, defined as the fraction of applied pressure on the particle contributing to material removal, is maximized. In this case, the mean contact pressure in rough contact is equal to the contact pressure in multi-particle contact model at the onset of the occurrence of direct contact. An optimization equation is obtained for this condition in order to find the optimum CMP parameters to maximize material removal efficiency. The results for the optimum CMP parameters indicate that the optimum particle concentration η_w decreases with larger porous elastic modulus ratio E_s / E_p or SD of pad roughness to asperity radius ratio σ_s / R_s. The ability of calculating optimum particle concentration is useful for minimizing the utilization of consumables (abrasive particles) while maintaining the RFF to be constant, which can be achieved by controlling the porosity and pad topography.

The RFF due to pad-wafer contact at this optimum condition can be calculated by closed-form equations as described in Section 6.6.2. It is seen that the RFF due to both adhesive and abrasive wear is linearly proportional to applied pressure in agreement with Preston's

equation. The RFF due to abrasive wear increases with pad elastic modulus as $R_{ab} \propto E_s^{1/2}$ while the RFF due to adhesive wear remains constant with respect to E_s.

The relative effect of surface forces becomes important for a soft and small particle size. The magnitude of van der Waals force increases with larger effective Hamaker constant, while double layer force is a function of zeta potentials of pad and wafer, and molar concentration of ions. The effect of van der Waals force is to enhance the RFF since van der Waals interaction is attractive whereas double layer forces are repulsive causing the RFF to decrease.

References

1. Greenwood J. A., Williamson J. B. P., 1966. Contact of nominally flat surfaces. Proceedings of the Royal Society of London, Series A295, 300-319.
2. Williams J. A., 2000. Engineering tribology, Oxford University Press, UK.
3. Shan L., 2000. Mechanical interactions at the interface of chemical mechanical. polishing. Ph.D. Thesis, Georgia Institute of Technology, Atlanta, GA.
4. Guo L., Subramanian R.S., 2004. Mechanical removal in CMP of copper using alumina abrasives. J Electrochem Soc, 151, 104-108.
5. Bielmann M., Mahajan U., Singh R. K., 2002. Effect of particle size during tungsten chemical mechanical polishing. Electrochem Solid State Letters, 2, 401-403.

CHAPTER 7

RESULTS AND DISCUSSION

7.1 Overview

In this chapter, the effects of various CMP processing parameters on material removal rate (MRR) are investigated, by using the mechanical models presented in Chapters 4 and 5. In general, the removal force function (RFF) is the main output of the models and depends on whether the wear mechanism is mainly adhesive (R_{ad}) or abrasive (R_{ab}). The influence of each parameter is studied by varying the parameter in the range given in Table 7.1, while the remaining parameters are kept constant at their base values.

In addition to predicting the RFF, the mean contact pressure, real contact area, direct contact area ratio, particle contact pressure ratio and mean particle contact force are also calculated in order to probe the details of the predicted behavior of the RFF. Finally, experimental observations related to the effect of the parameters investigated here are discussed for validating the modeling results.

Parameter	Base	Range
Standard deviation of particle radius (σ_p) Mean particle radius ($\mu_p = 4\sigma_p$)	6.25 nm 25 nm	3.125 – 12.5 nm 12.5 – 50 nm
Particle concentration (η_w)	2.5%	0% - 10%
Particle to slurry density ratio (ρ_p/ρ_s)	3.7 (alumina)	NA
Pad asperity radius (R_s)	50 µm	25 – 100 µm
Pad asperity density (η_s)	$2\text{x}10^{-4}$ / µm^2	$1\text{x}10^{-4}$ – $4\text{x}10^{-4}$ / µm^2
Solid pad elastic modulus (E_s)	10 (soft), 100 (hard) MPa	10 - 100 MPa
Porous pad elastic modulus ratio (E_s/E_p)	1, 4	1 - 4
Applied pressure (P_o)	0.007 (low), 0.07 (high) MPa 1, 10 psi	0 – 0.07 MPa 0 - 10 psi

Table 7.1: Physical values of parameters.

The effect of interfacial particles on single asperity contact captured by single asperity (SA) contact model is investigated in Section 7.2 by calculating the RFF due to the contact of a wafer with a rough pad. Section 7.3 focuses on the influence of pad elastic modulus considering the effects of the pad elastic modulus of the solid pad material as well as pad porosity. The effects of particle concentration are addressed in Section 7.4. The parameters related to pad topography such as pad roughness, skewness of asperity summit height distribution, asperity radius and asperity density are the other important factors studied in Section 7.5. The surface forces acting between wafer and particle such as van der Waals and electrical double layer forces are included in the model to demonstrate their effect in Section 7.6. Note that the effects of surface forces are neglected in other sections. The effect of particle size is studied in Section 7.7, considering the influence of surface forces and passivated layer formed due to slurry chemicals. The thickness and hardness of passivated layer are varied for evaluating the

effect of slurry chemicals on MRR. The role of each wear mechanism (adhesive and abrasive wear) is the subject of discussion in Section 7.8, where wear constants are calculated using the models and experiments to compare with experimentally measured values. The optimization of CMP parameters for maximum material removal efficiency is demonstrated in Section 7.9.

7.2 Effect of Particles on RFF in Pad-Wafer Rough Contact

The effect of interfacial particles on single asperity contact is described by the single asperity (SA) contact model developed in Section 4.5. The results of this model, in Section 4.5.3, indicate that interfacial particles alter the contact pressure distribution due to the contact of a single asperity.

The RFF for a single asperity calculated by contact pressure altered by particles is shown to deviate from that based Hertz contact model, as discussed in Section 5.4.4. In this section, the RFF of a single asperity calculated in Section 5.4 is used in a multi-asperity model in order to evaluate the effect of interfacial particles on the RFF due to the contact of a wafer and a rough pad. This is achieved by comparing the RFF calculated using the SA and Hertz contact models for the single asperity contact behavior. This comparison is made by computing the relative error,

$$e = \frac{R^{sa} - R}{R^{sa}} \tag{7.1}$$

The error e is determined for different process parameters such as particle concentration, pad elastic modulus, particle size and pad topography. The RFF for the SA and Hertz contact models are indicated by R^{sa} and R, respectively. The adhesive and abrasive wear models are indicated by the subscripts “ad” and “ab”, respectively.

7.2.1 Effect of particle concentration

Figs. 7.1a and 7.1b show the relative error, e of RFF calculated by using the Hertz contact (R) and the SA contact (R^{sa}) models as a function of applied pressure and particle concentration. In this example, the elastic modulus of a hard pad is E_s = 100 MPa and the porous elastic modulus ratio is $E_s / E_p = 4$. The other parameters are the base parameters listed in Table 7.1. Fig. 7.1 shows that the error for RFF due to adhesive contact e_{ad} becomes larger with higher particle concentration η_w in the range of applied pressure studied, 10^{-4} MPa < P_o < 10^{-1} MPa. The RFF due to abrasive wear R_{ab} at low abrasive concentration η_w is predicted to be higher when the Hertz contact is used, $R_{ab} > R_{ab}^{sa}$, whereas the opposite ($R_{ab} < R_{ab}^{sa}$) is true at high η_w. The error for both adhesive and abrasive wear (e_{ad} and e_{ab}) decreases as the applied pressure P_o becomes higher. These results for the error in the RFF due to pad-wafer rough contact R are in agreement with

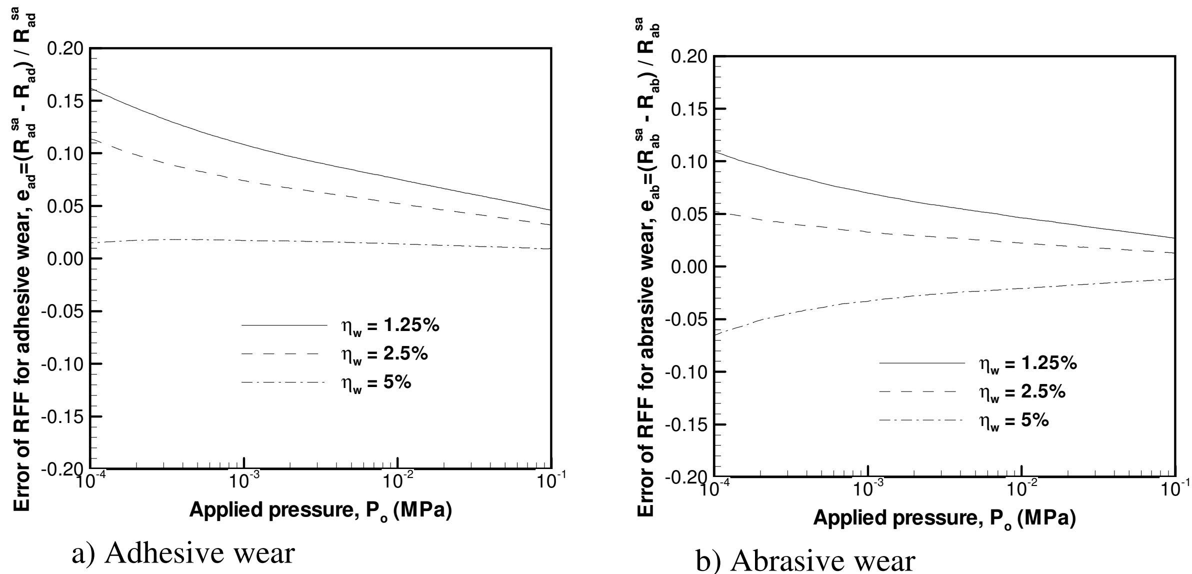

a) Adhesive wear

b) Abrasive wear

Fig. 7.1: The error of the RFF due to a) adhesive wear e_{ad} and b) abrasive wear e_{ab} introduced by contact pressure distribution based on Hertz contact for different particle concentration η_w.

the error in the RFF achieved by a singe asperity R^s explained in Section 5.4.4. It is seen that the error of Hertz contact for RFF due to adhesive wear e_{ad} varies between 1% - 8%, and 1% - 5% for low particle concentration η_w = 1.25% and high η_w, η_w = 5%, respectively in the range of applied pressure, 0.007 MPa < P_o < 0.07 MPa typically used in CMP. The corresponding values for the error of Hertz contact due to abrasive wear are found in the range -2% - 5% and -1% - 3%.

In addition to the effect on the RFF, spreading of the contact over a larger area due to the presence of interfacial particles, causes the particle contact pressure ratio P_p / P_o (Fig. 7.2a) and the number of active particles n_a (Fig. 7.2b) predicted by SA model to be larger than those predicted by Hertz contact. This is the main reason for the error in adhesive wear to be positive $e_{ad} > 0$, i.e. the RFF predicted using SA contact model is greater than that of Hertz contact, $R_{ad}^{sa} > R_{ad}$. In the case of the RFF due to abrasive wear, the error may be positive and negative based on the particle concentration. Although larger particle contact pressure ratio P_p / P_o promotes higher RFF, the RFF decreases with the larger number of active particles n_a for a given P_p / P_o. As a result of these two competing effects, the error for abrasive wear e_{ab} becomes negative, $e_{ab} < 0$ at high particle concentration η_w = 5% while e_{ab} remain positive, $e_{ab} > 0$ at η_w = 1.25%.

7.2.2 Effect of pad elastic modulus

The effect of pad elastic modulus E_s and porous elastic modulus ratio E_s / E_p on the error e of Hertz contact using the base parameters in Table 7.1 is illustrated in Figs. 7.3 (E_s / E_p = 4) and 7.4 (E_s = 100 MPa), respectively. It is seen in Fig. 7.3 that the error e for both adhesive and abrasive wear decreases when pad elastic modulus E_s decreases. This is due to the fact that particles become embedded in the pad, which reduces the effect of

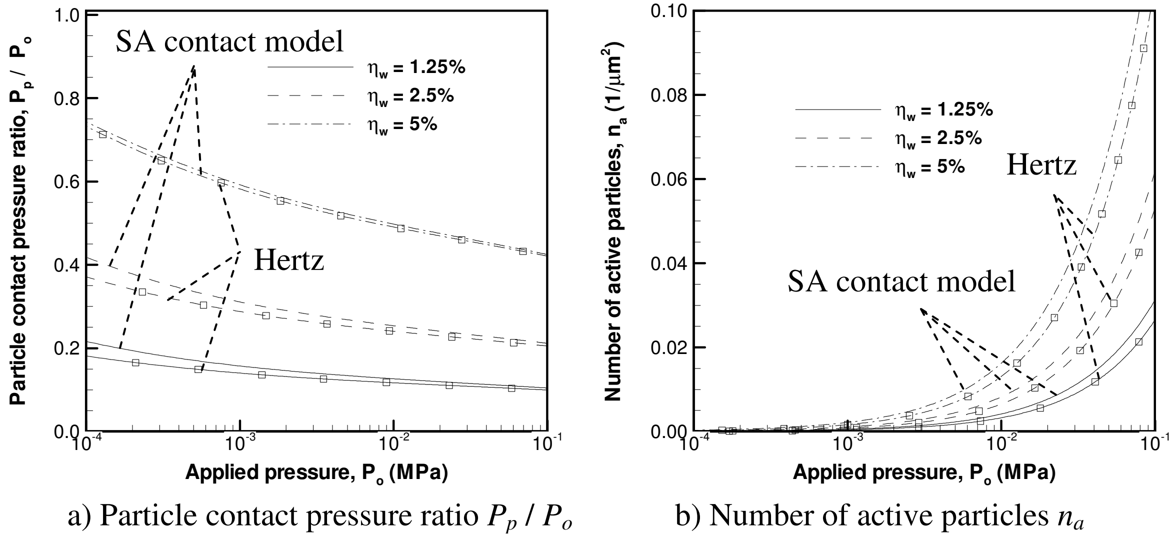

a) Particle contact pressure ratio P_p / P_o b) Number of active particles n_a

Fig. 7.2: The effect of different assumptions for contact pressure distribution on particle contact pressure ratio P_p / P_o and number of active particles n_a for different particle concentration η_w.

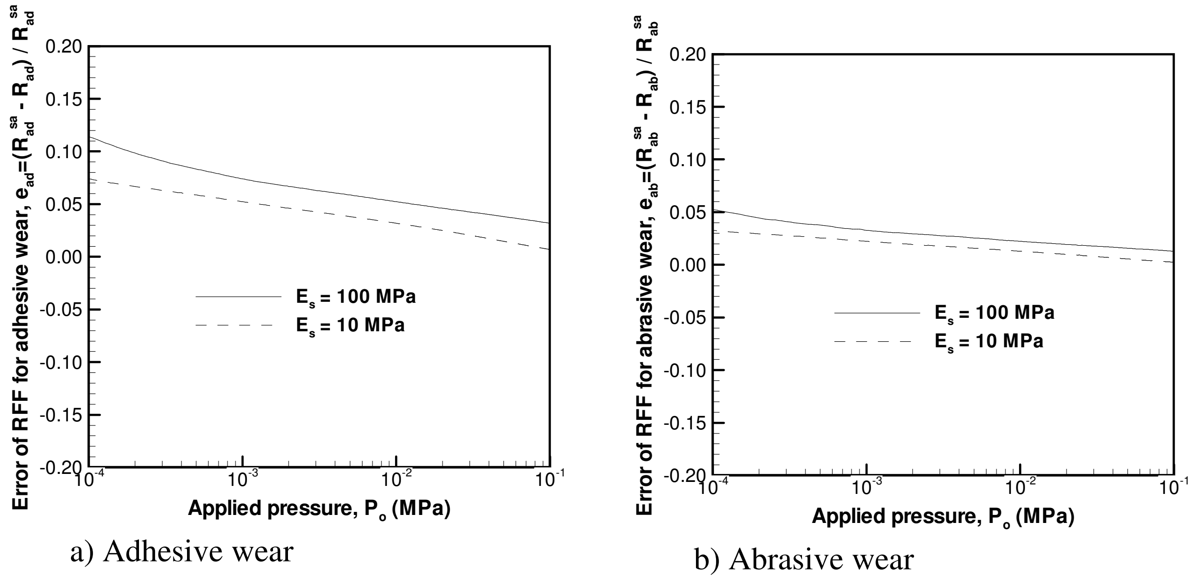

a) Adhesive wear b) Abrasive wear

Fig. 7.3: The error of the RFF due to a) adhesive wear e_{ad} and b) abrasive wear e_{ab} introduced by contact pressure distribution based on Hertz contact for different pad elastic modulus E_s ($E_s / E_p = 4$)

particles on the single asperity contact behavior becomes less significant. This result is in agreement with the error e^s for RFF of a single asperity R^s, which decreases with higher asperity contact force $\tilde{f}_c^s$ $(= f_c^s / E_s \sigma_p^2)$, given in Section 5.4.

Fig. 7.4 shows that the error e of Hertz contact increases with higher porosity (larger E_s / E_p). This result can be explained by the contact force f_c^s in the pad asperity-wafer interface, which becomes smaller, with decreasing porous pad elastic modulus E_p. This is due to the fact that the number of asperities in contact increases with lower porous pad elastic modulus E_p, thereby decreasing the contact force on each asperity f_c^s. As explained earlier, the error e^s of Hertz contact for a single asperity is more significant when the asperity contact force f_c^s is low.

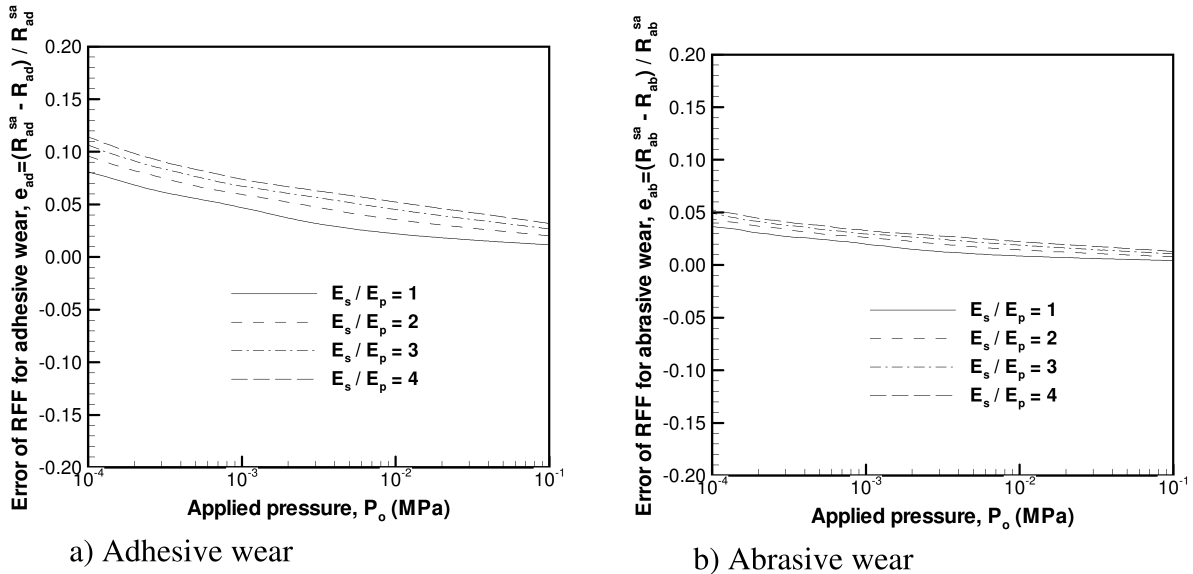

Fig. 7.4: The error of the RFF due to a) adhesive wear e_{ad} and b) abrasive wear e_{ab} introduced by contact pressure distribution based on Hertz contact for different porous elastic modulus ratio E_s / E_p (E_s = 100 MPa).

7.2.3 Effect of particle size

The mean particle radius has a significant effect on the error of Hertz contact as shown in Fig. 7.5. Large particles cause the error for both adhesive and abrasive wear to increase. The error for adhesive wear is as high as 11.5% for particle radius μ_p = 50 nm and P_o = 0.007 MPa, while the error for abrasive wear is found to be 6.5% under the same conditions. This can be explained by considering the dimensionless asperity contact force, $\tilde{f}_c^s$ $(= f_c^s / E_s \sigma_p^2)$, which decreases with particle radius μ_p (=4σ_p). Large particles alter the contact pressure distribution in single asperity contact (Section 4.5.3) and the RFF of single asperity as a result (Section 5.4.4).

7.2.4 Effect of pad topography

The parameters investigated so far in this section (particle concentration η_w, pad elastic modulus E_s and particle size μ_p) alter the contact behavior of a single asperity, therefore

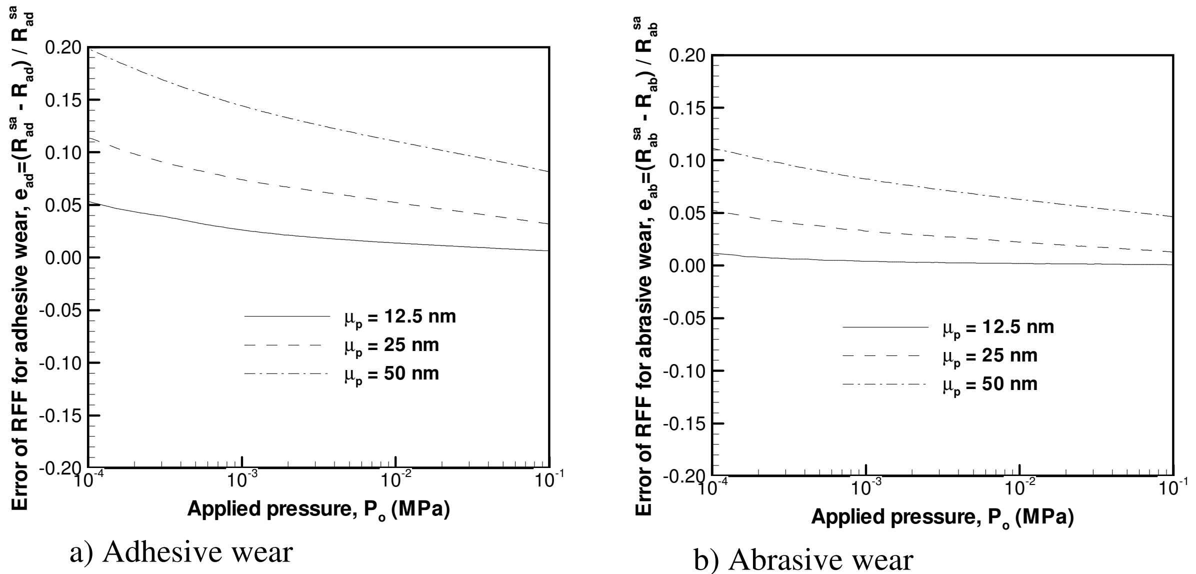

a) Adhesive wear b) Abrasive wear

Fig. 7.5: The error of the RFF due to a) adhesive wear e_{ad} and b) abrasive wear e_{ab} introduced by contact pressure distribution based on Hertz contact for different mean particle radius μ_p.

the error of Hertz contact varies as a function of these parameters. The effect of parameters related to pad topography on the other hand, influence the rough contact behavior causing the contact force on each asperity to vary as a function of pad topography parameters such as asperity radius R_s, asperity density η_s and pad roughness σ_s. Note that the exception is the asperity radius R_s, as R_s has an effect on both single asperity contact and rough contact behavior.

Fig. 7.6 shows that the error e of Hertz contact for RFF increases as asperity radius R_s becomes smaller. This result is consistent with the dependence of the error for the RFF of a single asperity on asperity radius R_s studied in Section 5.4.4, which shows that R_s causes the error for RFF of a single asperity to increase. Also note that the mean contact force on a single asperity in pad-wafer rough contact becomes lower when asperity radius R_s decreases, thus contributing to larger error in the case of small R_s.

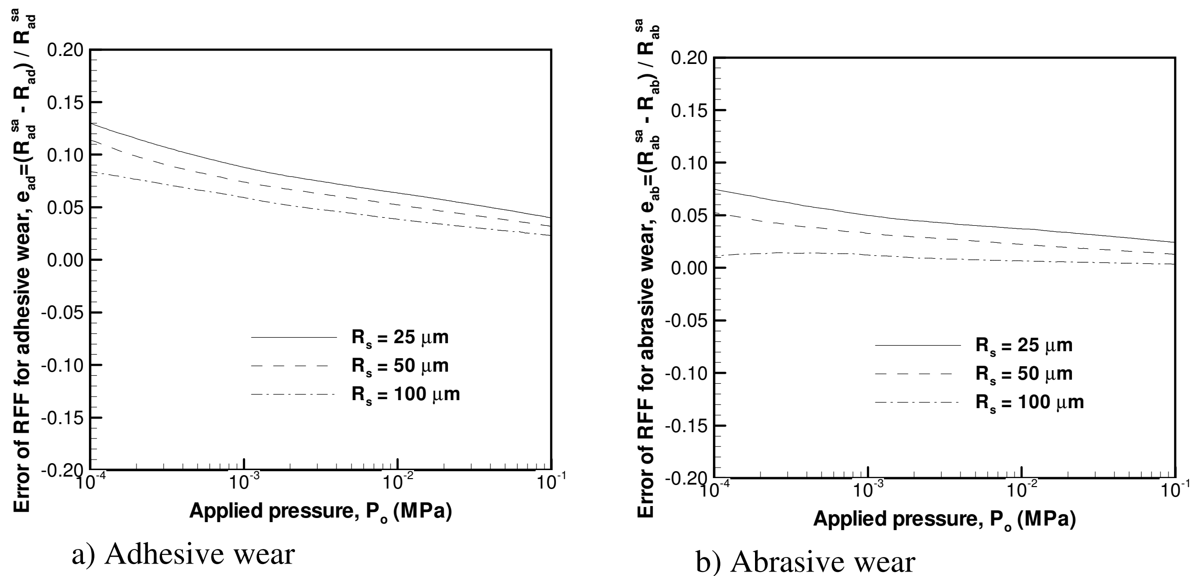

a) Adhesive wear b) Abrasive wear

Fig. 7.6: The error of the RFF due to a) adhesive wear e_{ad} and b) abrasive wear e_{ab} introduced by contact pressure distribution based on Hertz contact for different asperity radius R_s.

The effect of pad roughness σ_s on the error e is demonstrated in Fig. 7.7. As the pad roughness σ_s becomes smaller, the applied pressure is distributed over a larger number of asperities, thus the mean asperity contact force decreases. The error e of Hertz contact therefore increases with smaller pad roughness σ_s. A similar effect is also seen for the error e in Fig. 7.8 when asperity density η_s is varied. In this case, the error e of Hertz contact becomes larger when asperity density η_s increases since a larger number of asperities get engaged in contact decreasing the mean asperity contact force.

7.3 Effect of Pad Elastic Modulus and Pad Porosity

In this section, the effect of pad elastic modulus E_s on the RFF is investigated by varying E_s in the range, 10 MPa $< E_s <$ 100 MPa. The effects of pad porosity are modeled by using the elastic modulus ratio E_s / E_p, as described in Section 3.4. This ratio is taken in the range $1 < E_s / E_p < 4$.

7.3.1 Variation of RFF with applied pressure

<u>Results</u>

Figs. 7.9 and 7.10 show the variation of RFF due to adhesive R_{ad} and abrasive R_{ab} wear, respectively as a function of applied pressure, P_o for porous elastic modulus ratio, $1 \leq E_s/E_p \leq 4$. In Figs. 7.9a and 7.10a, pad elastic modulus E_s is taken to be 10 MPa representing a soft pad, while E_s of 100 MPa (hard pad) is used in Figs 7.9b and 7.10b. Sub-linear variation of the RFF due to both adhesive and abrasive wear are observed for a soft pad (E_s = 10 MPa) with high porosity (e.g. $E_s / E_p = 4$). On the other hand, the RFF increases almost linearly with applied pressure P_o for a hard pad (E_s = 100 MPa) or a non-porous pad ($E_s / E_p = 1$).

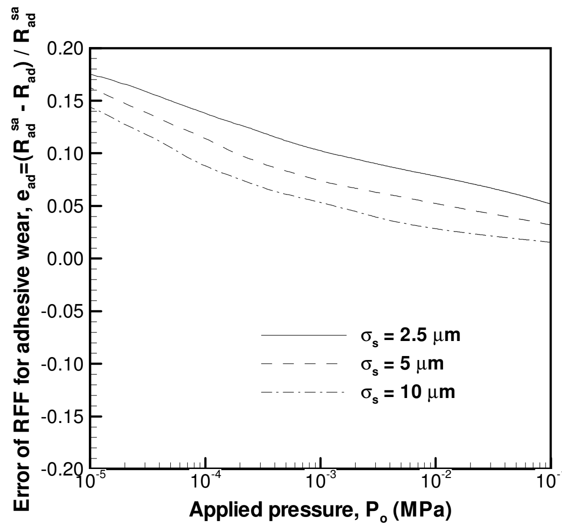

a) Adhesive wear

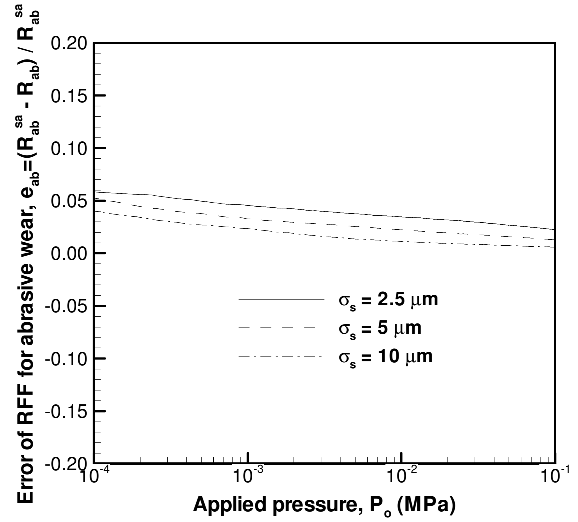

b) Abrasive wear

Fig. 7.7: The error of the RFF due to a) adhesive wear e_{ad} and b) abrasive wear e_{ab} introduced by contact pressure distribution based on Hertz contact for different pad roughness σ_s.

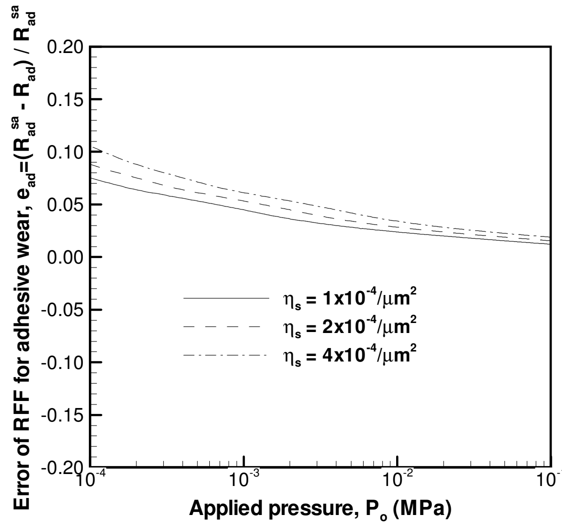

a) Adhesive wear

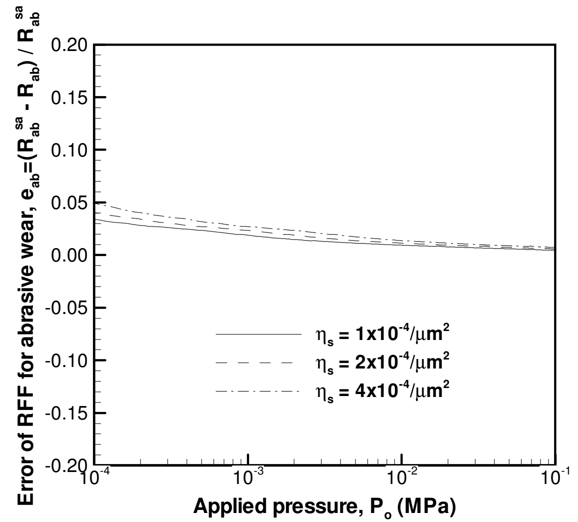

b) Abrasive wear

Fig. 7.8: The error of the RFF due to a) adhesive wear e_{ad} and b) abrasive wear e_{ab} introduced by contact pressure distribution based on Hertz contact for different asperity density η_s.

The non-linearity of the RFF with respect to applied pressure P_o is quantified by applying a power law curve-fit in the form, $R = cP_o^n$. Power law exponents for adhesive (n_{ad}) and abrasive (n_{ab}) wear are plotted in Fig. 7.11. A decreasing trend for the power law

exponent n for more porous pads is seen for a soft pad, E_s = 10 MPa, while n does not vary with pad porosity (E_s / E_p), significantly for a hard pad, E_s = 100 MPa. The exponent for abrasive wear is slightly greater (closer to 1) than adhesive wear, $n_{ab} > n_{ad}$. The power law exponent varies in the range $0.89 < n_{ad} < 0.93$ and $0.90 < n_{ab} < 0.95$, respectively for adhesive and abrasive wear, respectively.

<u>Discussion</u>

These results can be explained by considering the real contact area ratio A_r and the mean contact pressure P_m at the tip of asperities in "rough" contact of a pad and a wafer. The real contact area ratio A_r is the main controlling parameter for number of active particles n_a. Real contact area ratio A_r and number of active particles n_a are plotted in Fig. 7.12a and 7.12b, respectively for a soft pad (E_s = 10 MPa). It is seen that the sub-linear variation of real contact area ratio A_r and number of active particles n_a are similar to that of the RFF as shown in Figs 7.9a and 7.10a. This sub-linear increase in real contact area

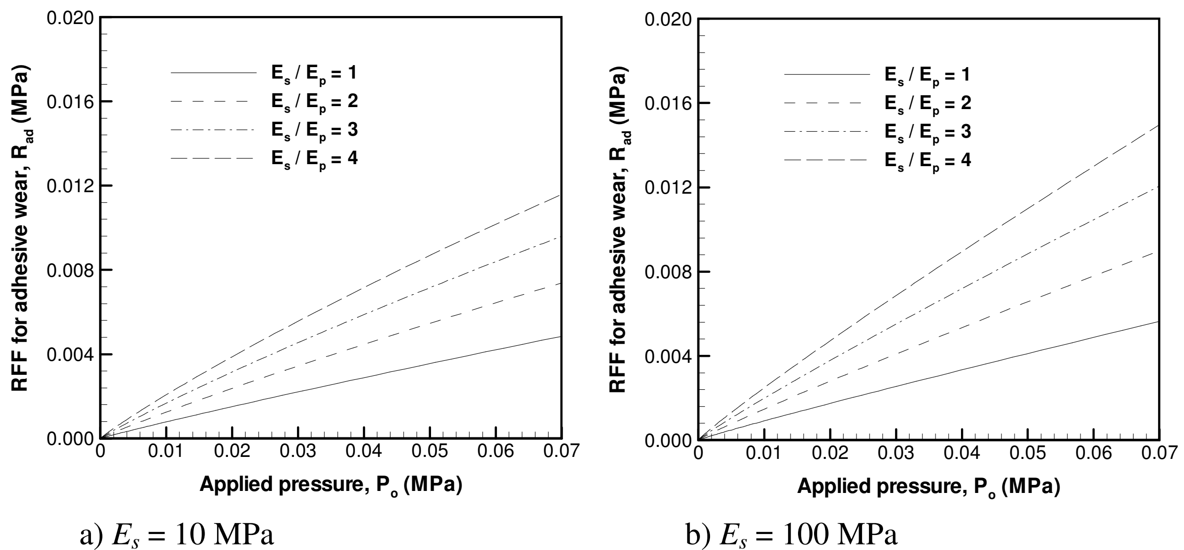

a) E_s = 10 MPa b) E_s = 100 MPa

Fig. 7.9: The variation of the RFF due to adhesive wear R_{ad} with applied pressure P_o for a soft and hard pad with different porous elastic modulus ratio E_s / E_p.

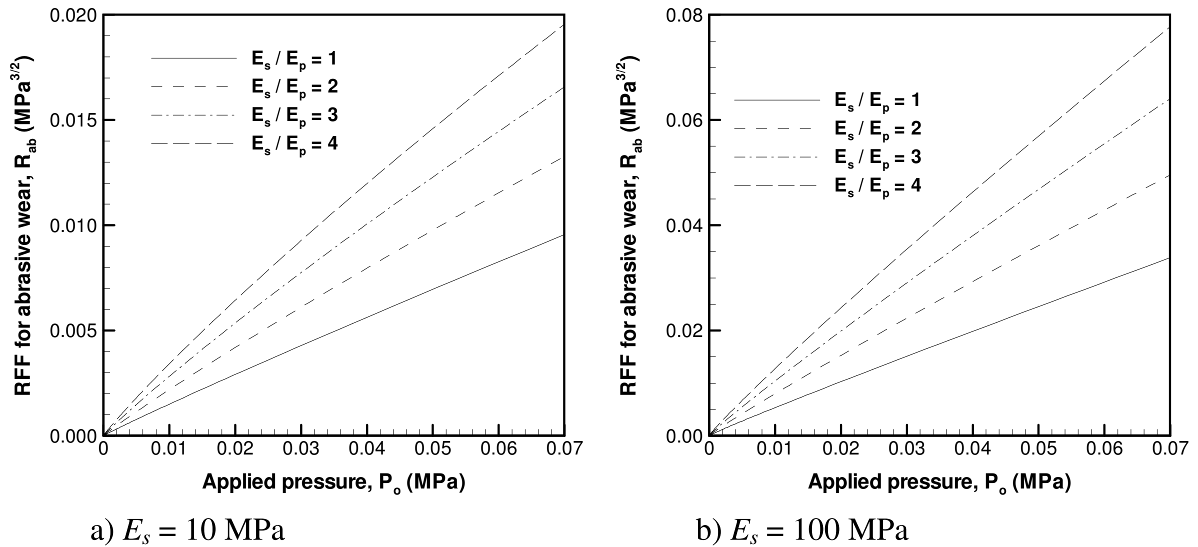

a) E_s = 10 MPa b) E_s = 100 MPa

Fig. 7.10: The variation of the RFF due to abrasive wear R_{ab} with applied pressure P_o for a soft and hard pad with different porous elastic modulus ratio E_s / E_p.

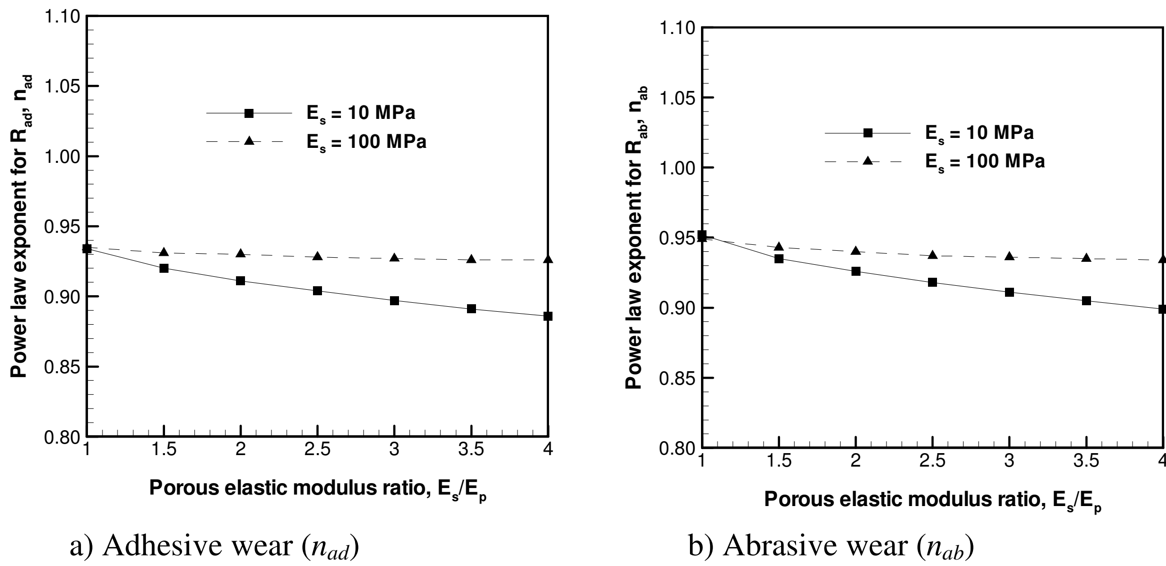

a) Adhesive wear (n_{ad}) b) Abrasive wear (n_{ab})

Fig. 7.11: Power law exponents n_{ad} and n_{ab} ($R = cP_o^n$) for the variation of the RFF with applied pressure P_o for different pad elastic modulus E_s and porous elastic modulus ratio E_s / E_p.

ratio A_r, and number of active particles n_a is explained by using Fig. 7.13, which shows the equilibrium separation distance d_{wp} between pad and wafer normalized by standard deviation (SD) of pad roughness σ_s for different pad elastic modulus E_s and porosity

(E_s/E_p) levels. It is seen that only the tall asperities included in the upper part of Gaussian distribution of asperity summit heights are in contact for a hard pad E_s = 100 MPa as separation distance remains above, $d_{wp} / \sigma_s > 0.7$. It is well known that real contact area ratio A_r increases linearly with applied pressure P_o in this case [1] (Section 3.1.2). For a soft pad E_s = 10 MPa, some of the asperities in the lower part of Gaussian distribution start to engage in contact ($d_{wp} / \sigma_s > -0.9$) causing a sub-linear behavior in the variation of real contact area ratio A_r. Furthermore, this behavior seen for a soft pad, E_s = 10 MPa becomes stronger with larger porosity, since porous pad elastic modulus E_p controlling the rough contact behavior decreases with larger porous elastic modulus ratio E_s / E_p. It is noted that a different probability density function for pad asperity summit heights may result in a different variation for both real contact area A_r and number of active particles n_a causing a similar effect on the RFF. This is studied in Section 7.5.

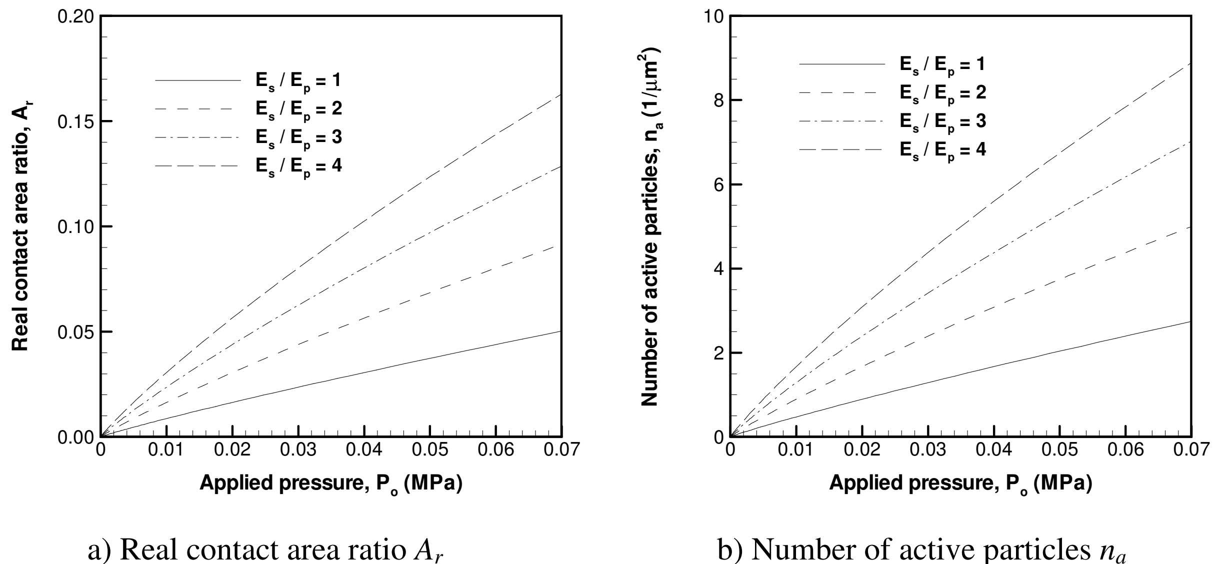

a) Real contact area ratio A_r b) Number of active particles n_a

Fig. 7.12: The effect of applied pressure P_o on a) real contact area ratio A_r and b) number of active particles n_a for a soft pad , E_s = 10 MPa with different porous elastic modulus ratio E_s / E_p.

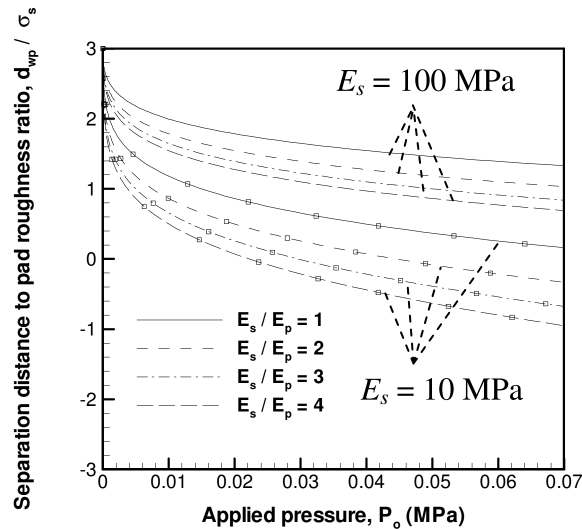

Fig. 7.13: The equilibrium separation distance d_{wp} / σ_s as a function of applied pressure P_o for different pad elastic modulus E_s and porous elastic modulus ratio E_s / E_p.

The mean contact pressure P_m, on the other hand, determines the local contact behavior affecting the distribution of contact pressure to particle and direct contacts. The mean contact pressure P_m varies slightly with respect to applied pressure P_o as depicted in Fig. 7.14. As a result, the variation of direct contact area A_d / A_r and particle contact pressure ratio P_p / P_o with applied pressure P_o remain to be small as shown in Fig. 7.15a and 7.15b, respectively. Fig. 7.15b shows that direct contact is dominant, covering a large fraction of contact area for the range of applied pressure P_o used in this study.

7.3.2 Effect of pad elastic modulus on RFF

Results

Fig. 7.16 shows the effect of pad elastic modulus E_s on the RFF due to adhesive R_{ad} (Fig. 7.16a) and abrasive R_{ab} (Fig. 7.16b) wear for applied pressure, P_o = 0.007 MPa (= 1 psi). Note that the behavior observed for applied pressure in the range, 0.007 MPa < P_o < 0.07 MPa remains to be similar, therefore only the plots for P_o = 0.007 MPa are included

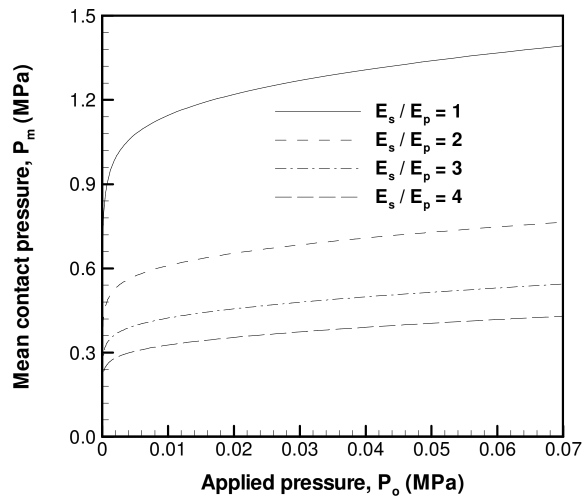

Fig. 7.14: The effect of applied pressure P_o on mean contact pressure P_m for a soft pad, E_s = 10 MPa with different porous elastic modulus ratio E_s / E_p.

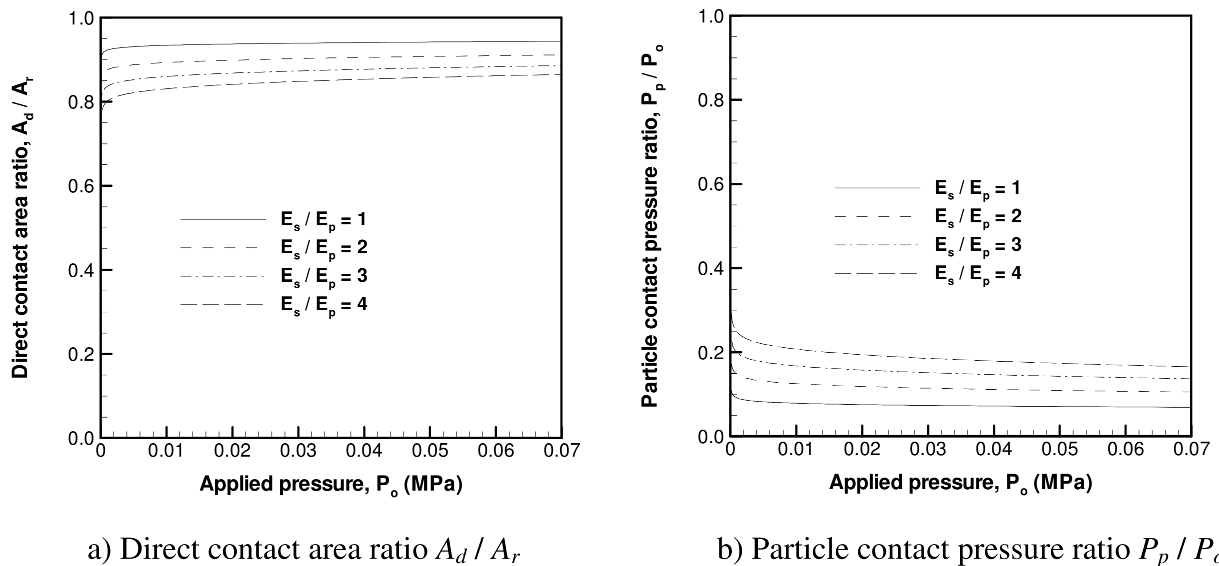

a) Direct contact area ratio A_d / A_r

b) Particle contact pressure ratio P_p / P_o

Fig. 7.15: The variation of a) direct contact area ratio A_d / A_r and b) particle contact pressure ratio P_p / P_o for a soft pad , E_s = 10 MPa with different porous elastic modulus ratio E_s / E_p.

here. It is seen in Fig. 7.16a that the RFF increases slightly with pad elastic modulus E_s for adhesive wear. An order of magnitude increase in pad elastic modulus E_s (E_s = 10 MPa to E_s = 100 MPa) results in only ~18% higher RFF for adhesive wear. This increase

does not depend on porosity (E_s / E_p). The RFF for abrasive wear is found to be more sensitive to pad elastic modulus E_s as demonstrated in Fig. 7.16b. The RFF due to abrasive wear R_{ab} for E_s = 100 MPa is ~3.7-times R_{ab} for E_s = 10 MPa. The reason for this strong dependence of the RFF due to abrasive wear R_{ab} on pad elastic modulus E_s is discussed next.

Discussion

The ability of the pad to transfer the applied pressure on the particles influences the RFF significantly. As the direct contact area A_d becomes larger, the pad can only transfer a fraction of applied pressure on particles, thus having a negative effect on the material removal. Pad elastic modulus E_s affects direct contact area A_d as particles are more easily embedded in the softer pads. This is presented in Fig. 7.17a, which shows that the direct contact area A_d decreases slightly with larger pad elastic modulus while causing particle contact pressure ratio P_p / P_o to decrease (Fig. 7.17b). The slight increase in the RFF for

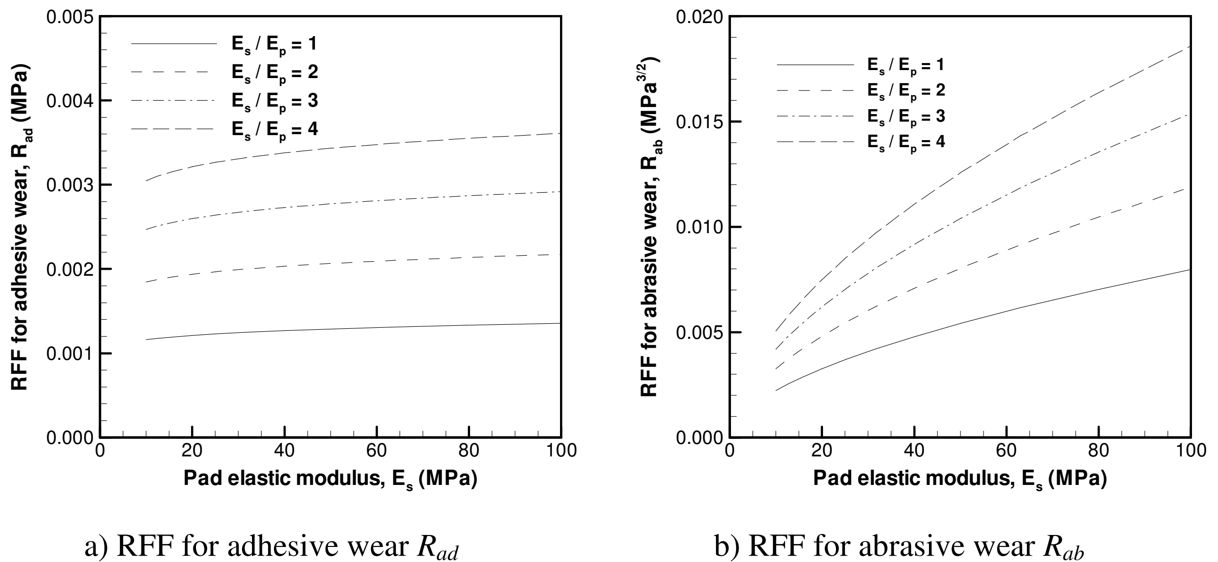

a) RFF for adhesive wear R_{ad}

b) RFF for abrasive wear R_{ab}

Fig. 7.16: The effect of pad elastic modulus E_s on the RFF due to a) adhesive R_{ad} and b) abrasive R_{ab} wear for P_o = 0.007 MPa (or P_o = 1 psi).

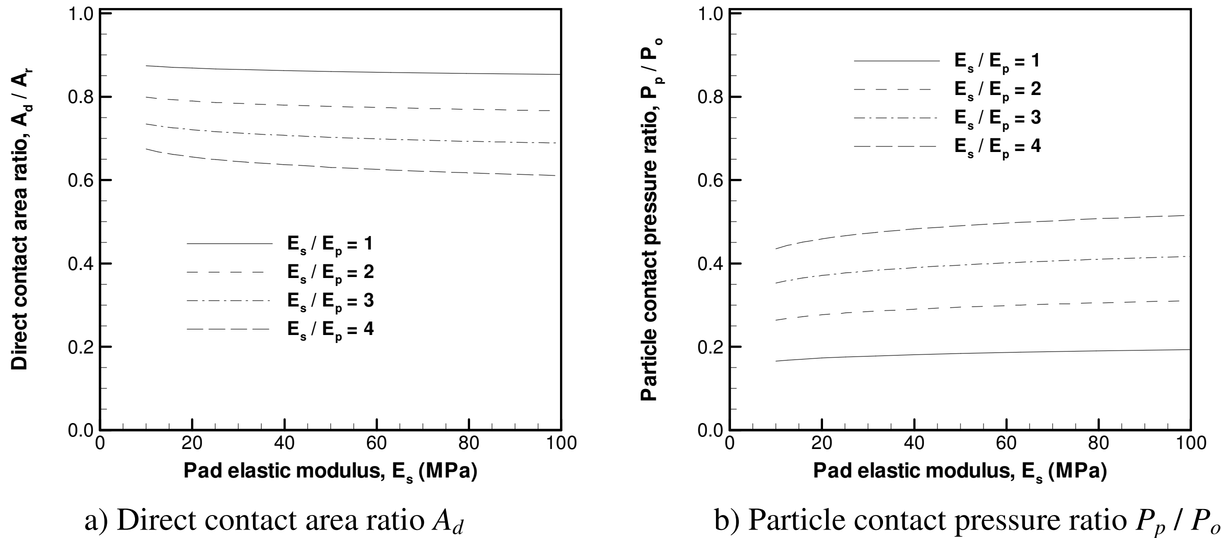

a) Direct contact area ratio A_d b) Particle contact pressure ratio P_p / P_o

Fig. 7.17: The effect of pad elastic modulus E_s on a) direct contact area ratio A_d / A_r and b) particle contact pressure ratio P_p / P_o for P_o = 0.007 MPa (or P_o = 1 psi).

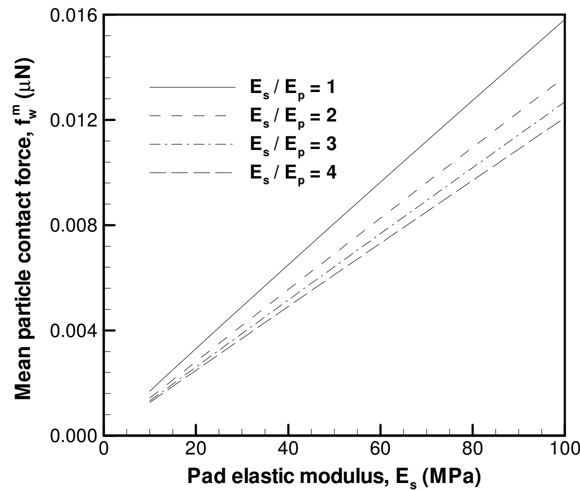

Fig. 7.18: The effect of pad elastic modulus E_s on mean particle contact force f_w^m for P_o = 0.007 MPa (or P_o = 1 psi).

adhesive wear R_{ad} is attributed to this effect. In addition, the effect of pad elastic modulus E_s on mean particle contact force f_w^m as shown in Fig. 7.18 is another factor to be considered in order to explain the significant increase in the RFF for abrasive wear R_{ab} with larger E_s. Mean particle contact force f_w^m increases with larger pad elastic modulus

E_s as a result of smaller real contact area ratio A_r and number of active particles n_a due to the increase in E_s. This is a favorable condition for abrasive wear since the RFF for abrasive wear varies with mean particle contact force as $R_{ab} \propto f_w^{m3/2}$.

7.3.3 Effect of porous elastic modulus ratio on RFF

Results

Pad porosity controls the porous elastic modulus ratio E_s / E_p and has a significant effect on the RFF as shown in Fig. 7.19a for a soft (E_s = 10 MPa) and Fig. 7.19b for a hard (E_s = 100 MPa) pad. The applied pressure is taken to be P_o = 0.007 MPa, although similar results are obtained at higher P_o. Increasing porous elastic modulus ratio from E_s / E_p = 1 to E_s / E_p = 4 causes the RFF due to adhesive R_{ad} and abrasive R_{ab} wear to increase to ~2.6-times and ~2.3-times, respectively. Porous elastic modulus ratio E_s / E_p seems to have a more significant influence on the RFF for adhesive wear R_{ad} while pad elastic modulus E_s does not result in such a significant influence on R_{ad} as explained in Section

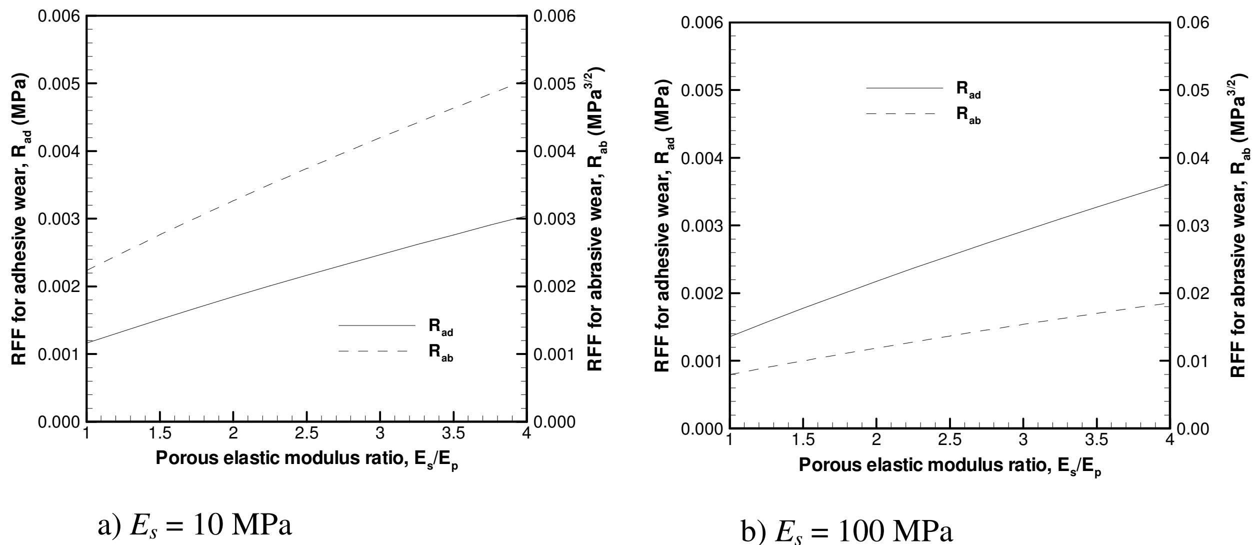

a) E_s = 10 MPa b) E_s = 100 MPa

Fig. 7.19: The effect of porous elastic modulus ratio E_s / E_p on the RFF for E_s = 10 MPa and b) E_s = 100 MPa (P_o = 0.007 MPa (or P_o = 1 psi)).

7.3.1. On the other hand, an opposite behavior is observed for the RFF due to abrasive wear R_{ab}, where R_{ab} is a strong function of pad elastic modulus E_s, but not a strong function of E_s / E_p. The role of pad elastic modulus E_s and porous elastic modulus ratio E_s / E_p for the variation of the RFF due to adhesive R_{ad} and abrasive wear R_{ab} is explained next.

Discussion

The elastic modulus of solid pad material E_s affects the penetration at the pad-particle interface. For stiffer pads (large E_s), pad-wafer direct contact becomes more difficult, i.e. the direct contact area ratio A_d / A_r becomes smaller, as illustrated in Fig. 7.17a. The response of the overall (large scale) pad deformation is influenced by the pad porosity. Therefore the porous pad elastic modulus E_p is used to model the contact between a rough pad and a wafer. As the pad porosity increases (smaller E_p), asperity contact spreads over a larger area, i.e. the real contact area A_r increases, thus causing mean contact pressure P_m at the tip of asperities (local contact pressure) decrease. Note that lower mean contact pressure P_m also decreases the direct contact area A_d / A_r.

Fig. 7.20a shows that the direct contact area ratio A_d / A_r decreases with increasing pad material stiffness E_s. This is accompanied by increased particle contact pressure ratio P_p / P_o as expected. The combined effect explains the increase of the RFF predicted in Fig. 7.19. Fig. 7.20 also confirms the opposite effect of increasing pad porosity (smaller E_p). If solid E_s and porous E_p pad elastic modulus increases or decreases at the same rate such that porous elastic modulus ratio E_s / E_p is constant, the RFF due to adhesive wear does not change significantly since the effects of E_s and E_p on R_{ad} offset each other.

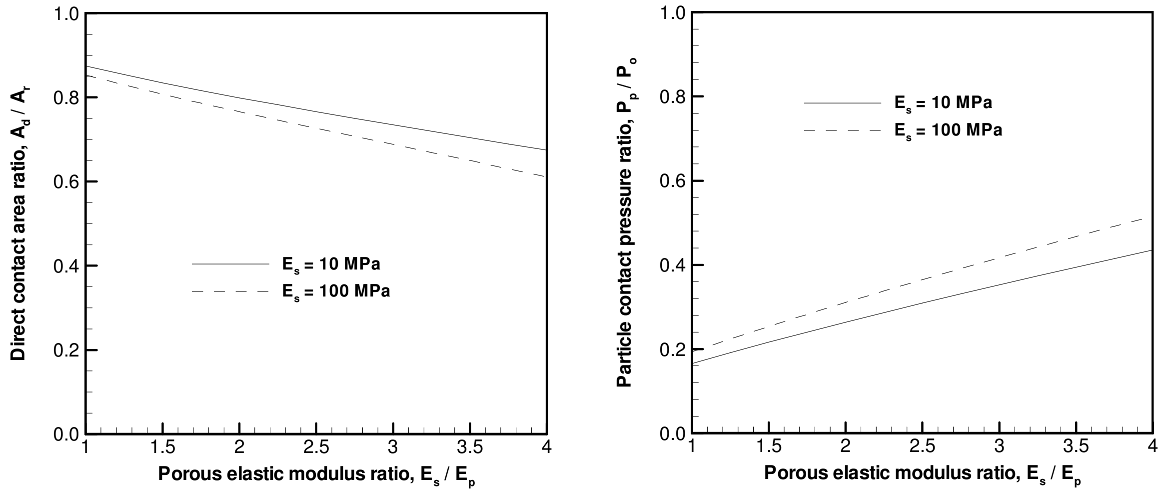

a) Direct contact area ratio A_d / A_r b) Particle contact pressure ratio P_p / P_o

Fig. 7.20: The effect of porous elastic modulus ratio E_s / E_p on a) direct contact area ratio A_d and b) particle contact pressure ratio P_p / P_o (P_o = 0.007 MPa (or P_o = 1 psi)).

In addition to the effects of local contact characteristics explained above, the RFF due to abrasive wear R_{ab} is also a strong function of the mean particle contact force, $R_{ab} \propto f_w^{m^{3/2}}$. In the case abrasive wear, larger pad elastic modulus E_s increases R_{ab} even if porous elastic modulus ratio E_s / E_p is constant due to larger mean particle contact force f_w^m, as discussed in Section 7.3.2. The smaller increase seen in the RFF due to abrasive wear R_{ab} as porous elastic modulus ratio E_s / E_p becomes larger is also attributed to this effect, where larger E_s / E_p decreases mean particle contact force f_w^m (Fig. 7.21).

7.3.4 Comparison with experiments

Preston equation [2], $RR = k_p P_o V_r$ has been widely used for predicting MRR as a function of applied pressure P_o and relative velocity V_r in CMP. The effects of other parameters such as particle concentration, particle size, pad elastic modulus, pad roughness etc. are implicitly included in Preston constant, k_p. The experimental studies

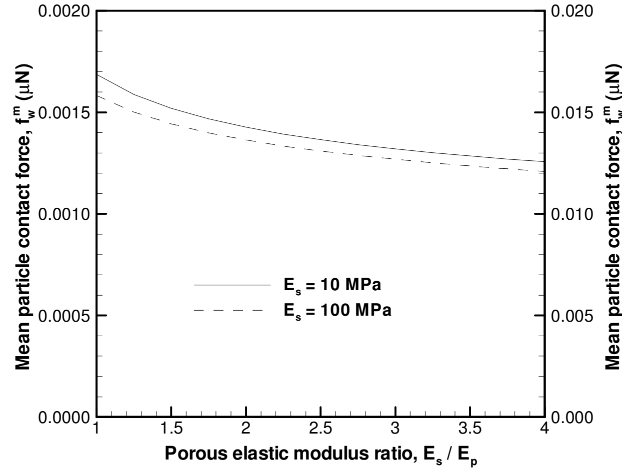

Fig. 7.21: The effect of porous elastic modulus ratio E_s / E_p on mean particle contact force f_w^m (P_o = 0.007 MPa (or P_o = 1 psi)).

for CMP however indicate both a linear (Prestonian) and a non-linear (non-Prestonian) variation of MRR as a function of applied pressure P_o and relative velocity V_r. The degree of non-linearity and the parameters affecting the non-linear behavior observed in the experiments is discussed next. Modeling results explained in this section are re-visited in order to explain the trends seen in the experiments.

Preston equation was first developed based on experimental observations for the variation of MRR with respect to applied pressure and velocity in glass polishing. One of the fundamental differences between glass-polishing and CMP is that the pads used in CMP are relatively softer than the pads in glass polishing [3]. This fundamental difference is considered to be the main reason for non-Prestonian behavior, and demonstrated in the following experimental studies. Ouma [4] conducted CMP experiments on tetra-ethyl ortho-silicate (TEOS) films using silica slurry. Two different types of hard pads (IC1400 and IC1000 from Rodel Inc.) were utilized in the experiments. A similar experiment was conducted by Stein et al. [5], where TEOS films were polished with silica slurry using

both a hard pad (IC1400) and a soft pad (POLITEX from Rodel Inc.). The MRR normalized with respect to the maximum MRR obtained from these experiments are plotted in Fig. 7.22. It is seen that MRR became a non-linear function of the product of pressure and velocity, P_oV_r, in the case of a soft pad [5]. The power law exponent for curve fit of MRR indicated a dependence, $RR \propto (P_oV_r)^{0.59}$. On the other hand, a different behavior is seen for hard pads, where the power law exponents for a hard pad showed a closely linear variation, $MRR \propto (P_oV_r)^{0.87}$ [4] and $MRR \propto (P_oV_r)^{1.01}$ [5].

Effect of relative velocity

Note that the trends explained above include the effect of both applied pressure P_o and relative velocity V_r since the effect of the product, P_oV_r was investigated. The effect of velocity V_r has been the subject of many experimental studies as explained in Section 2.3.1, which revealed both linear and non-linear variation of MRR with respect to V_r.

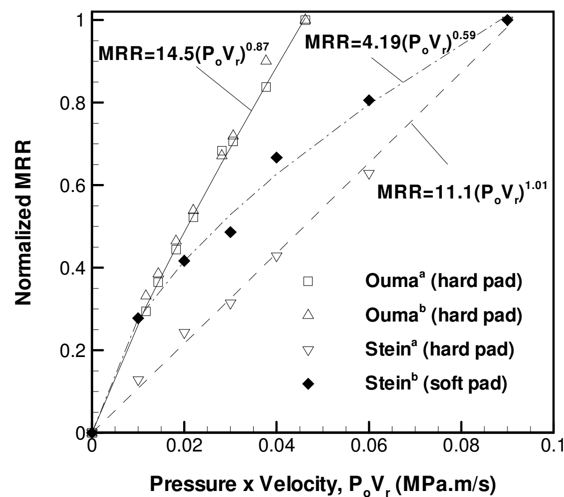

Fig. 7.22: Experimental findings of Ouma [4] and Stein et al. [5] for the variation of normalized MRR with respect to the product of pressure and velocity, P_oV_r for soft and hard pads. The MRR was normalized with respect to the maximum MRR observed in the experiments.

Theoretical studies conducted to understand these experimental results showed that the effect of velocity V_r can be explained by studying the mechanics of hydrodynamic lubrication taking place due to the slurry flow between pad and wafer. An extensive review of experimental and theoretical work on this subject was reviewed in Section 2.1. The mechanics of hydrodynamic lubrication in CMP is not in the scope of this work and MRR was assumed to increase linearly with relative velocity V_r as consistent with Preston equation. The models developed in this work focus on the effect of applied pressure P_o, which can also be influenced by the effects of hydrodynamic lubrication. However experimental studies explained in Section 2.1.1 indicated that the operating lubrication regime in CMP is most likely to be boundary lubrication and a continuous slurry film does not exist at pad-wafer interface. Therefore the interactions between pad and wafer are dominated by pad-wafer contact, which is the subject of our modeling efforts. The experiment results available in the literature for dependence of MRR on applied pressure P_o are summarized next.

Effect of applied pressure

The experiments found in literature for the effect of applied pressure P_o were classified in two groups based on the pad elastic modulus E_s (hard or soft pads). Nguyen et al. [6] conducted CMP experiments on a copper film using two different slurry chemistry containing alumina particles. Two pads with different surface morphology were used by Clark et al. [7] in CMP of oxide films with silica particles. In these experiments, IC1400 [6] and IC1000 [7] pads were used. These pads are considered to be in the category of hard pads in CMP [8]. The results for the normalized MRR are shown in Fig. 7.23a. It is

seen that MRR increased almost linearly with applied pressure P_o when a hard pad was used. The power law exponents were in the range $0.84 < n < 1.04$.

In another set of experiments, shown in Fig. 7.23b, the variation of normalized MRR with respect to applied pressure was investigated by using soft pads. The experiments by Forsberg involved CMP of oxide films with a silica slurry (Suba500 pad from Rodel Inc.), while silica slurry was used for CMP of TEOS films in the experiments by Chandrasekaran et al. [9] (UR2 pad from Rodel Inc.). Two sets of experiments were conducted [9] by using different slurry, where the particle size was 122 nm in the first slurry and the second slurry included 35 nm particles. Copper films were polished in experiments by Guo and Subramanian [10], where alumina slurry and Suba500 pads were

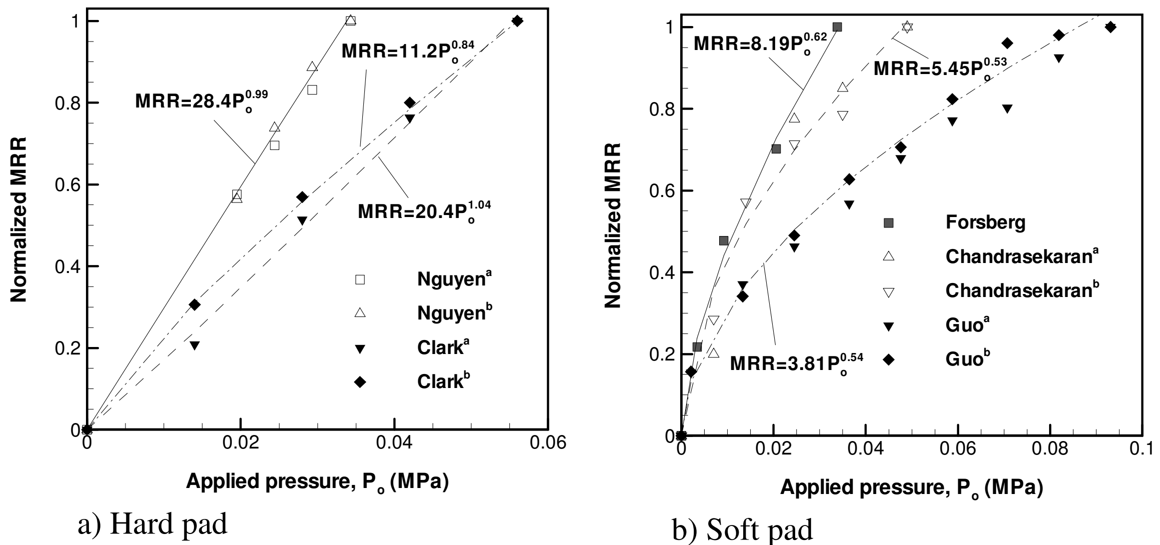

Fig. 7.23: Experimental findings for the variation of the normalized MRR with respect to applied pressure P_o for a) hard pads (Nguyen[ab] et al. [6], Clark[ab] et al. [7]) and b) soft pads (Forsberg [22], Chandrasekaran[ab] et al. [9], Guo and Subramanian[ab] [10]). Note that two different slurry chemistry in Nguyen[ab] et al. [6], two pads with different surface morphology in Clark[ab] et al. [7], two different slurry in Chandrasekaran[ab] et al. [9] and two different velocity in Guo and Subramanian[ab] [10] were used.

used. The experiments were run with two different relative velocities V_r (0.47 m/s and 0.67 m/s). The results of these experiments utilizing soft pads plotted in Fig. 7.23b exhibited a different behavior as compared to the experiments with hard pads shown in Fig. 7.23a. MRR increased sub-linearly with applied pressure P_o when a soft pad was used. The power law exponents varied in the range, $0.53 < n < 0.62$.

In addition to these results, oxide CMP experiments by silica particles [11] indicated a power law exponent of 0.96 and 0.89 for hard and soft pads, respectively. Wrschka et al. [12] reported power law exponents for MRR achieved by a soft pad in CMP of aluminum. They obtained a power law exponent of $n = 0.80$ using alumina particles (3.4%) and a power law exponent of $n = 0.86$ was found when silica particles (12.5%) were used.

The power law exponents of the P_o term of the MRR obtained from experiments are summarized in Table 7.2. It is seen that power law exponent varies in the range, $0.84 < n < 1.04$ for hard pads, whereas for soft pads, it is in the range, $0.53 < n < 0.89$. Note that the tendency for the MRR to become sub-linear with softer pad is in agreement with modeling results as shown in Fig. 7.11.

The results presented in Section 7.3 indicate that pad elastic modulus E_s and porous elastic modulus ratio E_s / E_p play an important role for the behavior of MRR (or RFF) with respect to applied pressure P_o. In these models, the power law exponent n decreases from 0.93 to 0.88 for adhesive and 0.94 to 0.90 for abrasive wear, as the pad elastic modulus is reduced from $E_s = 100$ MPa to $E_s = 10$ MPa for a porous pad ($E_s / E_p = 4$). This result is in good agreement with oxide CMP experiments conducted by Hernandez et al. [11] indicating a decrease in power law exponent n from 0.96 to 0.89 when a soft

Experiments	Polishing pad	Polished film	Slurry	Applied pressure (psi)	Power law exponent
Nguyen [6]	hard	copper	alumina	2.8 – 4.9	0.99
Clark [7]	hard	oxide	silica	2 – 8	1.04[a] – 0.84[b]
Hernandez[b] [11]	hard	oxide	silica	2.8 – 5.8	0.96
Forsberg [22]	soft	oxide	silica	0.5 – 4.8	0.62
Chandrasekaran[ab] [9]	soft	TEOS	silica	1 – 7	0.53
Guo [10]	soft	copper	alumina	0.3 – 13.3	0.54
Hernandez[a] [11]	soft	oxide	silica	2.8 – 5.8	0.89
Wrschka[a] [12]	soft	aluminum	alumina	2.8 – 5.8	0.80
Wrschka[b] [12]	soft	aluminum	silica	2.8 – 5.8	0.86

Table 7.2: Summary of power law exponents determined in experiments, organized to demonstrate the effect of pad elastic modulus..

pad is used instead of a hard pad. However the power law exponent can be as small as n = 0.53 in the experiments, while modeling results using base parameters did not result in a power law exponent, $n < 0.88$. We think this discrepancy can be explained as follows.

Note that the model results show that direct contact is the dominant contact mechanism when base parameters are used in the model. This means that the variation of RFF with respect to applied pressure is determined by the number of active particles n_a, which is a strong function of real contact area. For a randomly rough surface characterized by Gaussian probability density function (PDF) of asperity summit heights, the increase in the real contact area with applied pressure is linear for a hard pad, whereas for a soft pad, sub-linear dependence starts to occur due to the fact that asperities included in the lower part of the PDF start come into contact. This behavior is true for a random surface surface, while different pad topography may alter this behavior. This is considered to be

the main reason for small power law exponents as low as n = 0.53 seen in the experiments. In fact, Ahmadi and Xia [13], and Luo and Dornfeld [14] explain the sub-linear behavior, by considering a wavy pad topography, which gives a relation between applied pressure P_o and real contact area A_r as $P_o \propto A_r^{2/3}$. Using this relationship, our model for a soft pad would result in a power law exponent of $n \approx 2/3$. This is discussed in more detail in Section 7.5.

These observations are valid for particle concentration, η_w = 2.5% selected as the base value used in this section. However, it will be later shown in Section 7.4 that a fundamental difference appears between soft and hard pads at high particle concentration e.g. η_w = 10%, where direct contact does not dominate the contact for hard pads and as a result number of active particles n_a is not the only mechanism affecting the variation of RFF with respect to applied pressure P_o. In this case, direct contact area ratio A_d decreases significantly with applied pressure P_o while causing an increase in particle contact pressure ratio P_p / P_o and thus affecting RFF.

Effect of pad elastic modulus

Experimental studies listed in Table 7.3 indicated that the MRR is typically higher for a hard pad as compared to a soft pad. Note that experimental conditions such as relative velocity, particle concentration, wafer material etc. have an important effect on the actual MRR values. In the experiments listed in Table 7.3, all the actual parameters used in the experiments were not available, however a decreasing trend for softer pads can be observed. Guo and Subramanian [10] carried out copper CMP experiments with alumina slurry using the same conditions (P_o = 6.8 psi, V_r = 0.47 m/s, η_w = 2.5%) for a soft (Suba-500) and a hard (IC-1000) pad. They found that the MRR for a hard pad was ~ 245

nm/min, while it was ~ 110 nm/min for a soft pad. The ratio of MRR for a hard to a soft pad was ~ 2.2. The same ratio calculated from Figs. 7.16a and 7.16b for adhesive and abrasive wear and using E_s = 10 MPa for a soft pad and E_s = 100 MPa for a hard pad with $E_s / E_p = 4$ was 1.2 and 3.7, respectively indicating that the experimental trend can be explained by considering both adhesive and abrasive wear taking place simultaneously. A similar experiment was carried out by Saxena et al. [15] for CMP of copper films with alumina slurry (P_o = 4 psi, η_w = 3%). A soft PANW pad (Freudenberg Nonwovens) and a hard IC-1400 were used in this study. The ratio of MRR achieved by a hard pad (165 nm/min) to a soft pad (140 nm/min) was found to be 1.18, which is very close to the ratio (~1.2) calculated by our model with adhesive wear, as shown in Fig. 7.16a.

Castillo-Mejia et al. [16] carried out CMP experiments in order to evaluate the influence of immersion time of the IC1000 pads in water, on mechanical properties of pad. It was shown that the elastic modulus of wet pads was ~25% lower than the elastic modulus of dry pads. CMP experiments conducted on TEOS films by using different immersion time for pads showed a decrease in MRR when pads were not conditioned prior to polishing while no difference in MRR was observed when pads were conditioned as demonstrated

Experiments	**Polishing pad**	**Polished film**	**Slurry**	**Applied pressure (psi)**	**Maximum MRR (nm / min)**
Nguyen [6]	hard	copper	alumina	4.9	368 - 474
Clark [7]	hard	oxide	silica	6	340
Forsberg [22]	soft	oxide	silica	4.8	238
Chandrasekaran[ab] [9]	soft	TEOS	silica	7	10.7 – 12.3
Guo [10]	soft	copper	alumina	6.8	180

Table 7.3: Comparison of the maximum MRR achieved in experiments using a soft and a hard pad.

in Fig. 7.24. This was explained by considering water penetration, which was estimated to be in the order of 20 μm causing softening of the pad material. This soft layer is removed if conditioning is performed on the pad. It can be assumed that this layer dominates the contact for each particle since the depth of the layer is large as compared to particle size. In our model, solid pad elastic modulus E_s determines the particle scale contact. Therefore immersion of pad in water decreases solid pad elastic modulus E_s, whereas porous pad elastic modulus E_p remains relatively constant with immersion of pad in water. Since the reduction in solid pad elastic modulus E_s was not quantified, only qualitative conclusions for the relation between solid pad elastic modulus E_s and MRR (or RFF) can be drawn from this study. It is seen in Fig. 7.24 that decreasing solid pad elastic modulus E_s due to immersion in water for 24 and 48 hrs resulted in 5% and 10% smaller MRR, respectively. If the base parameters listed in Table 7.1 are used in our model, RFF (or MRR) becomes smaller by 18% for adhesive wear if solid pad elastic modulus E_s is decreased from 100 MPa to 10 MPa by keeping porous elastic modulus

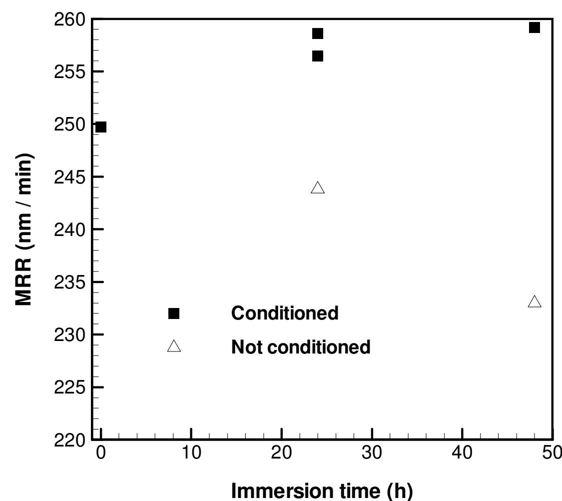

Fig. 7.24: Experimental results [16] for the effect of pad immersion time on MRR using a conditioned or an unconditioned pad.

ratio constant, $E_s / E_p = 4$ (Fig. 7.16a). A much larger decrease in RFF (~ 70%) is found for abrasive wear. It is noted that in the case of a smaller solid pad elastic modulus E_s while porous pad elastic modulus E_p is kept constant, porous elastic modulus ratio E_s / E_p also becomes smaller. Therefore there may be an additional effect due to the change in porous elastic modulus ratio E_s / E_p. According to the models, smaller porous elastic modulus ratio E_s / E_p causes a further reduction in RFF. Quantitative evaluation cannot be performed since the change in solid pad elastic modulus E_s was not determined in experiments, however experiment and modeling results agree qualitatively.

<u>Effect of pad porosity</u>

There have been a few studies investigating the effect of pad porosity on MRR. The pad porosity plays an important role since porous elastic modulus ratio E_s / E_p is determined by pad porosity. The experimental work by Fury and James [17] is one of the complete studies done to evaluate the effect of pad porosity. In this study, one porous pad with relative density $\rho_{po} / \rho_{so} = 0.6$, (IC1000) and one solid pad $\rho_{po} / \rho_{so} = 1$ (IC2000) made from the same polyurethane material were used. Since the pads were made of the same polyurethane material, it can be assumed that solid pad elastic modulus E_s is same for these two pads, while porous elastic modulus ratio E_s / E_p can be calculated using Fig. (3.13) to be $E_s / E_p \approx 3$ for $\rho_{pr} / \rho_{sl} = 0.6$. The pads were roughened by using the same conditioning parameters to ensure that the surface topography of the pads were similar.

Fig. 7.25 shows MRR obtained from a large number of oxide CMP experiments using these two pads. One of the conclusions drawn from this study was that MRR of a solid pad (IC2000) was more consistent as compared to MRR of a porous pad (IC1000), which was attributed to the variations in physical properties of porous pads [8]. In addition to

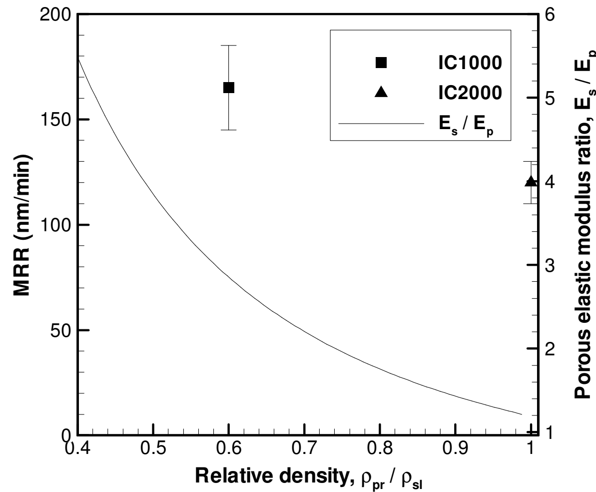

Fig. 7.25: Experimental results [17] for the effect of pad porosity on MRR. The solid line indicates the E_s / E_p ratio.

the difference in consistency, the average MRR for a porous pad (IC1000) was found to be ~40% higher than that of a solid pad (IC2000). This finding is in qualitative agreement with the results of our model indicating an increasing trend for MRR as pad porosity becomes larger, as also illustrated in Fig. 7.19.

In Fig. 7.26, pad elastic modulus and porous elastic modulus ratio was taken to be E_s = 100 MPa and E_s / E_p = 3, respectively while applied pressure was maintained at P_o = 0.007 MPa. Since particle concentration η_w used in experiments was not specified, the ratio of RFF for a pad with porous elastic modulus ratio E_s / E_p = 3 to a solid pad E_s / E_p = 1 was plotted as a function of particle (silica) concentration. It is seen that RFF for a porous pad E_s / E_p = 3 was greater than a solid pad by 40% for adhesive wear at particle concentration, η_w = 5% and for abrasive wear at η_w = 6%. Therefore, the increase in MRR for larger porosity is predicted well by the model.

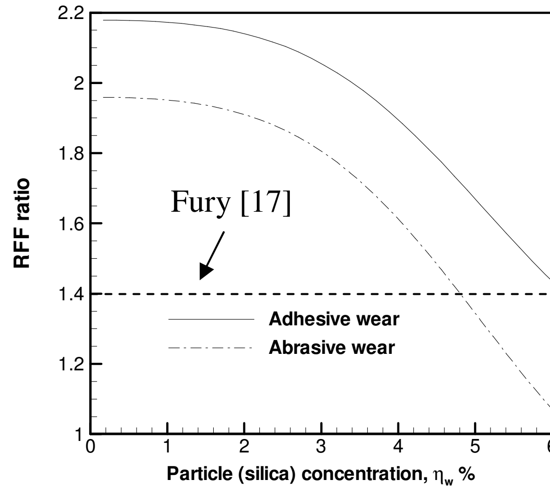

Fig. 7.26: Model predictions for the ratio of RFF for a porous (E_s / E_p = 3) to RFF for a solid pad (E_s / E_p = 1) as a function of particle (silica) concentration η_w. The dotted line indicates the ratio determined in the experiments by Fury and James [17].

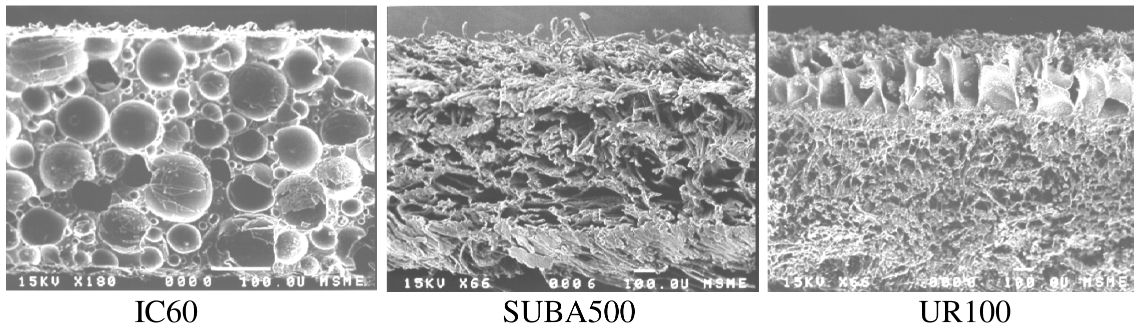

Fig. 7.27: Different porous structure of pads from Moon et al. [18].

Experiments conducted by Moon et al. [18,19] involved CMP of bare silicon wafers with silica slurry using three commercially available pads (IC60, SUBA500 and UR100) having different porous structure and density. The IC60 pad was a micro-porous polyurethane polishing pad. The Suba500 pad was an impregnated felt substrated-coagulated urethane in a fiber matrix and The UR100 pad was a napped poromerics-porous urethane layers on supporting substrates [20]. The cross-sections of these pads are

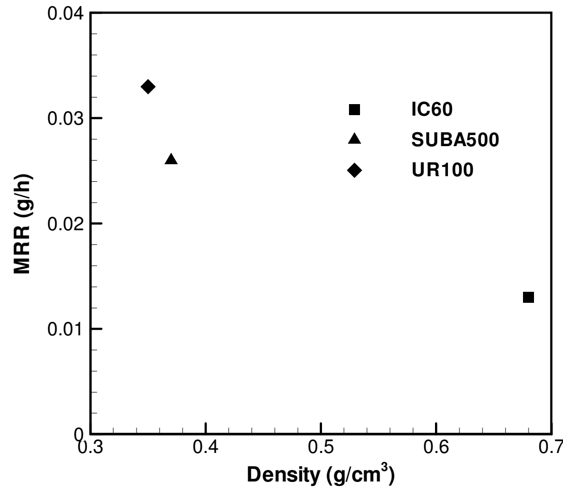

Fig. 7.28: Effect of pad density on MRR determined in experiments [18].

depicted in Fig. 7.27. Fig. 7.28 shows that MRR became larger with smaller density. Although smaller density is an indication for higher porosity, it is not possible to quantify the actual porosity by calculating the relative density if the density of solid pad material is not known. A direct comparison of these experiments to our model is not possible since relative density (or porous elastic modulus ratio) is not known. However it is observed that the prediction of our model indicating larger RFF (or MRR) with higher porosity as shown in Fig. 7.19 agrees qualitatively with experiments showing larger MRR with smaller pad density (or higher porous elastic modulus ratio E_s/E_p).

7.4 Effect of Particle Concentration

Next, we will investigate the effect of particle concentration on the RFF. In the models developed in this work, volumetric particle concentration η_v is the main parameter controlling the number of particles entering the calculations. Particle concentration by weight-ratio η_w is commonly used in practice since it is easier to measure for a slurry. For a given particle concentration η_w by weight-ratio, volumetric particle concentration η_v can be calculated using the density of particle material, ρ_p in Eqn (4.8). Despite the fact that

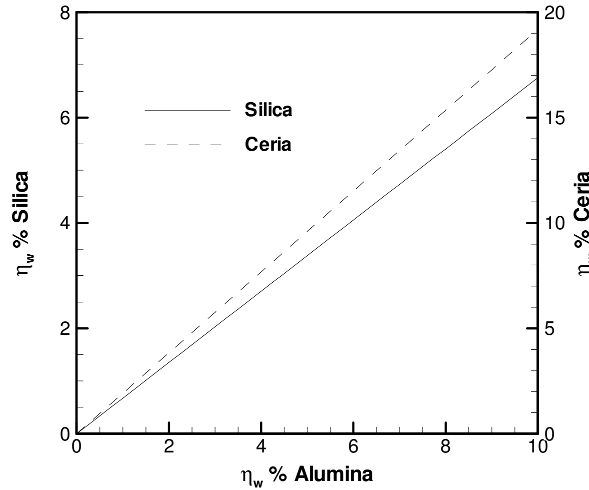

Fig. 7.29: Equivalent particle concentration, η_w by weight-ratio of particles of different materials to result in the same volumetric particle concentration, η_v.

the modeling results are obtained for alumina particles (ρ_{al} = 3.7 g/cc), results can be evaluated for different particle materials such as silica, (ρ_{si} = 2.5 g/cc) or ceria (ρ_{ce} = 7.1 g/cc) by utilizing Fig. 7.29, which shows the equivalent particle concentration η_w by weight-ratio of different particle materials resulting in the same volumetric particle concentration η_v.

7.4.1 Variation of RFF with applied pressure

<u>Results</u>

The particle concentration η_w influences the response of the RFF as applied pressure P_o is varied. Figs. 7.30 and 7.31 show the variation of RFF due to adhesive R_{ad} and abrasive R_{ab} wear, respectively for different particle concentrations η_w's. These figures show that at a given applied pressure P_o, R_{ad} could remain constant with increasing particle concentration η_w (Figs. 7.30b and 7.30d), and R_{ab} could even decrease with higher η_w (Figs. 7.31b and 7.31d). A detailed study of this behavior is presented later in this section.

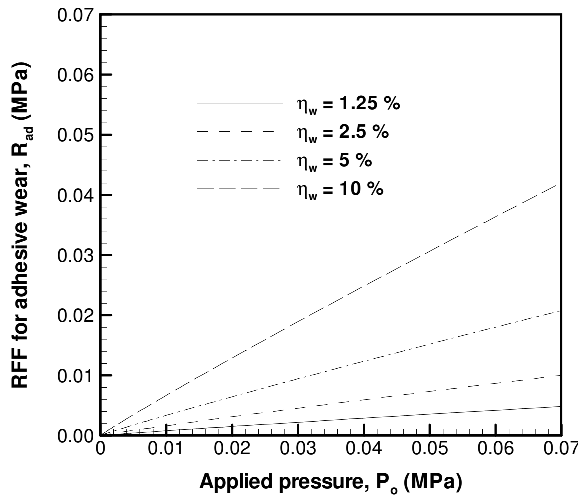

a) E_s = 10 MPa and E_s / E_p = 1

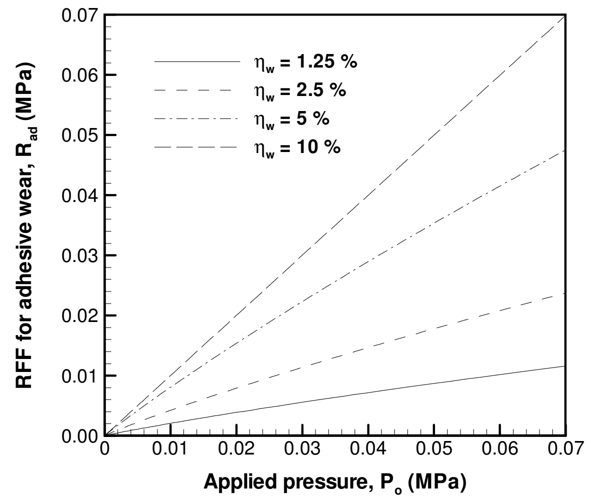

b) E_s = 10 MPa and E_s / E_p = 4

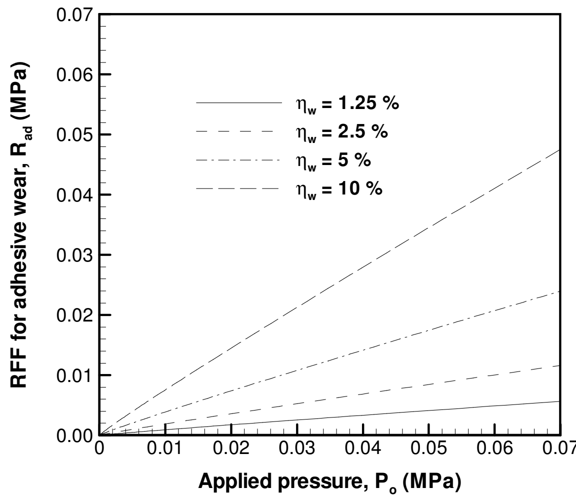

c) E_s = 100 MPa and E_s / E_p = 1

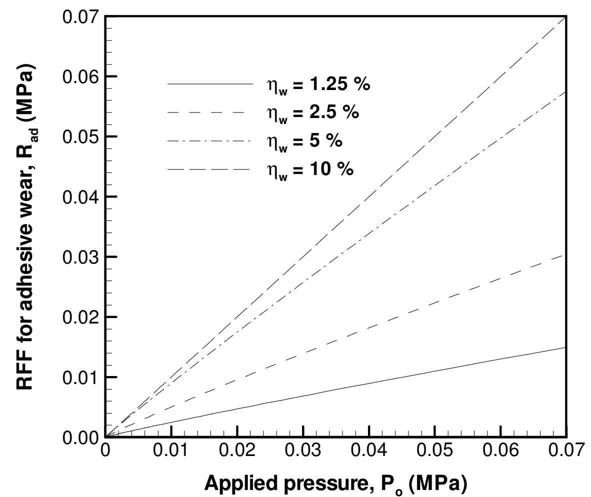

d) E_s = 100 MPa and E_s / E_p = 4

Fig. 7.30: The RFF due to adhesive wear R_{ad} as a function of applied pressure P_o for different particle concentration η_w.

The RFF presented in Figs. 7.30 and 7.31 is curve-fit to a power law function of the form $R = cP_o^n$. The power law exponents n thus obtained are given in Fig 7.32 for R_{ad} and R_{ab} as a function of particle concentration η_w, pad elastic modulus E_s and porous elastic modulus ratio E_s / E_p. Fig. 7.32 indicates that particle concentration η_w alters the dependence of RFF on applied pressure P_o, especially for a pad with a large porous

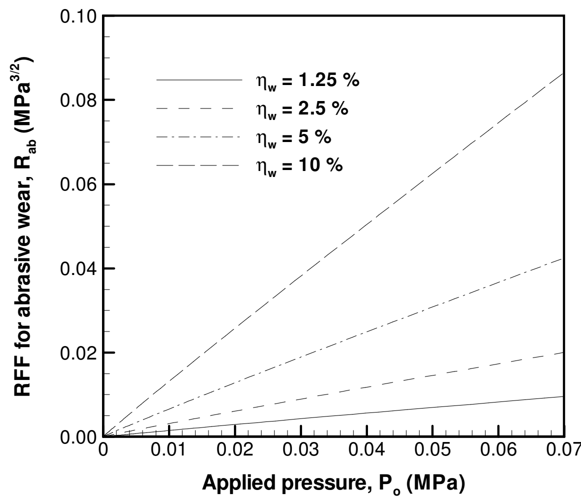

a) E_s = 10 MPa and E_s / E_p = 1

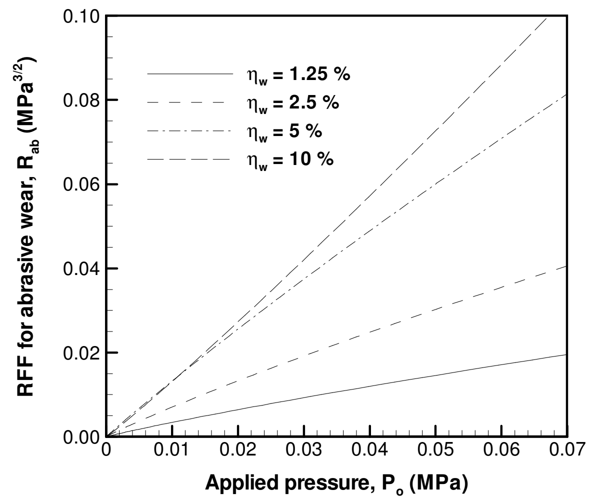

b) E_s = 10 MPa and E_s / E_p = 4

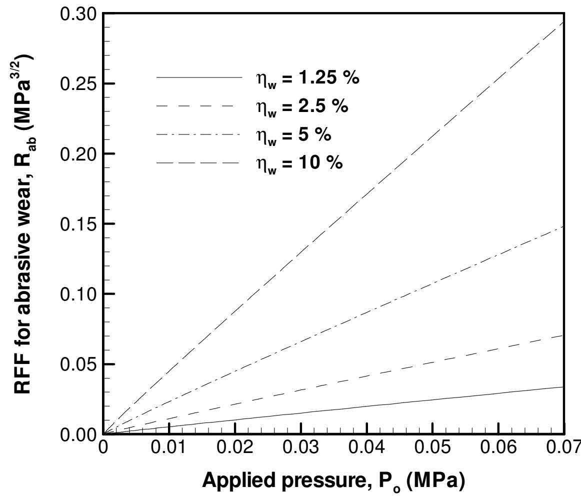

c) E_s = 100 MPa and E_s / E_p = 1

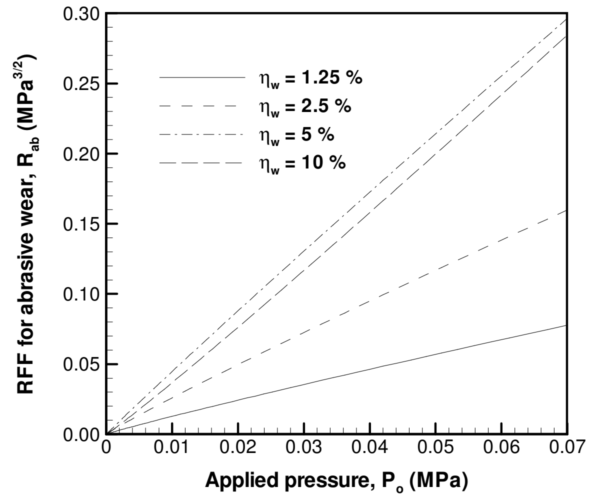

d) E_s = 100 MPa and E_s / E_p = 4

Fig. 7.31: The RFF due to abrasive wear R_{ab} as a function of applied pressure P_o for different particle concentration η_w.

elastic modulus ratio, e.g. E_s / E_p = 4 whereas the power law exponent n is not influenced by η_w for E_s / E_p = 1. In the case of a pad with high porous elastic modulus ratio E_s / E_p = 4, RFF increases sub-linearly at low particle concentration, e.g. η_w = 1.25% (n_{ad} ~ 0.88 for E_s = 10 MPa and n_{ad} ~ 0.93 for E_s = 100 MPa), but an increase in n is observed with increasing particle concentration, e.g. η_w = 10% (n_{ad} ~ 1.01). Both RFF due to

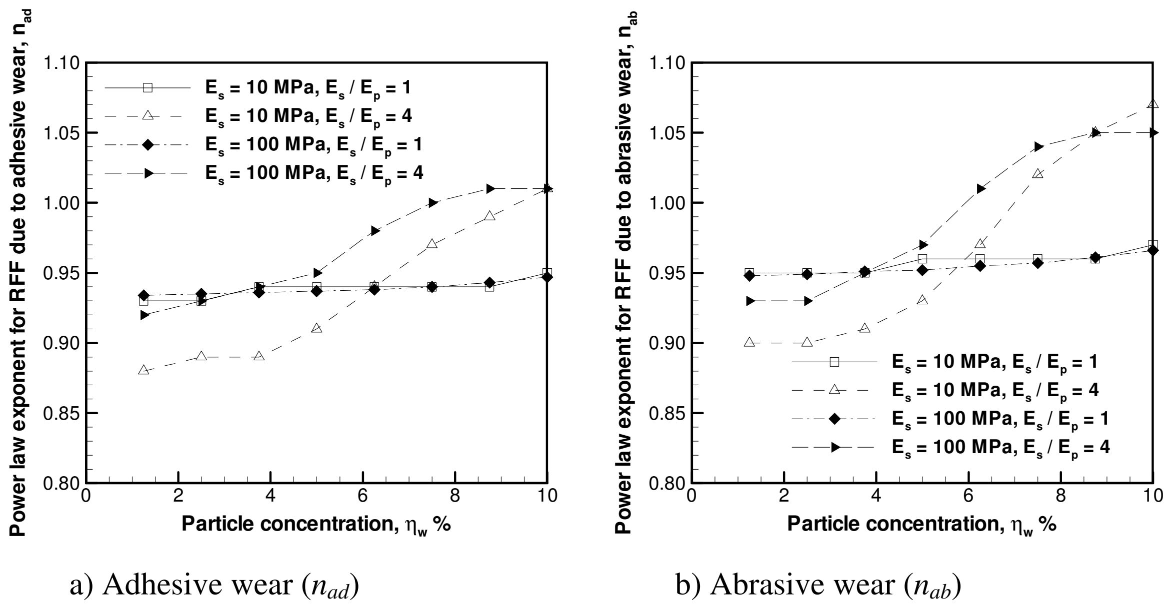

a) Adhesive wear (n_{ad})   b) Abrasive wear (n_{ab})

Fig. 7.32: Power law exponents n_{ad} and n_{ab} ($R = cP_o^n$) for the variation of RFF with applied pressure P_o at different particle concentrations η_w.

adhesive R_{ad} and abrasive R_{ab} wear exhibit this similar trend, while power law exponents are slightly higher for R_{ab}, $n_{ab} > n_{ad}$.

Discussion

As explained in Section 4.6, particles trapped between pad and wafer do not influence the single asperity contact behavior therefore particle concentration η_w does not have an effect on the characteristics of rough contact, such as real contact area ratio A_r or mean contact pressure P_m. Real contact area ratio A_r and mean contact pressure P_m plotted, respectively in Figs. 7.12a and 7.14 using particle concentration η_w = 2.5 % is also valid for other η_w's. Although number of active particles n_a increases linearly with particle concentration η_w, the shape of the curve illustrating the variation of n_a with applied pressure P_o in Fig. 7.12b remains the same. Therefore effect of particle concentration η_w cannot be explained by the number of active particles n_a. However particle concentration

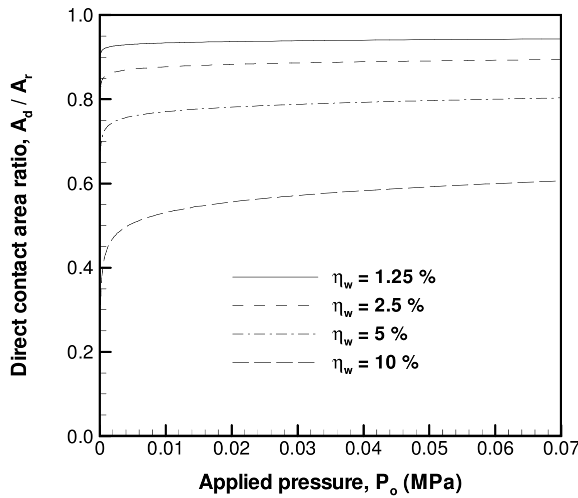

a) E_s = 10 MPa and E_s / E_p = 1

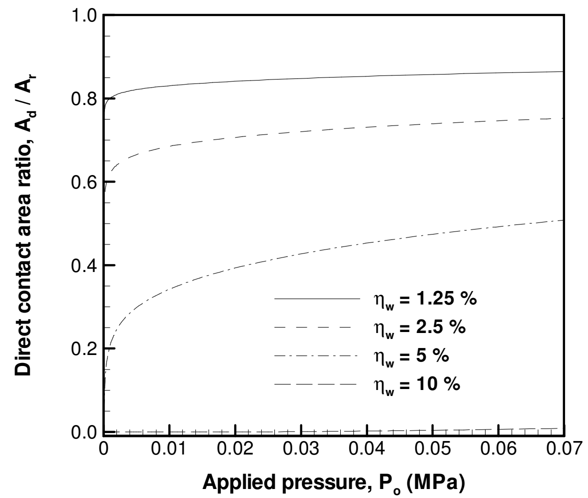

b) E_s = 10 MPa and E_s / E_p = 4

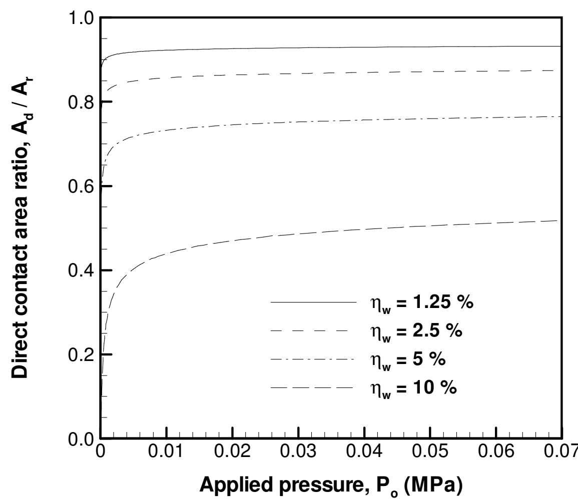

c) E_s = 100 MPa and E_s / E_p = 1

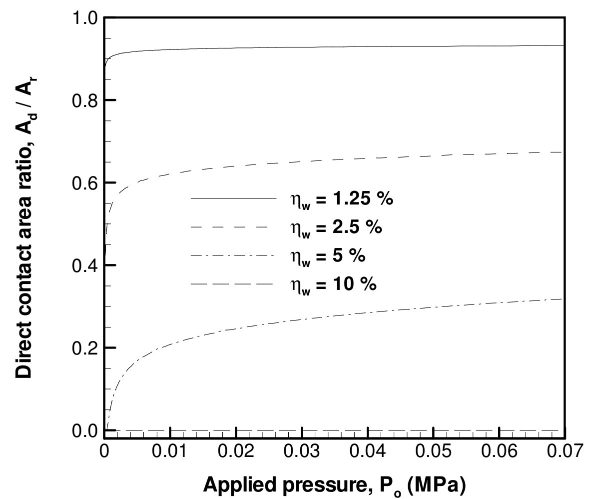

d) E_s = 100 MPa and E_s / E_p = 4

Fig. 7.33: The variation of direct contact area ratio A_d / A_r with applied pressure P_o for different particle concentration η_w.

η_w plays a significant role at the local contact level by affecting the direct contact area ratio A_d as discussed next.

Fig. 7.33 shows that the contact regime is significantly influenced by the porous elastic modulus ratio, plotted for E_s / E_p = 1 in Figs. 7.33a and 7.33c and for E_s / E_p = 4 in Figs.

7.33b and 7.33d. Direct contact dominates the contact for the whole range of applied pressure P_o for the case of E_s / E_p = 1 (solid pad), while for the case of E_s / E_p = 4, direct contact area ratio A_d approaches zero, faster with increasing particle concentration η_w. Note that A_d = 0 indicates particle contact regime. This is also demonstrated in Fig. 7.34 showing the particle contact pressure ratio to be P_p / P_o = 1 at high particle concentration,

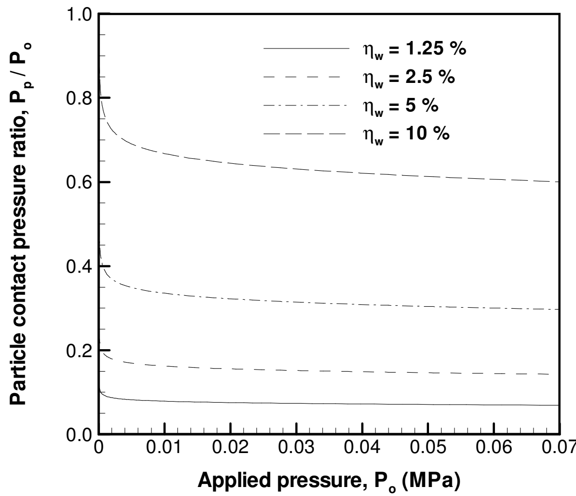

a) E_s = 10 MPa and E_s / E_p = 1

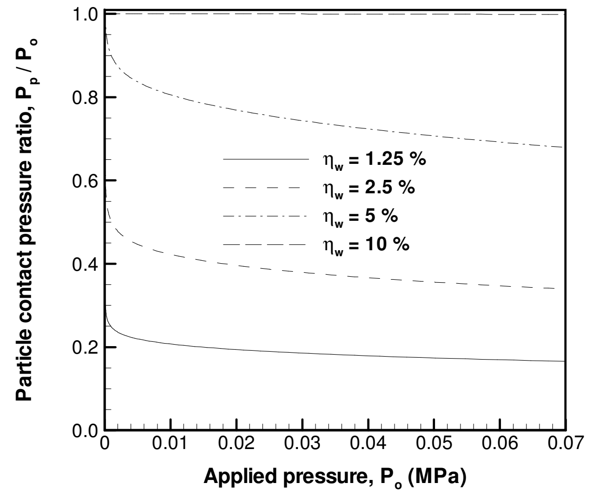

b) E_s = 10 MPa and E_s / E_p = 4

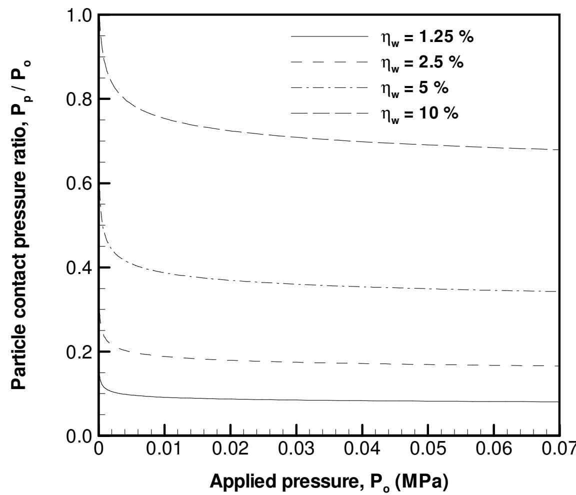

c) E_s = 100 MPa and E_s / E_p = 1

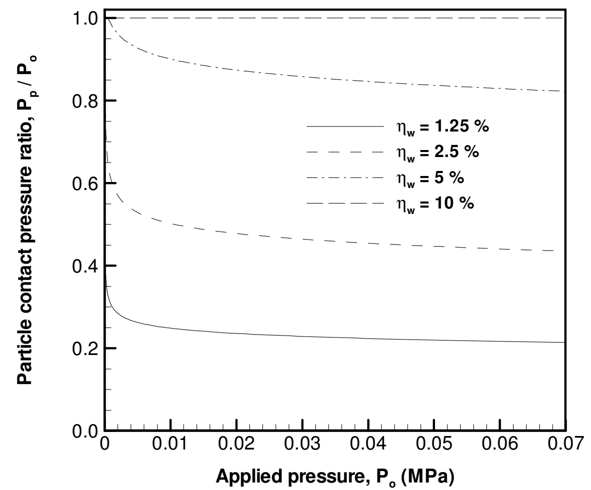

d) E_s = 100 MPa and E_s / E_p = 4

Fig. 7.34: The variation of particle contact pressure ratio P_p / P_o with applied pressure P_o for different particle concentration η_w.

e.g. η_w = 10% for E_s / E_p = 4. As a result, particle contacts start to play an important role at high particle concentration η_w = 10%. In the case of particle contact regime P_p / P_o = 1, all the applied pressure P_o is distributed on the particles, and as a result RFF for adhesive wear R_{ad} becomes linear and number of active particles n_a does not influence RFF. The non-linearity of RFF introduced by number of active particles n_a therefore does not exist at high particle concentration. Thus, RFF becomes almost linear at high particle concentration, η_w for E_s / E_p = 4. Note that similar trends are observed for a soft and a hard pad, since porous elastic modulus ratio E_s / E_p has a greater influence on the local contact regime than pad elastic modulus E_s. Although increasing pad elastic modulus E_s causes the contact regime to shift towards particle contact, the increase in pad elastic modulus from E_s = 10 MPa to E_s = 100 MPa is not sufficient to result in significant change in local contact as compared to the increase in porous elastic modulus ratio from E_s / E_p = 1 to E_s / E_p = 4.

7.4.2 Effect of particle concentration on RFF

Results

In Figs. 7.35 and 7.36, RFF due to adhesive wear R_{ad} is plotted as a function of particle concentration, η_w for low applied pressure, P_o = 0.007 MPa (or P_o = 1 psi) and high applied pressure, P_o = 0.07 MPa (or P_o = 10 psi), respectively. Fig. 7.35a shows that RFF due to adhesive wear R_{ad} increases linearly with particle concentration η_w for a soft (E_s = 10 MPa), non-porous (E_s / E_p = 1) pad. As the porosity of pad increases with higher porous elastic modulus ratio E_s / E_p, the variation of RFF due to adhesive wear R_{ad} with particle concentration η_w becomes sub-linear. In fact, RFF due to adhesive wear R_{ad} levels off when particle concentration, η_w > 8% for porous elastic modulus ratio E_s/E_p = 4

which is called as the saturation particle concentration, η_w^c. This saturation effect is also seen even at a larger extend in Fig. 7.35b illustrating the variation of RFF due to adhesive wear R_{ad} with particle concentration η_w for a hard pad (E_s = 100 MPa). The saturation particle concentration η_w^c of a hard pad is lower than a soft pad (E_s = 10 MPa). RFF due

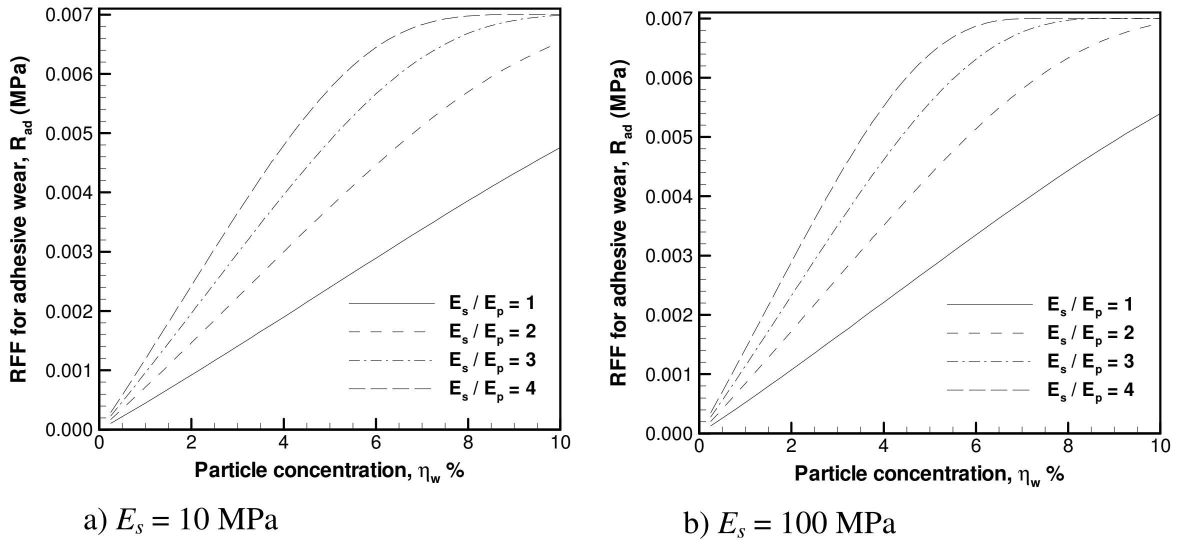

Fig. 7.35: The effect of particle concentration η_w on RFF due to adhesive wear R_{ad} for low applied pressure, P_o = 0.007 MPa (or P_o = 1 psi).

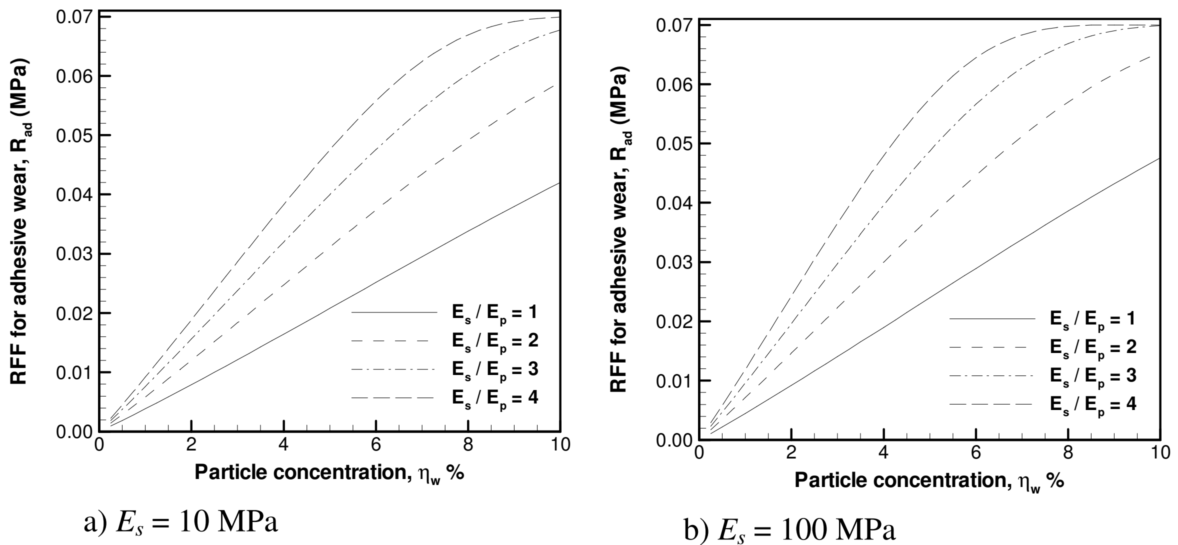

Fig. 7.36: The effect of particle concentration η_w on RFF due to adhesive wear R_{ad} for high applied pressure, P_o = 0.07 MPa (or P_o = 10 psi).

to adhesive wear, R_{ad} exhibits a similar dependence on particle concentration, η_w when applied pressure is increased to P_o = 0.07 MPa (or P_o = 10 psi) as illustrated in Fig. 7.36. Fig. 7.36 shows that the saturation particle concentration η_w^c increases when applied pressure P_o becomes higher.

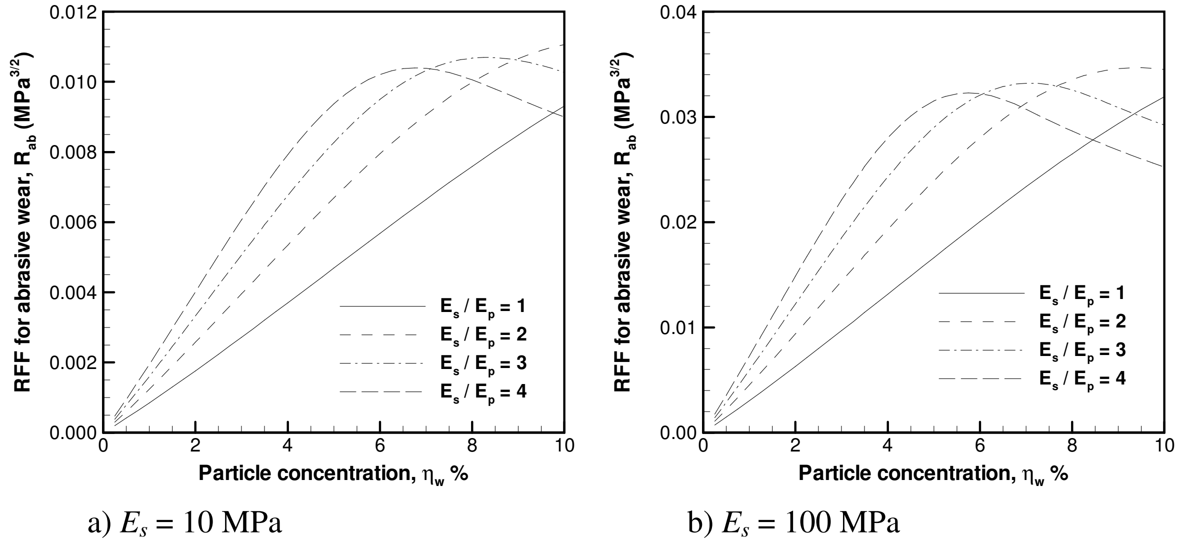

a) E_s = 10 MPa b) E_s = 100 MPa

Fig. 7.37: The effect of particle concentration η_w on RFF due to abrasive wear R_{ab} for low applied pressure, P_o = 0.007 MPa (or P_o = 1 psi).

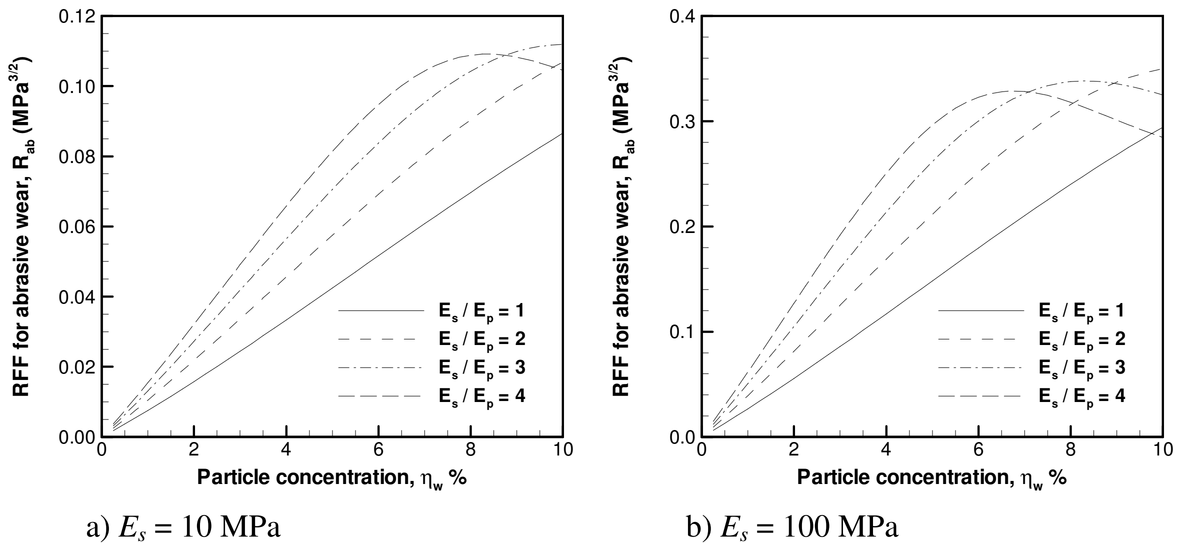

a) E_s = 10 MPa b) E_s = 100 MPa

Fig. 7.38: The effect of particle concentration η_w on RFF due to abrasive wear R_{ab} for high applied pressure, P_o = 0.07 MPa (or P_o = 10 psi).

The effects of computing the RFF by using adhesive wear formulation are presented in Figs. 7.37 and 7.38 for $P_o = 0.007$ MPa and 0.07 MPa, respectively. Similar to the behavior of the adhesive wear function R_{ad}, the abrasive wear function R_{ab} also increases with increasing particle concentration η_w. However, in the case of abrasive wear, we see that R_{ab} reaches a peak at a critical particle concentration $\eta_w = \eta_w^c$ and drops with increasing η_w.

The reasons for the saturation in the case of adhesive, and peaking in the case of abrasive wear on the RFF with particle concentration η_w is explained next.

Discussion

Particle concentration η_w is an important parameter determining the contact regime at the interface between pad asperity and wafer (local contact). At low particle concentration η_w, there are a few active particles at the contact interface, and the mean spacing between particles is large allowing direct contact to occur. As a result of direct contact, a fraction of applied pressure P_o is carried by direct contacts, and the particle contact pressure becomes $P_p / P_o < 1$. An increase in the particle concentration η_w results in an increase in number of active particles n_a. Thus in turn causes the mean spacing between particles to become smaller, reducing the direct contact area A_d. This effect is quantified in the results presented in Fig. 7.39. As particle concentration reaches a critical value, $\eta_w = \eta_w^c$, mean spacing between particles becomes such that direct contact is prevented and all the applied pressure is transferred through the particles. Note that this was termed as the particle contact regime in the multi-particle (MP) contact model (Chapter 4). As a result, at the saturation particle concentration η_w^c, the direct contact becomes zero,

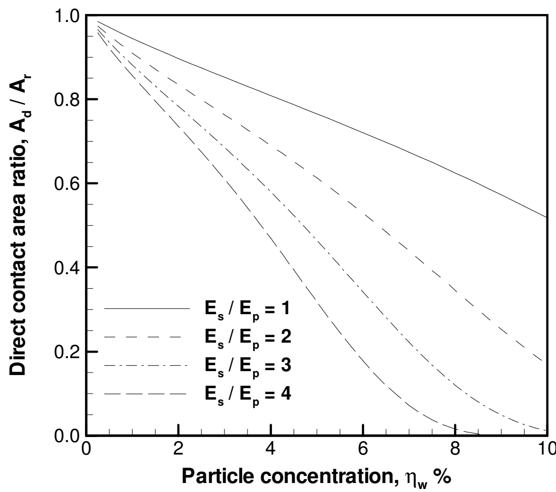

a) E_s = 10 MPa

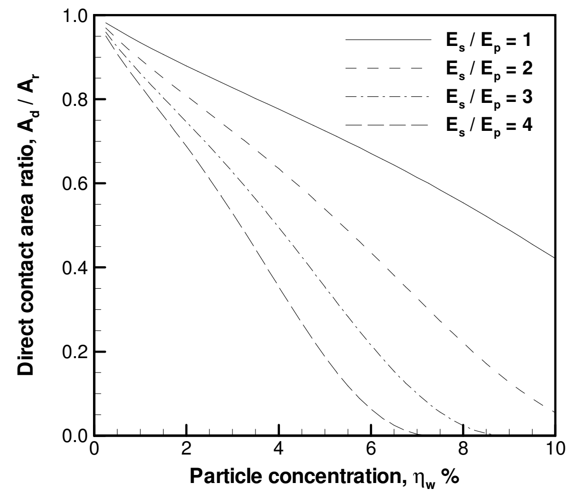

b) E_s = 100 MPa

Fig. 7.39: The effect of particle concentration η_w on direct contact area ratio, A_d / A_r, P_o = 0.007 MPa (or P_o = 1 psi).

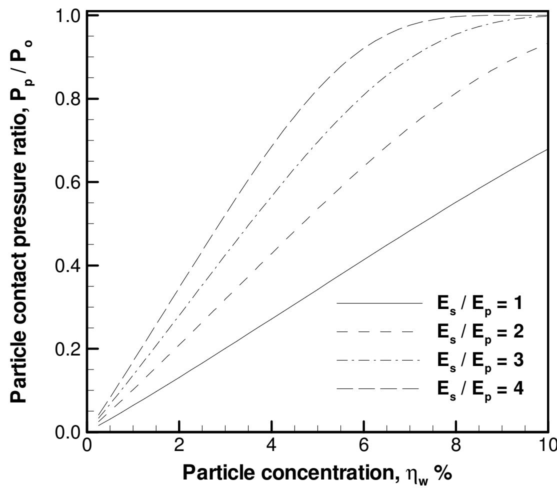

a) E_s = 10 MPa

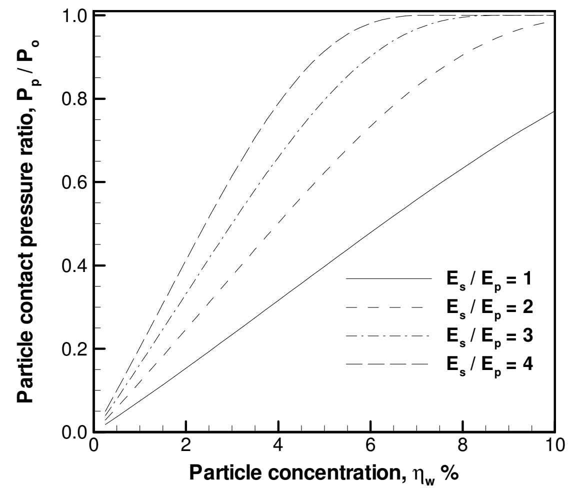

b) E_s = 100 MPa

Fig. 7.40: The effect of particle concentration η_w on particle contact pressure ratio, P_p / P_o, P_o = 0.007 MPa (or P_o = 1 psi).

A_d = 0 and the particle contact pressure becomes P_p / P_o = 1 as shown in Fig. 7.40. Increasing particle concentration above this saturation value, $\eta_w > \eta_w^c$ does not change the fraction of applied pressure P_o carried by particle contacts. Thus we see that the saturation particle concentration η_w^c is a critical factor in material removal. The

magnitude of η_w^c increases using softer (small E_s) or lower porosity (small E_s / E_p) pads or by applying higher pressure P_o.

The behavior of adhesive (R_{ad}) and abrasive (R_{ab}) RFFs, when the particle concentration is greater than saturation particle concentration, $\eta_w > \eta_w^c$ can be explained by considering the mean contact force f_w^m on each particle. In Section 3.5, it is shown that the RFF due to a single particle is proportional to contact force f_w^m ($R_{ad}^{sp} \propto f_w^m$) for the case of adhesive wear, whereas the RFF due to abrasive wear is proportional to $f_w^{m^{3/2}}$ $R_{ab}^{sp} \propto f_w^{m^{3/2}}$. The mean particle contact force f_w^m is determined by the particle contact pressure P_p and number of active particles n_a as, $f_w^m = P_p / n_a$. Number of active particles n_a increases linearly with particle concentration η_w, whereas the behavior of particle contact pressure P_p depends on the occurrence of direct contact. If the rate of increase of number of active particles n_a with η_w is identical to that of the particle contact pressure P_p, then the mean particle contact force f_w^m remains constant, which is seen to be approximately the case at low particle concentration η_w in Fig. 7.41. As the particle concentration η_w approaches its saturation value, the particle contact pressure P_p (Fig. 7.40) increases at a lower rate, causing the mean particle contact force f_w^m to decrease. However, the most significant decrease in mean particle contact force f_w^m takes place above saturation particle concentration, $\eta_w > \eta_w^c$, where the number of active particles, n_a continues to become larger with higher particle concentration η_w, while the particle contact pressure, P_p remains constant. If the variation of RFF due to adhesive R_{ad} and abrasive R_{ab} wear achieved by all active particles is considered, $R_{ad} \propto n_a f_w^m$ and

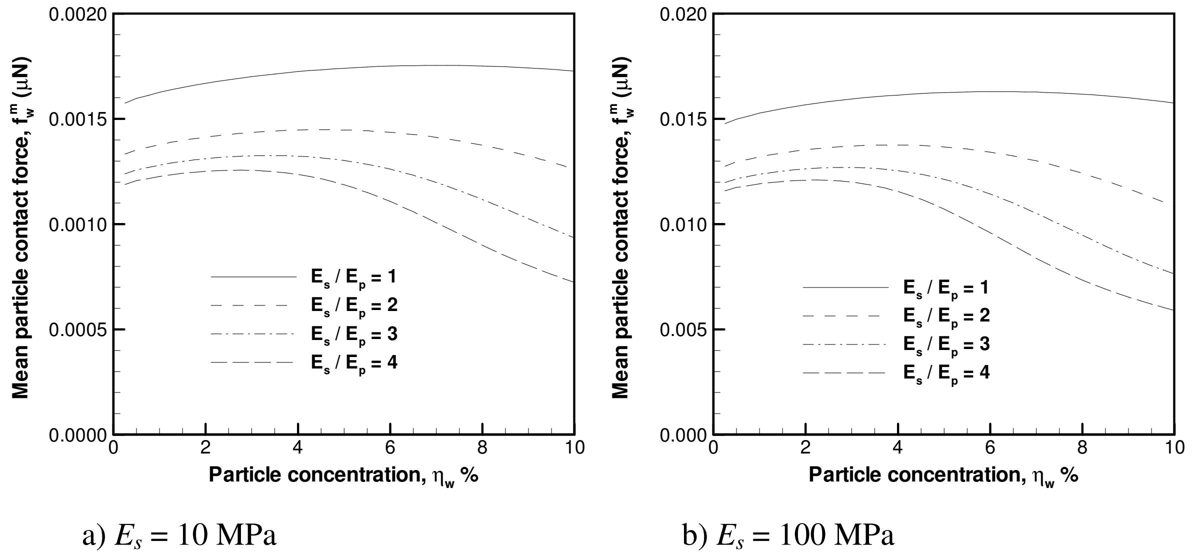

a) E_s = 10 MPa b) E_s = 100 MPa

Fig. 7.41: The effect of particle concentration η_w on mean particle contact force f_w^m, P_o = 0.007 MPa (or P_o = 1 psi).

$R_{ab} \propto n_a f_w^{m^{3/2}}$, it can be seen that the increase in number of active particles n_a offsets the decrease in mean contact force f_w^m and R_{ad} remains constant in this regime. Whereas a reduction in the mean particle contact force f_w^m causes R_{ab} to decrease as R_{ab} is proportional to $f_w^{m^{3/2}}$ as ($R_{ab} \propto n_a f_w^{m^{3/2}}$).

7.4.3 Comparison with experiments

The saturation of the MRR with increasing particle concentration was also observed experimentally. Bielmann et al. [21] conducted W CMP experiments using alumina particles with different particle sizes (145 nm ≤ μ_p ≤ 1000 nm) and concentrations (2% ≤ η_w ≤ 15%). Experiments were performed with a hard pad (IC1000) under an applied pressure of P_o = 0.045 MPa (or P_o = 6 psi). In Fig. 7.42, we plot the MRR determined in these experiments. Note that the MRR was normalized with respect to the largest MRR measured and plotted as a function of particle concentration η_w for different particle radii

μ_p. The experimental conditions were simulated by our model using applied pressure, P_o = 0.045 MPa, pad elastic modulus, E_s = 100 MPa and porous elastic modulus ratio, E_s / E_p = 4. The base parameters listed in Table 7.1 were used in the simulations. Fig. 7.42 shows that the model using adhesive wear assumption predicted the experimentally observed saturation effect accurately for small particles ($\mu_p \leq 300$ nm). The experimentally observed saturation effect takes place, for small particles, at somewhere in the range, $5\% < \eta_w^c < 10\%$ (Fig. 7.42), while the model predicts the critical particle concentration to be $\eta_w^c \approx 6.5$ %. The decrease in MRR above saturation particle concentration η_w^c predicted by abrasive wear model was not seen in experiments. The saturation effect was not observed for large particles in the experiments ($\mu_p > 300$ nm). Note that the model prediction for critical particle concentration η_w^c does not depend on particle size.

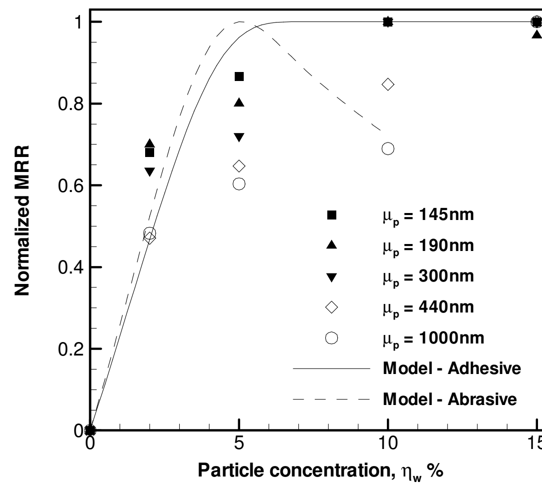

Fig. 7.42: The comparison of the variation of normalized MRR with particle concentration η_w determined in experiments by Bielmann et al. [21] and models.

The discrepancy between the experiment and model results for large particles can be explained by considering the assumptions used to calculate the number of active particles. In the model, particles become active in contact when the local separation distance between pad and wafer becomes smaller than particle diameter, $d_{wp} < 2\mu_p$. Moreover the particles are assumed to be uniformly distributed within the slurry volume in the clearance between pad and wafer. The clearance between pad and wafer is a function of hydrodynamic lubrication pressure, pad deformation as well as pad roughness. In the case of a small clearance, large particles cannot flow into the pad-wafer gap between pad and wafer and the assumption of uniformly distributed particles becomes no longer valid. On the other hand, particles with diameter significantly smaller than clearance should not be affected. Effectively, the situation may be described as one where the PDF of the particle size and particle concentration in the pad-wafer interface changes according to available pad-wafer clearance. The proposed model is not accurate in contact conditions dominated by large particle sizes.

Forsberg performed CMP experiments on a silicon (Si(100)) wafer, using silica slurry and a soft pad (Suba500) [22]. Applied pressure was adjusted to be $P_o = 0.009$ MPa ($P_o = 1.3$ psi) while particle concentration was varied in the range, $0\% < \eta_w < 6.5\%$. The results of this experimental work are compared to the predictions of our model, where simulations were carried out by using pad elastic modulus, $E_s = 10$ MPa (for a soft pad), porous elastic modulus ratio, $E_s / E_p = 4$ and applied pressure, $P_o = 0.009$ MPa. Other parameters of the model are listed in Table 7.1. Fig. 7.43 shows the comparison of normalized MRR found in the experiments and predicted by the simulations using adhesive and abrasive wear assumptions. The original data from the experiments is also

shown in Fig. 7.43. It is seen that material removal is achieved in the experiments even when the particle concentration is reduced to 0, MRR ~ 50 nm/min for η_w = 0%. This is attributed to the etching of wafer material by slurry chemicals. In order to quantify the effect of particle concentration considering mechanical removal, MRR due to etching at η_w = 0% was subtracted from the experimental MRR and then MRR was normalized with respect to maximum MRR. Comparing the normalized MRR determined in the experiments and model results, good agreement was found for both adhesive and abrasive wear assumptions, except that the slight decrease in MRR for abrasive wear above saturation particle concentration η_w^c was not seen in experiments. Note that the saturation particle concentration predicted by our model is η_w^c ≈ 6.5 % for adhesive wear, which is very similar to η_w^c predicted by the models for a hard pad E_s = 100 MPa and higher applied pressure, P_o = 0.045 MPa given for comparison with experiments by Bielmann et al. [21] (Fig. 7.42). The effect of a softer pad is to increase saturation concentration η_w^c,

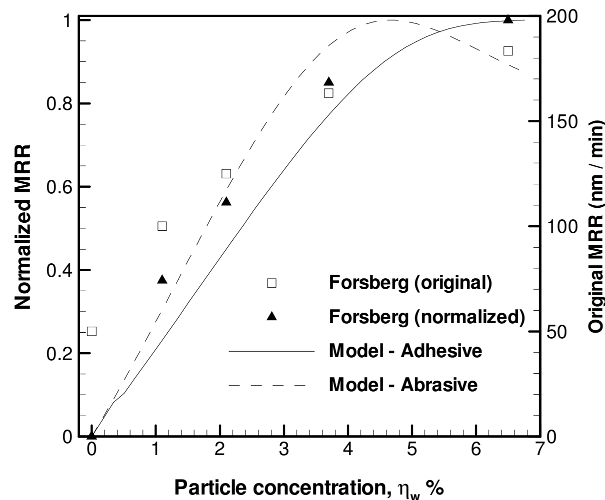

Fig. 7.43: The comparison of the variation of normalized MRR with particle concentration η_w determined in experiments by Forsberg [22] and models.

while smaller particle material density ρ_p causes a decrease in η_w^c. The material density of silica particles (ρ_{si} = 2.5 g/cc) is smaller as compared to alumina particles (ρ_{al} = 3.7 g/cc), which gives more particle volume for a given particle weight concentration η_w of silica particles. These two opposing effects offset each other, and the model predicts similar saturation particle concentration η_w^c values as observed in these separate experiments.

The variation of MRR as a function of particle concentration η_w was also studied experimentally for CMP of copper films with alumina slurry by Guo and Subramanian [10]. In these experiments, CMP was performed with a hard pad (IC1000) and applied pressure was fixed at P_o = 0.048 MPa (P_o = 6.8 psi) while three different relative velocities, V_r were used. The results of these experiments were compared to our model, where simulations were carried out for pad elastic modulus E_s = 100 MPa (hard pad), porous elastic modulus ratio E_s / E_p = 4 and applied pressure, P_o = 0.048 MPa. The results are depicted in Fig. 7.44. In Fig. 7.44a, where the pad asperity radius is taken as R_s = 50 µm, the model over-predicts the saturation particle concentration. The deviation between experiment and model results decreased for an asperity radius of R_s = 100 µm used in the model (σ_s = 5 µm), in Fig. 7.44b. We thus note that larger asperity radius R_s shifts the model results for saturation particle concentration η_w^c to a lower level. A similar effect can be obtained by decreasing pad roughness σ_s, which also causes mean contact pressure P_m to decrease, as smaller number of particles n_a will be sufficient to prevent direct contact at lower local contact pressure. A good agreement was found between experiment and model results when pad roughness of σ_s = 3 µm is used in the model as shown in Fig. 7.44c. Considering the effect of pad conditioning parameters on pad topography, it is possible that asperity radius R_s and pad roughness σ_s was different in experiments by Guo

and Subramanian [10] than the default values used in the model (Table 7.1). The values in literature reflect this variation for different conditioning methods as asperity radius in the range, 30 µm ≤ R_s ≤ 100 µm and pad roughness, 3 µm ≤ σ_s ≤ 29 µm were reported as listed in Table 2.2. Therefore the model results are assumed to be accurate although some

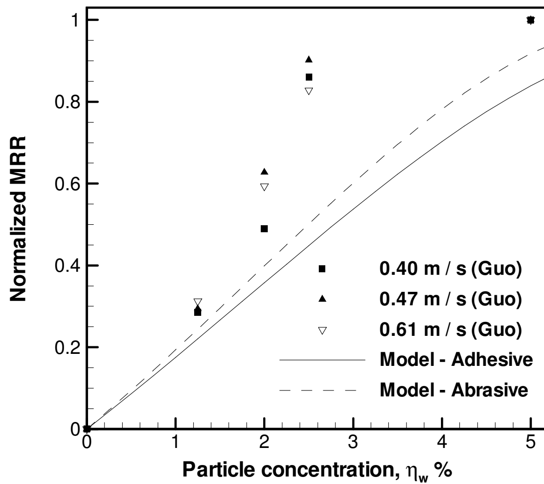

a) R_s = 50 µm and σ_s = 5 µm

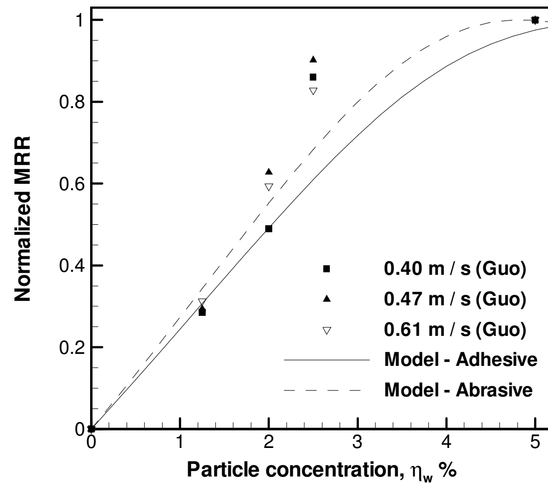

b) R_s = 100 µm and σ_s = 5 µm

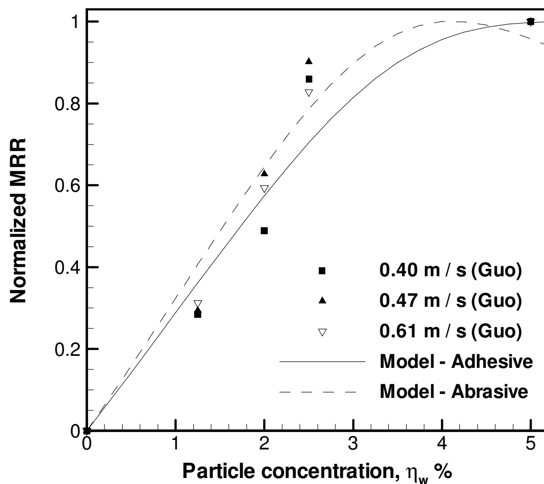

c) R_s = 100 µm and σ_s = 3 µm

Fig. 7.44: The comparison of the variation of normalized MRR with particle concentration η_w determined in experiments by Guo and Subramanian [10] and models with asperity radius and pad roughness a) R_s = 50 µm and σ_s = 5 µm, b) R_s = 100 µm and σ_s = 5 µm and c) R_s = 100 µm and σ_s = 3 µm.

adjustment for asperity radius R_s and pad roughness σ_s within the ranges given in literature is required to match experimental results more closely.

Based on the comparison of the variation of MRR with particle concentration, a good agreement between experiment and model results is found. The model results obtained using abrasive wear assumption indicate a decreasing trend for MRR once the saturation particle concentration is exceeded. This trend was not observed in the experiments reported here. An experimental study conducted by Choi et al. [23] involving CMP of oxide films with silica slurry revealed that a decrease of MRR with increasing particle concentration following a saturation particle concentration value. This effect was only observed for large particles. The authors explained this effect by considering the particle dynamics since in-situ friction force measurements indicated a decrease in friction force with higher particle concentration. Rolling of particles was initiated above saturation particle concentration, due to the fact that particles were not embedded in the pad completely, which promoted rolling of particles. This effect can not be captured by our model since sliding is the only particle motion considered in this work.

The majority of experiment results showing a saturation effect at high particle concentration in the range predicted by the model were obtained for CMP using alumina particles. A different behavior is generally observed for silica particles, where saturation of MRR occurs at very high particle concentration [8]. This trend seen for silica particles was attributed to the effect of surface forces that may play an important role in determining the number of active particles. In this work, the effect of surface forces on number of active particles was neglected. The fact that silica particles have a much lower Hamaker constant [24] causing the attractive van der Waals forces to become smaller as

compared to repulsive double layer forces may be the reason for saturation effect occurring at high particle concentration. In this case, the particle concentration near the wafer surface may become lower than slurry particle concentration as particles are forced away from the wafer surface due to weak van der Waals forces.

7.5 Effect of Pad Topography

Although applied pressure P_o is one of the important process parameters in CMP, the real contact pressure acting at the interface between pad asperity and wafer determines the characteristics of material removal. Surface topography of a rough pad influences the contact and the distribution of applied pressure through the asperities on the wafer, and the mean real contact pressure P_m on each asperity and the real contact area A_r are strong functions of pad topography. Mean contact pressure P_m and real contact area A_r are related as $P_m = P_o / A_r$ where P_m decreases as contact spreads over a larger area, i.e. A_r becomes larger. Real contact area A_r is the main controlling parameter for the number of active particles n_a, whereas the direct contact area ratio A_d is a strong function of mean contact pressure P_m. Pad roughness σ_s, asperity radius R_s and asperity density η_s are the parameters related to pad topography used as the inputs for the models, in the case of random pad roughness, where Gaussian distribution for PDF of asperity summit heights is employed. In addition, the effect of skewness S_s of the PDF of the asperity summit heights is taken into account by using the Weibull distribution. In this section, the effects of these parameters related to pad topography are studied for their effect on the RFF for adhesive wear. Note that the results obtained for adhesive wear is also valid for abrasive wear.

7.5.1 Variation of RFF with applied pressure

<u>Results</u>

The RFF due to adhesive wear R_{ad} is plotted as a function of the applied pressure P_o for different parameters related to pad surface topography (pad roughness σ_s, asperity radius R_s, asperity density η_s and skewness S_s) in Figs. 7.45-7.48. Close inspection of these figures shows that in the range studied, the SD of pad roughness σ_s and the asperity radius R_s have a stronger influence on RFF as compared to the asperity density η_s and the skewness S_s. The influence of these parameters on RFF is investigated in detail in Sections 7.5.2 – 7.5.5.

The variations of the RFF presented in Figs. 7.45-7.48 have been curve fit in power law form $R = cP_o^n$. The power law exponents are summarized in Fig. 7.49. This figure shows that all the parameters related to pad surface topography have a significant effect on the

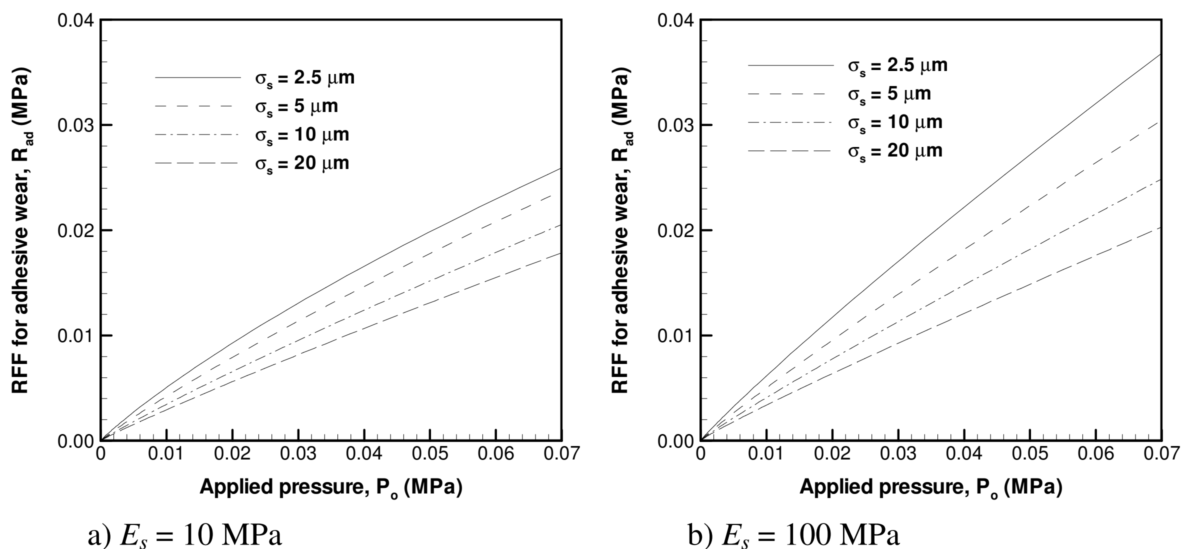

a) E_s = 10 MPa b) E_s = 100 MPa

Fig. 7.45: The RFF due to adhesive wear R_{ad} as a function of applied pressure P_o for different pad roughness σ_s (E_s / E_p = 4).

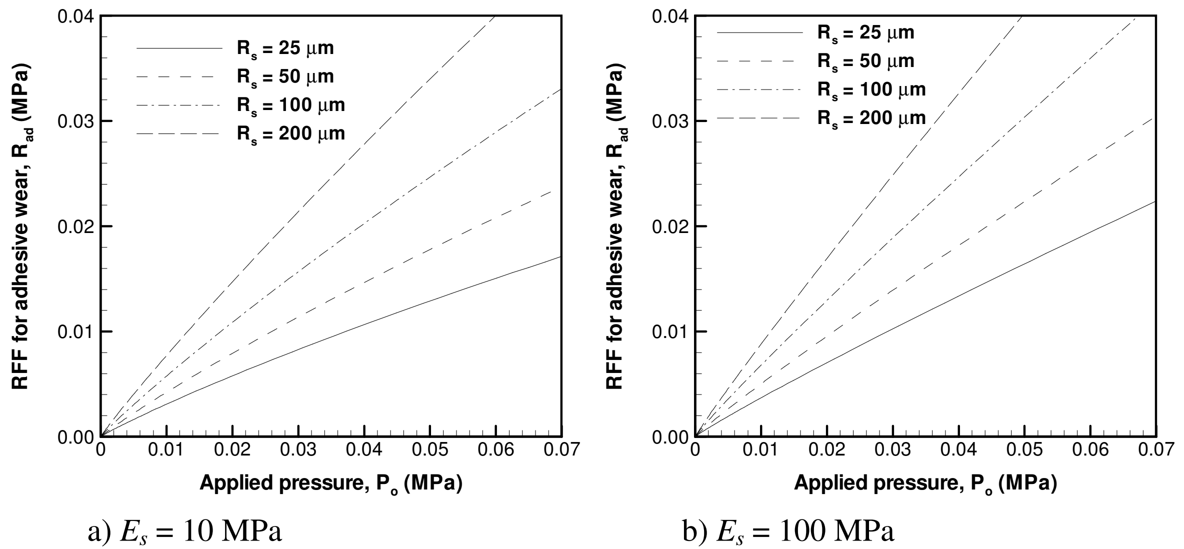

a) E_s = 10 MPa b) E_s = 100 MPa

Fig. 7.46: The RFF due to adhesive wear R_{ad} as a function of applied pressure P_o for different asperity radius R_s (E_s / E_p = 4).

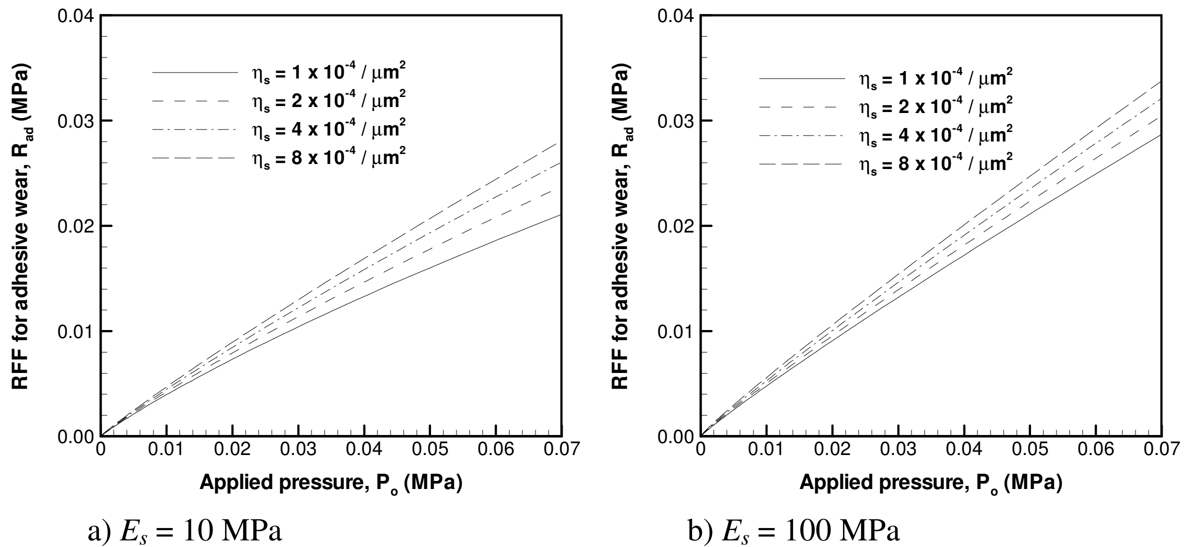

a) E_s = 10 MPa b) E_s = 100 MPa

Fig. 7.47: The RFF due to adhesive wear R_{ad} as a function of applied pressure P_o for different asperity density η_s (E_s / E_p = 4).

non-linearity of RFF especially for a soft pad, E_s = 10 MPa with high porous elastic modulus ratio, E_s / E_p = 4. Real contact area A_r determines the number of active particles n_a, thus, the parameters related to pad surface topography influence non-linear variation of RFF with applied pressure P_o. As pad surface parameters are varied in the ranges

studied here, no significant change in power law exponent (n_{ad}) of the RFF is observed for the hard (E_s = 100 MPa) or low porosity (E_s / E_p = 1) pads.

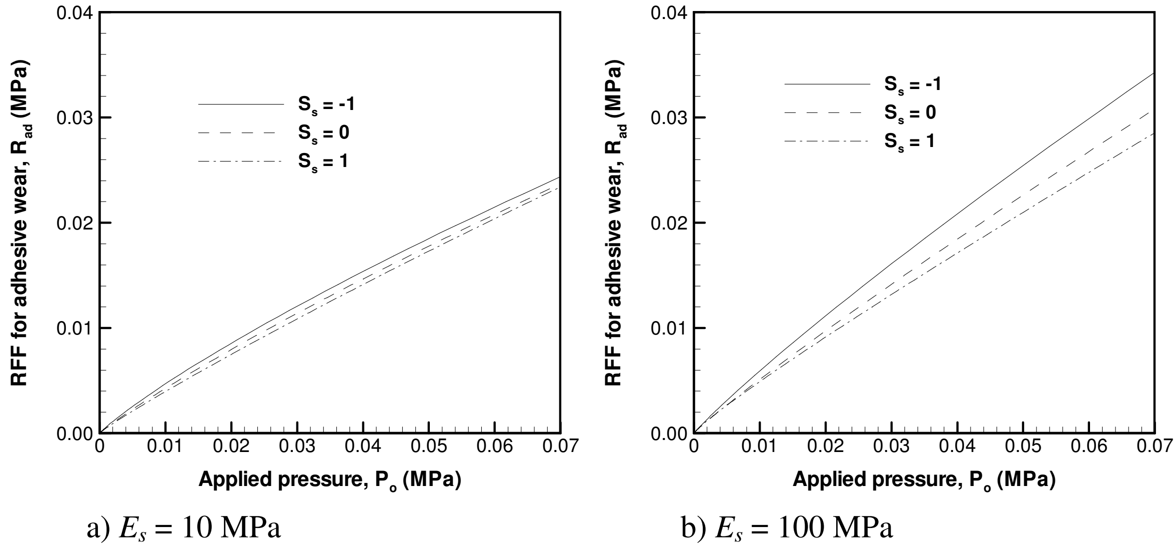

a) E_s = 10 MPa b) E_s = 100 MPa

Fig. 7.48: The RFF due to adhesive wear R_{ad} as a function of applied pressure P_o for different skewness S_s (E_s / E_p = 4).

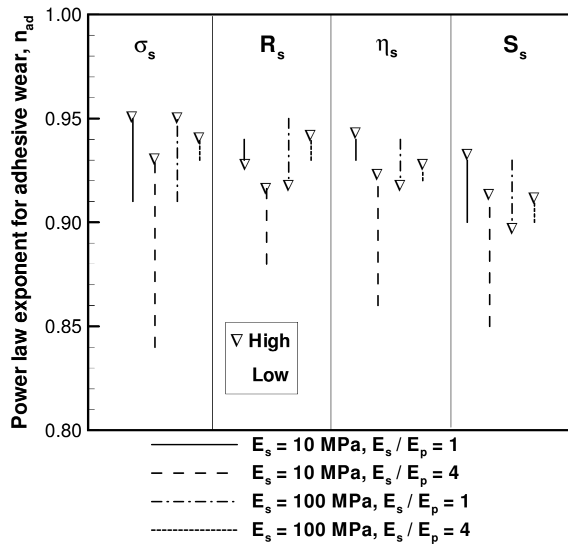

Fig. 7.49: Power law exponents for adhesive n_{ad} and abrasive n_{ab} ($R = cP_o^n$) wear for the variation of RFF with applied pressure P_o for pad roughness 2.5μm < σ_s < 20μm, asperity radius 25μm < R_s < 200μm, asperity density 1x10^{-4}/μm^2 < η_s < 8x10^{-4}/μm^2 and skewness -1 < S_s < 1.

Discussion

Fig. 7.50 illustrates the effect of pad surface parameters on equilibrium separation distance d_{wp} for a soft, porous pad (E_s = 10 MPa, E_s / E_p = 4). It is seen that equilibrium separation distance is $d_{wp} \sim 3\sigma_s$ at low applied pressure P_o. The separation decreases to negative values for the low end of the pad surface roughness parameters presented in Fig. 7.50b. This leads to the sub-linear behavior observed for the RFF. On the other hand, equilibrium separation distance remains positive, $d_{wp} > 0$ in the range of applied pressure P_o, for the high values of the pad surface roughness parameters shown in Fig. 7.50a. The pad roughness σ_s has a significant effect on RFF. The effect of pad roughness σ_s on RFF is investigated as a function of P_o, for a hard, non-porous pad (E_s = 100 MPa, E_s / E_p = 1) in Fig. 7.51a and for a soft, porous pad (E_s = 10 MPa, E_s / E_p = 4) in Fig. 7.51b. Although the equilibrium separation distance d_{wp} is a function of pad roughness σ_s, d_{wp} is such that the pad asperities in contact with wafer remain within the upper part of Gaussian

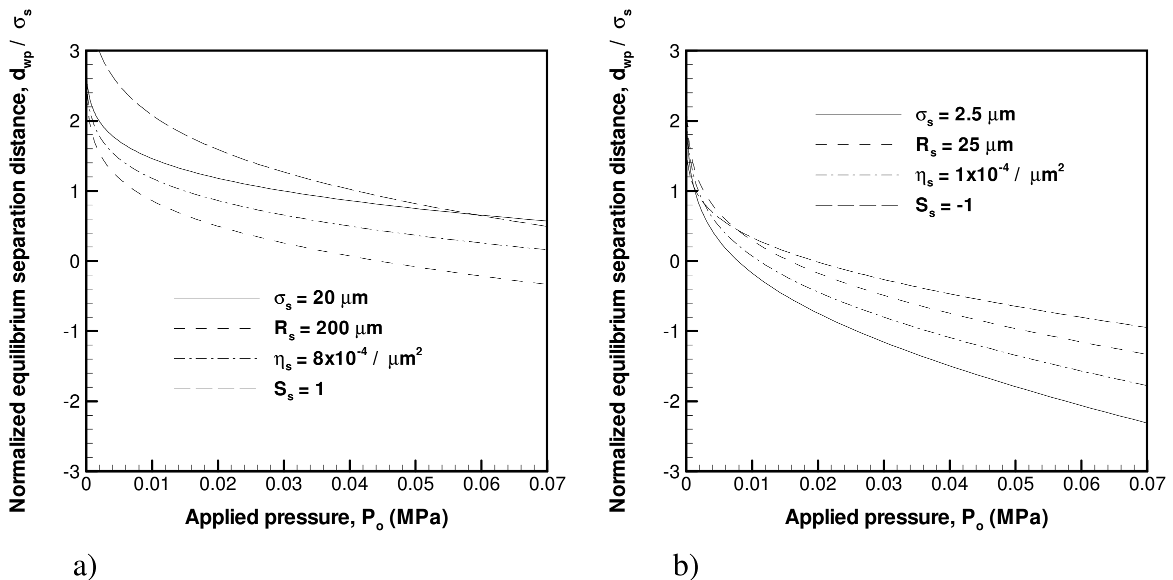

Fig. 7.50: Equilibrium separation distance d_{wp} using a) high values and b) low values of pad surface parameters for a soft E_s = 10 MPa, porous pad E_s / E_p = 4.

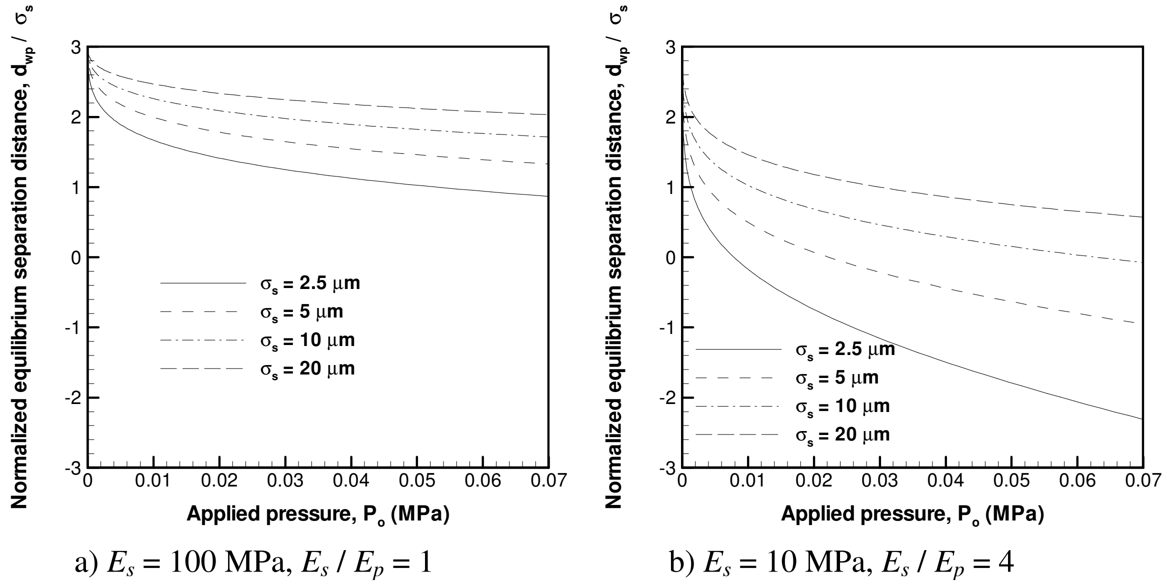

Fig. 7.51: Equilibrium separation distance d_{wp} for different pad roughness a) hard, non-porous pad, E_s = 100 MPa, E_s / E_p = 1 and b) soft, porous pad, E_s = 10 MPa, E_s / E_p = 4.

distribution. This gives nearly linear variation of the real contact area A_r with respect to applied pressure P_o for a hard, non-porous pad (E_s = 100 MPa, E_s / E_p = 1). On the other hand, for a soft, porous pad (E_s = 10 MPa, E_s / E_p = 4), the equilibrium separation distance becomes negative ($d_{wp} < 0$) as σ_s decreases, thus leading to sub-linear variation for the real contact area A_r.

7.5.2 Effect of pad roughness on RFF

Results

General trends seen for the variation of RFF with pad roughness, σ_s is similar for a soft (E_s = 10 MPa) or a hard (E_s = 100 MPa) pad and low (P_o = 0.007 MPa) or high (P_o = 0.07 MPa) applied pressure. Therefore, RFF due to adhesive wear R_{ad} and abrasive wear R_{ab} are shown for only one set of parameters (E_s = 10 MPa and P_o = 0.007 MPa) in Figs. 7.52a and 7.52b, respectively. These figures show that the RFF increases with smaller pad roughness σ_s for both adhesive and abrasive wear. This effect becomes more

significant with increasing pad porosity (E_s / E_p = 4). This behavior can be explained as follows.

Discussion

As pad becomes smoother (with smaller pad roughness σ_s), real contact area A_r due to pad-wafer rough contact increases (Fig. 7.53a) causing mean contact pressure P_m to decrease (Fig. 7.53b). A lower mean contact pressure P_m decreases the tendency for particles to become embedded in the pad, thus diminishing the direct contact area ratio A_d/A_r with smaller pad roughness σ_s as demonstrated in Fig. 7.54a. This improves the ability of the pad to transfer applied pressure on particles as indicated by greater particle contact pressure ratio P_p / P_o (Fig. 7.54b). These effects overall cause RFF to increase with smaller pad roughness σ_s. Fig. 7.54a also shows that the direct contact area ratio A_d/A_r does not vary significantly when porous elastic modulus ratio is small, e.g. E_s / E_p = 1, as direct contact remains dominant for different values of pad roughness σ_s. For large

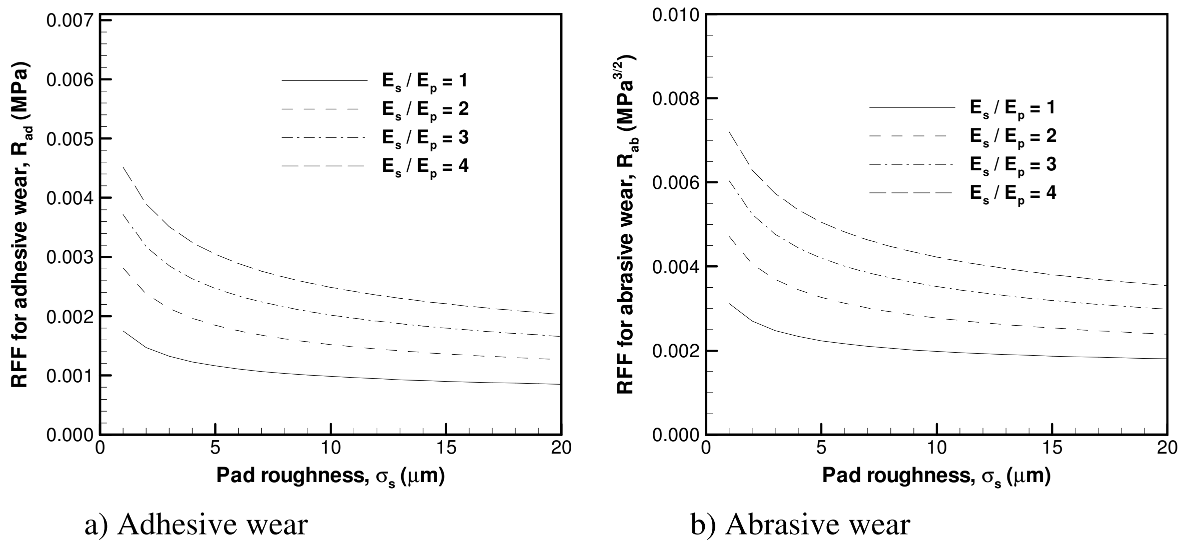

a) Adhesive wear   b) Abrasive wear

Fig. 7.52: The effect of pad roughness σ_s on RFF due to a) adhesive wear R_{ad} and b) abrasive wear R_{ab} for a soft pad E_s = 10 MPa with different porous elastic modulus ratio E_s / E_p.

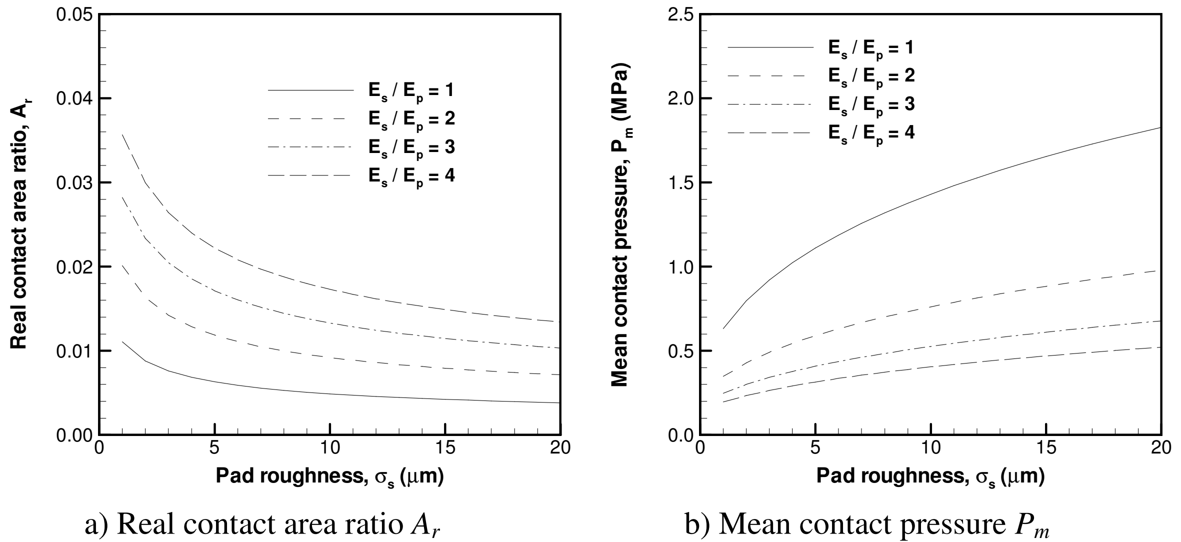

a) Real contact area ratio A_r b) Mean contact pressure P_m

Fig. 7.53: The effect of pad roughness σ_s on a) real contact area ratio A_r and b) mean contact pressure P_m for a soft pad E_s = 10 MPa with different porous elastic modulus ratio E_s / E_p.

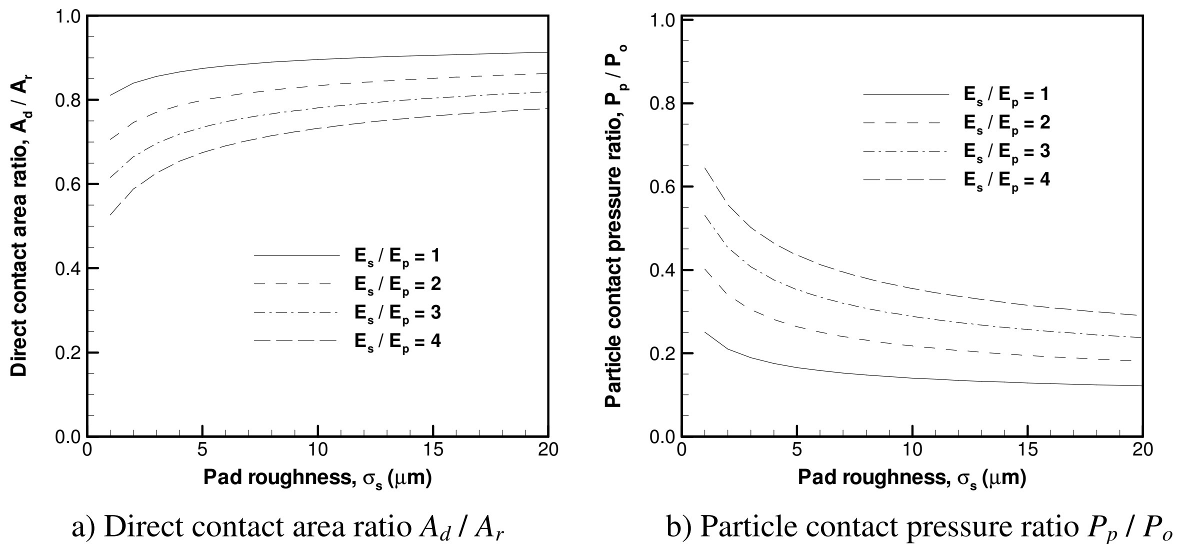

a) Direct contact area ratio A_d / A_r b) Particle contact pressure ratio P_p / P_o

Fig. 7.54: The effect of pad roughness σ_s on a) direct contact area ratio A_d / A_r and b) particle contact pressure ratio P_p / P_o for a soft pad E_s = 10 MPa with different porous elastic modulus ratio E_s / E_p.

porous elastic modulus ratio, e.g. E_s / E_p = 4, mean contact pressure P_m varies with pad roughness σ_s in a transition from particle to direct contact dominant regime where a small change in contact pressure translates to a significant variation in direct contact area A_d/A_r

and particle contact pressure ratio P_p / P_o magnifying the effect of pad roughness σ_s for large E_s / E_p.

7.5.3 Effect of asperity radius on RFF

Results

The effect of larger asperity radius R_s on RFF, as illustrated in Fig. 7.55a for adhesive wear R_{ad}, and in Fig. 7.55b for abrasive wear R_{ab}, is to enhance RFF. The elastic modulus of a soft pad E_s = 10 MPa subjected to a low applied pressure P_o = 0.007 MPa is used for calculating the results shown in Fig. 7.55, although a similar behavior is observed for a hard pad E_s = 100 MPa and high applied pressure P_o = 0.07 MPa.

Discussion

The effect asperity radius R_s can be explained in a similar manner as the effect of pad roughness σ_s considering the fact that both of these parameters influence real contact area

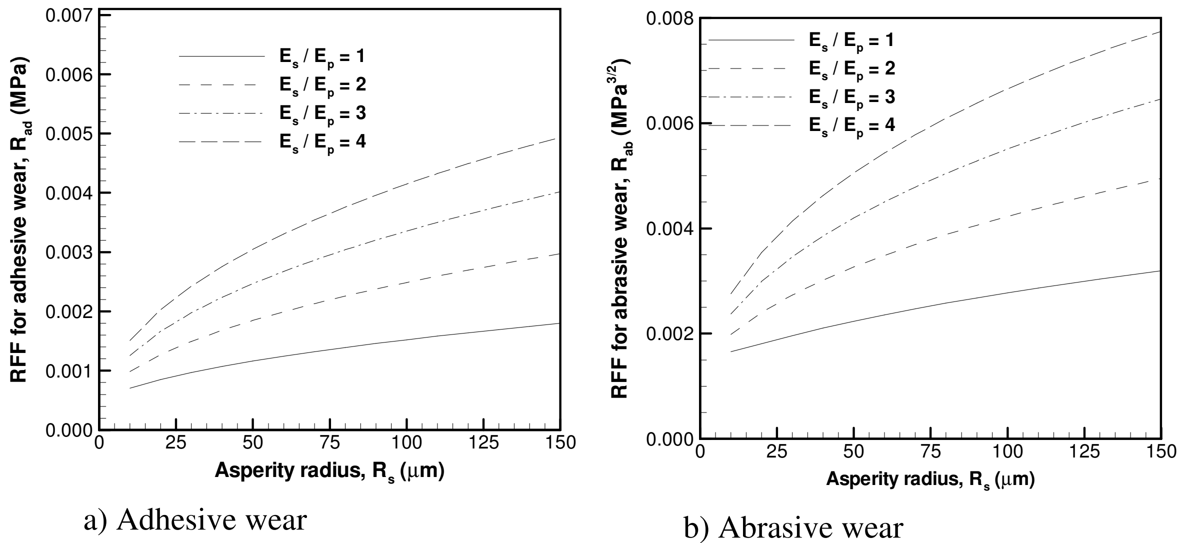

Fig. 7.55: The effect of asperity radius R_s on RFF due to a) adhesive wear R_{ad} and b) abrasive wear R_{ab} for a soft pad E_s = 10 MPa with different porous elastic modulus ratio E_s / E_p.

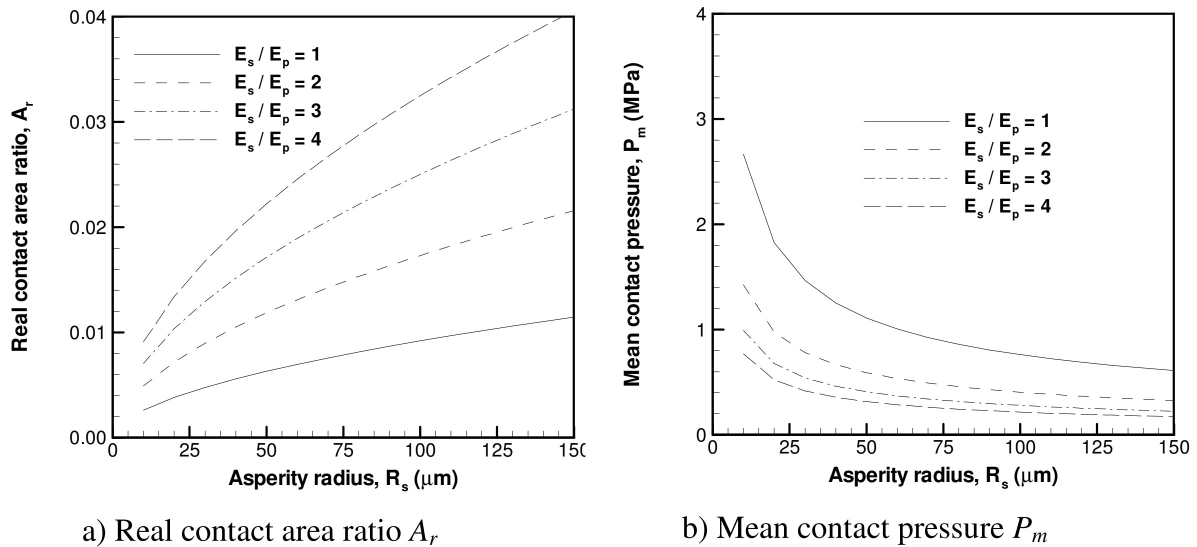

a) Real contact area ratio A_r b) Mean contact pressure P_m

Fig. 7.56: The effect of asperity radius R_s on a) real contact area ratio A_r and b) mean contact pressure P_m for a soft pad E_s = 10 MPa with different porous elastic modulus ratio E_s / E_p.

A_r and mean contact pressure P_m. Real contact area A_r increases with larger asperity radius R_s (Fig. 7.56a) lowering the mean contact pressure P_m (Fig. 7.56b). The tendency of a particle to be embedded in the pad becomes smaller as mean contact pressure P_m is reduced. Consequently direct contact area ratio A_d / A_r decreases with larger asperity radius R_s (Fig. 7.57a) causing the particle contact pressure ratio P_p / P_o to increase (Fig. 7.57b).

7.5.4 Effect of asperity density on RFF

Results

The effect of asperity density, η_s on RFF due to adhesive R_{ad} or abrasive R_{ab} wear is not as strong as pad roughness σ_s or asperity radius R_s. Fig. 7.58 shows the effect of asperity density η_s on RFF for a soft pad (E_s = 10 MPa) and low applied pressure (P_o = 0.007 MPa). An increase in asperity density, η_s causes RFF to become larger. This is attributed to the effect of asperity density η_s on real contact area A_r and mean contact pressure P_m.

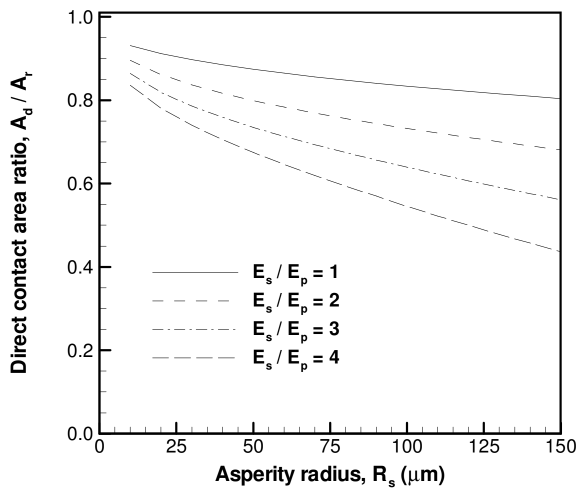

a) Direct contact area ratio A_d / A_r

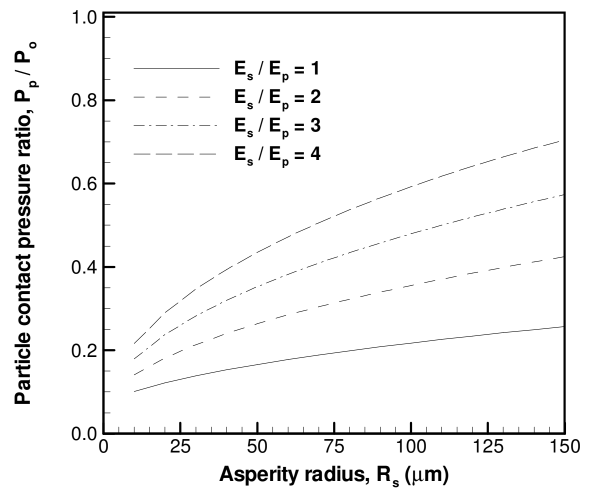

b) Particle contact pressure ratio P_p / P_o

Fig. 7.57: The effect of asperity radius R_s on a) direct contact area ratio A_d / A_r and b) particle contact pressure ratio P_p / P_o for a soft pad E_s = 10 MPa with different porous elastic modulus ratio E_s / E_p.

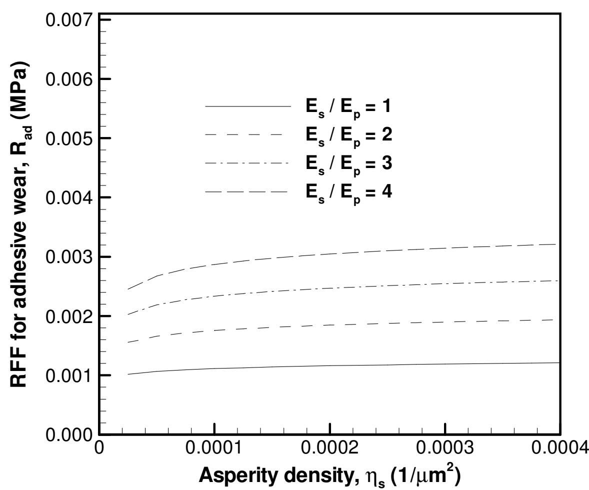

a) Adhesive wear

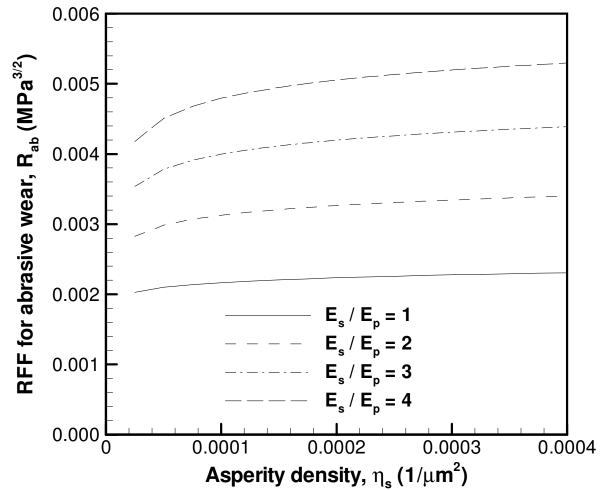

b) Abrasive wear

Fig. 7.58: The effect of asperity density η_s on RFF due to a) adhesive wear R_{ad} and b) abrasive wear R_{ab} for a soft pad E_s = 10 MPa with different porous elastic modulus ratio E_s / E_p.

Discussion

Figs. 7.59a and 7.59b show the variation of the real contact area A_r and the mean contact pressure P_m, respectively as a function of asperity density η_s. It is seen that real contact

area A_r becomes larger with asperity density η_s, while lowering mean contact pressure P_m. Asperity density η_s influences the equilibrium separation distance d_{wp} between pad and wafer as seen in Fig. 7.50b. Considering the fact that the height of asperity summits engaged in contact is determined by equilibrium separation distance d_{wp}, and asperities undergo more deformation with smaller d_{wp} facilitated by smaller asperity density η_s, mean contact pressure P_m at the tip of asperities becomes large with smaller η_s. This causes the direct contact area ratio A_d / A_r to increase (Fig. 7.60a), which results in decreasing particle contact pressure ratio P_p / P_o (Fig. 7.60b).

7.5.5 Effect of skewness on RFF

<u>Results</u>

The effect of skewness S_s of the asperity peak height PDF on RFF is investigated by utilizing Weibull distribution as the probability distribution function (PDF) of asperity

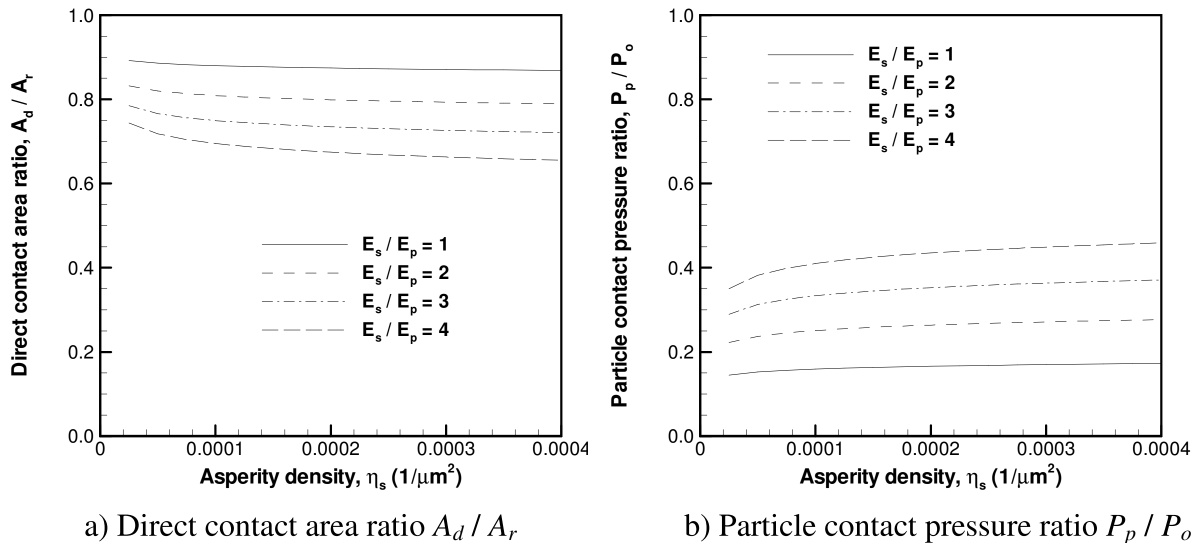

a) Direct contact area ratio A_d / A_r

b) Particle contact pressure ratio P_p / P_o

Fig. 7.60: The effect of asperity density η_s on a) direct contact area ratio A_d / A_r and b) particle contact pressure ratio P_p / P_o for a soft pad E_s = 10 MPa with different porous elastic modulus ratio E_s / E_p.

summit heights. Fig. 7.61 shows that RFF for adhesive wear R_{ad} increases slightly as skewness becomes negative $S_s < 0$ for applied pressure $P_o = 0.007$ MPa. The effect is more significant for a hard pad $E_s = 100$ MPa (Fig. 7.61b) as compared to a soft pad $E_s = 10$ MPa (Fig. 7.61a). A similar trend is observed for RFF due to abrasive wear R_{ab}.

Discussion

This trend is attributed to the influence of skewness S_s on the distribution of the applied pressure P_o on asperities in pad-wafer multi-asperity contact. Real contact area A_r (Fig. 7.62a) increases with smaller skewness S_s, which results in larger mean contact pressure P_m on asperities (Fig. 7.62b). Fig. 7.63 indicates that equilibrium separation distance d_{wp} becomes smaller as skewness S_s decreases, as a result the asperities are subjected to large deformations to support the applied pressure P_o. Higher local contact pressure leads to a larger direct contact area A_d / A_r (Fig. 7.64a) and a smaller particle contact pressure P_p / P_o (Fig. 7.64b). This condition has a negative effect on RFF. As a result, RFF decreases as skewness S_s decreases.

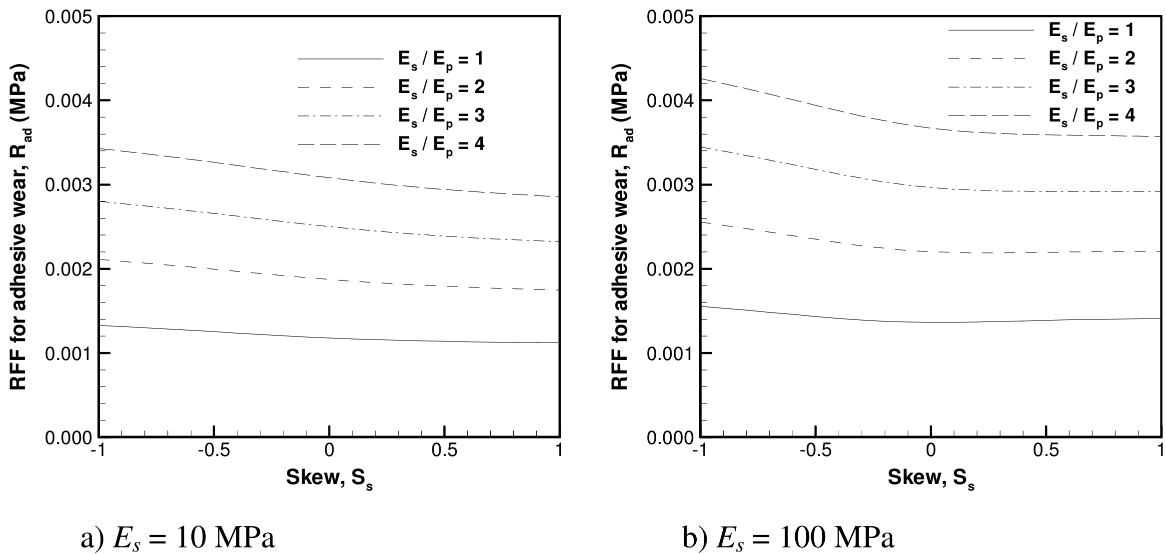

a) $E_s = 10$ MPa b) $E_s = 100$ MPa

Fig. 7.61: The effect of skewness S_s on RFF due to adhesive wear R_{ad} for a) a soft pad $E_s = 10$ MPa and b) a hard pad $E_s = 100$ MPa with different porous elastic modulus ratio E_s / E_p.

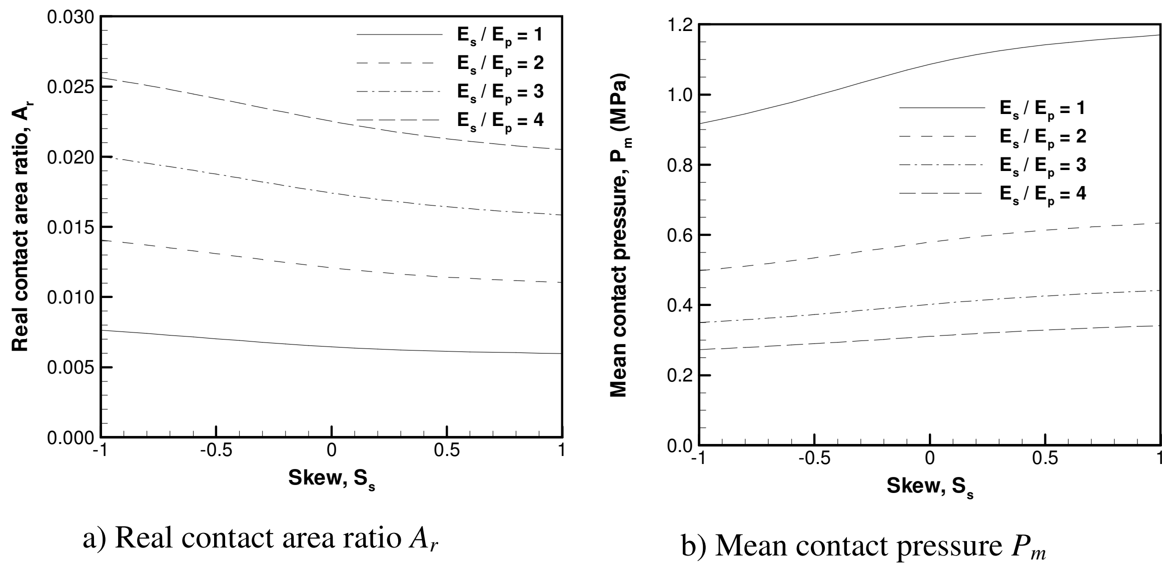

a) Real contact area ratio A_r

b) Mean contact pressure P_m

Fig. 7.62: The effect of skewness S_s on a) real contact area ratio A_r and b) mean contact pressure P_m for a soft pad E_s = 10 MPa with different porous elastic modulus ratio E_s / E_p.

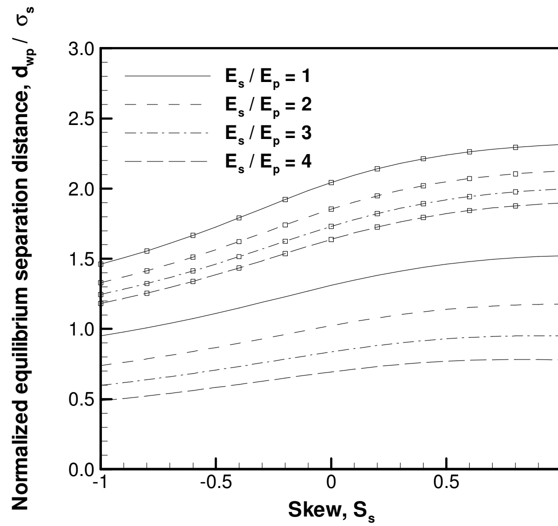

Fig. 7.63: Equilibrium separation distance d_{wp} as a function of skewness S_s for different pad elastic modulus E_s and porous elastic modulus ratio E_s / E_p.

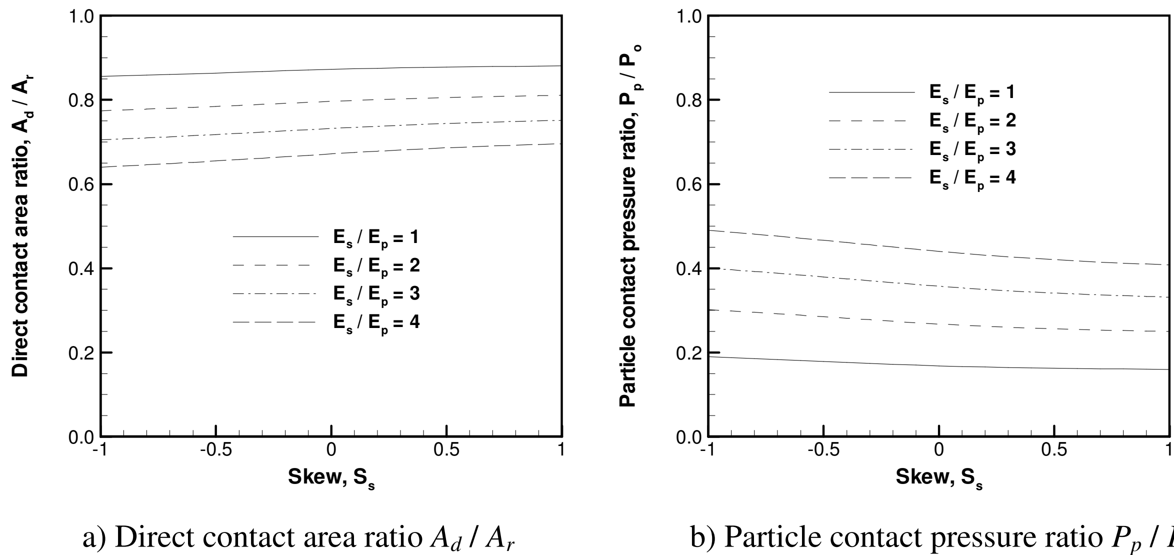

a) Direct contact area ratio A_d / A_r b) Particle contact pressure ratio P_p / P_o

Fig. 7.64: The effect of skewness S_s on a) direct contact area ratio A_d / A_r and b) particle contact pressure ratio P_p / P_o for a soft pad E_s = 10 MPa with different porous elastic modulus ratio E_s / E_p.

7.5.6 Comparison with experiments

The effect of pad topography was investigated by performing oxide CMP experiments with silica slurry [25]. Two different conditioning discs, random diamond disc (RDD) and uniform diamond disc (UDD), were used to generate different pad topographies. RDD had diamonds with different protrusion height and shapes distributed while the protrusions on UDD were pyramidal shape and the same height. As a result of the geometry of conditioning discs, pads conditioned by RDD had a roughness, σ_s = 4.94μm and skewness S_s = 0.19, whereas roughness and skewness of pads conditioned by UDD were σ_s = 2.96 μm and S_s = 0.44, respectively. CMP experiments were performed by each pad using an applied pressure, P_o = 0.035 MPa (= 5 psi). The average MRR achieved using RDD conditioned pad (MRR = 320 nm / min) was lower than MRR by UDD conditioned pad (MRR = 355 nm / min). We modeled the conditions of these experiments

by introducing the roughness σ_s and skewness S_s of each pad into a Weibull distribution. In addition to the pad elastic modulus E_s = 100 MPa and porous elastic modulus ratio E_s / E_p = 4, base parameters listed in Table 7.1 were used for the inputs required by the model. Fig. 7.65 shows the ratio of MRR achieved by RDD conditioned pad to MRR by UDD conditioned pad measured in experiments and predicted by simulations. It is seen that if the effect of skewness is neglected i.e. S_s = 0, the ratio was found to be 0.86 whereas experimental results indicated the ratio to be 0.90. Including the effect of skewness S_s by substituting the appropriate values for each pad, the predictions of the model were improved as the ratio predicted by the model increased to 0.88. Based on these results, it is concluded that the models predict the effect of pad roughness σ_s and skewness S_s accurately.

In addition, pad roughness σ_s and skewness S_s play an important role for the slurry flow in the pad-wafer interface. The effect of only the tall pad asperities making contact with

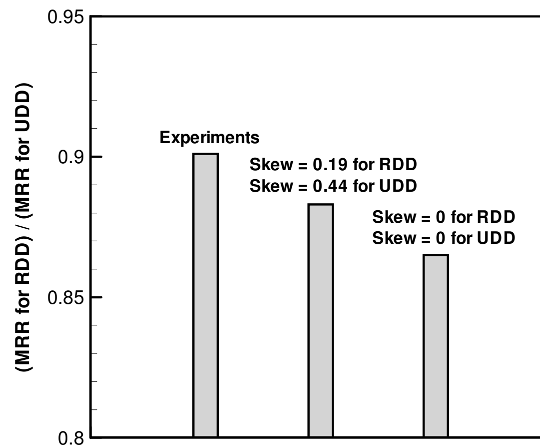

Fig. 7.65: The effect of pad roughness σ_s and skewness S_s on MRR as determined by experiments conducted by two different pad conditioner geometries, random diamond distribution RDD and uniform diamond distribution UDD (Park et al. [25]).

wafer is included in the model while the short asperities also have a crucial function for providing the necessary path for slurry flow, which is an important factor for distributing the slurry chemicals over the wafer surface and transport slurry particles resulting in material removal [25]. Therefore the higher MRR predicted by the model for smaller pad roughness σ_s and skewness S_s is only valid if the material removal is not limited by the effects of slurry flow for wafer passivation and particle transport.

Pad topography changes in CMP as the tall asperities of the pad start to wear due to contact with wafer and particles [8]. As a result, pad roughness decreases, which is predicted to have a positive effect on MRR predicted by the model. As opposed to the predictions of the model, experiments showed that MRR decreases with polishing time if no conditioning is applied to regenerate the pad asperities [8,26], however this behavior was explained by the decreased ability of pad to distribute slurry to the wafer surface as the asperities wear and pad pores closes due to the polishing debris. Stein et al. [26] conducted oxide CMP experiments and measured the pad roughness after each polishing experiment. They observed that pad topography remained constant after 5 minutes of polishing while the decay in MRR continued for the duration of the whole experiment (60 minutes). Therefore the decay in MRR with polishing time in the absence of conditioning can be attributed to the closing of the pores and smaller separation distance between pad and wafer having a negative effect on the ability of pad to distribute slurry over wafer surface.

7.6 Effect of Surface Forces

The RFF of a single particle depends on the contact force, f_w at the wafer-particle interface (Section 5.2). In the previous sections, the effect of surface forces acting

between the wafer and the particle f_s has been neglected, by assuming that the wafer-particle contact force is equal to pad-particle contact force $f_w = f_p$. In this section, the effects of the surface forces f_s are considered. The wafer-particle contact force is treated as $f_w = f_p + f_s$. The effect of surface forces, f_s on RFF is studied by highlighting the conditions where surface forces may play an important role for RFF in CMP.

Note that the overall influence of surface forces f_s on RFF due to adhesive wear R_{ad} can be calculated directly by using the number of active particles n_a and surface force f_s between wafer and a single particle as $R_{ad}^s = n_a f_s$ because R_{ad} varies with equilibrium wafer-particle contact force as $R_{ad} \propto f_w$. The effect of surface forces on RFF due to abrasive wear R_{ab}, on the other hand, cannot be determined directly using number of active particles n_a and surface force of a single particle f_s due to the non-linear relationship $R_{ab} \propto f_w^{3/2}$. Therefore the equilibrium contact force f_w is calculated for each particle and then R_{ab} is calculated using f_w.

7.6.1 Effect of van der Waals force on RFF

The van der Waals force f_{vdw} between wafer and particles is calculated using Eqn (3.29). The van der Waals force f_{vdw} is always attractive, and its magnitude depends on the separation distance d_o, particle size μ_p and effective Hamaker constant A_{wsp} calculated considering the effect of medium (slurry) between wafer and particle. Fig. 7.66 illustrates the variation of RFF due to adhesive (Fig. 7.66a) and abrasive wear (Fig. 7.66b) in the presence of van der Waals force. Equivalent Hamaker constant in the range $1\text{x}10^{-20}$ J < A_{wsp} < $5\text{x}10^{-20}$ J is considered. The contacting surfaces are assumed to be atomically smooth, i.e. separation distance d_o = 4 Å. Furthermore, a soft pad E_s = 10 MPa with

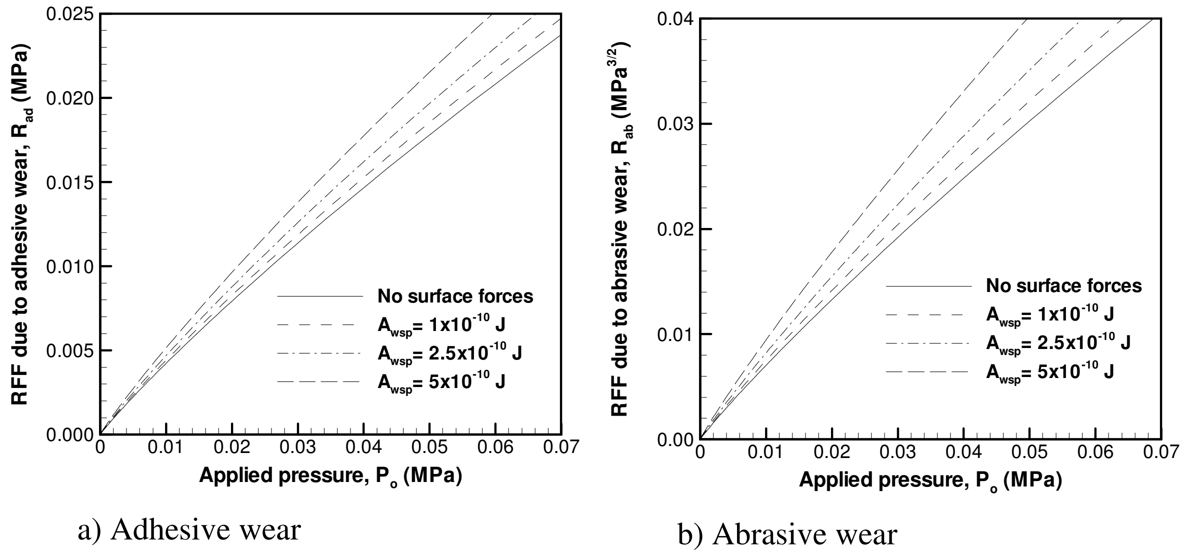

Fig. 7.66: The effect of van der Waals force on the RFF due to a) adhesive wear R_{ad} and b) abrasive wear R_{ab} for a soft E_s = 10 MPa, porous pad E_s / E_p = 4 and mean particle radius, μ_p = 5nm.

porous elastic modulus ratio, E_s / E_p = 4 and mean particle radius of μ_p = 5 nm are used. It is seen that van der Waals force f_{vdw} enhances RFF due to both adhesive R_{ad} and abrasive wear R_{ab} and the effect becomes more significant with higher effective Hamaker constant A_{wsp}. Fig. 7.66b demonstrates that the increase in RFF due to abrasive wear R_{ab} is larger than that of RFF due to adhesive wear R_{ad}. This is due to the non-linear relation between RFF due to abrasive wear R_{ab} and contact force on each particle f_w, $R_{ab} \propto f_w^{3/2}$. The relative effect of van der Waals force f_{vdw} remains constant with respect to applied pressure P_o due to the fact that van der Waals force on each particle is not a function of P_o and mean particle contact force f_p^m applied by pad does not vary significantly with P_o.

The effect of van der Waals force f_{vdw} on RFF is quantified by the ratio of the change in RFF due the presence of van der Waals force ΔR^s to RFF in the absence of van der Waals force R as $\Delta R^s / R$ plotted in Fig. 7.67. Porous elastic modulus ratio E_s / E_p = 4 and

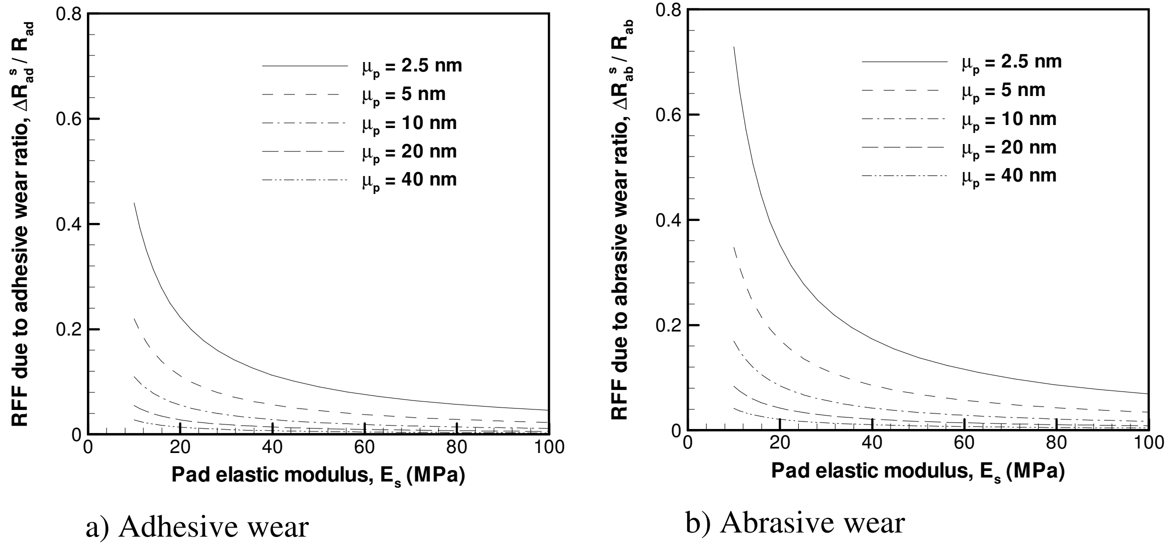

a) Adhesive wear b) Abrasive wear

Fig. 7.67: The effect of van der Waals force on a) RFF due to adhesive wear R_{ad} and b) RFF due to abrasive wear R_{ab} quantified by the ratio of change in R due to surface forces, ΔR^s, $\Delta R^s / R$ for different pad elastic modulus E_s ($E_s / E_p = 4$) and mean particle radius μ_p ($A_{wsp} = 5\text{x}10^{-20}$ J).

effective Hamaker constant $A_{wsp} = 5\text{x}10^{-20}$ J are used. Fig. 7.67 shows that the relative effect of van der Waals force $\Delta R^s / R$ increases as pad elastic modulus E_s and particle size μ_p become smaller. Larger pad elastic modulus E_s causes the mean particle contact force f_w^m to increase, diminishing the relative effect of van der Waals force $\Delta R^s / R$. Both van der Waals force f_{vdw} and pad-particle force f_p decreases with smaller particle radius μ_p however the rate of decrease is different for van der Waals force, $f_{vdw} \propto \mu_p$ and pad-particle force, $f_p \propto \mu_p^2$, thus pad-particle force f_p becomes rapidly small as compared to van der Waals force f_{vdw} as particles become smaller. It is found that the increase in RFF due to the presence of van der Waals force $\Delta R^s / R$ may be as large as 44% for adhesive and 73% for abrasive wear for equivalent Hamaker constant, $A_{wsp} = 5\text{x}10^{-20}$ J, pad elastic modulus, $E_s = 10$ MPa and mean particle radius $\mu_p = 2.5$ nm. The effect of van der Waals

force f_{vdw} on RFF due to adhesive wear R_{ad} becomes less than 5%, $\Delta R^s / R < 0.05$ when pad elastic modulus is greater than $E_s > 80$ MPa ($\mu_p = 2.5$ nm) or particle radius larger than $\mu_p > 30$ nm ($E_s = 10$ MPa).

7.6.2 Effect of double layer forces on RFF

Eqns (3.41)-(3.42) are used in order to calculate double layer force f_{dl} acting between wafer and particle. The formulations developed based on two different assumptions, HHF constant charge (HHF-CC) and compression approximation (CA) described in Section 3.2.2 are utilized here. The parameters used in the calculations are listed in Table 7.4.

Effect of the zeta potential

Figs. 7.68 and 7.69 show RFF in the presence of double layer force f_{dl} calculated by CA and HHF-CC assumptions, respectively. In addition to the base parameters listed in Table 7.1, the pad elastic modulus is taken to be $E_s = 10$ MPa with $E_s / E_p = 4$. Mean particle radius, $\mu_p = 5$ nm, separation distance, $d_o = 4$ Å and $P_o = 0.007$ MPa are used. The presence of double layer forces f_{dl} causes RFF to decrease when CA is used to calculate

Parameter	Value
Electron charge (e)	$1.6\text{x}10^{-19}$ C
Avagadro's number (N_a)	$6.02\text{x}10^{23}$
Dielectric constant of water (ε_r)	78.4
Permittivity of vacuum (ε_o)	$8.85\text{x}10^{-12}$ $C^2N^{-1}m^{-2}$
Temperature (T)	298 K
Boltzmann constant (k)	$1.38\text{x}10^{-23}$
Valence (z)	1

Table 7.4: Parameters used for the calculation of double layer forces.

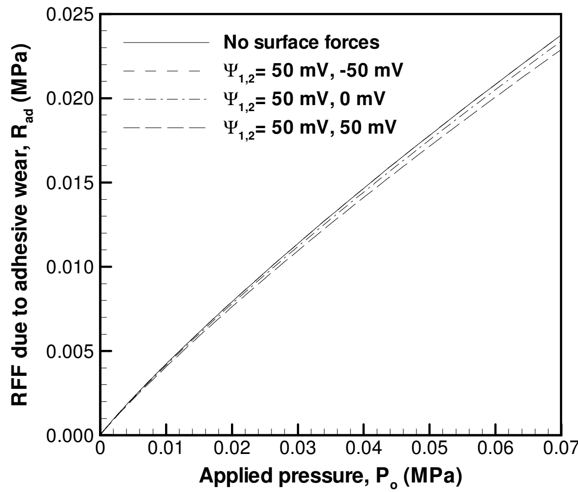

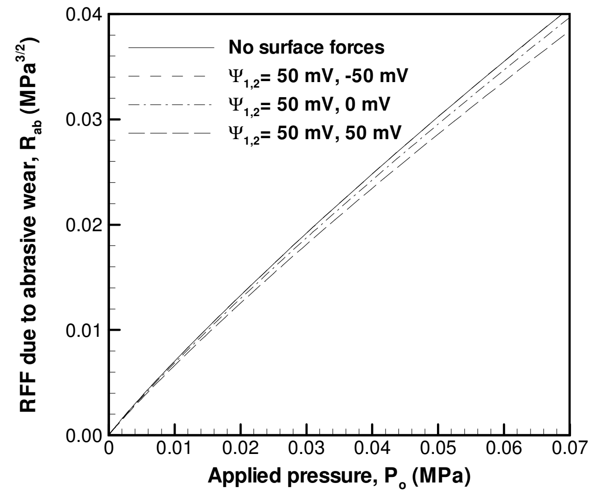

a) Adhesive wear b) Abrasive wear

Fig. 7.68: The effect of double layer force calculated by CA assumption on RFF due to a) adhesive wear R_{ad} and b) abrasive wear R_{ab} for a soft E_s = 10 MPa, porous pad E_s / E_p = 4 and mean particle radius, μ_p = 5nm.

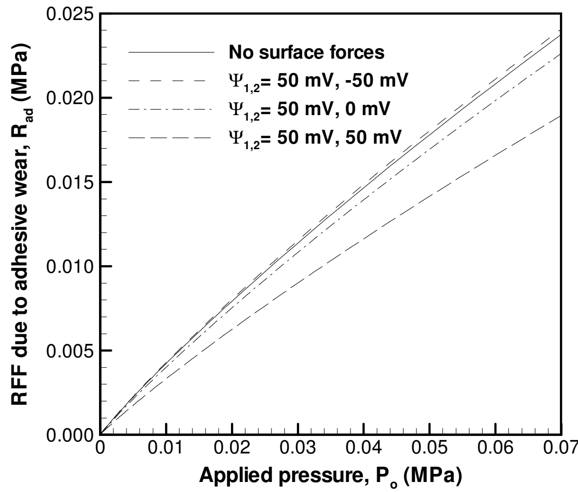

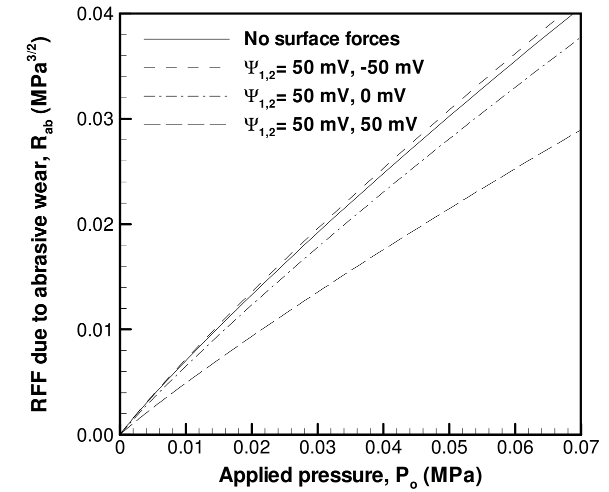

a) Adhesive wear b) Abrasive wear

Fig. 7.69: The effect of double layer force calculated by HHF-CC assumption on RFF due to a) adhesive wear R_{ad} and b) abrasive wear R_{ab} for a soft E_s = 10 MPa, porous pad E_s / E_p = 4 and mean particle radius, μ_p = 5nm.

f_{dl} even when the wafer and particle are oppositely charged ($\Psi_{1,2}$ = 50 mV, -25 mV) as shown in Fig. 7.68. According to CA assumption, the magnitude of double layer forces become zero, f_{dl} = 0, when wafer and particle are oppositely charged with the same zeta

potential, e.g. $\Psi_{1,2}$ = 50 mV, -50 mV. As the sum of zeta potentials ($\Psi_1 + \Psi_2$) increases, the effect of double layer forces f_{dl} become more important. It is seen in Fig. 7.69 that the magnitude of double layer forces f_{dl} calculated by HHF-CC assumption is larger than that of CA assumption therefore there is a greater effect of f_{dl} on RFF when HHF-CC assumption is employed. In contrast to CA assumption, HHF-CC assumption predicts a slightly attractive double layer force increasing RFF when the surface are oppositely charged with high zeta potentials, e.g. $\Psi_{1,2}$ = 50 mV, -50 mV.

Relative effect of double layer forces

The relative effect of double layer forces f_{dl} on RFF for different particle radius μ_p and pad elastic modulus E_s is further evaluated in Figs. 7.70 (CA) and 7.71 (HHF-CC), where zeta potential of wafer and particle is taken to be $\Psi_{1,2}$ = 50 mV, 50 mV, molar concentration $M = 0.01$, porous elastic modulus ratio $E_s / E_p = 4$ and applied pressure P_o = 0.007 MPa. Note that the change in RFF due to the presence of double layer forces $\Delta R^s / R$ is negative since double layer forces f_{dl} are repulsive under these conditions. According to the predictions for double layer force f_{dl} using CA assumption, the effect of double layer force is less than 10%, $\Delta R^s / R < 0.10$ in the range of particle size 2.5 nm < μ_p < 40 nm and pad elastic modulus 10 MPa < E_s < 100 MPa studied. The calculations using HHF-CC assumption yields much higher magnitude for double layer force f_{dl} and the effect is predicted to be as large as $\Delta R^s / R = 0.60$ when a small particle radius μ_p = 2.5 nm and a soft pad E_s = 10 MPa is used. As explained in Section 7.6.1, RFF for abrasive wear R_{ab} is influenced by double layer forces at a greater extend due to the dependence on particle contact force, $R_{ab} \propto f_w^{3/2}$.

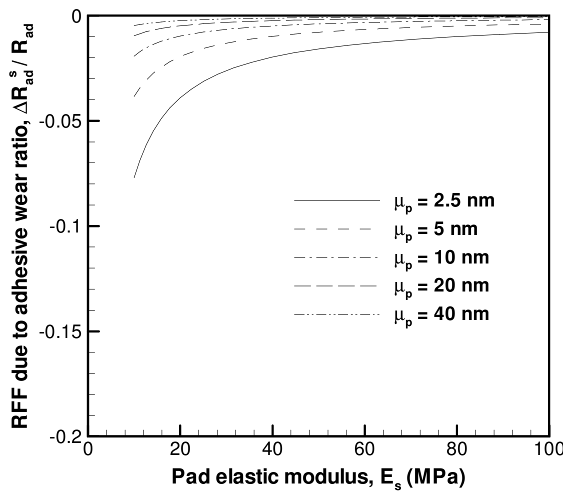

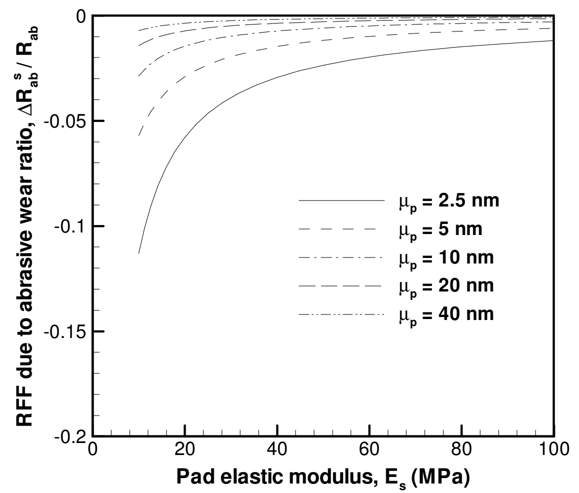

a) Adhesive wear b) Abrasive wear

Fig. 7.70: The effect of double layer force on a) RFF due to adhesive wear R_{ad} and b) RFF due to abrasive wear R_{ab} quantified by the ratio of change in R due to surface forces, ΔR^s, ΔR^s / R for different pad elastic modulus E_s (E_s / E_p = 4) and mean particle radius μ_p ($\Psi_{1,2}$ = 50 mV, 50 mV and M = 0.01). CA asumption is used to calculate double layer force.

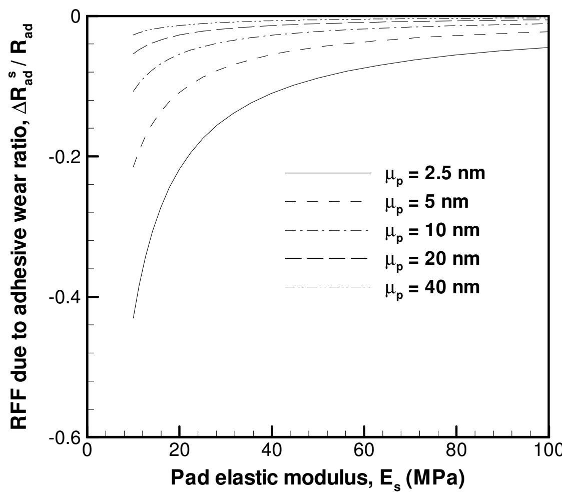

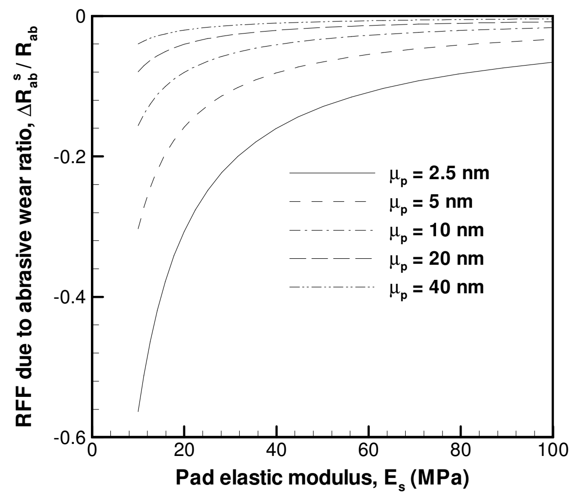

a) Adhesive wear b) Abrasive wear

Fig. 7.71: The effect of double layer force on a) RFF due to adhesive wear R_{ad} and b) RFF due to abrasive wear R_{ab} quantified by the ratio of change in R due to surface forces, ΔR^s, ΔR^s / R for different pad elastic modulus E_s (E_s / E_p = 4) and mean particle radius μ_p ($\Psi_{1,2}$ = 50 mV, 50 mV and M = 0.01). HHF-CC assumption is used to calculate double layer force.

Effect of molar concentration

In Fig. 7.72, the effect of molar concentration M on RFF due to adhesive wear R_{ad} is investigated for different separation distance d_o for CA (Fig. 7.72a) and HHF-CC (Fig. 7.72b). The calculations are performed for a soft pad E_s = 10 MPa with porous elastic modulus ratio E_s / E_p = 4, particle size μ_p = 5 nm, zeta potential $\Psi_{1,2}$ = 50mV, 50mV and applied pressure P_o = 0.007 MPa. An opposite trend is observed for the magnitude of double layer force f_{dl} calculated by CA and HHF-CC assumptions where larger molar concentration M causes the magnitude f_{dl} to increase for CA assumption while f_{dl} for HHF-CC assumption decreases with larger M. Larger separation distance d_o has a negative effect on magnitude of double layer forces for both CA and HHF-CC assumptions.

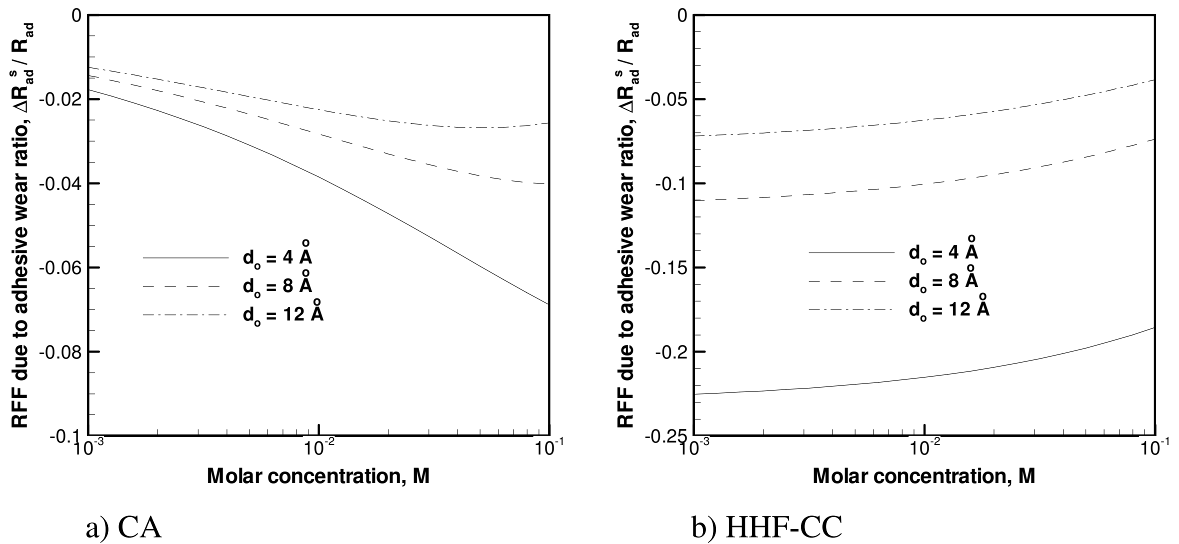

a) CA b) HHF-CC

Fig. 7.72: The effect of double layer force on RFF due to adhesive wear R_{ad} quantified by ΔR^s / R for different separation distance d_o and molar concentration calculated by a) CA and HFF-CC assumptions. ($\Psi_{1,2}$ = 50 mV, 50 mV, μ_p = 5 nm, E_s = 10 MPa, E_s / E_p = 4, P_o = 0.007 MPa)

7.6.3 Comparison with experiments

CMP experiments were carried out in order to investigate the effect of slurry pH on MRR of tantalum films polished by silica and alumina slurry [27] where the zeta potential of materials was measured as a function of pH. The variation of zeta potential of tantalum pentoxide, alumina and silica was described by curve-fit equations as follows [28],

$$\Psi_{\text{tantalum}} = \begin{cases} 80\,mV & pH \le 2 \\ 80\cos\dfrac{\pi\left(pH-1.8\right)}{10}\,mV & 2 \le pH \le 12 \\ -80\,mV & pH \ge 12 \end{cases} \tag{7.1}$$

$$\Psi_{\text{alumina}} = \begin{cases} 25\,mV & pH \le 7.4 \\ 25\cos\dfrac{\pi\left(pH-7.4\right)}{4.6}\,mV & 7.4 \le pH \le 12 \\ -25\,mV & pH \ge 12 \end{cases} \tag{7.2}$$

$$\Psi_{silica} = \begin{cases} 25\cos\dfrac{\pi\left(pH\right)}{4.2}\,mV & pH \le 4.2 \\ -25\,mV & pH \ge 4.2 \end{cases} \tag{7.3}$$

Fig. 7.73 demonstrates the variation of zeta potential Ψ of materials with respect to slurry pH described by Eqns (7.1) – (7.3). It is seen that zeta potential is positive for all materials at small pH. As pH increases, zeta potential Ψ decreases and Ψ becomes negative, $\Psi < 0$ for pH above iso-electric point, which occurs at pH = 6.8 for tantalum pentoxide, pH = 9.7 for alumina and pH = 2.1 for silica. Based on these results, it is determined that tantalum pentoxide wafer and alumina particle are oppositely charged, when pH is in the range, $6.8 < pH < 9.7$. The same condition appears for tantalum pentoxide wafer and silica particle for $2.1 < pH < 6.8$.

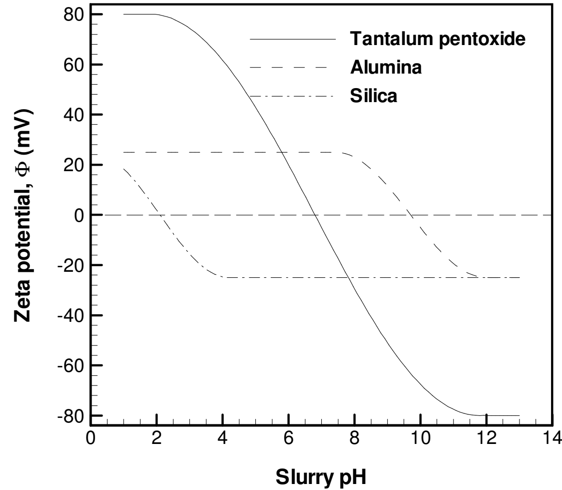

Fig. 7.73: The variation of zeta potential with slurry pH for different materials (tantalum pentoxide, alumina and silica) described by Eqns (7.1)-(7.3) [28].

The variation of MRR normalized with respect to maximum MRR obtained in tantalum CMP experiments using alumina and silica slurry is plotted as a function of slurry pH in Fig. 7.74. It is seen that MRR is influenced by the slurry pH significantly. This was attributed to the effect of double layer forces f_{dl} varying in magnitude with slurry pH. Simulations were carried out in order to calculate the magnitude of double layer forces f_{dl} and their effect on MRR. In the simulations, slurry pH influences the zeta potential of wafer and particle Ψ as described by Eqns (7.1) – (7.3), thereby the contact force between wafer and particle f_w varies with slurry pH. The elastic modulus of a soft pad (E_s = 1 MPa and E_s / E_s = 4) and particle concentration of η_w = 3% was used. The applied pressure was P_o = 0.044 MPa (= 6.3 psi). The simulations were run using mean particle radius μ_p = 10nm and μ_p = 100nm. Both CA and HHF-CC assumptions were employed.

Fig. 7.74 shows that experimental and simulation results for MRR agree qualitatively. Maximum MRR occurs around pH ~ 8 as determined by experiments and simulations for alumina slurry. Simulations predicted maximum MRR to occur at pH ~ 5, while

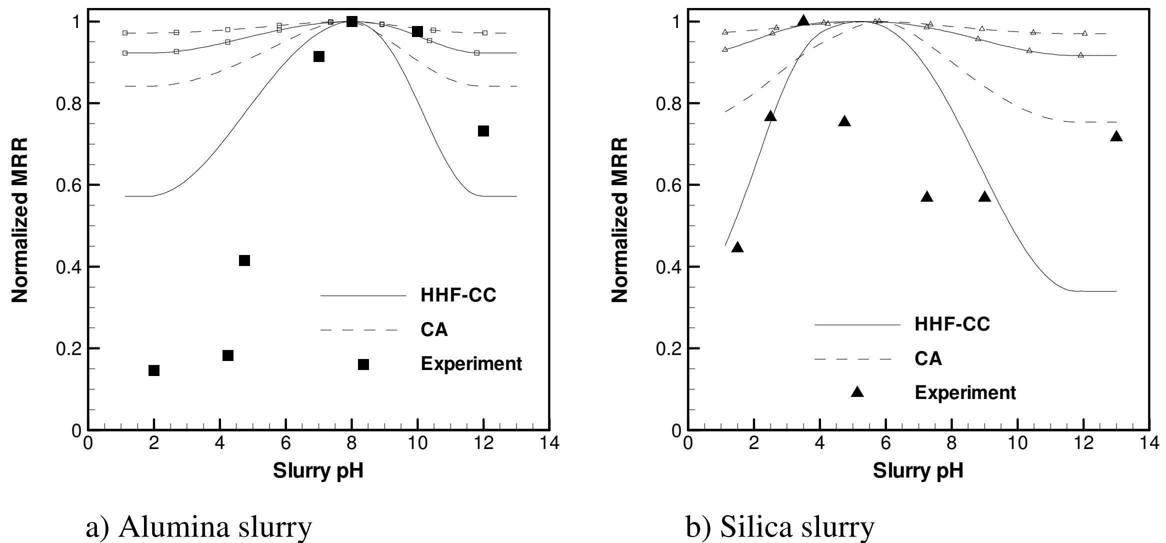

a) Alumina slurry b) Silica slurry

Fig. 7.74: The variation of normalized MRR with slurry pH using a) alumina and b) silica slurry [27].

maximum MRR was found at pH ~ 4 in the experiments for silica slurry. The effect of double layer forces f_{dl} was small when mean particle radius, μ_p = 100 nm was used in the simulations, whereas a significant influence of double layer forces was observed when μ_p = 10 nm was used. The simulations under-predicted the overall effect of pH for both alumina and silica slurry. HHF-CC assumption yielded a better quantitative agreement with experiment results than CA assumption.

The experiments reported by Ramarajan et al. [27] were also performed in order to evaluate the effect molar concentration of KCl ions in the slurry. The ion molar concentration controls the magnitude of double layer force and seems have a strong effect on MRR as shown in Figs. 7.75 and 7.76. Molar ion concentration M is used in simulations for the calculation of double layer forces f_{dl} for CA and HHF-CC assumptions, respectively. A particle radius of μ_p = 10 nm was used in the simulations along with the other parameters as given before. Opposite trends for the variation of MRR with molar concentration were predicted for CA and HHF-CC assumptions as

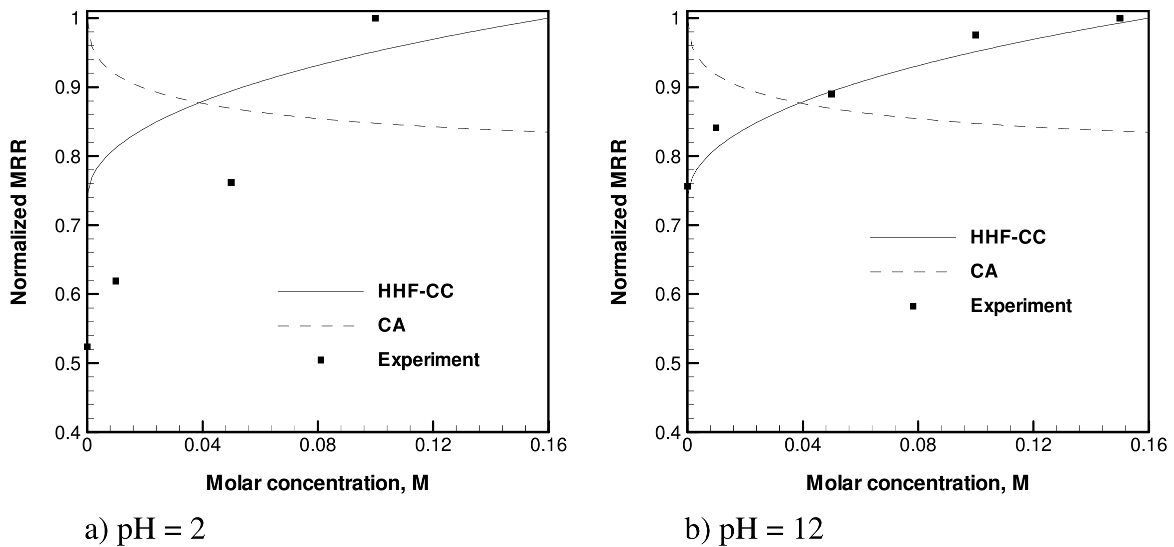

a) pH = 2 b) pH = 12

Fig. 7.75: The variation of normalized MRR of tantalum film polished with alumina slurry as a function of molar concentration *M* at a) pH = 2 and b) pH = 12 [27].

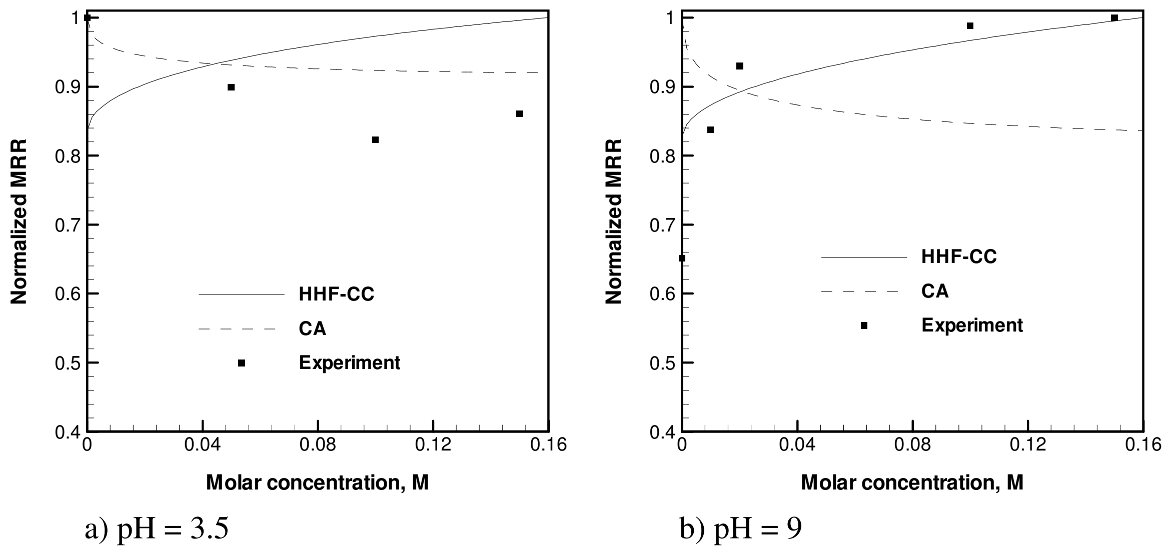

a) pH = 3.5 b) pH = 9

Fig. 7.76: The variation of normalized MRR of tantalum film polished with silica slurry as a function of molar concentration *M* at a) pH = 3.5 and b) pH = 9 [27].

explained in Section 7.6.2 (Fig. 7.72). Comparing the experiment and model results, it is found that double layer force calculated based on HHF-CC assumption resulted in a better agreement with experiments for alumina (pH = 2 and pH =12) and silica (pH = 9) slurry indicating a smaller MRR with larger molar concentration *M*. An opposite trend

was seen for silica slurry when pH was adjusted to be pH = 3.5. In this case, MRR decreased with larger molar concentration as predicted by CA assumption.

The effect of pH was in general under-predicted by the simulations. This result may be attributed to the influence of pH on wafer passivation, i.e. thickness and hardness of passivated layer is a strong function of slurry pH as explained in Section 2.2.3. Furthermore, slurry pH may influence particle size as colloidal stability of slurry particles depends on surface forces acting between particles. Furthermore, the number of active particles may also be influenced by surface forces. Similar to the colloidal behavior of particles due to particle-particle interactions, wafer and particle also interact with each other and this interaction may have a strong effect on number of active particles. A strong repulsive double layer force f_{dl} between wafer and particle may cause the number of active particles n_a to decrease as well as having a negative effect on wafer-particle contact force f_w for the active particles.

7.7 Effect of Particle Size

It can be shown that the RFF for adhesive and abrasive wear increase with particle size as, $R^{sp} \propto \mu_p^2$ in the absence of surface forces ($f_s = 0$) due to the fact that the RFF due to adhesive and abrasive wear vary with wafer-particle contact force as $R_{ad}^{sp} \propto f_w$ (Eqn (5.6)) and $R_{ab}^{sp} \propto f_w^{3/2} / \mu_p$ (Eqn (5.7)), respectively and $f_w = f_p$ when $f_s = 0$, where pad-particle contact force varies as $f_p \propto \mu_p^2$. Considering the relation between number of active particles and particle size, $n_a \propto 1/\mu_p^2$, total RFF for all active particles can be found as $R = R^{sp} n_a$. Therefore, according to the proposed model, the particle size μ_p (mean particle radius) does not have an effect on removal force function (RFF) if only pad-

particle contact force is considered. On the other hand, it will be shown in Section 7.7.1 that the RFF becomes a function of particle size, if the effect of surface forces on RFF is considered.

Particle size also plays an important role when the effect of passivated surface layer of the wafer is considered. If the indentation depth of a particle is greater than the passivated layer thickness, the effective wafer hardness becomes a function of indentation depth (Eqn (5.16b)), which is a function of particle size (Eqn (5.11)). The passivated layer may be softer or harder than the bulk material depending on the compounds forming at the wafer surface due to the reactions between wafer and slurry chemicals (Section 2.2.4). The effect of these two conditions on the variation of MRR with respect to particle size is studied in Section 7.7.2.

In addition to the effect of surface forces (Section 7.7.1) and passivated layer (Section 7.7.2), the particles trapped at pad asperity-wafer interface alter the contact pressure distribution, which can be otherwise described by Hertz contact. This effect becomes more significant as particle size becomes larger as illustrated in Fig. 7.5. The influence of the single asperity contact behavior on RFF is discussed in Section 7.7.3.

7.7.1 Surface forces

In this section, in order to investigate the effect of surface forces on the RFF, let us briefly neglect the effect of pad-particle force ($f_p = 0$). In this case, wafer-particle contact force is equal to the surface force acting between wafer and particle, $f_w = f_s$. According to Eqns (3.29) and (3.42), the surface forces increase linearly with particle size $f_s \propto \mu_p$. Using the expressions for the RFF of single particle for adhesive ($R_{ad}^{sp} \propto f_w$)

and abrasive wear ($R_{ab}^{sp} \propto f_w^{3/2} / \mu_p$) given in Eqns (5.6) and (5.7), it can be shown that RFF of a single particle for adhesive and abrasive wear are related to particle size as $R_{ad}^{sp} \propto \mu_p$ and abrasive wear $R_{ab}^{sp} \propto \mu_p^{1/2}$, respectively. The total RFF for all active particles can be found by using the number of active particles n_a ($n_a \propto 1/\mu_p^2$) and the RFF of a single particle, as $R = R^{sp} n_a$. This leads to the relation between RFF due to adhesive wear as, $R_{ad} \propto 1/\mu_p$ and abrasive wear as $R_{ab} \propto 1/\mu_p^{3/2}$.

Now returning to the more realistic scenario of $f_w = f_p + f_s$, we see that if surface forces f_s are attractive, then smaller particle size μ_p results in larger RFF, and the effect of f_s on RFF depends on the relative magnitude of the pad-particle contact force f_p . If surface forces f_s are repulsive, then f_s has a negative effect on RFF causing RFF to decrease with smaller particle size μ_p . This is illustrated in Fig. 7.77, where the variation of RFF is plotted as a function of particle size μ_p in the presence of attractive van der Waals f_{vdw} and repulsive double layer forces f_{dl} . The calculations are performed for a soft pad E_s = 10 MPa with porous elastic modulus ratio E_s / E_p = 4 and applied pressure P_o = 0.007 MPa. Double layer forces f_{dl} are calculated using HHF-CC assumption. Fig. 7.77 shows that the magnitude of surface forces f_s become small as compared to pad-particle contact force f_p for particle radius, μ_p > 20 nm, therefore RFF remains constant with respect to μ_p . Note that the effect of particle size μ_p due to the influence of surface forces f_s becomes more important as the magnitude of f_s increases. The conditions favorable for larger surface forces f_s are explained in Section 7.6.

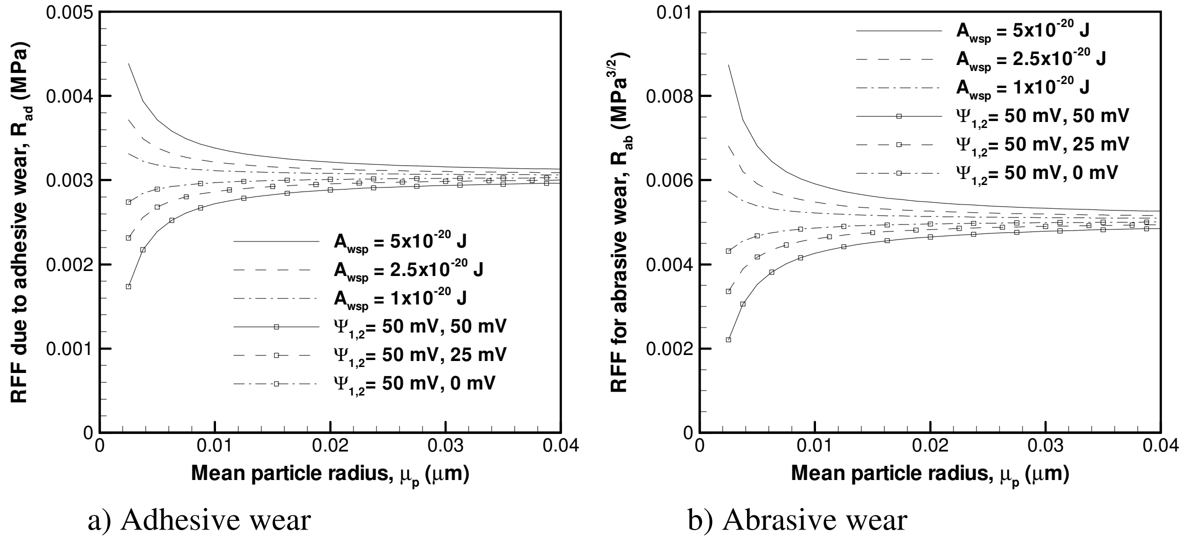

a) Adhesive wear b) Abrasive wear

Fig. 7.77: The effect of mean particle radius μ_p on RFF for a) adhesive R_{ad} and b) abrasive wear R_{ab} in the presence of surface forces.

7.7.2 Passivated surface layer

The slurry chemicals react with wafer surface, and form a passivated surface layer on the wafer. The hardness of this layer H_{pw} may be lower and higher than the hardness of bulk wafer material H_{bw} as explained in Section 2.2.4. A bi-layer hardness model is implemented in Section 5.2, where an effective wafer hardness H_w is calculated for a given indentation depth δ_w of the particle, considering the thickness t_{pw} and hardness of passivated layer H_{pw}. The indentation depth of a single particle δ_w can be calculated using the wafer-particle contact force f_w, particle radius r_p and the effective wafer hardness H_w as, $\delta_w = f_w / \left(\pi r_p H_w\right)$. Considering the dependence of the wafer-particle contact force on the particle radius, $f_w \propto r_p^2$, indentation depth is found to vary with particle size as, $\delta_w \propto r_p$. As particle size r_p increases, the indentation depth of a particle δ_w becomes larger. This causes the effective hardness H_w to increase (if passivated layer

is softer than bulk) or decrease (if passivated layer is harder than bulk) having an effect on MRR since MRR due to adhesive wear varies with $RR_{ad} \propto 1/H_w$ and abrasive wear as $RR_{ab} \propto 1/H_w^{3/2}$. Of course, the extend of this effect depends on the indentation depth δ_w relative to passivated layer thickness t_{pw} and passivated layer hardness H_{pw}, and it is explained as follows.

Soft passivated surface layer

In Figs. 7.78 and 7.79, the effect of particle size μ_p is demonstrated for different passivated layer thickness varied in the range $0 < t_{pw} < 16$ nm while passivated layer hardness, H_{pw} = 1000 MPa and bulk wafer hardness, H_{bw} = 4000 MPa are kept constant. The elastic modulus of a hard pad E_s = 100 MPa is used in the study and base values listed in Table 7.1 are used for the other parameters. It is seen in Fig. 7.78a that mean indentation depth of particles δ_w^m increases linearly with mean particle radius μ_p when the passivated layer thickness t_{pw} is very small (t_{pw} ~ 0) or very large (t_{pw} ~ 16 nm). However the slope for very small passivated layer thickness (t_{pw} ~ 0) is smaller than that of very large t_{pw} (t_{pw} ~ 16 nm). This is attributed to the effective hardness H_w as illustrated in Fig. 7.78b. The effective wafer hardness H_w is equal to passivated layer hardness $H_w = H_{pw}$ when thickness of passivated layer t_{pw} is very small (t_{pw} ~ 0). On the other hand, bulk wafer hardness H_{bw} dominates when the thickness of passivated layer t_{pw} is very large (t_{pw} ~ 16 nm). For intermediate values of passivated layer thickness e.g. t_{pw} ~ 4 nm or 8 nm, a change in slope occurs as mean particle size μ_p exceeds a critical value at which the particles start to indent through the passivated layer. As a result, effective hardness H_w increases with mean particle size μ_p and approaches the bulk wafer hardness $H_w \sim H_{bw}$

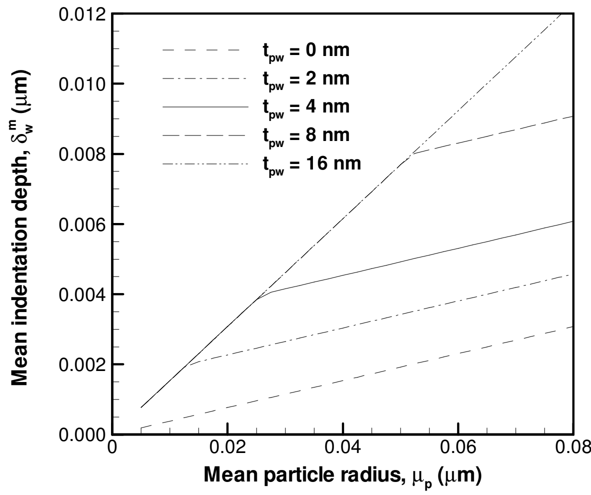

a) Mean indentation depth

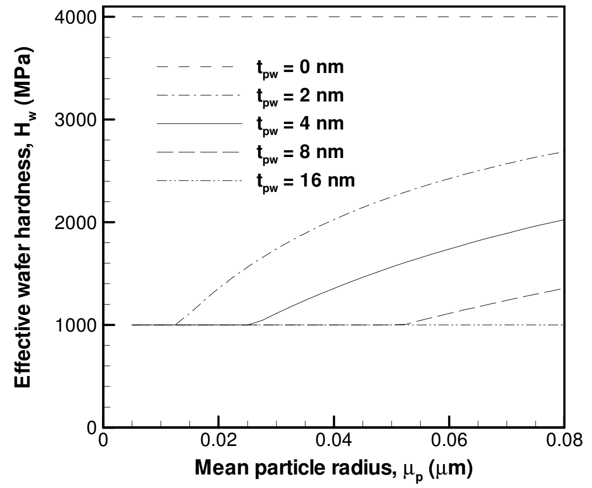

b) Effective wafer hardness

Fig. 7.78: The effect of mean particle radius μ_p on a) mean indentation depth δ_w^m and b) effective wafer hardness H_w for different passivated layer thickness t_{pw} (H_{bw}= 4000 MPa and H_{pw} = 1000 MPa).

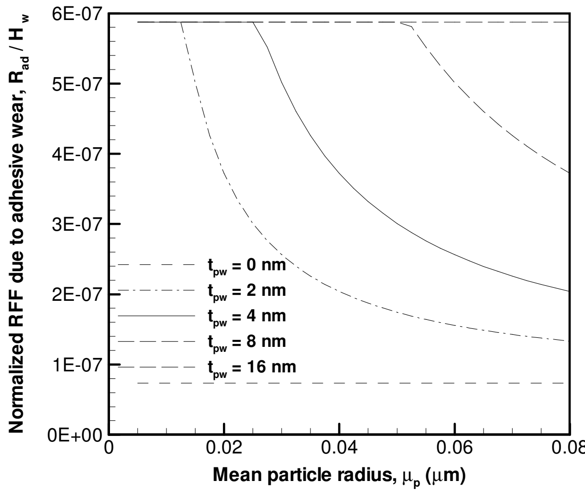

a) Adhesive wear

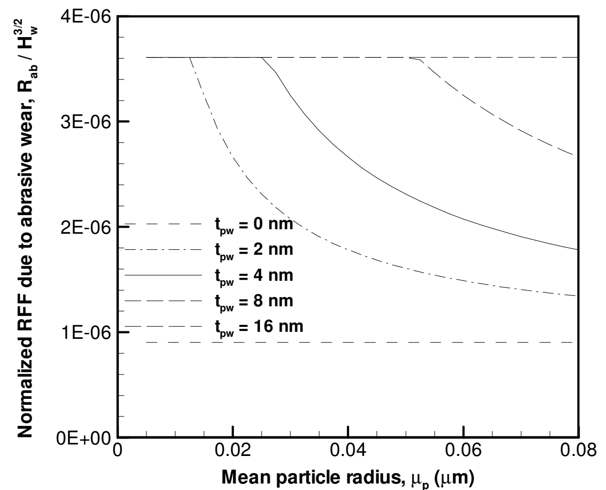

b) Abrasive wear

Fig. 7.79: The effect of mean particle radius μ_p on RFF due to a) adhesive wear R_{ad} and b) abrasive wear R_{ad} normalized with respect to effective wafer hardness (R_{ad} / H_w and R_{ab} / $H_w^{3/2}$) for different passivated layer thickness t_{pw} (H_{bw}= 4000 MPa and H_{pw} = 1000 MPa).

when μ_p becomes large. A larger effective hardness H_w translates to a lower MRR as quantified by RFF normalized by effective wafer hardness, R_{ad} / H_w or $R_{ab} / H_w^{3/2}$ plotted in Fig. 7.79, which shows that R_{ad} / H_w (Fig. 7.79a) or $R_{ab} / H_w^{3/2}$ (Fig. 7.79b) decrease with larger particle size μ_p for intermediate values of passivated layer thickness e.g. t_{pw} ~ 4 nm or 8 nm, while μ_p does not have an effect on R_{ad} / H_w or $R_{ab} / H_w^{3/2}$ since H_w remains constant with respect to μ_p if t_{pw} ~ 0 or t_{pw} ~ 16 nm.

The influence of passivated layer hardness H_{pw} is investigated in Figs. 7.80 and 7.81 by using a passivated layer thickness t_{pw} = 4 nm. Fig. 7.80 shows that mean indentation depth δ_w^m increases linearly with particle size μ_p with a slope determined by the bulk wafer hardness for $H_{pw} = H_{bw}$. As passivated layer hardness H_{pw} decreases, the rate of increase in indentation depth δ_w^m with particle size μ_p becomes larger when the mean indentation depth δ_w^m exceeds passivated layer thickness t_{pw}. Smaller passivated layer

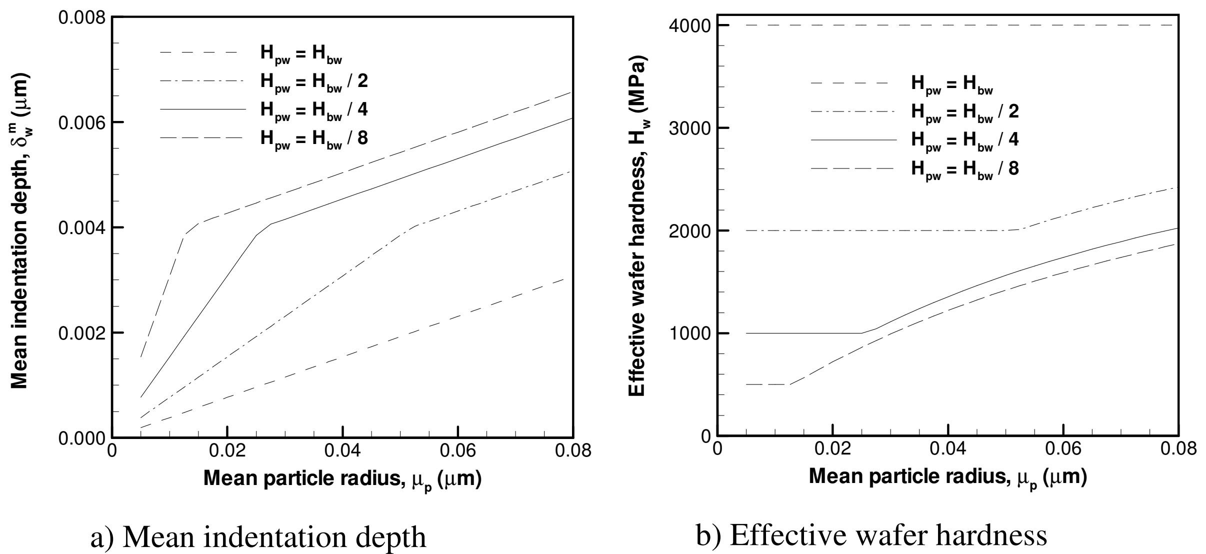

a) Mean indentation depth

b) Effective wafer hardness

Fig. 7.80: The effect of mean particle radius μ_p on a) mean indentation depth δ_w^m and b) effective wafer hardness H_w for different passivated surface hardness $H_{pw} < H_{bw}$ (t_{pw} = 4 nm).

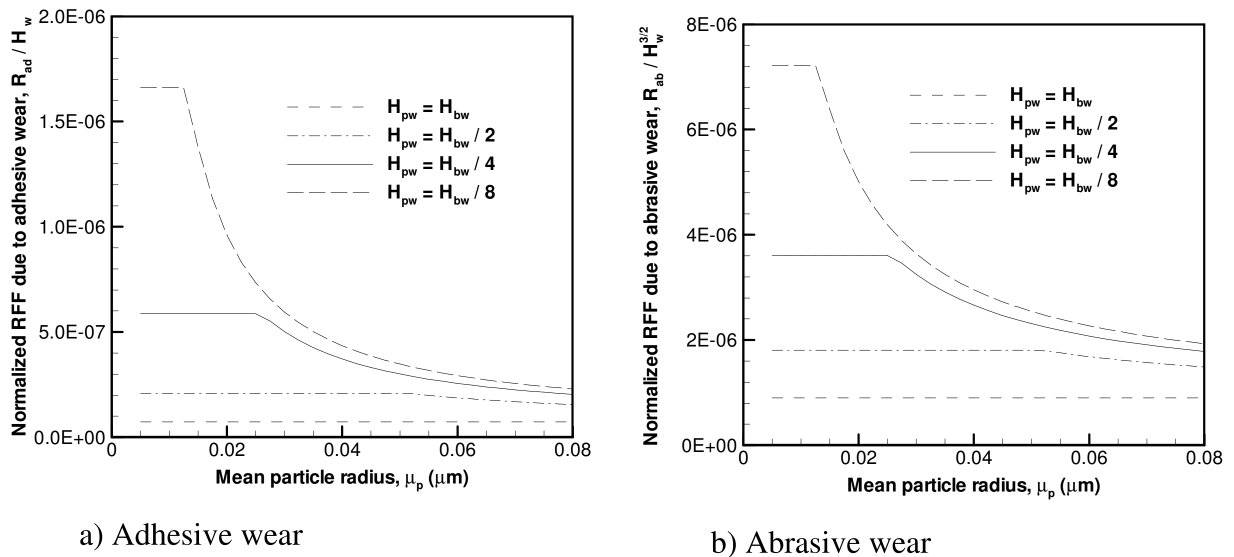

Fig. 7.81: The effect of mean particle radius μ_p on RFF due to a) adhesive wear R_{ad} and b) abrasive wear R_{ad} normalized with respect to effective wafer hardness (R_{ad} / H_w and R_{ab} / $H_w^{3/2}$) for different passivated surface hardness $H_{pw} < H_{bw}$ (t_{pw} = 4 nm).

hardness H_{pw} also decreases the critical particle size causing the particles to indent through the passivated layer. Fig. 7.81 shows that particle size μ_p affects MRR at a larger extend when the difference in hardness of bulk wafer H_{bw} and passivated layer H_{pw} increases due to smaller H_{pw}.

<u>Hard passivated surface layer</u>

Figs. 7.82-7.85 show the effect of passivated layer when passivated layer hardness is higher than bulk wafer hardness. The passivated layer hardness is kept constant, H_{pw} = 16000 MPa in Figs. 7.82 and 7.83, while passivated layer thickness of t_{pw} = 0.5 nm is used in Figs. 7.84 and 7.85. As indicated in the previous section, bulk wafer hardness dominates, $H_w \approx H_{bw}$ when passivated layer thickness is very small, e.g. t_{pw} = 0 and passivated layer hardness determines the contact behavior, $H_w \approx H_{pw}$ at very large passivated layer thickness e.g. t_{pw} = 2 nm. Due to the fact that hardness of passivated

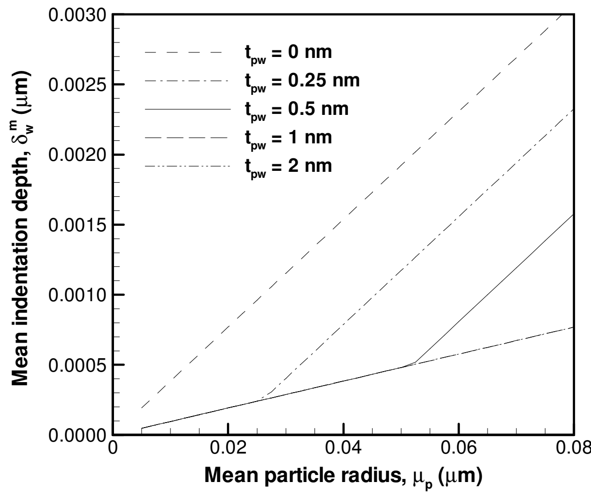

a) Mean indentation depth

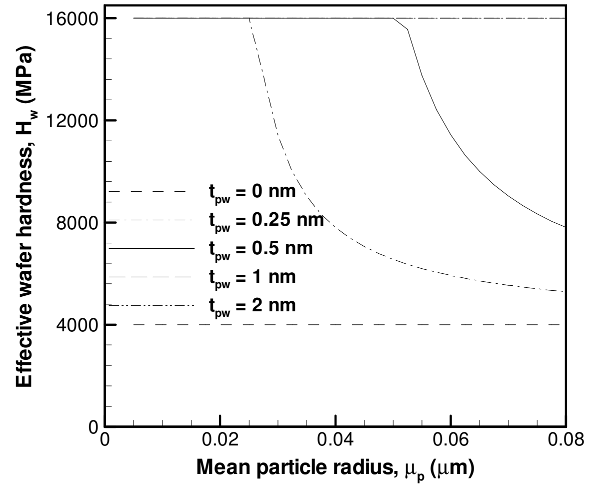

b) Effective wafer hardness

Fig. 7.82: The effect of mean particle radius μ_p on a) mean indentation depth δ_w^m and b) effective wafer hardness H_w for different passivated layer thickness t_{pw} (H_{bw}= 4000 MPa and H_{pw} = 16000 MPa).

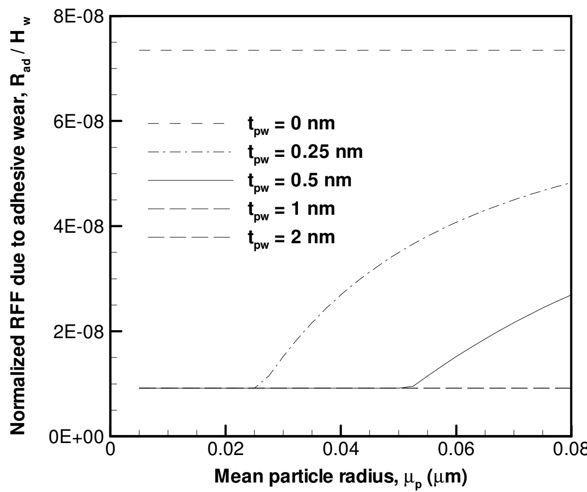

a) Adhesive wear

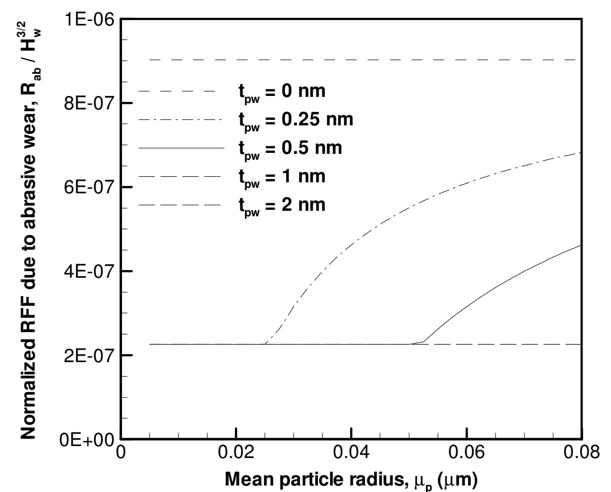

b) Abrasive wear

Fig. 7.83: The effect of mean particle radius μ_p on RFF due to a) adhesive wear R_{ad} and b) abrasive wear R_{ad} normalized with respect to effective wafer hardness (R_{ad} / H_w and R_{ab} / $H_w^{3/2}$) for different passivated layer thickness t_{pw} (H_{bw}= 4000 MPa and H_{pw} = 16000 MPa).

layer is greater than that of bulk wafer $H_{pw} > H_{bw}$, the indentation depth of particle δ_w^m becomes smaller when effective hardness is dominated by passivated layer hardness $H_w \approx H_{pw}$ as compared to bulk wafer hardness $H_w \approx H_{bw}$ (Figs. 7.82a and 7.84a). Figs. 7.83 and 7.85 show that RFF normalized by wafer hardness, R_{ad} / H_w or $R_{ab} / H_w^{3/2}$ increases as particle size becomes larger for intermediate values of passivated layer thickness. This behavior is opposite to that observed in the case of soft passivated layer.

7.7.3 Single asperity contact behavior

The interfacial particles trapped between pad and wafer alter the single asperity contact pressure distribution having an effect on RFF. Fig. 7.5 shows the error of Hertz contact in calculating the RFF due to adhesive R_{ad} and abrasive R_{ab} wear. It is seen that RFF due to both adhesive R_{ad} and abrasive R_{ab} wear increases with larger particle size in the range, 12.5 nm < μ_p < 50 nm in the case of a hard E_s = 100 MPa, porous E_s / E_p = 4 pad. At low

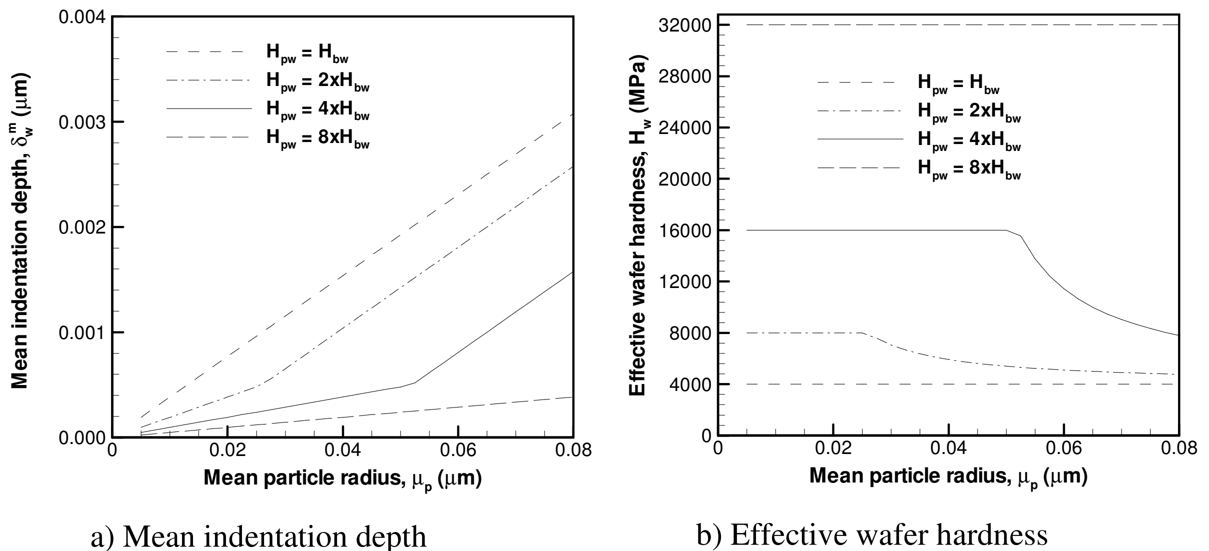

a) Mean indentation depth b) Effective wafer hardness

Fig. 7.84: The effect of mean particle radius μ_p on a) mean indentation depth δ_w^m and b) effective wafer hardness H_w for different passivated surface hardness $H_{pw} > H_{bw}$ (t_{pw} = 0.5 nm).

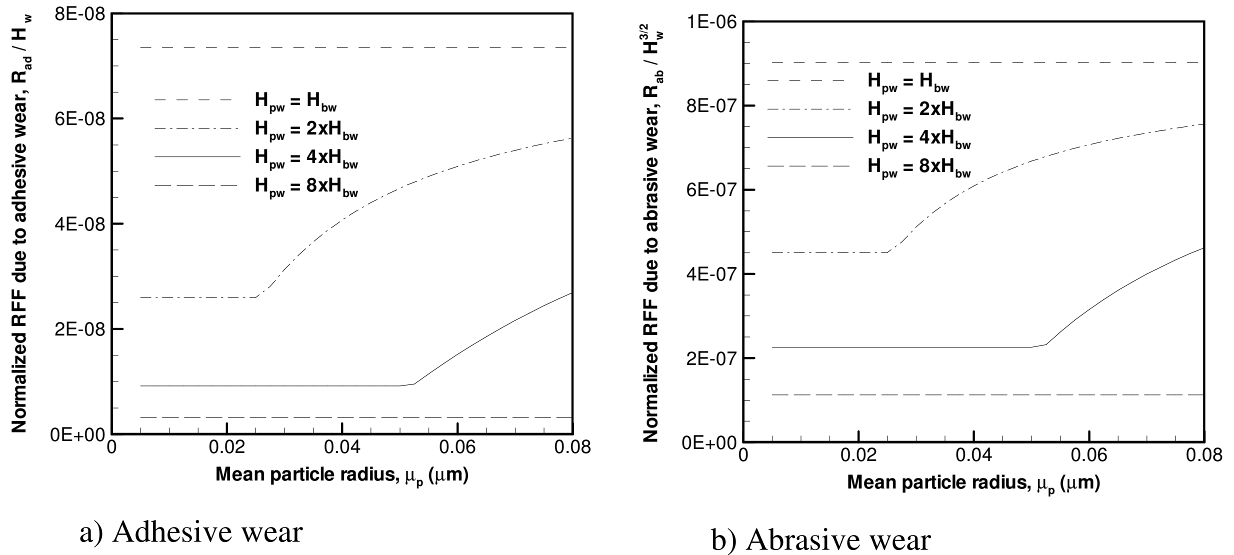

a) Adhesive wear

b) Abrasive wear

Fig. 7.85: The effect of mean particle radius μ_p on RFF due to a) adhesive wear R_{ad} and b) abrasive wear R_{ad} normalized with respect to effective wafer hardness (R_{ad} / H_w and R_{ab} / $H_w^{3/2}$) for different passivated surface hardness $H_{pw} > H_{bw}$ (t_{pw} = 0.5 nm).

applied pressure P_o = 0.007 MPa, RFF due to adhesive and abrasive wear increases by 10% and 6%, respectively when particle size is increased from 12.5 nm to 50 nm. The effect becomes smaller at high applied pressure, P_o = 0.07 MPa, where the increase for RFF due to adhesive and abrasive wear is 8% and 5%, respectively.

7.7.4 Comparison with experiments

The experimental findings show both increasing [29,30] and decreasing [21] trends for MRR with larger particle size, which is consistent with the results of the model. In addition to these trends, the effect of particle size was found to be different at low and high particle concentration [23,31]. The MRR was determined to increase with particle size when particle concentration is high (10-30 %), whereas an opposite trend was seen for small particle concentration (<5%) [23].

The magnitude of surface forces increase linearly with particle size ($f_s \propto \mu_p$) while the pad-particle contact force is proportional to $f_p \propto \mu_p^2$. Therefore, as particle size becomes

smaller, both surface forces and pad-particle contact force decrease at different rates, causing the relative magnitude of surface forces to increase. The proposed model indicates that MRR decreases with larger particle size if magnitude of attractive van der Waals forces between wafer and particle is greater than repulsive double layer forces. In the case of large double layer forces, MRR increases with larger particle size.

The passivated surface layer may have a hardness lower or higher than that of bulk wafer as explained in Section 2.2.4, which determines the variation of MRR with respect to particle size. This becomes an important factor when indentation depth of particles is larger than passivated layer thickness so that both passivated layer and bulk wafer hardness play a role. In the case where passivated layer hardness is lower than bulk wafer hardness, larger particle results in higher effective wafer hardness diminishing MRR. The opposite is true if passivated layer hardness is lower than bulk wafer hardness.

The model also indicates that MRR becomes larger with particle size due to the effect of particles on single asperity contact behavior. Note that the effect of particles on contact behavior is a strong function of parameters such as pad elastic modulus, pad topography, particle concentration etc.

One of the assumptions of the model is that particles embedded in pad material is assumed to slide over wafer surface, while another possibility for particles is rolling, which was shown to occur under some conditions in experiments [23]. In fact, some researchers [32,33] attributed the variation of MRR with respect to particle size at low and high particle concentrations to the dynamics of particle motion, where particles tend to roll in the case of high particle concentration and the tendency increases with larger particle size. This effect is not captured by our model.

7.8 Wear Mechanism

Adhesive and abrasive wear are the two wear mechanisms considered to contribute to the material removal. Material removal in a typical CMP process may be dominated by one of the wear mechanisms or may be a result of both wear mechanisms taking place simultaneously [13,34]. In this work, RFF is calculated by utilizing wear equations for each wear mechanism to obtain RFF for adhesive R_{ad} and abrasive wear R_{ab}. RFF can be then used to calculate MRR (*RR*) using Eqns (5.4) and (5.5), which requires relative velocity V_r, wafer hardness H_w and wear coefficient k_w for adhesive and abrasive wear respectively. Eqns (5.4) and (5.5) can be re-arranged to determine wear coefficient k_w as,

$$k_w^{ad} = \frac{RR_{ad} H_w}{R_{ad} V_r} \tag{7.4a}$$

$$k_w^{ab} = \frac{RR_{ab} {H_w}^{3/2}}{R_{ab} V_r} \tag{7.4b}$$

Eqn (7.4) is used to calculate wear coefficient for adhesive k_w^{ad} and abrasive wear k_w^{ab} by substituting the appropriate values for wafer hardness H_w = 1000 MPa, relative velocity (0.5 m/s is used if not specified in the experiments) and MRR (*RR*) measured in the experiments. The calculated values for wear coefficients k_w using modeling results for RFF and experiment results for MRR are compared with typical values for k_w reported in literature for different materials in order to evaluate the role of each wear mechanism in CMP. Typical values for adhesive wear coefficient is given as $10^{-5} < k_w^{ad} < 10^{-2}$ and abrasive wear coefficient (three-body wear) as $3 \times 10^{-4} < k_w^{ab} < 3 \times 10^{-3}$ [35].

Table 7.5 lists the parameters used in the CMP experiments for polishing copper films with alumina slurry. Note that the base parameters in Table 7.1 are used for other parameters not listed in Table 7.5. The assumed value of unknown parameters is given in parenthesis. These parameters are substituted in our model to find the wear coefficients (k_w^{ad} and k_w^{ab}) shown in Table 7.6.

It is seen in Table 7.6 that the adhesive wear coefficient varies in the range $2.2\text{x}10^{-4} < k_w^{ad} < 4\text{x}10^{-3}$, whereas abrasive wear coefficient is found to be varying as $2.1\text{x}10^{-3} < k_w^{ab} < 7.6\text{x}10^{-2}$. Comparing these values with the typical values for wear coefficients found in literature [35] ($10^{-5} < k_w^{ad} < 10^{-2}$ and $3\text{x}10^{-4} < k_w^{ab} < 3\text{x}10^{-3}$), it is seen that adhesive wear constant is within the range of typical values while an overlap between the range of calculated and typical values for abrasive wear coefficient is observed. Therefore it is concluded that both adhesive and abrasive wear is possible in CMP.

No	**Wafer**	**Particle**	**MRR nm / min**	η_w	**Pad**	P_o **psi**	V_r **m/s**	**Ref**
1	copper	alumina	230	2.5	IC1000 / hard	6.8	0.47	[10]
2	copper	alumina	110	2.5	Suba500 / soft	6.8	0.47	[10]
3	copper	alumina	775	3.1	(hard)	2.7	(0.5)	[11]
4	copper	alumina	945	3.1	(hard)	4.7	(0.5)	[11]
5	copper	alumina	165	3	IC1400 / hard	4	(0.5)	[15]
6	copper	alumina	140	3	PANW / soft	4	(0.5)	[15]
7	copper	alumina	100-1800	2.5	Suba500 / soft	2	1.3	[36]
8	copper	alumina	468	1.75	(hard)	7.1	0.28	[37]
9	copper	alumina	250	1.75	(hard)	4.3	0.28	[37]

Table 7.5: Experiment conditions.

No	k_w^{ad}	k_w^{ab}
1	3.8×10^{-4}	2.3×10^{-3}
2	2.3×10^{-4}	4.3×10^{-3}
3	2.4×10^{-3}	1.5×10^{-2}
4	1.7×10^{-3}	1.1×10^{-2}
5	3.5×10^{-4}	2.1×10^{-3}
6	3.6×10^{-4}	6.8×10^{-3}
7	$2.2 \times 10^{-4} – 4.0 \times 10^{-3}$	4.3×10^{-3} - 7.6×10^{-2}
8	1.8×10^{-3}	1.1×10^{-2}
9	1.5×10^{-3}	9.3×10^{-3}

Table 7.6: Wear coefficients calculated from models and experiments.

7.9 Optimization of CMP Parameters

The material removal efficiency can be maximized by eliminating the direct contact area, which can be achieved through optimization of CMP parameters. A closed-form equation (Eqn (6.32)) has been developed in Chapter 6 by considering constant particle size, uniform contact pressure across all pad asperities in contact and exponential distribution for asperity summit heights. Using the base parameters in Eqn (6.32), the optimum particle concentration η_w^c is determined to be 6% for a porous pad, $E_s / E_p = 4$. Note that the optimum particle concentration η_w^c does not vary with applied pressure P_o and pad elastic modulus E_s when Eqn (6.32) is used.

In the case of the model explained in Chapter 5 with variable particle size, non-uniform contact pressure at each asperity contact and Gaussian distribution for asperity summit heights, the optimum particle concentration η_w^c was shown to depend on applied pressure P_o and pad elastic modulus E_s in addition to the parameters in Eqn (6.32). It is seen that

as applied pressure P_o is increased or pad elastic modulus E_s is decreased, the optimum particle concentration η_w^c becomes greater as listed in Table 7.7. The optimum particle concentration for a hard pad (E_s = 100 MPa) was predicted well by Eqn (6.32) since only the asperities at the upper part of the Gaussian distribution is engaged in contact, where exponential distribution approximates the Gaussian distribution well. Therefore, Eqn (6.32) can be used to evaluate optimum CMP conditions especially for a hard pad (E_s = 100 MPa) in order to maximize the material removal efficiency as a function of pad topography, pad porosity and particle concentration as explained in Chapter 6.

P_o (MPa)	E_s (MPa)	η_w^c (%)	η_w^c (%) Eqn (6.32)
0.007	10	8.5	6
0.007	100	7	6
0.07	10	10	6
0.07	100	7.5	6

Table 7.7: Optimum particle concentration η_w^c for base parameters and E_s / E_p = 4.

References

1. Williams J. A., 2000. Engineering Tribology, Oxford University Press, UK.
2. Preston F.W., 1927. The theory and design of plate glass polishing machines. J Soc Glass Technol, 11, 214-256.
3. Shi F.G., Zhao B., 1998. Modeling of chemical-mechanical polishing with soft pads. Appl Phys A, 67, 249-252.
4. Ouma D. O., 1998. Modeling of chemical mechanical polishing for dielectric planarization. PhD Dis., MIT, Cambridge, MA.
5. Stein D. J., Hetherington D. L., Cecchi J. L., 1999. Investigation of the kinetics of tungsten chemical mechanical polishing in potassium iodate-based slurries. J Electrochem Soc, 146, 376-381.
6. Nguyen V. H., Daamen R., van Kranenburg H., et al., 2003. A physical model for dishing during metal CMP. J Electrochem Soc, 150, 689-693.
7. Clark A. J., Witt K. B., Rhoades R. L., 1999. Oxide removal rate interactions between slurry, pad, down force, and conditioning. 4th CMP-MIC Conference, Santa Clara, CA, 401-404.
8. Oliver M.R. (Editor), 2004. Chemical mechanical planarization of semiconductor materials. Springer Verlag, New York.
9. Chandrasekaran N., Ramarajan S., Lee W., 2004. Effects of CMP process conditions on defect generation in low-k materials. J Electrochem Soc, 151, 882-889.

10. Guo L., Subramanian R.S., 2004. Mechanical removal in CMP of copper using alumina abrasives. J Electrochem Soc, 151, 104-108.

11. Hernandez J., Wrschka P., Hsu Y., Kuan T. S., et al., 1999. Chemical mechanical polishing of Al and SiO2 thin films: the role of consumables. J Electrochem Soc, 146, 4647-4653.

12. Wrschka P., Hernandez J., Hsu Y., Kuan T. S., et al., 1999. Polishing parameter dependencies and surface oxidation of chemical mechanical polishing of Al thin films. J Electrochem Soc, 146, 2689-2696.

13. Ahmadi G., Xia X., 2001. A model for mechanical wear and abrasive particle adhesion during the chemical mechanical polishing process. J Electrochem Soc, 148, 99-109.

14. Luo J., Dornfeld D.A., 2001. Material removal mechanism in chemical mechanical polishing: Theory and modeling. IEEE Trans Semiconduct Manuf, 14, 112-133.

15. Saxena R., Thakurta D. G., Gutmann R. J., Gill W. N., 2004. A feature scale model for chemical mechanical planarization of damascene structures. Thin Solid Films, 449, 192-206.

16. Castillo-Mejia D., Gold S., Burrows V., Beaudoin S., 2003. The effect of interactions between water and polishing pads on chemical mechanical polishing removal rates. J Electrochem Soc, 150, 76-82.

17. Fury M., James D., 1996. Relationships between physical properties and polishing performance of planarization pads. SPIE Microelectronic Manufacturing Symposium, Austin, TX.

18. Moon Y., Park I., and Dornfeld D. A., 1998. Mechanical properties and relationship to process performance of the polishing pad in chemical mechanical polishing (cmp) of silicon. ASPE 1998 Spring Topical Meeting on Silicon Machining, Monterey, CA, vol 17, 78–82., 1998.

19. Moon Y., Park I., and Dornfeld D. A., 1998. Investigation of the relationship between Preston's coefficient and friction coefficient in chemical mechanical polishing (CMP) of silicon. ASPE 1998 Spring Topical Meeting on Silicon Machining, Monterey, CA, vol 17, 83–87, 1998.

20. Ng S. H., 2005. Measurement and modeling of fluid pressures in chemical mechanical polishing. PhD Dis., Georgia Inst. of Tech., Atlanta, GA.

21. Bielmann M., Mahajan U., Singh R. K., 1999. Effect of particle size during tungsten chemical mechanical polishing. Electrochem Solid State Letters, 2, 401-403.

22. Forsberg M., 2005. Effect of process parameters on material removal rate in chemical mechanical polishing of Si(1 0 0). Microelectron Eng, 77, 319-326.

23. Choi W., Abiade J., Lee S., Singh R.K., 2004. Effects of slurry particles on silicon dioxide CMP. J Electrochem Soc, 151, 512-522.

24. Cooper K., Eichenlaub S., Gupta A., Beaudoin S., 2002. Adhesion of alumina particles to thin films. J Electrochem Soc, 149, 239-244.

25. Park K., Jeong H., 2008. Investigation of pad surface topography distribution for material removal uniformity in CMP process. J Electrochem Soc, 8, 595-602.

26. Stein D. J., Hetherington D. L., Dugger M., Stout T., 1996. Optical interferometry for surface measurements of CMP pads. J Electron Mater, 25, 1623-1627.

27. Ramarajan S., Li Y., Hariharaputhiran M., et al., 2000. Effect of pH and ionic strength on chemical mechanical polishing of tantalum. Electrochem Solid State Letters, 5, 232-234.

28. Mazaheri A.R., Ahmadi G., 2003. A model for effect of colloidal forces on chemical mechanical polishing. J Electrochem Soc, 150, 233-239.

29. Tamboli D., Banerjee G., Waddell M., 2004. Novel interpretations of CMP removal rate dependencies on slurry particle size and concentration. Electrochem Solid State Letters, 7, 62-65.

30. Lai J. Y., 2001. Mechanics, mechanisms and modeling of the chemical mechanical polishing process. Ph.D. Dissertation, Massachusetts Institute of Technology, Massachusetts.

31. Mahajan U., 2000. Fundamental studies on silicon dioxide chemical mechanical polishing, University of Florida, Ph.D Thesis, FL.

32. Basim G.B., Adler J.J., Mahajan U., Singh R.K., Moudgil B.M., 2000. Effect of particle size of chemical mechanical polishing slurries for enhanced polishing with minimal defects. J Electrochem Soc, 147, 3523-3528.

33. Castillo-Mejia D., Beaudoin S., 2003. A locally relevant wafer-scale model for CMP of silicon dioxide. J Electrochem Soc, 150, 581-586.

34. Chen K. W., Wang Y. L., 2007. Study of non-Preston phenomena induced from the passivated additives in copper CMP. J Electrochem Soc, 154, 41-47.

35. Rabinowicz E., 1995. Friction and wear of materials. John Wiley & Sons, New York.

36. Sundararajan S., Thakurta D.G., Schwendeman D.W., Murarka S.P, Gill W.N., 1999. Two-dimensional wafer-scale chemical mechanical planarization models based on lubrication theory and mass transport. J Electrochem Soc, 146, 761-766.

37. Luo Q., Ramarajan S., Babu S. V., 1998. Modification of the Preston equation for the chemical-mechanical polishing of copper. Thin Solid Films, 335, 160–167.

CHAPTER 8

SUMMARY AND CONCLUSIONS

Modeling Approach

In this thesis, the *material removal rate* (MRR) in chemical mechanical polishing (CMP) was modeled from a mechanical contact perspective. The contact of a rough, deformable pad and a smooth, rigid wafer with interfacial rigid abrasive particles was analyzed. The interactions due to the 2-body contact between the pad and the wafer (*direct contact*) and 3-body contact between the pad, the abrasive particles and the wafer (*particle contact*) were considered.

In the model, the contact pressure at pad-wafer interface was carried by a combination of direct and particle contacts, where direct contacts were assumed to have negligible effect on the MRR, which was assumed to be due to wafer-to-particle contacts. Therefore, *material removal efficiency* defined as the fraction of applied pressure carried by particle contacts was used to evaluate the effectiveness of CMP process.

The effect of surface forces consisting of *van der Waals* and *electrical double layer* forces acting between wafer and abrasive particles were included. The wear rate of each abrasive particle was calculated based on the wafer-abrasive particle contact force and by considering *adhesive* and *abrasive wear* mechanisms. The chemical effects were included in the model by considering a *passivated surface layer* on the wafer with hardness and thickness that depend on the distance from wafer surface.

Modeling Results

In this work, the following effects were studied:

• ***Effect of particles on single asperity (SA) and multi-asperity (MA)contact***

The single asperity (SA) contact model showed that the contact pressure distribution due to single asperity contact in the presence of interfacial particles deviate from that of Hertz contact. In comparison to Hertz contact, the particles cause the contact pressure to be distributed over a larger area by decreasing the maximum contact pressure. In multi-asperity (MA) contact models built by using the SA and the Hertz contact models, similar MRR results were obtained. This was due to high asperity contact forces in the contact of a rough pad with a flat wafer under typical CMP conditions.

• ***Effect of pad elastic modulus on the MRR***

The modeling results showed that larger pad elastic modulus E_s causes the MRR due to both adhesive and abrasive wear to increase, where the rate of increase of the MRR was smaller for adhesive wear. An order of magnitude increase in pad elastic modulus E_s (E_s

= 10 MPa to E_s = 100 MPa) resulted in only ~18% higher MRR for adhesive wear, whereas the MRR increased by ~3.7-times for abrasive wear under the same conditions. This result was attributed to decreased tendency of particles to become embedded in the pad, and lowered direct contact area A_d for larger E_s values.

• ***Effect of pad porosity on the MRR***

The model showed that higher pad porosity (or increasing E_s/E_p = 1 to 4) causes the MRR due to adhesive and abrasive wear to increase by ~2.6-times and ~2.3-times, respectively. This effect was explained by considering the fact that the material removal efficiency becomes greater as the solid pad elastic modulus E_s increases, by decreasing the direct contact area A_d; or as the porous pad elastic modulus E_p decreases, by lowering the real contact pressure.

• ***Effect of particle concentration on the MRR***

The model shows that the MRR increases linearly with the particle concentration η_w when η_w is small. A saturation effect was observed at a critical saturation particle concentration η_w^c, above which the MRR due to adhesive wear remains constant. On the other hand, for $\eta_w > \eta_w^c$, the MRR due to abrasive wear was found to decrease. At the saturation particle concentration η_w^c, the number of active particles n_a is such that the particles start to prevent direct contact and the transition from mixed to particle contact regime occurs, where all the applied pressure P_o is carried by particle contacts, i.e. P_p / P_o = 1. Therefore, as the particle concentration η_w becomes higher in the range $\eta_w > \eta_w^c$, the fraction of applied pressure P_p / P_o carried by particle contacts does not change and the

MRR due to adhesive wear remains to be the same. Under the same conditions, the MRR due to abrasive wear starts to decrease with higher particle concentration η_w as the abrasive wear rate is also a strong function of the mean particle contact force. Therefore, this decrease in MRR for abrasive wear with higher particle concentration η_w is attributed to smaller mean contact force in the particle contact regime, as the same amount of load is distributed over more active particles in contact.

- ***Effect of pad topography on the MRR***

The standard deviation of pad roughness σ_s, asperity radius R_s, asperity density η_s were the parameters related to pad topography modeled in this work. The model results indicated that the MRR increases with smaller standard deviation of pad roughness σ_s, whereas larger asperity radius R_s, and asperity density η_s cause the MRR to decrease. This result was explained by the influence of pad topography on the "rough" contact of the pad and the wafer. As the contact is distributed over a larger area, the real contact pressure at the tip of the pad asperities decreases, thus the direct contact area becomes smaller while causing the material removal efficiency to increase. As a result, the MRR becomes greater due to greater material removal efficiency.

- ***Effect of surface forces on the MRR***

The electrical double layer forces f_{dl}^{sp} were calculated to be repulsive even in the case of same surface charges for wafer and abrasive particles since the separation distance between two contacting surfaces (wafer and abrasive) is small. The effect of double layer forces was therefore to decrease the MRR. The attractive van der Waals forces cause the

MRR to become larger. The relative magnitude of surface forces as compared to pad-particle force increases with smaller particle size μ_p and pad elastic modulus E_s. This is due to the fact that the pad-particle contact force decreases more rapidly with smaller particle size as $f_p^{sp} \propto 1/\mu_p^2$, in comparison to the surface forces, $f_s^{sp} \propto 1/\mu_p$. Furthermore the pad elastic modulus E_s does not have an effect on the magnitude of surface forces f_s^{sp}, whereas the pad-particle contact force f_p^{sp} increases with E_s. The MRR was found to depend on the slurry pH since the magnitude of double layer forces is a strong function of zeta potential of wafer and particles, which vary with the slurry pH.

- ***The variation of the MRR with applied pressure***

The non-linearity of the MRR with respect to applied pressure P_o, was quantified by applying a power law curve-fit in the form, $R = cP_o^n$. The model indicated both a linear and sub-linear variation for MRR with respect to applied pressure as the power law exponent was found to be in the range $0.85 < n < 1.1$. The sub-linear behavior was determined for a soft pad (e.g. $E_s = 10$ MPa) with high porosity (e.g. $E_s / E_p = 4$). The power law exponent decreased with decreasing particle concentration η_w and standard deviation of pad roughness σ_s. The number of active particles n_a was found to be a significant parameter affecting the variation of the MRR with respect to applied pressure P_o for a soft and porous pad. The sub-linear variation for the MRR was attributed to the variation of real contact area A_r, which becomes sub-linear for a soft pad with high porosity as the real contact area A_r controls the number of active particles n_a.

- ***Effect of particle size on the MRR***

The MRR becomes a function of particle size μ_p due to three different effects considered in the model: a) surface forces; b) effective hardness; and, c) single asperity contact behavior. As the particle size μ_p becomes smaller, the magnitude of surface forces f_s^{sp} relative to the pad-particle contact force f_p^{sp} increases. If the magnitude of repulsive double layer forces is greater than attractive van der Waals forces, $f_{dl}^{sp} > f_{vdw}^{sp}$, smaller particle size μ_p causes the MRR to decrease. The MRR increases with smaller particle size μ_p when the van der Waals forces are large $f_{vdw}^{sp} > f_{dl}^{sp}$.

The particle size μ_p plays an important role when the effect of passivated surface layer of wafer is considered. If the indentation depth of particles is greater than the passivated layer thickness $\delta_w^m > t_{pw}$, the effective wafer hardness H_w becomes a function of the indentation depth δ_w^m. Due to the fact that the indentation depth of particles δ_w^m increases linearly with particle size μ_p, the effective wafer hardness H_w for each μ_p is different. The passivated layer may be softer or harder than the bulk material depending on the compounds forming at the wafer surface due to the reactions between wafer and slurry chemicals. In the case of soft passivated surface layer, larger particle size μ_p results in lower MRR, while the opposite is true in the case of hard passivated surface layer.

In addition, the effect of particles on the single asperity contact behavior captured by the SA contact model depends on the particle size μ_p. As the particle size μ_p increases, the influence of particles on the contact pressure distribution between pad asperities and wafer becomes more prominent. Therefore, the contact is distributed over a larger area and the contact pressure is lower in the case of large particles, which causes the material

removal efficiency to be greater. As a result, the MRR increases with larger particle size μ_p.

• ***Effect of different wear mechanisms***

The wear coefficients for adhesive k_w^{ad} and abrasive wear k_w^{ab} were calculated by our model and from published experimental results. It was found that both adhesive and abrasive wear mechanisms are possible in CMP as the calculated values for wear coefficients were in the range of the typical values.

• ***Optimization of CMP parameters for maximum material removal efficiency***

A closed-form equation was developed in order to optimize the CMP parameters for maximizing the material removal efficiency based on the following assumptions: a) constant particle size; b) exponential distribution for the asperity summit heights; and, c) contact pressure at the pad asperity-wafer interface is equal to mean contact pressure for every pad asperity. The optimum CMP parameters for maximum material removal efficiency were calculated by considering that the mean contact pressure from rough contact is equal to the contact pressure in multi-particle contact model at the onset of the occurrence of direct contact.

The results for the optimum CMP parameters indicated that the optimum particle concentration η_w is determined by the porous elastic modulus ratio and standard deviation of pad roughness to asperity radius ratio σ_s / R_s. The applied pressure and particle size were shown to have no effect on the optimum particle concentration. The optimum

particle concentration η_w was found to decrease with larger porous elastic modulus ratio E_s / E_p or standard deviation of pad roughness to asperity radius ratio σ_s / R_s.

Future Work

- The hydrodynamic effects due to the slurry flow between the pad and the wafer was neglected in this work. As a result of this assumption, the MRR was taken to be linearly proportional to the relative velocity; however a non-linear variation for the MRR with respect to relative velocity is commonly determined in the experiments. The model may be improved by solving for the slurry flow using the Reynold's lubrication equation and coupling the results with the model presented in this work.

- In the model, the effect of surface forces was simulated by considering their effect on the contact force at the wafer-particle interface. The model results agree qualitatively with experimental observations for the variation of the MRR with slurry pH; however the model fails to predict the change in the MRR quantitatively. This is attributed to the effect of surface forces on the number of active particles. For example, if the surface forces are repulsive, the number of active particles is expected to become smaller. This effect may be simulated by solving for the slurry flow at pad-wafer interface and finding the frequency of collision between wafer and particle. This problem is similar to a common problem seen in the colloidal suspensions, where the agglomerate size of particles is determined by the collision frequency and the surface forces between the particles.

- The hardness and thickness of the passivated surface layer of wafer is an important input for the model. The model results may become sensitive to the slurry chemicals if the reaction kinetics models are incorporated in order to define the hardness and the thickness of the passivated surface layer as a function of slurry temperature and slurry chemicals. This model may be further enhanced by combining the reaction kinetics with the transport equations to find the concentration of the slurry chemicals using the slurry flow field solution.